Ion Cyclotron Range of Frequencies (ICRF) Power Coupling and Plasma Density Profile

Koppeling van het ICRF-vermogen en het profiel van de plasmadichtheid

Ivan Stepanov

Promotoren: prof. dr. ir. J.-M. Noterdaeme, dr. V. Bobkov
Proefschrift ingediend tot het behalen van de graad van
Doctor in de Ingenieurswetenschappen: Toegepaste Natuurkunde

Vakgroep Toegepaste Fysica
Voorzitter: prof. dr. ir. C. Leys
Faculteit Ingenieurswetenschappen en Architectuur
Academiejaar 2014 - 2015

UNIVERSITEIT
GENT

ISBN 978-90-8578-809-6
NUR 926, 928
Wettelijk depot: D/2015/10.500/53

Acknowledgements

I would like to express my appreciation and gratitude to my advisor, Prof. Jean-Marie Noterdaeme, for his patient guidance throughout this dissertation, discussions and advice on the structure of the thesis, and for providing the opportunity to continue the work after the completion of the contract at IPP Garching.

I am furthermore greatly indebted to the following people, without whom this work could not have been completed:

- Dr. Volodymyr Bobkov at the ICRF group, IPP Garching, for his invaluable help in planning and execution of the dedicated plasma experiments on ASDEX Upgrade, his advice and help with the overall structure of this work.
- Helmut Faugel, Helmut Fünfgelder, Gerhard Siegl, Franz Braun, Friedrich Fischer, and Bernd Eckert at the ICRF group, IPP Garching, for providing invaluable help with the planning, setup, execution and analysis of RF measurements, use of lab equipment, ASDEX Upgrade data storage and access.
- Dr. Rodolphe D'Inca, at the ICRF group, IPP Garching, for helping me learn use the ASDEX Upgrade data storage and access system, and extensive discussions about ICRF and fusion technology.
- Drs. Roberto Bilato and Marco Brambilla at the Dept. of Tokamak Physics, IPP Garching, for extensive and detailed explanations of the physics of the fast wave, as well as the theory and numerical modeling of ICRF antennas (Ch. 6).
- Dr. David Coster at the Dept. of Tokamak Physics, IPP Garching, for extensive discussions about the modeling and parametrization of the electron density profile, as well as his following and advice on the overall structure of this dissertation.
- Drs. Elisabeth Wolfrum and Rainer Fischer at the Dept. of Plasma Edge and Wall, IPP Garching, for valuable discussions about density measurement via Lithium beam and Integrated Data Analysis (IDA).
- Prof. Arne Kallenbach, Dr. Wolfgang Suttrop and Dr. Josef Schweinzer at the Dept. of Tokamak Scenario Development, IPP Garching, for assistance with the planning of the dedicated shots on ASDEX Upgrade.

- Dr. Daniele Milanesio, at the Dept. of Electronics and Telecommunications, Politecnico di Torino, for providing access to TOPICA, teaching me to use the code, and his support and valuable discussions of the results throughout this work.

- Dr. Riccardo Maggiora, at the Dept. of Electronics and Telecommunications, Politecnico di Torino, for the invitation to Torino, as well as reading this thesis and providing detailed feedback.

- Prof. Geert Verdoolaege, at the Dept. of Applied Physics, Gent University, for extensive advice and support with statistical analysis of experimental and simulated results, reading this thesis and providing detailed and useful feedback.

- Dr. Frédéric Durodié, at the Laboratory for Plasma Physics, Royal Military Academy, Brussels, for providing detailed descriptions of the ITER antenna and transmission network, and extensive support and advice regarding its analysis.

- Dr. Kristel Crombé, at the Laboratory for Plasma Physics, Royal Military Academy, Brussels / Dept. of Applied Physics, Gent University, for reading the thesis and providing feedback.

- Prof. Hendrik Rogier, at the Dept. of Information Technology, Gent University, for reading the thesis and providing feedback.

- Mr. Frank Janssens and Ms. Kathleen Van Oost, at the Dept. of Applied Physics, Gent University, for their invaluable help with formal procedures at Gent University.

- Mrs. Waltraud Sinz, IPP Garching, for her immense help with formal procedures at the IPP and search for accommodation in Munich.

Gent, March 2015
Ivan Stepanov

Dedication

This thesis is dedicated to my family: Sergei, Valeria, Nikolai, Victor, Flavia and Marion. Thank you for your love, support and patience.

Table of Contents

Acknowledgements **i**

Dedication **iii**

List of Acronyms **ix**

Summary (English) **xxxi**

Summary (Dutch) **xxxv**

1 Context, motivation and aim **1-1**
1.1 Introduction 1-1
1.2 Nuclear fusion as an energy source 1-1
1.3 Background and motivation 1-5
1.4 Aim and structure 1-7

2 The fast magnetosonic wave **2-1**
2.1 The dielectric tensor of a cold magnetized plasma 2-1
2.2 The fast wave dispersion relation 2-3
2.3 Cutoff and resonance layers 2-5
2.4 Fast wave polarization 2-6
2.5 Summary 2-7

3 Transmission line and antenna theory **3-1**
3.1 Transmission line theory 3-1
3.2 Antenna theory 3-6
3.3 Summary 3-10

4 Impedance measurement methods **4-1**
4.1 Introduction 4-1
4.2 Directional couplers 4-2
4.3 Voltage probe arrays 4-7
4.4 Voltage and current probe pairs 4-13
4.5 Experimental comparison of measurement methods 4-17
4.6 Standard measurement of coupled power, antenna impedance and loading resistance on ASDEX Upgrade 4-20

4.7 Determination of Z_T from Z_{inp} on each line on ASDEX Upgrade 4-24
4.8 Summary and conclusions 4-25

5 Implementation of voltage and current probes on ASDEX Upgrade 5-1
5.1 Introduction 5-1
5.2 Probe calibration 5-1
5.3 Testbed measurements 5-6
5.3.1 Low power 50 Ω testbed 5-7
5.3.2 Low power 25 Ω testbed 5-12
5.3.3 Medium power 25 Ω testbed 5-14
5.4 RF measurements with voltage and current probes on ASDEX Upgrade 5-18
5.5 Summary and conclusions 5-22

6 Numerical modeling of ICRF antennas 6-1
6.1 General remarks 6-1
6.1.1 FELICE 6-2
6.1.2 TOPICA 6-5
6.1.3 Rsolver 6-7
6.2 Computing the coupling resistance of a simple flat antenna: the Rsolver code 6-8
6.2.1 Fields in the plasma 6-8
6.2.2 Fields in the vacuum region 6-11
6.2.3 Finding the coupling resistance 6-13
6.3 Code implementation 6-15
6.4 Code applicability and validity domain 6-17
6.4.1 Integration length 6-18
6.4.2 Averaging of the n_e profile 6-21
6.4.3 Hydrogen concentration 6-24
6.5 Summary 6-25

7 Experimental studies of antenna coupling on ASDEX Upgrade 7-1
7.1 Introduction 7-1
7.2 Neutral gas injection 7-1
7.3 Plasma triangularity 7-3
7.4 Magnetic perturbation fields 7-17
7.5 Summary 7-21

8 Comparison of TOPICA results with experimental data on ASDEX Upgrade 8-1
8.1 Introduction 8-1
8.2 First comparison 8-3
8.3 Second comparison 8-9
8.4 Conclusions 8-25

9 Estimating ICRF power coupling from the plasma density profile 9-1
9.1 Introduction 9-1
9.2 Estimation of coupled power from fast code results 9-3
9.3 Dependence of R_C on the density profile 9-5
9.4 TOPICA simulations of the ITER antenna 9-9
9.5 Rsolver simulations of the ITER antenna 9-23
9.6 Summary 9-31

10 Summary and conclusions 10-1

List of Acronyms

4PJ	Four-port Junction

A

AORSA	All-ORders Spectral Algorithm
ASDEX	Axially Symmetric Divertor EXperiment
AUG	ASDEX Upgrade

B

BNC	Bayonet Neill-Concelman

D

DC	Direct Current, Directional Coupler
DCN	Deuterium Cyanide

E

ECRH	Electron Cyclotron Resonant Heating
ELM	Edge-Localized Mode

F

FELICE	Finite ELement Ion Cyclotron Emulator
FLR	Finite Larmor Radius
FW	Fast wave

G

GLS	Geodesic Least Squares

H

H-mode	High confinement mode
HFS	High Field Side

I

IDA	Integrated Data Analysis
ILA	ITER-like Antenna
ICRF	Ion Cyclotron Range of Frequencies
ICRH	Ion Cyclotron Resonance Heating
IO	ITER Organization
ITER	International Thermonuclear Experimental Reactor

J

JET	Joint European Torus

L

L-mode	Low confinement mode

LCFS	Last Closed Flux Surface
LFS	Low Field Side
LiB	Lithium Beam

M

MP	Magnetic Perturbation
MST	Medium-sized Tokamak
MTL	Movable Transmission Line
MWS	Microwave Studio

N

NA	Network Analyzer
NBI	Neutral Beam Injection
NRMS	Normalized Root Mean Square error
NSTX	National Spherical Torus eXperiment

O

OLS	Ordinary Least Squares

R

RF	Radio Frequency
RMS	Root Mean Square
RMSE	Root Mean Square Error
ROG	Radial Outer Gap
Rsolver	Resistance Solver
RVTL	Removable Vacuum Transmission Line

S

SCK	Swanson-Colestock-Kashuba

SOL	Scrape-off Layer
SS	Service Stub

T

TEXTOR	Tokamak EXperiment for Technology Oriented Research
TOPICA	TOrino Politecnico Ion Cyclotron Antenna

V

VCW	Vaccum Window
VSWR	Voltage Standing Wave Ratio
VTL	Vacuum Transmission Line

W

WKB	Wentzel-Kramers-Brillouin

List of publications

- Bobkov V., Jacquet P., Ochoukov R., Zhang W., Bilato R., Braun F., Carralero D., Colas L., Czarnecka A., Dux R., Faugel H., Fünfgelder H., Jacquot J., Krivska A., Lunt T., Milanesio D., Maggiora R., Meyer O., Monakhov I., Noterdaeme J.-M., Potzel S., Pütterich T., Stepanov I. and the ASDEX Upgrade Team. *Progress in Controlling ICRF-edge Interactions in ASDEX Upgrade.* To be published in the Proceedings of the 21st Topical Conference on Radiofrequency Power in Plasmas, 2015.

- Stepanov I., Noterdaeme J.-M., Bobkov V., Faugel H., Coster D., Milanesio D., Maggiora R., Siegl G., Bilato R., Brambilla M., Verdoolaege G., Braun F., Fünfgelder H., D'Inca R., Suttrop W., Kallenbach A., Schweinzer J., Wolfrum E., Fischer R., Mlynek A., Nikolaeva V., Guimarais L. and the ASDEX Upgrade team. *A detailed comparison of antenna impedance measurements at ASDEX Upgrade with the ICRF antenna code TOPICA.* Submitted to *Nucl. Fusion*.

- Bobkov V., Stepanov I., Jacquet P., Monakhov I., Bilato R., Colas L., Czarnecka A., Dux R., Faugel H., Kallenbach A., Müller H. W., Noterdaeme J.-M., Potzel S., Pütterich T., Suttrop W. and the ASDEX Upgrade team. *Influence of Gas Injection Location and Magnetic Perturbations on ICRF Antenna Performance in ASDEX Upgrade. AIP Conf. Procs.* **1580** (2014) 271-274.

- Stepanov I., Noterdaeme J.-M., Bobkov V., Coster D., Faugel H., Bilato R., Brambilla M., Suttrop W., Kallenbach A., Schweinzer J., Wolfrum, E., Fischer R., Mlynek A., Nikolaeva V., Guimarais L., Milanesio D. and the ASDEX Upgrade team. *Improved Measurements of ICRF Antenna Input Impedance at ASDEX Upgrade during ICRF Coupling Studies. AIP Conf. Procs.* **1580** (2014) 275-278.

- Faugel H., Bobkov V., Eixenberger H., Podoba Y., Stepanov I. and the ASDEX Upgrade team. *Upgrading the ICRF data acquisition system at ASDEX Upgrade. AIP Conf. Procs.* **1580** (2014) 378-381.

- Stepanov I., Noterdaeme J.-M., Faugel H., Fünfgelder H., Braun F., Bobkov V., Milanesio D. and the ASDEX Upgrade team. *Improved measurements of ICRF antenna coupling at ASDEX Upgrade and comparison with the ICRF coupling code TOPICA. Fus. Eng. Des.* **68** (2013) 990-993.

- Jacquet P., Bobkov V., Mayoral M.-L., Monakhov I., Noterdaeme J.-M., Scarabosio A., Stepanov I., Vrancken M., Wolfrum E. and the ASDEX Upgrade team. *Improvement of ICRF antenna loading by local gas injection on ASDEX Upgrade. Nucl. Fusion* **52** (2013) 042002.

- Faugel H., Bobkov V., Fünfgelder H., Siegl G., Stepanov I. and the ASDEX Upgrade team. *Measuring Impedance and Power in ICRF Antenna Feeding Lines with Voltage and Current Probes. AIP Conf. Procs.* **1406** (2011).

- Stepanov I., Van Wassenhove G., Dumortier P., Koch R., Messiaen A., Vervier M., Brezinsek S., Krämer-Flecken A., Schmitz O. and the TEXTOR team. *Analysis of ICRH antenna loading data in TEXTOR obtained during gas injection experiments. AIP Conf. Procs.* **1406** 2011.

List of Figures

1.1 A simplified schematic of a tokamak, showing the sources of the magnetic field and its resulting shape [1]. 1-4

3.1 Mapping of the complex z-plane onto the Smith chart (Γ-plane); image reproduced from [2]. 3-3

3.2 The ASDEX Uprade standard two-strap ICRF antenna and its principal components. 3-7

3.3 Schematic of the transmission network for one ASDEX Upgrade antenna, pre-2014 configuration. The lower and upper lines, feeding ports 1 and 2, are joined into a common line at the T-section. . 3-9

4.1 A generic directional coupler [3]. The isolated port (4) is terminated by a matched load. 4-2

4.2 Directivity errors in a directional coupler. The phasors V_{FWD} and V_{BWD} are the actual forward and reflected voltage amplitudes. V_{DBWD} is the fraction of forward voltage V_{FWD} "leaking" into the measurement port due to finite directivity; likewise V_{DFWD} is the fraction of reflected voltage V_{BWD} "leaking" into the measurement port. V_{TFWD} and V_{TBWD} are the forward and reflected amplitudes seen by the directional coupler as a result, due to finite directivity. 4-3

4.3 The effect of directivity on Γ measured with a directional coupler. With a given directivity value, the measured Γ can occupy any point in the gray region, centered around its true value. $P_{FWD} = 500$ kW. P_{BWD} is indicated for each case. The phase difference between the reflected and forward waves is $45°$. 4-5

4.4 The effect of directivity on measured $\Delta|\Gamma|$, $\Delta\Phi(\Gamma)$ and ΔP_{CPL}. The latter one is especially sensitive to directivity errors, even with D = 30 dB. 4-5

4.5 The effect of directivity on Γ measured with directional coupler, including coupling and phase errors $\Delta C = 0.1$ dB and $\Delta\phi = 1°$ respectively. Note that at high reflection the effect is noticeable even at high directivity. 4-6

4.6 The effect of directivity on measured $\Delta|\Gamma|$, $\Delta\Phi(\Gamma)$ and ΔP_{CPL}, with additional coupling and phase errors $\Delta C = 0.1$ dB and $\Delta\phi = 1^\circ$ respectively. Compare with Fig. (4.4). The results are noisy because here Δ does not represent the standard deviation of the resulting distribution function, but the maximum distance of an erroneous result from the expected one (10^6 runs for each value of $|\Gamma|$). 4-6
4.7 The effect of uncertainty in probe coupling factors (ΔC) and array position (Δx) on Γ. With a given uncertainty value, the measured Γ can occupy any point in the gray region, centered around its true value (black). $P_{FWD} = 500$ kW. P_{BWD} is indicated for each case. The phase difference between the reflected and forward waves is 45°. 4-8
4.8 The two feeding lines of antenna 2. E refers to the T-section (with the antenna side stub on top), H and J are strap feeding points. Voltage probes are labeled 2oUX and 2uUX on the upper and lower lines resp.; except 2oU1 and 2uU1 they are distributed among two straight segments on each line, separated by an elbow and two ceramic spacers, making it difficult to precisely determine their relative positions. Schematic provided by G. Siegl. 4-9
4.9 The effect of uncertainty in probe coupling factors (ΔC) and individual probe position (Δx) on Γ. 4-10
4.10 Voltage standing wave profile along the line, 8 probes with random variations in relative positions. Black circles represent the actual voltage sampled at the probe positions, black lines are the actual profiles, and gray lines are the profiles reconstructed from the "erroneous" measurements. 4-10
4.11 $\Delta|\Gamma|$, $\Delta\Phi(\Gamma)$ and ΔP_{CPL} as functions of $|\Gamma|$ for different values of (ΔC) and Δx, which now represents the uncertainty in the *relative* positions of the probes. 4-11
4.12 The effect of uncertainty in probe coupling factors (ΔC) and individual probe position (Δx) on Γ, 16 probes with a separation of 11.5 cm. 4-12
4.13 The effect of uncertainty in probe coupling factors (ΔC) and individual probe position (Δx) on Γ, 8 probes with a separation of 23 cm, roughly centered on voltage minimum. Points on the horizontal axis close to the center of the chart are cases where the fitting routine fails (see also Fig. (4.14)). 4-12
4.14 Voltage standing wave profile along the line, 8 probes with random variations in relative positions, centered roughly on the voltage minimum. Black circles represent the actual voltage sampled at the probe positions, black lines are the actual profiles, and gray lines are the profiles reconstructed from the "erroneous" measurements. Note the cases where the fitting routine fails altogether, visible as "flat" profiles (see also Fig. (4.13)). 4-12

4.15 The effect of uncertainty in probe coupling factors (ΔC) and individual probe position (Δx) on Γ, 8 probes with a separation of 23 cm, roughly centered on voltage maximum. 4-13
4.16 Voltage standing wave profile along the line, 8 probes with random variations in relative positions, centered roughly on the voltage maximum. Black circles represent the actual voltage sampled at the probe positions, black lines are the actual profiles, and gray lines are the profiles reconstructed from the "erroneous" measurements. Note the difficulty in resolving the voltage minimum, i. e., the results of the fit in gray can be significantly less "sharp" than the actual profiles, leading to the large radial spread on Fig. (4.15). This is in contrast with Figs. (4.10) and (4.14) - the closer the probes are to the minimum, the easier it is to resolve. 4-13
4.17 The effect of uncertainty in probe coupling factors (ΔC) and phase difference ($\Delta\phi$) on Γ. With a given uncertainty value, the measured Γ can occupy any point in the gray region, with the true value shown in black. $P_{FWD} = 500$ kW and P_{BWD} is indicated for each case. The phase difference between the reflected and forward waves is $45°$. 4-14
4.18 $\Delta|\Gamma|$, $\Delta\Phi(\Gamma)$ and ΔP_{CPL} as functions of $|\Gamma|$ for different values of (ΔC) and $\Delta\Phi$. Note that measurement of P_{CPL} is especially sensitive to $\Delta\Phi$. 4-15
4.19 The effect of uncertainty in probe coupling factors (ΔC) and phase difference ($\Delta\phi$) on R_L. Note the very high sensitivity to $\Delta\phi$. . . . 4-16
4.20 The effect of uncertainty in probe coupling factors (ΔC) and phase difference ($\Delta\phi$) on V_{max}. 4-17
4.21 Low-power testbed. 4-17
4.22 Low-power testbed (schematic). 4-18
4.23 Antenna diagnostics on one (of four) ASDEX Upgrade transmission network. Lengths are approximate and different for each system. Not shown are the voltage probe arrays on each 25 Ω feeding line. Note that is the pre-2014 feeding configuration. 4-20
4.24 Translation lengths and stub lengths. DC = directional coupler.L_{DC} = distance from directional couplers to generator side stub, L_S = distance between stubs, L_G = total length of generator side stub, L_A = total length of antenna side stub. 4-21
4.25 Sensitivity of Γ_T to errors in translation and stub length. The black circles near the center are the actual directional coupler measurements, whereas Γ_T itself is in the upper right corner. Note the very significant spread of the results for $\Delta x \geq 5$ cm. 4-23
4.26 Standard deviation of the distribution of R_L, for different values of ΔC and Δx. The actual situation on ASDEX Upgrade corresponds to $|\Gamma| \sim 0.9$. 4-23

4.27 Loading resistance and voltage maximum, $V_{FWD} = 4.2 \times 10^4$ kV, $\Delta C = 0.1$ dB, $\Delta x = 10$ cm. Real values in black, error values in gray. 4-24
4.28 Sensitivity of Γ_T to ΔC and $\Delta\phi$ on the upper and lower lines. The error values of Γ_T are plotted in gray (10^6 runs), while the correct value is black. The error values of Γ_U and Γ_L are omitted for clarity.4-25
4.29 to ΔC, $\Delta\phi$ and Δx on the upper and lower lines. The error values of Γ_T are plotted in gray (10^6 runs), while the correct value is black. Γ_U and Γ_L are omitted for clarity. 4-26

5.1 A photograph of the 50 Ω setup used for probe calibration, showing a portion of the 9" line with a mounted probe, adapter cone and network analyzer. 5-2
5.2 Typical calibration results on the 50 Ω setup. The wavelike variations in the first trace were found to be caused by multiple internal reflection in low quality cables, which was corrected in a subsequent calibration. 5-3
5.3 Close-up of the calibration curves for the voltage probes on systems 1-3. The original results (with the faulty cables) are displayed as smooth curves; the two noisier signals correspond to the recalibration of 2OU00 and 2UU00. The only difference between the original curves is a systematic vertical shift of a few tenths of a dB, since they were all calibrated using the same cables. 5-5
5.4 Close-up of the reconstructed calibration curves for the voltage probes on systems 1-3, displaying the same relative shift as the original curves. 5-5
5.5 The 50 Ω test setup. The adjustable load consists of a fixed 50 Ω termination and a 50 Ω coaxial stub tuner, with a variable length between 0 and 70 cm. 5-7
5.6 The 50 Ω test setup with voltage source, amplifier, RF detector/-data acq. system and power monitor. 5-8
5.7 Measurements of Γ by network analyzer during a trombone scan on the 50 Ω testbed. The four concentric "broken rings" correspond to parallel stub lengths of 10, 30, 50 and 70 cm (in order of descending radius). The small amplitude jump is due to results obtained with and without the additional 2.5 m between load and line output. 5-10
5.8 Measurements of Γ by voltage and current probes during a trombone scan on the 50 Ω testbed. No DC breaks. Bold black curves are NA measurements, blue dots are probe measurements. 5-10
5.9 Effect of adding (left) or subtracting (right) 0.5 dB to the voltage probe coupling. Bold black curves are NA measurements, blue dots are probe measurements. 5-11
5.10 Effect of adding (left) or subtracting (right) 7° to Φ_{IV}. Bold black curves are NA measurements, blue dots are probe measurements. . 5-11

5.11 Measurements of Γ by network analyzer and voltage/current probes during a trombone scan on the 25 Ω testbed, no DC breaks. Bold black curves are NA measurements, blue dots are probe measurements. 5-15

5.12 Measurements of Γ by network analyzer and voltage/current probes during a trombone scan on the 25 Ω testbed, with DC breaks connected at probe output. Notice the severe signal distortion. Bold black curves are NA measurements, blue dots are probe measurements. 5-15

5.13 Measurements of Γ by network analyzer and voltage/current probes during a trombone scan on the 25 Ω testbed, without DC breaks (blue) and with DC breaks connected at RF detector input (green). There is a significant amount of noise but the results coincide. Bold black curves are NA measurements, blue and green dots are probe measurements. 5-16

5.14 Measurements of Γ by network analyzer and voltage/current probes during a trombone scan on the 25 Ω testbed, with 30 dB RF amplifiers at probe output. Results without DC breaks (blue) and with DC breaks (red) are shown. There is a significant amount of distortion but the results coincide.Bold black curves are NA measurements, blue and red dots are probe measurements. 5-16

5.15 Γ measurements with probes 1OU00, 1OI00, detector #19, cables C1OU+C1UU and C1OI+C1UI. Bold black curves are NA measurements, blue dots are probe measurements. 5-17

5.16 Γ measurements with probes 2UU00, 2UI00, detector #22, cables C2OU+C2UU and C2OI+C2UI. Bold black curves are NA measurements, blue dots are probe measurements. 5-17

5.17 Γ measurements with probes 3OU00, 3OI00, detector #1, cables C3OU+C3UU and C3OI+C3UI. Bold black curves are NA measurements, blue dots are probe measurements. 5-19

5.18 Γ measurements on the medium power 25 Ω testbed, with probes 2UU00, 2UI00, detector #21 (left), probes 2OU00, 2OI00, detector #22 (right). Measurements with DC breaks are shown in red, without DC breaks in blue. Aside from small phase difference (seen as a vertical shift), the two measurements agree with each other, but not with the NA measurements (shown in black). Bold black curves are NA measurements, blue and red dots are probe measurements. 5-19

6.1 The complex model of an ASDEX Upgrade two-strap antenna, produced in GiD. The triangular mesh on the right is used is used as TOPICA input. 6-7

6.2 Antenna model. Straps shown on right. 6-9

6.3 Current (J_y) and coupled power (P) spectra for the AUG-like antenna model, at 30.0 and 36.5 MHz (right) with $k_y = 0$. The J_y spectra peak at $k_z = 7.727\ \mathrm{m}^{-1}$, the P spectra at 5 and 5.455 m^{-1} respectively. The input electron density profile is plotted on the left; note that in this example, the edge density is above cutoff. 6-16

6.4 Relation of coupling resistance computed by FELICE and Rsolver, for the same profiles and parameters. Although the proportionality factor and offset are different for the two frequencies, the results are clearly proportional to one another. 1242 simulation points are shown. 6-17

6.5 R_C computed by FELICE with different values of integration length ("alengr"), 30, 50 and 70 cm; the last case is the result of integration through the whole plasma slab (thickness is twice the minor radius) with a conducting wall at the HFS ($f_0 = 30$ MHz, 2 T on axis, 5% H in D, n_e and T_e profiles averaged over 50 ms windows). The results with 30 and 50 cm are essentially identical (red line hidden by green); the results with 70 cm and conducting wall are also very similar. The two groups are qualitatively different from one another. On the right the R_L measurements for the same shot are shown, antennas 2 and 3; the results with 30 and 50 cm clearly show a better qualitative agreement with the measurements. The difference in loading on the two antennas in the second half of the time interval shown here is due to local density profile modification by gas injection. 6-19

6.6 Several representative cases from Fig. 6.5, R_C plotted as function of integration length. The value of R_C is essentially constant throughout the plasma slab, with a jump happening when the ion-ion cutoff layer is included in the integration region. 6-20

6.7 The effect of ELMs on strap R_L. 6-21

6.8 Line-integrated pedestal density (top) and outer divertor current (bottom) during ELMs, shot 29823 (172 ELMs); three different time windows for ELM synchronization are shown. 6-22

6.9 R_C computed by FELICE corresponding to cases 1, 2 and 3, and with averages over 50 ms windows without ELM synchronization, plotted on top of the experimentally observed R_L on both straps of antenna 1 (voltage and current probe data). Selecting these time windows for ELM sync. reproduces only approximately a "stable" R_C as would be expected between ELMs, that is, changing only on time scales of ~ 1 second due to separatrix scans ($2-3$ and $4-5$ seconds approximately) and a global density increase at ~ 5.75 seconds. 6-23

6.10 R_C computed by FELICE corresponding to cases 1, 2 and 3, and with all available IDA profiles (1 ms resolution), plotted on top of the experimentally observed R_L on both straps of antenna 1 (voltage and current probe data). While the measured loading is constant between ELMs over the whole time window, the calculated R_C is not, due to fluctuations in the reconstructed density profile. This can be seen even when all profiles are used; R_C is lower by $\sim 1\ \Omega$ in the right half of the figure. Note also the gaps where no IDA data is available at the required time resolution, clearly visible around ~ 3.45, 3.525, 3.6, 3.7, 3.775 and 3.85 s. 6-24

6.11 R_C computed with Rsolver, using the same sequence of density profiles with different H concentration. The variation in loading due to the H fraction are significantly smaller than those due to density changes. 6-25

7.1 Time traces of separatrix position R_{sep} and upper triangularity in shots 29822, 29823 and 29833. 7-5

7.2 Shot 29822, time traces of RF measurements on antennas 1, 2 and 3 along with separatrix position R_{sep} and upper triangularity δ_U. Antenna coupling increases significantly from $t \simeq 6$ s on; coupling changes due to R_{sep} scans are also visible between 2-3 and 4-5 seconds. Each time trace displays the behavior of an individual strap (six in total), but the legend is omitted here and in similar figures for clarity; see Fig. 7.5. 7-6

7.3 Shot 29823, time traces of RF measurements on antennas 1, 2 and 3 along with separatrix position R_{sep} and upper triangularity δ_U. Antenna coupling increases significantly from $t \simeq 6$ s on; coupling changes due to R_{sep} scans are also visible between 2-3 and 4-5 seconds. 7-6

7.4 Shot 29833, time traces of RF measurements on antennas 1, 2 and 3 along with separatrix position R_{sep} and upper triangularity δ_U. Antenna coupling increases significantly from $t \simeq 6$ s on. 7-7

7.5 Antenna loading resistance versus upper triangularity in shots 29822, 29823 and 29833 (left to right). The small increase in R_L right after $\delta_U \approx 0.1$ in shot 29833 is consistent with a rapid density increase seen by the DCN interferometer. 7-7

7.6 Magnetic surface shape for several time points in shot 29822. Note that the plasma shape stays largely constant in front of the antenna, with the changes mostly taking place at the top of the plasma column. The poloidal positions of the density diagnostics are also shown. 7-8

7.7 DCN density signals, core and edge, in shots 29822, 29823 and 29833 (left to right). Only a portion of the edge density signal for shot 29833 is available. 7-9

7.8 Density profiles at constant δ_U, averaged over 0.5 s after ELM synchronization. 7-10
7.9 Shot 30629, time traces of RF measurements on antennas 1, 2 and 3 along with separatrix position R_{sep} and upper triangularity δ_U. Note that the increase in coupling is significantly smaller than in shots 29822 - 29833. 7-12
7.10 Antenna loading resistance versus upper triangularity in shots 30629, 30630 and 30631 (left to right). 7-12
7.11 R_L on antenna 1 (averaged over the two straps) and main chamber neutral flux density versus time, 5 to 7 seconds in all shots. It can be seen that R_L increases only in those shots where Γ_0^{main} also increases. 7-14
7.12 Antenna loading resistance versus main chamber neutral flux density Γ_0^{main}, all shots. A clear correlation is seen between R_L and Γ_0^{main}. 7-15
7.13 R_C computed with FELICE vs. R_L measured during shots 29822, 29823 and 29833. There is qualitative agreement between the simulated and the measured data, but a large spread can be seen in the code results as well. 7-16
7.14 R_C computed with FELICE and R_L measured in shot 29823 as function of time. 7-17
7.15 Time traces of separatrix position R_{sep} in shots 29851, 29861 and 29863, and B-coil current during shot 29861 (only one shot is displayed as the setup was virtually identical in all discharges). . . . 7-17
7.16 Shot 29861, time traces of RF measurements on antennas 1, 2 and 3 along with separatrix position R_{sep} and B-coil current (four current traces are shown in different colors). ELM reduction is observed when the B-coils are switched on, with the exception of the last interval. 7-18
7.17 Antenna loading resistance as a function of R_{sep} in shots 29851, 29861 and 29863, with and without magnetic perturbations. 7-19
7.18 Antenna loading resistance as a function of time in shots 29851, 29861 and 29863, at R_{sep} = const., with and without magnetic perturbations. 7-20
7.19 R_C computed with FELICE vs. R_L measured during shots 29851, 29861 and 29863. Notice the significant scatter. 7-22
7.20 R_C computed with FELICE vs. R_{sep}, with and without MPs, for shots 29851, 29861 and 29863. 7-22
7.21 Density profiles with and without MPs, averaged over the entire shot. 7-23

8.1 Position of the density diagnostics used for profile reconstruction by IDA, as well as the four ICRF antennas. 8-2
8.2 Antenna models for TOPICA input. The Faraday screen bars have been removed on all models for clarity. 8-3

8.3 Computed and measured reflection coefficients for antennas 1 and 3, shot 25634, flat baseline model. $\Delta\Phi$ is the phase difference between simulation and measurement for each point. Large differences in $|\Gamma|$ are observed, and the trend agreement is only partial. . 8-5
8.4 Computed and measured reflection coefficients for antennas 2 and 4, shot 25634, flat baseline and flat wide limiter models. $\Delta\Phi$ is the phase difference between simulation and measurement for each point. Large differences in $|\Gamma|$ are observed, and the there is no agreement in trend. 8-5
8.5 Computed and measured reflection coefficients for antennas 1 and 3, shot 25634, curved baseline model. There is substantial difference with the results of the flat baseline model, and here the agreement is significantly worse. 8-6
8.6 Computed and measured reflection coefficients for antenna 2, shot 25634, curved baseline model. There is substantial difference with the results of the flat baseline model. 8-6
8.7 Individual reflection coefficients for the two baseline antenna models. With the convention adopted here the indices 1 and 2 correspond to the lower and upper lines, respectively. Very little difference is seen between the two in terms of $|\Gamma|$. 8-7
8.8 Computed and measured reflection coefficients for antennas 1 and 3, shot 25654, flat baseline model. No agreement in trend is observed. 8-8
8.9 Computed and measured reflection coefficients for antenna 2, shot 25654, flat baseline model. No agreement in trend is observed. . . 8-8
8.10 Magnitude (a) and phase (b) of Γ, shot 29093, antenna 3. The increase and subsequent decrease in $|\Gamma|$ correspond to a scan in separatrix position, which is shown in Fig. 8.11. 8-11
8.11 Separatrix position time trace, shot nr. 29093. 8-11
8.12 Magnitude (a) and phase (b) of Γ, shot 29110, antenna 3. 8-13
8.13 Magnitude (a) and phase (b) of Γ, shot 29113, antenna 3. 8-13
8.14 Time traces of separatrix position R_{sep} and upper triangularity in shots 29822, 29823 and 29833. 8-14
8.15 Magnitude (a) and phase (b) of Γ, shot 29822, antenna 1. The average relative errors in $|\Gamma|$ are 9.3% and 6.5% (upper and lower line respectively). 8-15
8.16 Magnitude (a) and phase (b) of Γ, shot 29822, antenna 2. The average relative errors in $|\Gamma|$ are 9.0% and 6.8% (upper and lower line respectively). 8-16
8.17 Magnitude (a) and phase (b) of Γ, shot 29822, antenna 3. Excellent agreement is seen in $|\Gamma|$, with the exception of the downward 'spike' around ~ 5 seconds. The average relative errors in $|\Gamma|$ are 2.2% and 1.8% (upper and lower line respectively). 8-16

8.18 Magnitude (a) and phase (b) of Γ, shot 29823, antenna 1. The average relative errors in $|\Gamma|$ are 5.7%, 5.4% (upper and lower line respectively). 8-17

8.19 Magnitude (a) and phase (b) of Γ, shot 29823, antenna 2. The average relative errors in $|\Gamma|$ are 5.5%, 3.3% (upper and lower line respectively). 8-17

8.20 Magnitude (a) and phase (b) of Γ, shot 29823, antenna 3. Excellent agreement is seen in $|\Gamma|$ throughout the entire discharge. The average relative errors in $|\Gamma|$ are 1.8% and 1.6% (upper and lower line respectively). 8-18

8.21 Variations in separatrix shape at several times during shot 29822; it can be seen that the changes are mostly confined to the upper part of the plasma and do not occur in front of the antenna. The poloidal location of the diagnostics used for the reconstruction of the density profile is also shown. 8-18

8.22 IDA reconstruction of four representative n_e profiles from shots 29822 and 29823, used in FELICE. All profiles are ELM-synchronized and averaged over the indicated time window. The radial position of the antenna limiter and the approximate fast wave cutoff density ($\sim 3\times10^{18}$ m^{-3}) are also shown. Note that in the last two cases in both shots, the edge n_e is significantly above cutoff density. This causes an abrupt change in density at the aperture of the antenna cavity, since TOPICA assumes there is no plasma in the cavity; this in turn leads to a possible overestimation of $|\Gamma|$ at high δ_o. . . 8-19

8.23 Magnitude (a) and phase (b) of Γ, shot 29833, antenna 1. Agreement is similar to that observed in shots 29822 and 29823. 8-20

8.24 Magnitude (a) and phase (b) of Γ, shot 29833, antenna 2. Agreement is similar to that observed in shots 29822 and 29823. 8-20

8.25 Magnitude (a) and phase (b) of Γ, shot 29833, antenna 3. Agreement is similar to that observed in shots 29822 and 29823. 8-21

8.26 Magnitude (a) and phase (b) of Γ, shot 29990, antenna 2. 8-22

8.27 Magnitude (a) and phase (b) of Γ, shot 29990, antenna 3. 8-22

8.28 Results for all shots, antennas 1, 2 and 3. The agreement with antenna 3 is very good, while a substantially higher (than predicted) loading is observed on antennas 1 and 2. Because of the usually very high VSWR on the feeding lines during normal operation, even moderate differences in $|\Gamma|$ mean rather large relative differences in R_L. 8-23

8.29 Overall differences between measurement and simulation results. $\Delta\Phi$ is given in centimeters as equivalent mechanical length; the horizontal axis indicates the shot number from 29093 (1) to 29990 (7). 8-23

8.30 Magnitude of Γ, antennas 1 (a) and 2 (b), shot 29822, using correction factors calculated with the constraint of equal coupled power on both lines. There are substantial differences in coupling between the two antennas, as well as between the two straps of antenna 1. 8-25

9.1 Absolute error of the R_L computed by TOPICA, according to Eq. (9.1). All simulated shots are shown. For each antenna the values are the average over the two straps. 9-2
9.2 Relationship between TOPICA and Rsolver results, ASDEX Upgrade antenna. 9-4
9.3 Typical electron density profiles at ASDEX Upgrade and some associated parameters. On the L-mode profiles, the minimum ∇n_e point coincides with the cutoff position. 9-7
9.4 R_C predicted with the linear model of Eq. (9.7) versus the calculated R_C. 9-8
9.5 R_C predicted with the exponential model versus the calculated R_C. 9-10
9.6 Section through one of the eight triplets of straps and feeding vacuum transmission line, showing some relevant components. (1) Faraday screen, (2) RF current straps, (3) four-port junction, (10) removable vacuum transmission line (RVTL), (11) service stub, (13) rear vacuum window (VCW). Figure reproduced from [4]. . . 9-11
9.7 Coupled power per ITER launcher, given maximum values for voltage and/or electric field in different parts of the structure. In order to fulfill all requirements, the coupled power must stay below the minimum of all curves throughout the frequency range. The density profile used here is the "Low density SOL" case provided by IO. Figure reproduced from [4]. 9-13
9.8 The ITER ICRF antenna model used in TOPICA. 9-14
9.9 Port labeling for the integration of the $\mathbf{S_{20}}$ and 4-port junction matrices. 9-18
9.10 Electron density profiles used for the ITER simulations and the corresponding maximum coupled power. Profiles 1 to 10 are the ten rescaled ASDEX Upgrade profiles, while H and L (11 and 12 on the right) are the 'High' and 'Low' density cases provided by IO. The horizontal dashed line indicates the cutoff density corresponding to $k_{\|} \simeq 8.5$ m^{-1}. 9-22
9.11 Relationship between TOPICA and Rsolver results, ITER antenna. 9-24
9.12 Exponential model, shot 29823 only. 9-26
9.13 Exponential model, shots 29822, 29823 and 29833. 9-26
9.14 Simplest exponential model, shots 29822, 29823 and 29833. . . . 9-27
9.15 Analytical model, shots 29822, 29823 and 29833. 9-28

9.16 Exponential model with geodesical least squares, shots 29822, 29823 and 29833. The error bars are significantly larger than with ordinary least squares, because GLS takes into account the uncertainty on the predictor variables. 9-30
9.17 Power coupled by the ITER launcher (in MW) as function of ∇_{eff} and d_{co} computed with Eq. (9.61). The predicted values for the 'High' and 'Low' cases are indicated on the plot. 9-31

List of Tables

1.1 Estimated fossil fuel reserve and depletion times, assuming they are used to satisfy world energy needs at current levels [5]. 1-2

4.1 Measurement results at 36.5 MHz. Lines 2 and 3, where $|\Gamma| = 1$, correspond to open and short, respectively. 4-19
4.2 Translation lengths and stub lengths (offset included), A3, AUGD 29110. 4-21

5.1 Voltage/current probe measurements of coupled power and V_{max} in comparison with standard measurements, averaged over all available shots in the 2013 experimental campaign, no corrections; σ is the standard deviation. U and L stand for upper and lower line, respectively. 5-20
5.2 Phase correction factors at 30.0 MHz. 5-21
5.3 Phase correction factors at 36.5 MHz. 5-21
5.4 Voltage/current probe measurements of coupled power and V_{max} in comparison with standard measurements, averaged over all available shots in the 2013 experimental campaign, with the corrections from Tables 5.2 and 5.3. 5-21

6.1 Parameters used in the Rsolver code for an "AUG-like" antenna simulation. 6-15

7.1 Global parameters of the March 2013 discharges. I_P is plasma current (in MA), n_0 is central electron density (flattop end) in 10^{19} m^{-3}, B_0 is the toroidal field (in T), P_T (in MW) is the sum of NBI, ICRH (P_{IC}, maximum from standard diagnostics) and ECRH heating power, and f is the antenna operating frequency in MHz. 7-4
7.2 Global parameters of the April 2014 discharges. I_P is plasma current (in MA), n_0 is central electron density (flattop end) in 10^{19} m^{-3}, B_0 is the toroidal field (in T), P_T (in MW) is the sum of NBI, ICRH (P_{IC}, maximum from standard diagnostics) and ECRH heating power, and f is the antenna operating frequency in MHz. 7-11

8.1 ASDEX Upgrade discharges used in this study; δ_o is upper triangularity. 8-9

9.1 Absolute error of the results computed by TOPICA, averaged over all simulated shots excepting the abnormally high density cases. . 9-2
9.2 Results of fitting Eq. (9.7) with the parameters in (9.8) to the database; for each parameter, μ is the estimated value, σ is the standard deviation and t denotes the t-statistic. The parameter corresponding to each coefficient is indicated in parenthesis. 9-7
9.3 Results of fitting Eq. (9.7) with the parameters in (9.9) to the database; for each parameter, μ is the estimated value, σ is the standard deviation and t denotes the t-statistic. The parameter corresponding to each coefficient is indicated in parenthesis. 9-8
9.4 Results of fitting Eq. (9.10) to the database; for each parameter, μ is the estimated value, σ is the standard deviation and t denotes the t-statistic. The parameter corresponding to each coefficient is indicated in parenthesis. 9-9
9.5 Results of fitting Eq. (9.11) to the database; for each parameter, μ is the estimated value, σ is the standard deviation and t denotes the t-statistic. The parameter corresponding to each coefficient is indicated in parenthesis. 9-10
9.6 Parameters used in the Rsolver code for an ITER-like antenna simulation. 9-24
9.7 Results of fitting Eq. (9.58) to the database, profiles from shot 29823 only; for each parameter, μ is the estimated value, σ is the standard deviation and t denotes the t-statistic. 9-26
9.8 Results of fitting Eq. (9.58) to the database, profiles from shots 29822, 29823 and 29833; for each parameter, μ is the estimated value, σ is the standard deviation and t denotes the t-statistic. . . . 9-27
9.9 Results of fitting Eq. (9.60) to the database, profiles from shots 29822, 29823 and 29833; for each parameter, μ is the estimated value, σ is the standard deviation and t denotes the t-statistic. . . . 9-28
9.10 Results of fitting Eq. (9.58) to the database, profiles from shots 29822, 29823 and 29833, using the geodesic least squares method. 9-29
9.11 Selected parameters for the 'High' and 'Low' density cases. . . . 9-30

Summary (English)

ICRF power coupling is extremely sensitive to the shape of the electron density profile on the plasma edge, mainly because of the existence of a cutoff density, below which the fast wave is evanescent. This will be especially important in ITER due to the large antenna-plasma gap. Therefore it is desirable to know which features of the density profile are most relevant for coupling, and how the profile can be influenced in order to improve antenna coupling while staying within the constraints imposed by the need of protecting the plasma-facing components. Additionally, in view of the importance of the ICRF system for ITER, and the difficulty of reproducing tokamak-relevant plasma conditions outside of an actual fusion device, numerical modeling is crucially important for antenna design. The state of the art modeling tool, currently used to evaluate the ITER launcher (among other antennas) is the TOPICA (TOrino Politecnico Ion Cyclotron Antenna) code. In recent years, TOPICA has been extensively tested against experimental results obtained on Alcator C-Mod, Tore Supra, DIII-D and JET, and found to have good agreement with experimental data. However, one limitation of most of these studies is that the loading resistance, which is a real number, is used in the experiments as figure of merit for antenna performance; this implies that some information is lost because TOPICA produces complex quantities to characterize an antenna (namely scattering, impedance and/or admittance matrices). Another limitation is that the shape of the electron density profile in front of the antenna is usually not known in detail and assumptions of varying strength are normally used to reconstruct it. Because of the availability of detailed density diagnostics, particularly Lithium beam recombination spectroscopy, ASDEX Upgrade is suitable for a detailed TOPICA comparison with experimental data.

Therefore the first aim of the present work is to carry out a TOPICA comparison study using previously unavailable experimental data, in the form of both density and RF measurements, in order to refine the confidence limits of the code; the second is to find out whether, on the basis of measurements already done on ASDEX Upgrade and the corresponding TOPICA / fast code simulations, it is possible to predict the power coupling capability of the ITER launcher, given some characteristics of the density profile, without having to simulate each case separately.

The present work is composed of four main parts. First, we describe the im-

plementation of a new RF diagnostic system on ASDEX Upgrade, namely voltage and current probe pairs positioned close to the antenna input ports on each feeding transmission line. Besides from measuring RF parameters very close to the antenna input, unlike the directional couplers that constitute part of the standard RF diagnostics, the voltage/current probes are not affected by directivity errors due to high VSWR. We describe probe calibration, test stand experiments and actual experience during ICRF operation on ASDEX Upgrade. Although not yet fully independent from the standard RF diagnostics (directional couplers and maximum voltage probes), this system offers the possibility to measure the input impedance of each individual antenna port, which was not accessible with the standard diagnostics.

Second, we describe a series of dedicated experiments on ASDEX Upgrade where two methods of improving antenna coupling were tested, namely variation of the separatrix shape (triangularity) and non-axisymmetric magnetic perturbation fields (MPs). Antenna impedance was measured in detail using the voltage/current probe pairs. We observe that triangularity variation, within the limits of these experiments, does not significantly affect antenna loading; however, at high triangularity a strong increase in SOL density was observed in most discharges, with a corresponding increase in coupling, accompanied by a transition into a type-II ELMy regime. On the other hand, it was observed that antenna loading increases when the MP coils are switched on, leading to an improvement in coupling of 30% - 50%, independently of the perturbation field phasing.

Third, we present two studies comparing TOPICA simulation results with ASDEX Upgrade experimental data. The first uses RF data measured using standard diagnostics and a limited number of density profiles. The quantity compared was the complex voltage reflection coefficient Γ, with the results showing poor to moderate agreement (both in magnitude and phase) on all antennas. In contrast, the second study makes use of RF data measured with the new voltage/current probes and a wide variety of plasma density profiles, most of which were measured during the triangularity variation experiments referred to above. The agreement in magnitude of Γ is $< 9\%$ for antenna 1, $< 8\%$ for antenna 2 and $< 3\%$ for antenna 3, observed consistently in all analyzed shots. Errors in the phase of Γ appear to be systematic and related to line length measurement. Good agreement in loading trend is obtained for all antennas. The limitations, caveats and consequences of the comparison are discussed.

Fourth, we attempt to find empirical formulas to predict the power coupled on ITER as a function of selected plasma parameters. In order to do this, we first relate the results of TOPICA simulations to the results of a fast numerical code (Rsolver), which uses significantly simplified antenna and plasma models with much shorter running times. Second, using Rsolver we calculate the coupling resistance (another figure of merit of antenna performance) of a large number of density profiles which were measured on ASDEX Upgrade; we relate this coupling resistance to a set of selected profile parameters via a scaling law. This procedure is carried out both for ASDEX Upgrade and for ITER, where for the latter we use suitably rescaled ASDEX Upgrade profiles since only two are currently available for ITER. We

show that, at least in the form treated here, these empirical formulas do reproduce the main trends in antenna loading but are not good enough if accuracy of a few percent is required. However, we also show that, given certain conditions, Rsolver (or an equivalent fast code) can be used to estimate coupled power for any given plasma density profile, for a fixed set of antenna operational parameters, once a few TOPICA results are available.

Summary (Dutch)

Koppeling van vermogen door middel van ICRF is extreem gevoelig voor de vorm van het elektronendichtheidsprofiel in de plasmarand, voornamelijk vanwege het voorkomen van een cutoff-dichtheid waar beneden de snelle golf uitdovend is. Dit is in het bijzonder van belang voor ITER omwille van de grote afstand tussen de antenne en de plasma. Daarom is het wenselijk vast te stellen welke karakteristieken van het dichtheidsprofiel het meest relevant zijn voor de koppeling, en hoe het profiel beïnvloed kan worden om de antennekoppeling te verbeteren, rekening houdend met de vereiste randvoorwaarden ter bescherming van de eerste wand. Gezien het belang van het ICRF-systeem voor ITER en de moeilijk te reproduceren tokamak-relevante plasmacondities buiten een eigenlijke fusiemachine, is numerieke modellering bovendien cruciaal voor het ontwerp van antennes. De TOPICA-code (TOrino Politecnico Ion Cyclotron Antenna) is momenteel het state-of-the-art-instrument om onder meer de ITER-antenne te evalueren. Recent werd TOPICA uitgebreid getest door te vergelijken met experimentele resultaten afkomstig van Alcator C-Mod, Tore Supra, DIII-D en JET. Daarbij werd een goede overeenkomst met de experimentele data vastgesteld. Een beperking van de meeste van deze studies is echter dat de ballastweerstand, een reel getal, gebruikt werd als maat voor de antenneprestatie in de experimenten. Dit impliceert een verlies van informatie vermits TOPIC complexe grootheden produceert om de antenne te karakteriseren (namelijk verstrooiings-, impedantie- en admittantiematrices). Een andere beperking is dat de vorm van het elektronendichtheidsprofiel vr de antenne meestal niet in detail gekend is, waardoor gewoonlijk verschillende aannames, zwakke en sterkere, vereist zijn om het profiel te reconstrueren. Wegens de beschikbaarheid van nauwkeurige diagnostieken om de dichtheid te meten, in het bijzonder recombinatiespectroscopie met behulp van een lithiumstraal, is ASDEX Upgrade geschikt voor een gedetailleerde vergelijking tussen TOPICA en experimentele data.

Bijgevolg is de eerste doelstelling van dit werk een vergelijking tussen TOPICA en experimentele gegevens die eerder niet beschikbaar waren, in de vorm van zowel dichtheids- als RF-metingen, ten einde de betrouwbaarheid van de code te verbeteren. Het tweede doel is om vast te stellen, op basis van eerdere metingen op ASDEX Upgrade en overeenkomstige simulaties met behulp van TOPICA en snelle codes, of het mogelijk is het gekoppeld vermogen door de ITER-antenne te

voorspellen, gegeven enkele karakteristieken van het dichtheidsprofiel, zonder elk geval afzonderlijk te hoeven simuleren.

Dit werk bestaat uit vier delen. Om te beginnen beschrijven we de implementatie van een nieuwe RF-diagnostiek op ASDEX Upgrade, namelijk een stel gecombineerde stroom-spanningsprobes, gepositioneerd dichtbij de ingangspoorten van de antenne op elk van de inkomende transmissielijnen. Naast de mogelijkheid om de RF-parameters vlakbij de antenne-ingang te meten, bieden de probes het voordeel dat ze niet benvloed worden door richtingsfouten vanwege de hoge VSWR (voltage standing wave ratio). Dit in tegenstelling tot de directionele koppelingen die deel uitmaken van de standaard RF-diagnostieken. We beschrijven de ijking van de probes, experimenten op een testbank en directe ervaringen tijdens ICRF-operatie op ASDEX Upgrade. Hoewel nog niet volledig onafhankelijk van de standaard RF-diagnostieken (de directionele koppelingen en de maximum-spanningsprobes), biedt dit systeem de mogelijkheid om de ingangsimpedantie van elke afzonderlijke antennepoort op te meten, hetgeen niet mogelijk was met de standaard diagnostieken.

In het tweede deel beschrijven we een reeks specifieke experimenten op ASDEX Upgrade, waarbij twee methodes getest werden om de antennekoppeling te verbeteren, namelijk variatie van de vorm van de separatrix (triangulariteit) en niet-axisymmetrische magnetische storingsvelden (MSVs). De antenne-impedantie werd in detail opgemeten door middel van de stroom-spanningsprobes. We stelden vast dat variaties in de triangulariteit de antennebelasting niet significant be¨nvloeden, binnen de limieten van deze experimenten. Bij hoge triangulariteit werd in de meeste ontladingen echter een sterke stijging opgemerkt van de dichtheid in de SOL, die gepaard ging met een verbeterde koppeling en overgang naar het ELM-regime van het type II. Anderzijds werd vastgesteld dat de antenneweerstand toeneemt wanneer de MSV-spoelen ingeschakeld worden, met een verbeterde koppeling tot gevolg van 30 tot 50%, onafhankelijk van de fasering van het storingsveld.

Ten derde presenteren we twee studies waarin door TOPIC gesimuleerde resultaten vergeleken werden met de experimentele data van ASDEX Upgrade. In de eerste studie werden RF-data opgemeten met behulp van de standaard diagnostieken en een beperkt aantal dichtheidsprofielen. Hierbij werd de complexe spanningsreflectiecofficint Γ vergeleken. De overeenkomst bleek zwak tot matig (zowel in grootte als fase) voor alle antennes. In de tweede studie daarentegen, werd gebruik gemaakt van RF-gegevens die opgemeten werden door middel van de nieuwe stroom-spanningsprobes en een grote variteit aan plasmadichtheidsprofielen, waarvan de meerderheid afkomstig was van de bovengenoemde experimenten waarbij de triangulariteit gevarieerd werd. Wat de grootte van Γ betreft, was de overeenkomst beter dan 9% voor antenne 1, 8% voor antenne 2 en 3% voor antenne 3. Dit was een consistent resultaat voor alle geanalyseerde ontladingen. De fouten in de fase van Γ lijken systematisch van aard en gerelateerd aan de meting van de lengte van de transmissielijn. Een goede overeenkomst werd bekomen in de trend van de belasting voor alle antennes. De beperkingen, redenen tot voorbehoud en gevolgen van deze vergelijkingen worden besproken.

Ten slotte trachten we empirische formules te vinden die het gekoppeld ver-

mogen in ITER voorspelt in functie van een aantal plasmaparameters. Daartoe zoeken we vooreerst het verband tussen de resultaten van de TOPICA-simulaties en de resultaten van de snelle numerieke code (Rsolver). Deze laatste gebruikt een aanzienlijk eenvoudiger model voor zowel de antenne als het plasma, wat leidt tot een veel kortere looptijd. Vervolgens berekenen we met Rsolver de koppelingsweerstand (een andere maat voor de antenneperformantie) voor een groot aantal dichtheidsprofielen gemeten op ASDEX Upgrade. Daarna zoeken we het verband tussen deze koppelingsweerstand en een aantal specifieke profielparameters via een schalingswet. Deze procedure wordt zowel voor ASDEX Upgrade als ITER uitgevoerd. In het laatste geval gebruiken we adequaat herschaalde profielen van ASDEX Upgrade, vermits momenteel slechts twee profielen voor ITER zelf beschikbaar zijn. We tonen aan dat, in ons geval, deze empirische formules de algemene trend in the antenneweerstand wel degelijk reproduceren, maar een nauwkeurigheid van enkele procenten niet toelaten. Anderzijds tonen we eveneens aan dat, onder specifieke voorwaarden, Rsolver (of een equivalente snelle code) gebruikt kan worden om het gekoppeld vermogen te schatten voor een willekeurig gegeven plasmadichtheidsprofiel en een aantal antenneparameters, op basis van enkele TOPICA-resultaten.

1 Context, motivation and aim

1.1 Introduction

The subject of this thesis is ion cyclotron resonance heating, or ICRH for short; it is a method of increasing the fuel temperature in a magnetic confinement fusion device, so that fusion reactions can occur. In order to place ICRH in context, Section 1.2 gives a very brief overview of nuclear fusion as an energy source and the practical methods developed so far in pursuit of this goal. The role of ICRH in this endeavor is then introduced, and finally the motivation and aim of this work are stated in sections 1.3 and 1.4.

1.2 Nuclear fusion as an energy source

Global energy demand is expected to grow from the current $\sim$ 14 TW to about 30 TW by 2050 [6]. At present, 80% of global energy consumption is based on fossil fuels [7]. This has caused a sustained growth in the concentration of CO_2 and other greenhouse gases in the Earth's atmosphere, leading to a steady increase in global temperatures.

Because of their direct role in climate change, increasing the use of fossil fuels to meet growing energy demands is not an option; even if their use were not associated with climate change, depletion of these resources in the relatively near future makes them unusable for sustaining a long-term technological society. Table 1.1 shows an estimate of the energy available from coal, oil and natural gas,

Resources	Global reserve in GJ	Depletion time
Coal	3×10^{14}	500 years
Oil	2×10^{13}	30 years
Natural gas	2×10^{13}	30 years

Table 1.1: Estimated fossil fuel reserve and depletion times, assuming they are used to satisfy world energy needs at current levels [5].

along with depletion time assuming they are used for global power consumption *at current rates*.

The remaining choices are 'conventional' renewable energy sources, such as wind and solar, nuclear fission and nuclear fusion. Renewable energy sources have an important role to play in the solution of the energy problem; however, they cannot maintain a constant power output, e. g. solar power is dependent on the time of the day, weather conditions and latitude. Furthermore, they suffer from low energy densities. Energy storage systems that have to be implemented to mitigate these disadvantages inevitably produce significant losses [6]. Nuclear fission offers an alternative that is both high in energy density and free from greenhouse emissions; however, it faces political hurdles in many countries [6]. In addition to this, world reserves of ^{235}U are estimated to be 10^{13} GJ, for a depletion time of 20 years if used to sustain present energy consumption levels [5]. This could be extended to about 20,000 years by the use of breeder reactors, but would bring about production of ^{239}Pu as an intermediate step [5] and the associated nuclear proliferation issues.

Controlled nuclear fusion offers another alternative. Although many fusion reactions are possible, deuterium (D) and tritium (T) constitute the fusion fuel relevant for short-term reactor development. The reaction results in an α-particle (a ^{4}He nucleus) and a neutron, and releases 17.6 MeV of energy [8]:

$$\mathrm{D} + \mathrm{T} \rightarrow \alpha + \mathrm{n} + 17.6\ \mathrm{MeV}. \tag{1.1}$$

This choice of fuel is primarily due to the low temperature required to make the reaction self-sustaining; note that this temperature is around 1.5×10^8 K and is only 'low' in comparison to that required to initiate other fusion reactions, such as D-D or D-^{3}He, which would otherwise be more attractive due to their low neutronicity.

The advantages of fusion as an energy source are already apparent from Eq. (1.1). First of all, fusion is a very energetic process. The energy release in the D-T reaction is equivalent to 338×10^6 MJ/kg; this is 8.5×10^6 times more energetic than e. g. gasoline burning, which produces ~ 40 MJ/kg [8]. Second, fuel is abundant: the basic fuels are deuterium and lithium (which is used to breed tritium) with a total energy content of about 10^{19} GJ in the oceans, for a depletion time of ten million years if used to sustain present energy consumption levels [5]. Third,

fusion reactions do not produce toxic or greenhouse gases; structural materials will be activated due to the high neutron flux from the reactions but storage time will be of the order of 100 years with appropriately chosen materials [9], extremely short when compared to the equivalent times for fission products. Finally, a Chernobyl-type accident is ruled out since no chain reaction is involved, and - in contrast to fission power plants - very small amounts of fuel, namely a few grams, are present in the reactor at any given time. Fusion is therefore an efficient, environmentally friendly, and safe energy source with an abundant and readily available fuel supply.

Because the fuel nuclei are positively charged, they need to collide with a sufficiently high energy to overcome the Coulomb repulsion. For a macroscopic mass of fuel this means, in practice, that the reactants must be brought to a high temperature. For D-T fusion, the optimum operating temperature is $15 - 20$ keV [8], that is $150 - 200$ million Kelvin. This has two important implications: first, that the fuel exists as fully ionized plasma and second, that material walls cannot be used to confine it. Two confinement methods are currently used: *inertial* and *magnetic*.

In *inertial confinement fusion* (ICF), a D-T pellet is compressed and heated by an array of laser beams, either directly or by irradiating a high-Z *hohlraum* surrounding the target and making use of the X-ray radiation thus produced [10]. The outer layers of the fuel capsule are ablated and exert inward pressure, this compressing and heating the capsule. The name for this scheme is thus derived from the fact that it is the inertia of the pellet itself that prevents expansion of the fuel during the burn. The National Ignition Facility at the Lawrence Livermore National Laboratory in California is currently the largest ICF project in the world, delivering 4 MJ to the target at a power level of 500 TW [10].

The *magnetic confinement* method, on the other hand, makes use of the Lorentz force acting on charged particles and hence relies on strong magnetic fields (typically several Teslas) to confine a low-density plasma. Current research is focused on closed configurations, i. e. geometries where the confined plasma is bent back onto itself to avoid end losses; this produces toroidal shapes of varying degree of symmetry. The magnetic field in such configurations usually forms nested surfaces of constant intensity that are perpendicular to the plasma pressure gradient, that is $\mathbf{B} \cdot \nabla p = 0$. In order to prevent plasma loss due to particle drift, the field lines must connect the inner and outer regions of the plasma torus and so the magnetic field has a helical shape on each surface [11]. Therefore the magnetic field has two components, *toroidal* - along the torus - and *poloidal*, perpendicular to it. The toroidal component of the field is always produced by external coils, whereas the poloidal component is produced either by a current flowing in the plasma, in which case the configuration is called a *tokamak*, or by specially shaped external coils, in which case the configuration is called a *stellarator*. Fig. 1.1 shows a simplified schematic of a tokamak, with the sources and the resulting shape of the magnetic

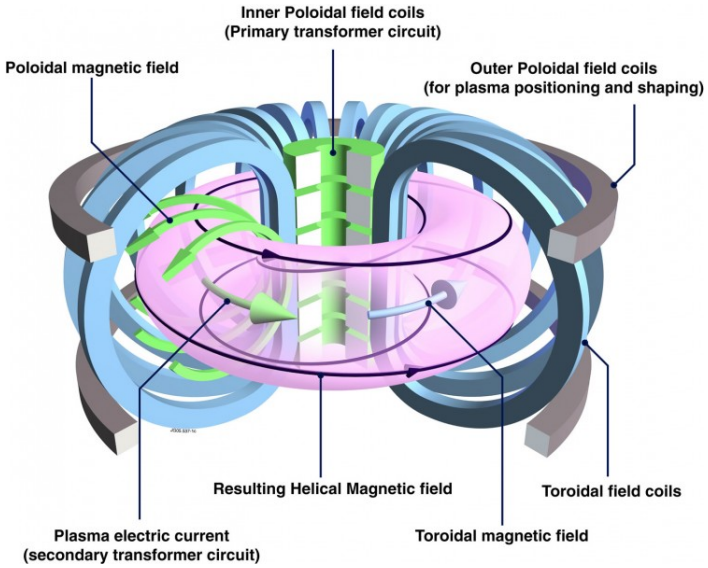


Figure 1.1: A simplified schematic of a tokamak, showing the sources of the magnetic field and its resulting shape [1].

field. Tokamak research began in the USSR in the 1960s, the concept was invented by Andrei Sakharov and Igor Tamm [9]; the International Thermonuclear Experimental Reactor (ITER), being built in France by China, the European Union, India, Japan, Korea, Russia and the United States is a tokamak and aims at demonstrating a fusion power output of 500 MW with an external input of 50 MW, i. e. a power gain factor of 10 [12]. Stellarators offer several operational advantages over tokamaks but are significantly more complex to design; invented in 1952 by Lyman Spitzer at Princeton, they had been initially outperformed by tokamaks but are being greatly improved with the advent of supercomputers. A large optimized stellarator, Wendelstein 7-X, has been completed in 2014 at the Max-Planck-Institut für Plasmaphysik in Greifswald, Germany and aims to demonstrate steady-state plasma operation for up to 30 minutes [13].

Both tokamaks and stellarators require external heating systems in order to raise the temperature of the plasma to the 15 keV required for fusion. Three techniques are commonly used to achieve this goal: ohmic heating, neutral beam injection (NBI) and electron/ion cyclotron resonance heating (ECRH/ICRH). Ohmic heating, as the name implies, induces a strong electrical current in the plasma whose kinetic energy is dissipated as heat. However, plasma resistivity decreases with temperature as $T_e^{-3/2}$ and maximum current is limited by magnetohydrodynamic instabilities; achievable plasma temperatures are below ~ 4 keV. NBI, on the other hand, focuses intense beams of neutral particles that deposit energy

in the plasma through collisions. Two neutral beam injectors will be installed in ITER, for a total power of 33 MW. Finally, ECRH/ICRH makes use of externally launched electromagnetic waves, which are absorbed by a population of electrons or ions in a selected layer within the plasma. ICRH is described in more detail in the next section, and related to the motivation of the present work.

1.3 Background and motivation

Ion cyclotron resonance heating (ICRH) has been successfully used as an auxiliary heating system in magnetic confinement experiments from the beginning of controlled fusion research, starting with the B-65 stellarator at Princeton in 1958 [14]. In ICRH, an electromagnetic wave is excited in the plasma by an external antenna structure, such that its frequency matches the cyclotron frequency of an ion species at some location in the plasma. At that point, the electric field rotates in phase with the particle motion; power is transferred from the wave to the particles by resonant absorption. A non-maxwellian resonant population builds up against the restoring force of collisions between this population and the remainder of the plasma, and this collisional process heats the background plasma [15]. ICRH systems usually operate in the 10 - 100 MHz range and are capable of coupling several megawatts of RF power to the plasma per antenna. Because waves in this frequency range are also used for non-inductive current drive and wall conditioning in fusion devices, the acronym commonly used is ICRF, for Ion Cyclotron Range of Frequencies.

In addition to its routine use in almost all present-day medium and large fusion devices such as JET, ASDEX Upgrade, DIII-D, Alcator C-Mod, Tore Supra, JT-60 and others, ICRH is one of the auxiliary heating systems to be implemented in the International Thermonuclear Experimental Reactor (ITER) currently being built in St.-Paul-lès-Durance, France, whereby the first plasma is expected in 2020. The ITER ICRF system includes two antennas, each designed to couple up to 20 MW of RF power to the plasma in the 40 - 55 MHz range [16]; each launcher is an array of 4 toroidal by 6 poloidal RF current straps, inserted as a port plug into one of ITER's vacuum vessel ports [4].

At this point we stress two important issues. The first is that ICRF power coupling is extremely sensitive to the shape of the electron density profile on the plasma edge, mainly because of the existence of a minimum cutoff density, below which the fast wave is evanescent; this is described in detail in Chapter 2. This will be especially important in ITER due to the large antenna-plasma gap [17]. Therefore it is desirable to know which features of the density profile are most relevant for coupling, and how the profile can be influenced in order to improve antenna coupling while staying within the constraints imposed by the need of protecting the plasma-facing components. The second issue is that, in view of the importance of the ICRF system for ITER, and the difficulty of reproducing

tokamak-relevant plasma conditions outside of an actual fusion device, numerical modeling is crucially important for antenna design. The state of the art modeling tool, currently used to evaluate the ITER launcher (among other antennas) is the TOPICA (TOrino Politecnico Ion Cyclotron Antenna) code. In recent years, TOPICA has been extensively tested against experimental results obtained on Alcator C-Mod [18], Tore Supra [19], DIII-D [20] and JET [21], and found to have good agreement with experimental data. However, one limitation of most of these studies is that the *loading resistance* R_L is used, which is a *real* number used as figure of merit for antenna performance in the experimental community; this implies that some information is lost because TOPICA produces *complex* quantities to characterize an antenna (namely scattering, impedance and/or admittance matrices). Another limitation is that the shape of the electron density profile in front of the antenna is usually not known in detail and assumptions of varying strength are normally used to reconstruct it.

A driving motivation for the present work is therefore the need to further test TOPICA in detail. ASDEX Upgrade possesses very detailed density diagnostics which are very well-suited for this purpose. Furthermore, in this work we have taken significant steps towards the development of a detailed RF diagnostic system, with the aim of measuring the *complex* input impedance of each antenna port. This system, consisting of voltage and current probe pairs located close to the antenna ports, while not yet fully independent, provides information not previously available on ASDEX Upgrade and offers significant advantages for the validation of TOPICA or any other ICRF antenna code.

A second motivation for this work is the need to study, as stated above, which features of the density profile most affect antenna coupling. An extensive study of this kind has already been undertaken for the ITER antenna, approximating the profile by an *a priori* analytical model [22]. In this work, in contrast, we opt for a statistical approach, taking a large number of density profiles which were actually measured during operation at ASDEX Upgrade and keeping the shape *as is*, and calculating for each case a figure of merit for the performance of an AUG-like antenna (in this specific instance the *coupling resistance* R_C). We then look for a statistical relationship between R_C and selected features in the density profiles. Due to computational cost, TOPICA is not suitable to carry out the large number of simulations required in this approach, and therefore we use somewhat simpler but faster codes for this purpose. The already existing Finite ELement Ion Cyclotron Emulator (FELICE) code is well suited for this task; however it was not yet available at the time and another fast code, Rsolver (for *resistance solver*) was written, implemented and used for the statistical study.

A related issue is the ability to modify the density profile during operation by external means, either locally or globally, in order to improve antenna coupling. Altering the properties of the SOL by puffing neutral gas close to the antenna

location has been investigated on several tokamaks (see for instance [17], [23], [24], [25], [26] and [27]), as well as changes in the magnetic surface shape ([28] and [29]). In this work, the results of a series of experiments on ASDEX Upgrade are reported where we have investigated the effect of changing triangularity on antenna coupling, as well as the effect of non-axisymmetric magnetic perturbation fields.

1.4 Aim and structure

Having extensively tested TOPICA against experimental data obtained on ASDEX Upgrade and determined the empirical relationship between the "AUG-like" antenna performance and selected features of the density profile, we use TOPICA to evaluate the performance of the ITER ICRF antenna for a reduced number of density cases. The fast code Rsolver is used once again to derive a statistical relationship between the performance of this antenna and selected density features, as in the AUG case. Keeping certain caveats in mind, a tentative empirical formula is then proposed to predict the ITER antenna coupling as a function of these density features, within a specified applicability domain. The (ideal) aim of the present work is then *to investigate whether, on the basis of measurements already done on ASDEX Upgrade and the corresponding TOPICA / fast code simulations, it is possible to predict the power coupling capability of the ITER launcher, given some characteristics of the density profile, without having to simulate each case separately.* We will see that the answer to this question is far from unambiguous, owing mostly to still existing uncertainties in RF and density measurements on one hand, and on the other to the numerous simplifications that need to be introduced into the numerical analysis in order for the work to remain within the limits of a doctoral thesis. The resulting expressions - given in Chapter 9 - do capture the main trends in power coupling as a function of density parameters, but are not appropriate for predictions with an accuracy within a few percent. It is found, however, that given some conditions a fast code can be used instead of TOPICA for estimating the coupled power on a given density profile.

The work is divided as follows:

- Chapter 2 contains the basics of the theoretical description of the fast magnetosonic wave.
- Chapter 3 gives a brief overview of transmission line theory, as well as a short description of antennas in this context. In particular, figures of merit that describe antenna performance - *loading resistance, coupling resistance* and others - are introduced.
- Chapter 4 describes available methods of measuring antenna impedance and discusses the advantages, disadvantages and caveats of each method. Details

of the use of each method on ASDEX Upgrade are given and the methods are compared with regards to sensitivity to different sources of error.

- Chapter 5 describes the implementation of a specific diagnostic set, namely voltage and current probe pairs, on ASDEX Upgrade in the course of this work, including probe calibration, testing, caveats and operational experience.

- Chapter 6 gives an overview of the numerical modeling of ICRF antennas, and introduces the three numerical codes used in this work. The calculation of the coupling resistance of a simple plasma-loaded antenna is described in detail. The applicability and validity domains of the numerical tools are discussed.

- Chapter 7 describes the experiments that were carried out on ASDEX Upgrade in the course of this work to improve antenna coupling via triangularity variation and magnetic perturbation fields. Results are discussed and analyzed.

- Chapter 8 presents the results of the comparison of TOPICA results with experimental data on ASDEX Upgrade. Two studies are presented: the first study makes use of standard RF data already available, while the second uses data obtained with the new diagnostic set described in Chapter 5.

- Chapter 9 describes the method followed here in order to obtain coupled power predictions for the ITER antenna. This includes TOPICA simulations of the ITER launcher, and the derivation of 1) an empirical formula for coupling resistance, as computed by a fast code, in terms of selected density profile features, and 2) an empirical formula for the relationship between this coupling resistance and the full coupled power computed with TOPICA. This procedure is applied first in the ASDEX Upgrade case and then for ITER. The limitations of the procedure are discussed.

- Chapter 10 summarizes the contents of the work and further discusses the conclusions drawn from the previous chapters. The general limitations and caveats of the work are also discussed, and steps for further work are outlined.

2

The fast magnetosonic wave

2.1 The dielectric tensor of a cold magnetized plasma

The canonical derivation of the cold dielectric tensor relation can be found in many texts, notably [30], [31] and [32]. Following, e. g., [31], we start with Maxwell's equations

$$\nabla \times \mathbf{E} = -\frac{\partial \mathbf{B}}{\partial t}, \tag{2.1}$$

$$\nabla \times \mathbf{B} = \mu_0 \mathbf{J} + \frac{1}{c^2}\frac{\partial \mathbf{E}}{\partial t}. \tag{2.2}$$

The plasma is assumed to be uniform and homogeneous, so we may write the fields as combinations of plane waves

$$\mathbf{E} = \mathbf{E}_1 e^{i(\mathbf{k}\cdot\mathbf{r}-\omega t)}, \tag{2.3}$$

$$\mathbf{B} = \mathbf{B}_0 + \mathbf{B}_1 e^{i(\mathbf{k}\cdot\mathbf{r}-\omega t)}, \tag{2.4}$$

where$\mathbf{B_0}$ is the equilibrium magnetic field. Then Maxwell's equations (2.1) and (2.2) become

$$i\mathbf{k} \times \mathbf{E} = i\omega \mathbf{B}, \tag{2.5}$$

$$i\mathbf{k} \times \mathbf{B} = -i\omega\epsilon_0\mu_0 \mathrm{K} \cdot \mathbf{E}, \tag{2.6}$$

where

$$\mathrm{K} = \frac{i\sigma}{\omega\epsilon_0} + \mathrm{I} \tag{2.7}$$

is the cold plasma dielectric tensor, with σ the conductivity tensor and $\mathbf{I}$ the unit dyadic. Combining (2.5) and (2.6) we obtain the wave equation

$$\mathbf{n} \times (\mathbf{n} \times \mathbf{E}) + \mathrm{K} \cdot \mathbf{E} = 0, \tag{2.8}$$

with the refractive index $\mathbf{n} = c\mathbf{k}/\omega$.

The elements of the dielectric tensor in the cold plasma approximation are customarily obtained as follows. For a particle of species j with mass m_j and velocity $\mathbf{v}_j$ the equation of motion is

$$m_j \frac{\mathrm{d}\mathbf{v}_j}{\mathrm{d}t} = q_j(\mathbf{E} + \mathbf{v}_j \times \mathbf{B}). \tag{2.9}$$

Again, due to plasma uniformity and homogeneity, $\mathbf{v}_j = \mathbf{v}_{1j} e^{i(\mathbf{k}\cdot\mathbf{r} - \omega t)}$ and so (2.9) becomes $-i\omega m_j \mathbf{v}_{1j} = q_j(\mathbf{E}_1 + \mathbf{v}_{1j} \times \mathbf{B}_0)$, ignoring the second order terms as we assume the waves are of sufficiently low amplitude that the linear approximation is valid [31]. Usually $\mathbf{B}_0$ is oriented along the positive $z-$axis. Eq. (2.9) is solved for the particle velocities; using the definitions of the plasma current $\mathbf{J} = \sum_j n_j q_j \mathbf{v}_j$ and the conductivity tensor $\mathbf{J} = \sigma \cdot \mathbf{E}$, we get

$$\sigma = \begin{pmatrix} \sigma_1 & -\sigma_2 & 0 \\ \sigma_2 & \sigma_1 & 0 \\ 0 & 0 & \sigma_3 \end{pmatrix} \tag{2.10}$$

with

$$\sigma_1 = i\epsilon_0 \omega \sum_j \frac{\omega_{pj}^2}{\omega^2 - \omega_{pj}^2}, \tag{2.11}$$

$$\sigma_2 = \epsilon_0 \sum_j \frac{\omega_{cj} \omega_{pj}^2}{\omega^2 - \omega_{pj}^2}, \tag{2.12}$$

$$\sigma_3 = \frac{i\epsilon_0}{\omega} \sum_j \omega_{pj}^2. \tag{2.13}$$

Here ω_{cj} and ω_{pj} are the cyclotron and plasma frequencies of the species j, given by

$$\omega_{cj} = \frac{q_j B_0}{m_j}, \tag{2.14}$$

$$\omega_{pj} = \sqrt{\frac{n_j q_j^2}{m_j \epsilon_0}}. \tag{2.15}$$

The dielectric tensor is then obtained from (2.7); using the Stix notation [30],

$$\mathrm{K} = \begin{pmatrix} S & -iD & 0 \\ iD & S & 0 \\ 0 & 0 & P \end{pmatrix} \tag{2.16}$$

with

$$S = \frac{1}{2}(R+L) = 1 - \sum_j \frac{\omega_{pj}^2}{\omega^2 - \omega_{cj}^2}, \tag{2.17}$$

$$D = \frac{1}{2}(R-L) = \sum_j \frac{\omega_{cj}\omega_{pj}^2}{\omega(\omega^2 - \omega_{cj}^2)}, \tag{2.18}$$

$$R = 1 - \sum_j \frac{\omega_{pj}^2}{\omega(\omega + \omega_{cj})}, \tag{2.19}$$

$$L = 1 - \sum_j \frac{\omega_{pj}^2}{\omega(\omega - \omega_{cj})}, \tag{2.20}$$

$$P = 1 - \sum_j \frac{\omega_{pj}^2}{\omega^2}. \tag{2.21}$$

$$\tag{2.22}$$

Furthermore, the wave equation (2.8) is customarily written in the form

$$\begin{pmatrix} S - n^2\cos^2\theta & -iD & n^2\cos\theta\sin\theta \\ iD & S - n^2 & 0 \\ n^2\cos\theta\sin\theta & 0 & P - n^2\sin^2\theta \end{pmatrix} \begin{pmatrix} E_x \\ E_y \\ E_z \end{pmatrix} = 0, \tag{2.23}$$

where θ is the angle between $\mathbf{n}$ and $\mathbf{B}_0$. The polarization of the electric field perpendicular to B_0 is obtained from the second row [14]:

$$\frac{iE_x}{Ey} = \frac{n^2 - S}{D}. \tag{2.24}$$

The non-trivial solution of the wave equation is obtained by setting the determinant of (2.23) to zero, and is usually written in the form

$$An^4 - Bn^2 + C = 0, \tag{2.25}$$

with

$$A = S\sin^2\theta + P\cos^2\theta, \tag{2.26}$$

$$B = RL\sin^2\theta + PS(1 + P\cos^2\theta), \tag{2.27}$$

$$C = PRL. \tag{2.28}$$

2.2 The fast wave dispersion relation

When writing the FW dispersion relation, it is customary to work with parallel and perpendicular (to B_0) components of the refractive index, $n_\parallel$ and $n_\perp$ respectively.

Then (2.23) becomes

$$\begin{pmatrix} S-n_\parallel^2 & -iD & n_\parallel n_\perp \\ iD & S-n_\perp^2-n_\parallel^2 & 0 \\ n_\parallel n_\perp & 0 & P-n_\perp^2 \end{pmatrix} \begin{pmatrix} E_x \\ E_y \\ E_z \end{pmatrix} = 0. \tag{2.29}$$

In the ion cyclotron frequency range the expressions for R, L and P are sometimes rewritten in an approximate form. Since now $\omega \sim \omega_{ci}$ and $\omega_{ce} \gg \omega_{ci}$, we have, for instance,

$$R \simeq 1 - \frac{\omega_{pe}^2}{\omega\omega_{ce}} - \sum_i \frac{\omega_{pi}^2}{\omega(\omega+\omega_{ci})}. \tag{2.30}$$

Furthermore, plasma quasineutrality $n_e q_e + \sum_i n_i q_i = 0$ can be written in the form [33]

$$\frac{\omega_{pe}^2}{\omega\omega_{ce}} + \sum_i \frac{\omega_{pi}^2}{\omega\omega_{ci}} = 0. \tag{2.31}$$

Inserting (2.31) into (2.30) results in

$$R \simeq 1 + \sum_i \frac{\omega_{pi}^2}{\omega_{ci}(\omega+\omega_{ci})}. \tag{2.32}$$

By the same reasoning,

$$L \simeq 1 - \sum_i \frac{\omega_{pi}^2}{\omega_{ci}(\omega-\omega_{ci})}. \tag{2.33}$$

Furthermore, as $\omega_{pe} \gg \omega_{pi}$,

$$P \simeq 1 - \frac{\omega_{pe}^2}{\omega^2}. \tag{2.34}$$

Finally,

$$S \simeq -\sum_i \frac{\omega_{pi}^2}{\omega^2-\omega_{ci}^2}. \tag{2.35}$$

Equation (2.29) can be written in a form similar to (2.25), with $n_\perp$ instead of n:

$$A_1 n_\perp^4 - B_1 n_\perp^2 + C_1 = 0, \tag{2.36}$$

with

$$A_1 = S, \tag{2.37}$$

$$B_1 = RL + PS - n_\parallel^2(P+S), \tag{2.38}$$

$$C_1 = P(n_\parallel^2 - R)(n_\parallel^2 - L), \tag{2.39}$$

where we have followed the notation used in [32]. The two roots of Eq. (2.36) are

$$n_{\perp F}^2 = -\frac{(n_\parallel^2 - R)(n_\parallel^2 - L)}{(n_\parallel^2 - S)} \tag{2.40}$$

and

$$n_{\perp S}^2 = -(n_\parallel^2 - S)\frac{P}{S}. \tag{2.41}$$

Eq. (2.40) is the dispersion relation of the fast wave, while Eq. (2.41) describes the slow wave. Alternatively, to decouple the FW dispersion relation from Eq. (2.29), the electron mass can be neglected [33] and hence $|P| \to \infty$. Therefore we must have $E_z \to 0$ in (2.29), and so the wave equation now becomes

$$\begin{pmatrix} S - n_\parallel^2 & -iD \\ iD & S - n_\perp^2 - n_\parallel^2 \end{pmatrix} \begin{pmatrix} E_x \\ E_y \end{pmatrix} = 0. \tag{2.42}$$

Again, the dispersion relation (2.40) is obtained by setting the determinant of Eq. (2.42) to zero.

2.3 Cutoff and resonance layers

It is seen from Eq. (2.40) that there are two cutoff surfaces associated with the fast wave, $n_\parallel^2 = R$ and $n_\parallel^2 = L$, called *right-hand* and *left-hand cutoff layers*, respectively. The right-hand cutoff always exists in the plasma, regardless of the ratio ω/ω_{ci}. Since the wave must satisfy the condition

$$n_\parallel^2 < R \tag{2.43}$$

for propagation, the R-cutoff defines a *cutoff density* n_{CO}, which can be written as

$$n_{CO} \simeq \frac{c^2 k_\parallel^2}{\omega^2}\left(\sum_i \frac{(\alpha_i q_i^2/m_i\epsilon_0)}{\omega(\omega+\omega_{ci})}\right)^{-1}, \tag{2.44}$$

where α_i is the density fraction of the i-th ion species. At a density below n_{CO}, a wave with the parallel wavenumber $k_\parallel$ is evanescent. To have an idea of the order of magnitude, for a pure D plasma and $\omega \sim 2\omega_{cD}$ we may from Eq. (2.44) write [5]

$$n_{CO} \simeq \frac{0.75 m_D \epsilon_0 c^2 k_\parallel^2}{q_D^2}. \tag{2.45}$$

For example, in the case of the ASDEX Upgrade antennas, the maximum of the nominal power spectrum is at $k_\parallel \sim 8\ m^{-1}$, so the above approximation gives $n_{CO} \sim 5 \times 10^{18}\ m^{-3}$; in reality it is actually closer to $\sim 3 \times 10^{18}\ m^{-3}$. In practice, an antenna will excite a $k_\parallel$ spectrum, so the cutoff region will not be

an infinitely thin surface. The existence of the evanescence region means that the distance between the antenna and the plasma, and the shape of the density profile in front of the antenna, will strongly affect power coupling.

The $n_\parallel^2 = L$ layer is also a cutoff layer. One can notice that, in the ion cyclotron range of frequencies, Eq. (2.33) can be written as

$$L \simeq -\sum_i \frac{\omega_{pi}^2}{\omega_{ci}(\omega - \omega_{ci})}, \tag{2.46}$$

since in tokamak plasmas $\omega_{pi}^2/\omega_{ci}^2 \sim m_i/m_e \gg 1$ [34]. In a single ion species plasmas, if $\omega > \omega_{ci}$ and near the cyclotron frequency, then

$$\frac{\omega_{pi}^2}{\omega_{ci}(\omega - \omega_{ci})} \gg 1 \tag{2.47}$$

except at very low ω_{pi}, i.e., very low density; therefore $L \ll -1$. Hence the $n_\parallel^2 = L$ layer is only found in a single species plasmas when $\omega < \omega_{ci}$.

Finally, $n_\parallel^2 = S$ is the *Alfvén resonance*, where the fast wave couples linearly to the *slow magnetosonic wave*, whose dispersion relation is given by Eq. (2.41). In a practical situation, if a minority ion species *m* is present in the plasma and $\omega \sim \omega_{cm}$ at the center of the plasma column, the $n_\parallel^2 = L$ and $n_\parallel^2 = S$ layers will be located on the high field side of the minority species cyclotron resonance layer [35]. In any case, near the Alfvén resonance the parallel phase velocity becomes comparable to the thermal velocity of the electrons, and therefore the SW is replaced by a hot plasma wave, the *kinetic Alfvén wave* [32].

2.4 Fast wave polarization

Writing the electric field in terms of the left- and right-hand rotating components $E_\pm = (E_x \pm iE_y)/2$, from the second row of Eq. (2.29) it is found that [33]

$$\frac{E_+}{E_-} = \frac{n_\parallel^2 - R}{n_\parallel^2 - L}. \tag{2.48}$$

But from Eq. (2.33), in a single-species plasma $L \to -\infty$ when $\omega \to \omega_{ci}$; the fast wave becomes purely right-hand polarized [35] and no absorption should take place at the cyclotron fundamental. However, this is an artifact of the cold plasma approximation. When finite temperature effects are taken into account, it can be shown that [33]

$$\frac{|E_+|}{|E_-|} = O\left(\frac{n_\parallel^2 v_{thi}^2}{c^2}\right), \tag{2.49}$$

where $v_{thi} = (2T_i/m_i)^{1/2}$ is the thermal velocity of the ions; hence for $n_\parallel \neq 0$, $|E_+|$ is small but non-zero.

2.5 Summary

In this chapter we have briefly summarized some of the most relevant properties of the fast wave, derived from the cold magnetized plasma model. The existence of the cutoff density n_{CO} already gives a glimpse of the difficulty inherent in ICRF power coupling; however, the equations describing the fast wave field inside the plasma, and its excitation by the antenna, are derived in detail in Chapter 6. In order to describe resonant absorption of the fast wave, the cold plasma approximation is not enough and kinetic effects have to be taken into account. However, as seen above, it is the edge plasma that is most relevant for the coupling of the fast wave. Poor absorption can affect coupling insofar as the power not absorbed in the plasma can be reflected back towards the antenna; otherwise the cold plasma model is enough for the purposes of this work. The details of the derivation of the homogeneous, hot, magnetized plasma tensor can be found, among others, in [30] and [31]; the idea is to find the perturbation of the distribution function due to the wave by integrating along the unperturbed orbits.

3

Transmission line and antenna theory

3.1 Transmission line theory

Standard treatment of transmission line theory can be found in a wide variety of textbooks, such as [3], [2] or [36]. A few general concepts are included here for convenience, as a large portion of experimental data analysis deals with them. Throughout this section and the remainder of the present work, the approach and notation of [3] is followed.

A fragment of a transmission line can be modeled by a series impedance per unit length

$$Z_l = R_l + jX_l, \tag{3.1}$$

and a shunt admittance per unit length

$$Y_l = G_l + jB_l. \tag{3.2}$$

In the direction z along the line, the variation in voltage and current are given by the *telegrapher's equations*

$$\frac{dV}{dz} = -IZ_l, \tag{3.3}$$

$$\frac{dI}{dz} = -VY_l. \tag{3.4}$$

These two can be combined and yield solutions for voltage and current as functions

of z:

$$V = V_o^+ e^{-\gamma z} + V_o^- e^{\gamma z}, \tag{3.5}$$

$$I = -\frac{1}{Z_l}\frac{dV}{dz} = \frac{1}{Z_0}\left(V_o^+ e^{-\gamma z} - V_o^- e^{\gamma z}\right), \tag{3.6}$$

where $V_0^\pm$ are $I_o^\pm$ (forward and backward) voltage and current wave amplitudes, $Z_0 = V_o^+/I_o^+ = -V_o^-/I_o^- = \sqrt{Z_l/Y_l}$ is the characteristic impedance of the line and $\gamma = \sqrt{Y_l Z_l} = \alpha + j\beta$ is the (generally complex) propagation constant. For lossless lines, $\alpha = 0$. Sometimes, however, it is more convenient to work with the normalized impedance

$$\widetilde{Z} = \frac{Z}{Z_0} = r + ix, \tag{3.7}$$

and normalized admittance

$$\widetilde{Y} = \frac{1}{\widetilde{Z}} = g + ib. \tag{3.8}$$

We consider a lossless line terminated at an arbitrary load impedance Z_L at $z = 0$, and an incident wave $V_o^+ e^{-j\beta z}$ generated from a source at $z < 0$. For such a traveling wave, Z_0 is the ratio of voltage to current; but at the load, the ratio of voltage to current must be Z_L, and hence a reflected wave with an appropriate amplitude must be excited to satisfy this condition. The total voltage on the line then must be of the form (3.5), and we must have

$$Z_L = \frac{V(0)}{I(0)} = \frac{V_o^+ + V_o^-}{V_o^+ - V_o^-} Z_0, \tag{3.9}$$

or equivalently

$$V_o^- = \frac{Z_L - Z_0}{Z_L + Z_0} V_o^+. \tag{3.10}$$

From (3.10) we can define the *voltage reflection coefficient* Γ as

$$\Gamma = \frac{V_0^-}{V_0^+} = \frac{Z_L - Z_0}{Z_L + Z_0}. \tag{3.11}$$

A positive distance $l = -z$ towards the generator, the reflection coefficient will be given by

$$\Gamma_{in} = \frac{V_0^- e^{-j\beta l}}{V_0^+ e^{j\beta l}} = \Gamma e^{-2j\beta l}. \tag{3.12}$$

Then the voltage and current on the line can be written as

$$V(z) = V_0^+\left(e^{-j\beta z} + \Gamma e^{j\beta z}\right), \tag{3.13}$$

$$I(z) = \frac{V_0^+}{Z_0}\left(e^{-j\beta z} - \Gamma e^{j\beta z}\right). \tag{3.14}$$

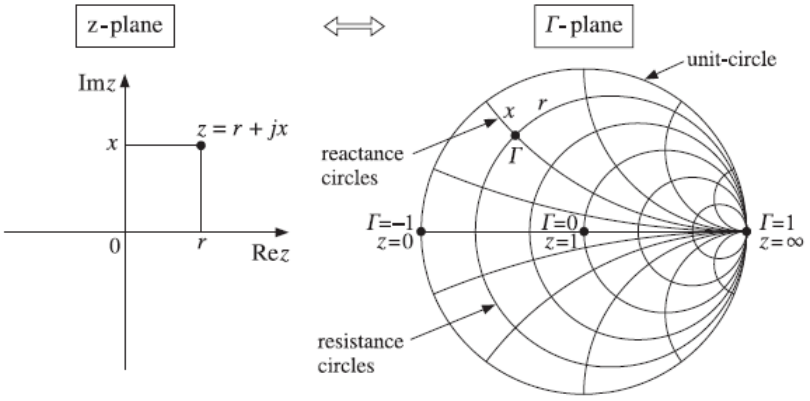


Figure 3.1: Mapping of the complex z-plane onto the Smith chart (Γ-plane); image reproduced from [2].

The absolute value of the voltage along the line will of course have the form

$$|V(z)| = |V_0^+||1 + |\Gamma|e^{j(\phi+2\beta z)}| \tag{3.15}$$

with $\Gamma = |\Gamma|e^{j\phi}$. Note that, using Γ, the time-averaged power flow along the line can be written as

$$P_{av} = \frac{1}{2}\mathrm{Re}\left[V\left(z\right)I^*\left(z\right)\right] = \frac{1}{2}\frac{\left|V_0^+\right|^2}{Z_0}\left(1 - |\Gamma|^2\right). \tag{3.16}$$

At this point we introduce the *Smith chart*, a rather convenient way of visualizing a variety of transmission line phenomena. The Smith chart is essentially a polar plot of the reflection coefficient Γ, onto which the complex normalized impedance plane (z-plane) is mapped via Eq. (3.11) [2]. This mapping is illustrated in Fig. 3.1. Vertical and horizontal lines on the z-plane, corresponding to constant normalized resistance and reactance, resp., are mapped onto circles on the Smith chart. The magnitude of Γ is plotted as a radius from the center of the chart, while its phase is measured from the right-hand side of the horizontal diameter; any passively realizable reflection coefficient ($|\Gamma| \leq 1$) corresponds to a unique point in the Smith chart [3]. In the remainder of this work the Smith chart is used extensively, because the polar visualization of Γ is much more intuitively meaningful than the visualization of z on the complex plane.

When it is not needed to specify the phase of the reflected voltage wave - e.g., as in the definition of power flow above - it is customary to use the *voltage standing wave ratio* VSWR as a measure of the mismatch between line and load. It is defined simply by

$$VSWR = \frac{V_{max}}{V_{min}} = \frac{1 + |\Gamma|}{1 - |\Gamma|}, \tag{3.17}$$

where use was made of Eq. (3.13). The real power flow on the line is a constant, but the voltage amplitude is oscillatory with position; therefore the impedance must also vary. At a distance $z = -l$ from the load, the impedance seen looking into the line is

$$Z_{in} = \frac{V(-l)}{I(-l)} = \frac{1 + \Gamma e^{-2j\beta l}}{1 - \Gamma e^{-2j\beta l}} Z_0 = Z_0 \frac{Z_L + jZ_0 \tan \beta l}{Z_0 + jZ_L \tan \beta l}. \tag{3.18}$$

The impedance transformation along a transmission line is readily visualized as a rotation of Γ on the Smith chart due to Eq. (3.12), by an angle $j\beta l$ clockwise, when going towards the generator, or counterclockwise, when going towards the load.

A useful description of a microwave network (with *N* ports in the general case) is given by the *admittance* and *impedance matrices.* At some specific distance from the port input a terminal plane is defined, at which the total voltage and current are given by

$$\begin{aligned} V_n &= V_n^+ + V_n^-, \\ I_n &= I_n^+ - I_n^-. \end{aligned} \tag{3.19}$$

The impedance matrix $\mathbf{Z}$ is then defined by

$$\begin{bmatrix} V_1 \\ V_2 \\ \vdots \\ V_N \end{bmatrix} = \begin{bmatrix} Z_{11} & Z_{12} & \dots & Z_{1N} \\ Z_{21} & Z_{22} & \dots & Z_{2N} \\ \vdots & \vdots & \ddots & \vdots \\ Z_{N1} & Z_{N2} & \dots & Z_{NN} \end{bmatrix} \begin{bmatrix} I_1 \\ I_2 \\ \vdots \\ I_N \end{bmatrix}, \tag{3.20}$$

with

$$Z_{ij} = \left. \frac{V_i}{I_j} \right|_{I_k = 0 \text{ for } k \neq j.} \tag{3.21}$$

Similarly, the admittance matrix $\mathbf{Y}$ is given by

$$\begin{bmatrix} I_1 \\ I_2 \\ \vdots \\ I_N \end{bmatrix} = \begin{bmatrix} Y_{11} & Y_{12} & \dots & Y_{1N} \\ Y_{21} & Y_{22} & \dots & Y_{2N} \\ \vdots & \vdots & \ddots & \vdots \\ Y_{N1} & Y_{N2} & \dots & Y_{NN} \end{bmatrix} \begin{bmatrix} V_1 \\ V_2 \\ \vdots \\ V_N \end{bmatrix}, \tag{3.22}$$

with

$$Y_{ij} = \left. \frac{I_i}{V_j} \right|_{V_k = 0 \text{ for } k \neq j.} \tag{3.23}$$

Furthermore, $\mathbf{Y} = \mathbf{Z}^{-1}$. Networks with the property $Z_{ij} = Z_{ji}$, $Y_{ij} = Y_{ji}$ are termed *reciprocal*.

Equivalent voltages and currents are not easily defined in high-frequency networks; a representation of the system which deals more directly with their wave-like behavior is given by the *scattering matrix* **S**, defined by

$$\begin{bmatrix} V_1^- \\ V_2^- \\ \vdots \\ V_N^- \end{bmatrix} = \begin{bmatrix} S_{11} & S_{12} & \dots & S_{1N} \\ S_{21} & S_{22} & \dots & S_{2N} \\ \vdots & \vdots & \ddots & \vdots \\ S_{N1} & S_{N2} & \dots & S_{NN} \end{bmatrix} \begin{bmatrix} V_1^+ \\ V_2^+ \\ \vdots \\ V_N^+ \end{bmatrix}, \tag{3.24}$$

with

$$S_{ij} = \left. \frac{V_i^-}{V_j^+} \right|_{V_k^+ = 0 \text{ for } k \neq j.} \tag{3.25}$$

If the ports have the same characteristic impedance Z_0, then the scattering and impedance matrices can be related by

$$\mathbf{Z} = Z_0 \left(\mathbf{I} + \mathbf{S}\right) \left(\mathbf{I} - \mathbf{S}\right)^{-1}, \tag{3.26}$$

where **I** is the $N \times N$ unit matrix. Finally, at some point we may be interested in the S-parameters of the network specified at a plane different from the terminal plane we defined. If l_i is a positive distance from the i-th input port (where we defined the terminal plane), then the i-th forward and reflected voltage at that point will be

$$V_i^{+'} = V_i^+ e^{j\theta_i}, \tag{3.27}$$

$$V_i^{-'} = V_i^- e^{-j\theta_i} \tag{3.28}$$

with $\theta_i = \beta l_i$. By Eq. (3.24),

$$\begin{bmatrix} e^{j\theta_1} & 0 & \dots & 0 \\ 0 & e^{j\theta_2} & \dots & 0 \\ \vdots & \vdots & \ddots & \vdots \\ 0 & 0 & \dots & e^{j\theta_N} \end{bmatrix} \mathbf{V}^{-'} = \mathbf{S} \begin{bmatrix} e^{-j\theta_1} & 0 & \dots & 0 \\ 0 & e^{-j\theta_2} & \dots & 0 \\ \vdots & \vdots & \ddots & \vdots \\ 0 & 0 & \dots & e^{-j\theta_N} \end{bmatrix} \mathbf{V}^{+'}, \tag{3.29}$$

and therefore the scattering matrix $\mathbf{S}'$ on the new reference plane is given by

$$\mathbf{S}' = \begin{bmatrix} e^{-j\theta_1} & 0 & \dots & 0 \\ 0 & e^{-j\theta_2} & \dots & 0 \\ \vdots & \vdots & \ddots & \vdots \\ 0 & 0 & \dots & e^{-j\theta_N} \end{bmatrix} \mathbf{S} \begin{bmatrix} e^{-j\theta_1} & 0 & \dots & 0 \\ 0 & e^{-j\theta_2} & \dots & 0 \\ \vdots & \vdots & \ddots & \vdots \\ 0 & 0 & \dots & e^{-j\theta_N} \end{bmatrix}, \tag{3.30}$$

or in a compact form

$$\mathbf{S}' = \mathbf{\Theta S \Theta}. \tag{3.31}$$

3.2 Antenna theory

The contents of this section is not intended to be a "formal" treatment of antennas from the point of view of electrical engineering, as this is not really necessary for the purpose of this work. What follows is rather a brief description of how an ICRF antenna is characterized in the framework of transmission line theory; in particular, which physical quantities are used as appropriate "indicators" of antenna behavior and how they are defined (how they are measured is described in Chapter 4. In a general sense however, a generic antenna - as currently used for ICRF heating of fusion plasmas - is a structure consisting of two or more *radiating straps*, which are poloidally extended strips of conductor material (similar to strip lines, with the back of the antenna playing the role of the second conductor), each one fed by a transmission line on one end and grounded on the other. As a rule the straps will have a curvature to follow the shape of the plasma column. It is the poloidal extension of each strap that ensures the excitation of fields in the plasma, since the magnetic field of the fast wave is parallel to the (mostly toroidal) static magnetic field. The straps' poloidal extension also ensures that the poloidal spectrum of the antenna is centered around zero with few large-wavenumber components, since their shorter evanescence length decreases antenna coupling [34]. Furthermore, the straps will be positioned in a *toroidal array* and fed with a certain phase difference, so that the radiated power spectrum peaks around some non-zero toroidal wavenumber $k_{\|}$. A Faraday screen is usually positioned between the straps and the plasma to shield the undesirable toroidal component of the electric field. The standard ASDEX Upgrade two-strap antenna is shown with its main components in Fig. 3.2.

The *feeders* are the points at which the transmission lines feeding the array are connected to the radiating straps, and form the input ports of the system. In the framework of transmission line theory, then, we take the antenna (more properly, the antenna-plasma system) to be a multiport microwave network that is fully characterized if its $\mathbf{Z}$, $\mathbf{Y}$ or $\mathbf{S}$ matrices are known.

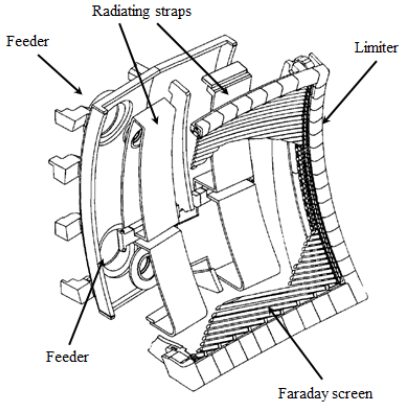
We consider first the relatively simple case of a one-port plasma-facing antenna. Following [34], the quantity which completely characterizes the coupling properties of the antenna-plasma system is the (complex) *antenna input impedance*

$$Z_{inp} = \frac{V_F}{I_F} = R_{inp} + jX_{inp}, \tag{3.32}$$

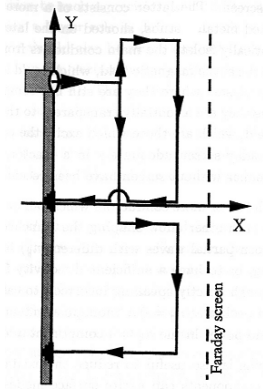
where V_F and I_F are the voltage and current at the antenna feeder. Furthermore, the *radiation impedance* is defined as

$$Z_{rad} = \frac{2P_{compl}}{|I_S|^2} = R_{rad} + jX_{rad}, \tag{3.33}$$

where R_{rad} is called *radiation resistance* and I_S is the current maximum, which is at the antenna short. Here the real part of P_{compl}, denoted P_{rad}, is the power



(a) Exploded view, reproduced from [37].



(b) Schematic drawing of one strap, fed from the top, reproduced from [33]. Arrows indicate the path of the current from feeder to ground.

Figure 3.2: The ASDEX Uprade standard two-strap ICRF antenna and its principal components.

radiated into the plasma, and the imaginary part is the power stored reversibly in the near field. P_{rad} is related to the currents and fields on the antenna by

$$P_{rad} = \frac{1}{2}\mathrm{Re}\int_A \mathbf{E}^* \cdot \mathbf{J_A} dS, \tag{3.34}$$

where $\mathbf{J_A}$ are the antenna currents and the integral is over all conductors. It is worth noting that R_{rad} is usually called *coupling resistance* in the experimental literature, so we will refer to it as R_C in the rest of this work to avoid confusion. We keep in mind that it is *this quantity* (R_C), and *not* the loading resistance R_L (defined below), that is computed by the two fast codes used in this work; the calculation of the coupling resistance of a simple antenna is described in detail in Chapter 6. If ohmic losses on the antenna conductors are neglected, then

$$R_C = \frac{2}{|I_S|^2}\mathrm{Re}(P_{compl}) = \frac{2P_{rad}}{|I_S|^2}. \tag{3.35}$$

In this lossless case we'll also have

$$P_{rad} = \frac{1}{2}R_C|I_S|^2 = \frac{1}{2}R_i|I_F|^2. \tag{3.36}$$

R_i is usually not straightforward to measure (see Chapter 4); for this reason another quantity, the *loading resistance*, is defined:

$$R_L = \frac{2P_{transm}}{|I_{max}|^2}, \tag{3.37}$$

where $|I_{max}|$ is now the current maximum *on the transmission line feeding the antenna* and P_{transm} is the net power flowing along that transmission line. In theoretical literature this quantity is often called *effective resistance*; here we will keep the experimental name for consistency. From Eqs. (3.13) and (3.14),

$$|I_{max}| = \frac{|V_0^+|}{Z_0}(1 + |\Gamma|), \tag{3.38}$$

$$|V_{max}| = |V_0^+|(1 + |\Gamma|), \tag{3.39}$$

so Eq. (3.37) can be written as

$$P_{transm} = \frac{R_L V_{max}^2}{2Z_0^2}, \tag{3.40}$$

$$R_L = \frac{2Z_0^2 P_{transm}}{V_{max}^2}, \tag{3.41}$$

which is how the loading resistance is usually defined. If the losses on the transmission line are negligible (which is a good approximation under most circumstances - in the ASDEX Upgrade case, resistive losses typically amount to a few percent of the coupled power along the $\sim$ 20 m of feeding line) then $P_{transm} = P_{rad}$, so we'll have

$$R_L = R_i \frac{|I_F|^2}{|I_{max}|^2}. \tag{3.42}$$

However, according to Eq. (3.14),

$$|I_F| = \frac{|V_0^+|}{Z_0}|1 - \Gamma| \tag{3.43}$$

if the position of the "load" is defined to be the feeder location. But Γ is a function of Z_{inp}; therefore one cannot deduce R_{inp} from R_L unless Z_{inp} is already known. From Eqs. (3.41), (3.16) and (3.17) we obtain the simple expression

$$R_L = \frac{Z_0}{VSWR}, \tag{3.44}$$

useful for computing the loading resistance when V_0^+ is not explicitly known.

Considering a two-port antenna with an associated **S**-matrix, we see that if we know the incident voltages $\overrightarrow{V^+} = \left[V_1^+ \; V_2^+\right]^{\mathrm{T}}$, the voltage reflection coefficients for both ports can be obtained by calculating the scattered voltage

$$\overrightarrow{V^-} = \begin{bmatrix} V_1^- \\ V_2^- \end{bmatrix} = \mathbf{S} \begin{bmatrix} V_1^+ \\ V_2^+ \end{bmatrix}, \tag{3.45}$$

from which

$$\Gamma_i = \frac{V_i^-}{V_i^+}. \tag{3.46}$$

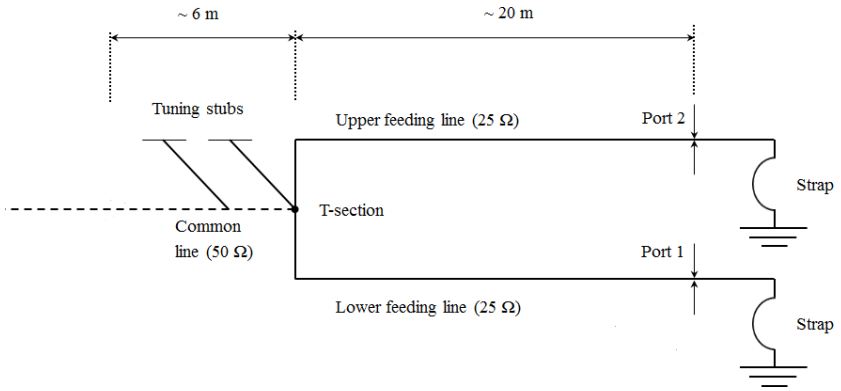


Figure 3.3: Schematic of the transmission network for one ASDEX Upgrade antenna, pre-2014 configuration. The lower and upper lines, feeding ports 1 and 2, are joined into a common line at the T-section.

Note that these are *active* reflection coefficients because while computing the scattered voltage on the $i-$th port, the other one is not terminated in a matched port but rather fed simultaneously. All relevant RF quantities can be obtained from these reflection coefficients as indicated above.

For a network configuration such as that of the pre-2014 ASDEX Upgrade antennas, it may be of interest to compute the reflection coefficient at the T-section, where the individual lines are joined (see Fig. 3.3). The **S**-matrix translated to the T-section is given by Eqs. (3.31), where

$$\mathbf{\Theta} = \begin{bmatrix} e^{-j\beta l_1} & 0 \\ 0 & e^{-j\beta l_2} \end{bmatrix}, \tag{3.47}$$

$\beta = 2\pi f/c$, and l_1, l_2 are the distances to the T-section along the lower and upper lines respectively. The impedance and admittance matrices at the T-section are

$$\mathbf{Z} = Z_{0I}\left(\mathbf{I} + \mathbf{S}'\right)\left(\mathbf{I} - \mathbf{S}'\right)^{-1}, \tag{3.48}$$

$$\mathbf{Y} = \mathbf{Z}^{-1}, \tag{3.49}$$

with $Z_{0I} = 25\ \Omega$ the characteristic impedance of the feeding lines and **I** being the unit matrix. From **Y** the voltage reflection coefficient looking into the T-section from the generator side is given by

$$\Gamma_T = \frac{1 - Z_{0C}(Y_{11} + Y_{12} + Y_{11} + Y_{22})}{1 + Z_{0C}(Y_{11} + Y_{12} + Y_{11} + Y_{22})}, \tag{3.50}$$

where $Z_{0C} = 50\ \Omega$ is now the characteristic impedance of the common line.

3.3 Summary

In this chapter we have outlined a few important definitions and results from transmission line theory that are used extensively throughout this work. It must be kept in mind that to *compute* the indicators of antenna performance as listed above - loading resistance, scattering matrices and so on - a much more detailed analysis is necessary than presented here. To compute the scattering matrix of a microwave network one needs to know the distribution of electromagnetic fields everywhere in the network, which in the case of a plasma loaded antenna also includes the fields inside of the plasma column and the (near-) vacuum region where the conducting elements are located. In a somewhat more simplified way this is also true for the coupling resistance R_C; the calculation of R_C for a specific antenna model is detailed in Chapter 6. However the concepts covered here are enough to manipulate the immediate results of measurements and simulations, in such a way that a meaningful comparison between the two is possible.

4

Impedance measurement methods

4.1 Introduction

As stated in Chapter 3, one would ideally want to measure the full **S**-matrix of a multiport antenna. Not only would the coupling properties of the antenna be fully known, but this would also enable direct comparison with numerical codes such as TOPICA. However, except when no plasma is present, it is (usually) not possible to measure the off-diagonal entries. Notably, measurement of the full (6×6) scattering matrix during plasma operation has been carried out on NSTX [38], sequentially powering up each one of the six transmitters, measuring the forward voltage on the corresponding line and the reflected voltages on all lines; the measurement was done on a short time scale (35 ms) under the assumption that plasma conditions do not change during this time. The next best thing, naturally, is to measure the individual voltage reflection coefficient Γ at each port (this is of course equivalent to knowing the input impedance of each port, but we use Γ instead throughout this work, as it is more intuitively related to coupling). Notably, in the vast majority of antenna studies in the literature, the *loading resistance* R_L is quoted instead.

There are three conventional methods of doing this, namely using 1) directional couplers, 2) voltage probe arrays or 3) voltage and current probe pairs. We briefly describe each method below and examine their advantages and disadvantages, since these ultimately determine which method is the most convenient one in a given situation.

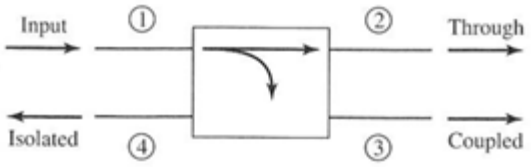


Figure 4.1: A generic directional coupler [3]. The isolated port (4) is terminated by a matched load.

4.2 Directional couplers

A *directional coupler* is a device that diverts a small fraction of the power flowing on a transmission line and delivers it into a coupled line. It is able to distinguish between the forward and backward traveling waves and can be made to sample one but not the other, hence the adjective *directional*. A generic directional coupler is illustrated in Fig. 4.1. It is a four-port device: the input and output ports are connected to the transmission line, the coupled port is the port where the power is diverted from the main line; ideally, no power is delivered into the isolated port, which is terminated with a matched load. The device is symmetrical: if the input and output ports are interchanged, so are the coupled and isolated ports.

The mode of operation of a directional coupler depends on the frequency range in which it is expected to operate, although the general principle is that of a length of secondary transmission line sampling the electromagnetic field in the primary. Standard literature mostly deals with directional couplers for the microwave range, consisting of coupled waveguides (for example [3]). In the ICRF frequency range, use is made of so-called ”loop-type” directional coupler. It consists of a segment of an auxiliary conductor located within the coaxial line; the plane of the loop is normally approximately parallel to the axis of the main line to which the loop is coupled [39].

Especially relevant in the context of this work is the *directivity* of the coupler, i. e., its ability to distinguish between forward and backward traveling waves. It is defined as

$$D = -10 \log \left(\frac{P_4}{P_3} \right), \tag{4.1}$$

where P_3 and P_4 stand for the power coupled to ports 3 and 4, respectively. If a reflected signal travels left to right in Fig. 4.1, a fraction of it will be coupled to port 3 and, if the coupler has a finite directivity, some of it will be coupled to port 4 as well, therefore interfering with the measurement, which is assumed to be forward power (and vice versa). The lower the directivity and/or the higher the reflected power, the higher the error will be.

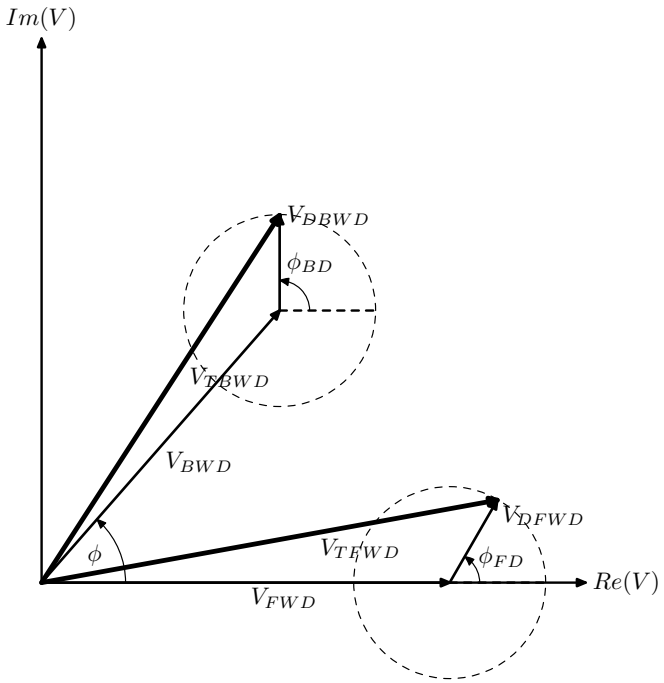


Figure 4.2: Directivity errors in a directional coupler. The phasors V_{FWD} and V_{BWD} are the actual forward and reflected voltage amplitudes. V_{DBWD} is the fraction of forward voltage V_{FWD} "leaking" into the measurement port due to finite directivity; likewise V_{DFWD} is the fraction of reflected voltage V_{BWD} "leaking" into the measurement port. V_{TFWD} and V_{TBWD} are the forward and reflected amplitudes seen by the directional coupler as a result, due to finite directivity.

This is illustrated in Fig. 4.2. A directional coupler has a directivity value D. Let P_{FWD} and P_{BWD} be the power flowing forward and backward, respectively; their voltage amplitudes will be $V_{FWD} = \sqrt{Z_0 P_{FWD}}$ and $V_{BWD} = \sqrt{Z_0 P_{BWD}}$, respectively (RMS values), where Z_0 is the characteristic impedance of the line.

Furthermore, because of the finite directivity, some fraction of the reflected power will be coupled to the port that samples the forward power - its amplitude will be given by $P_{DFWD} = P_{BWD}/R_D$, where $R_D = 10^{D/10}$. Likewise, some fraction of the forward power will be coupled to the port that samples the reflected power - its amplitude will be $P_{DBWD} = P_{FWD}/R_D$. The voltage amplitudes of these "leaked" signals will be $V_{DFWD} = \sqrt{Z_0 P_{DFWD}}$ and $V_{DBWD} = \sqrt{Z_0 P_{DBWD}}$ respectively. Because each of these erroneous signals will have its own phase, which is not known *a priori*, they will add as shown in Fig. 4.2, and the reflection coefficient seen by the directional coupler will have the form

$$\Gamma = \frac{V_{BWD} e^{j\phi} + V_{DBWD} e^{i\phi_{BD}}}{V_{FWD} + V_{DFWD} e^{i\phi_{FD}}}, \tag{4.2}$$

where ϕ is the phase of the reflected power, ϕ_{BD} and ϕ_{FD} are the phases of V_{DBWD} and V_{DFWD}, respectively (all phases are relative to V_{FWD}).

Therefore, the fundamental disadvantage of using directional couplers is that they will yield measurements with small error bars only if they have high directivity, and are preferably located on a relatively well matched line. This is shown in Fig. 4.3. Here $P_{FWD} = 500$ kW, and the reflected power P_{BWD} is indicated on the figure for each case. The phase difference between the reflected and forward waves is $45°$. A characteristic line impedance of 50 Ω is assumed, corresponding to the ASDEX Upgrade case. Here and in all further examples the frequency is 36.5 MHz. The measured Γ can occupy any point in the gray region centered around its real value. Fig. 4.4 gives a more quantitative description. Here $\Delta|\Gamma|$, for instance, represents the *maximum* difference between the true value of $|\Gamma|$ and a point in the gray region in Fig. (4.3). It must be borne in mind, however, that especially at lower reflection, the region occupied by the possible values is not a simply connected space, and it may not be possible to say in which region of the "ring" the values will lie, again because the phase of the spurious signals is not known. Whereas in the description of voltage probe arrays and voltage/current probe pairs the standard deviations in the probability distributions for $|\Gamma|$, $\Phi(\Gamma)$, etc., are taken as error indicators, this is far from straightforward to do in the present case, since one would deal with non-Gaussian distribution functions in multiply connected spaces, which is why maximum distances are used here instead.

Note that when the directivity is low (such as 20 dB in the figure), very large errors are present even at low reflected power, and the measurement of coupled power is particularly affected. The converse is also true: with high directivity

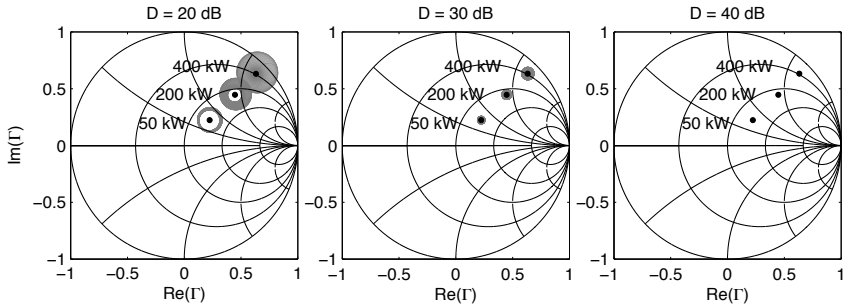


Figure 4.3: The effect of directivity on Γ *measured with a directional coupler. With a given directivity value, the measured* Γ *can occupy any point in the gray region, centered around its true value.* $P_{FWD} = 500$ *kW.* P_{BWD} *is indicated for each case. The phase difference between the reflected and forward waves is* 45°.

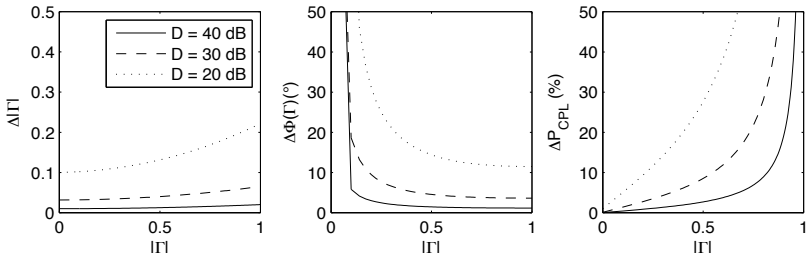


Figure 4.4: The effect of directivity on measured $\Delta|\Gamma|$, $\Delta\Phi(\Gamma)$ *and* ΔP_{CPL}. *The latter one is especially sensitive to directivity errors, even with D = 30 dB.*

(40 dB here) the coupler will yield accurate measurements even at high reflected power. It is considered that for a good quality measurement, the directivity should not be less than 30 dB [40].

It must also be taken into account that forward and reflected wave sampling will be done by two directional couplers, which a) may not be at the same location and b) may have cables of different length connecting them to an RF detector, which amounts to an introduction of a phase error between V_{FWD} and V_{BWD} and will show up simply as an angular displacement of Γ (in contrast to voltage/current probes, see Sec. 4.4). In addition, the coupling value of the directional coupler will be known with a finite accuracy as well, introducing further errors into the measurement. Fig. (4.5) illustrates the effect; all other conditions being the same as in Fig. 4.3, we introduce small variations into the coupling value of the directional coupler, which is sampled at random from a Gaussian distribution with a mean of -80 dB (the nominal coupling value) and a standard deviation $\Delta C = 0.1$ dB[1];

[1]Note that the probability distribution of the coupling C is taken as a Gaussian on a logarithmic

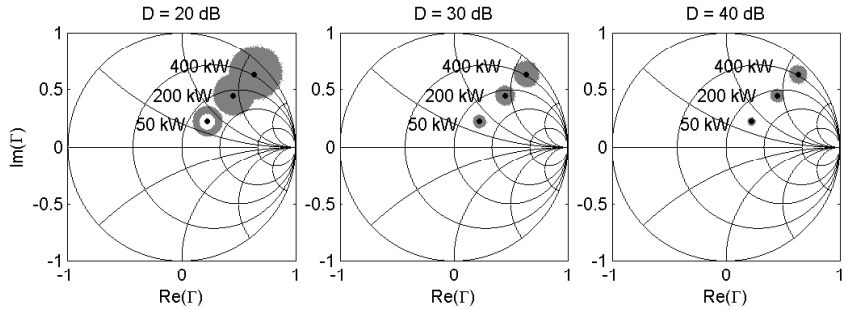


Figure 4.5: The effect of directivity on Γ measured with directional coupler, including coupling and phase errors $\Delta C = 0.1$ dB and $\Delta\phi = 1^\circ$ respectively. Note that at high reflection the effect is noticeable even at high directivity.

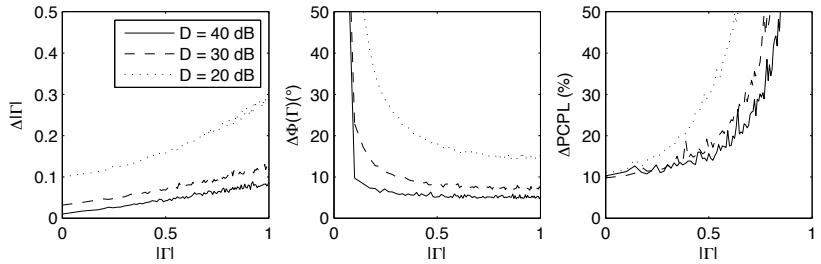


Figure 4.6: The effect of directivity on measured $\Delta|\Gamma|$, $\Delta\Phi(\Gamma)$ and ΔP_{CPL}, with additional coupling and phase errors $\Delta C = 0.1$ dB and $\Delta\phi = 1^\circ$ respectively. Compare with Fig. (4.4). The results are noisy because here Δ does not represent the standard deviation of the resulting distribution function, but the maximum distance of an erroneous result from the expected one (10^6 runs for each value of $|\Gamma|$).

likewise with the phase between the forward and backward signals, whose distribution is centered on 45° and has a standard deviation of $\Delta\phi = 1^\circ$[2]. Fig. 4.6 shows the spread of the results as a function of $|\Gamma|$; it can be seen that even relatively small errors in coupling and phasing can lead to a significantly larger spread in the results than that shown in Fig. 4.4. Directional couplers are universally used on all current tokamaks with an ICRF system as part of a setup to measure loading resistance (usually in conjunction with a voltage probe, by the definition of R_L), despite their limitations. Antenna loading studies at Alcator C-Mod [41], Tore Supra [42], ASDEX Upgrade ([29], [43], [25]), TEXTOR [24], JET (with ILA) [44] and DIII-D [45] (among many others) have been carried out using di-

scale, leading to a skewed distribution on the linear scale (this is conditioned by the fact that the measurements of C were taken in dB).

[2]The phase angle distribution is, strictly speaking, a truncated Gaussian since angle multiplicity is not taken into account. In this particular case, however, this is not so important because $\Delta\phi$ is small.

rectional couplers, in combination with voltage or current probes located at strap ground or voltage maximum on a feeding line. The use of directional couplers for measurement of R_L at ASDEX Upgrade is discussed in Sec. 4.6.

4.3 Voltage probe arrays

A voltage probe, in the present work, is a capacitive divider installed into the outer conductor of a coaxial line. In its simplest configuration it has an external capacitance C_1 formed by the probe cover and the inner conductor of the line, and an internal capacitance C_2. The output voltage is simply

$$V_{out} = \frac{V_{in} j\omega C_1}{j\omega(C_1 + C_2) - 1/R}, \tag{4.3}$$

with R being the input impedance of the measuring device connected to probe output.

A voltage standing wave with the form given by

$$V(x) = \left|V_{FWD}\right|\left|1 + |\Gamma| e^{j(\phi - 2\beta x)}\right| \tag{4.4}$$

will be present on a mismatched line, with β being the propagation constant (see Chapter 3); by placing a suitable number of voltage probes on the line this profile can be reconstructed and the voltage amplitude and reflection coefficient derived from this expression. However, for this method to work reliably, it is necessary either to have a large number of probes to accurately resolve the voltage minimum (which may be impractical, given the usual geometry of ICRF feeding lines) or to know with a high accuracy the probe coupling factors and their positions with respect to the load, the latter again being difficult due to the geometry of the transmission network.

Fig. 4.7 shows the effect of uncertainty in probe position and coupling factors on the measurement results. The frequency was taken to be 36.5 MHz and the standing wave pattern is reconstructed from eight voltage probe measurements located roughly "on the slope" of the voltage standing wave, spaced 23 cm apart, with a probe coupling of -73 dB. This corresponds to the situation on the test stand where the measurement methods were compared and the voltage probes were calibrated (see below), and is similar to the actual situation on the AUG ICRF feeding lines (see corresponding section). The three reflection coefficients are the same as in Fig. 4.3. Probe coupling values are sampled from a Gaussian distribution with a mean of -73 dB and a standard deviation of 0.1 dB (indicated as ΔC in the figure); probe positions are sampled from Gaussian distributions centered on their actual positions and having standard deviations indicated as Δx; the distance between the probes is kept constant (it is assumed that all the probes are located on a uniform line segment and are close to each other). The reflection

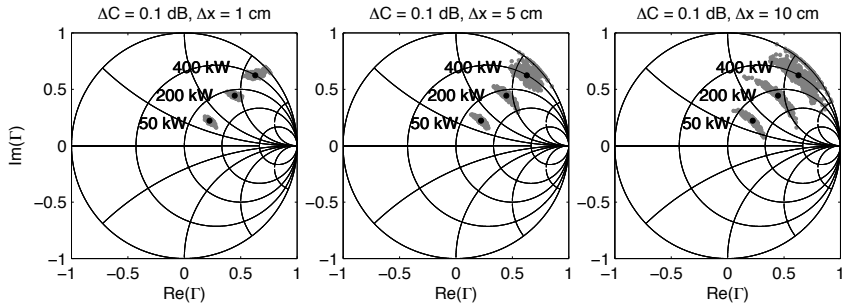


Figure 4.7: The effect of uncertainty in probe coupling factors (ΔC) and array position (Δx) on Γ. With a given uncertainty value, the measured Γ can occupy any point in the gray region, centered around its true value (black). $P_{FWD} = 500$ kW. P_{BWD} is indicated for each case. The phase difference between the reflected and forward waves is $45°$.

coefficient Γ is then estimated from these incorrect "measurements" by fitting a function of the form (4.4) by minimization of squared residuals; 1000 runs are shown for each Γ in gray. The correct results are plotted in black. Since ΔC is rather small, this simply corresponds to introducing an error phase shift into Γ as can be seen in Fig. 4.7. It is worth noting that a feeding line in ASDEX Upgrade is of the order of 20 m in length and highly non-uniform (see corresponding section) and an uncertainty of 10 cm is rather optimistic, as the probes are located relatively far from either end[3].

Although the situation where the spacing between the probes is perfectly known (or at least known much better than the position of the whole array) is true for a test stand, it is not necessarily so for the ASDEX Upgrade case, since not all the probes are located on the same straight section; for example, Fig. 4.8 shows the two feeding lines of antenna 2, with the voltage probes on each lines distributed among three different line sections. Therefore, the relative positions of the probes may themselves be unknown; the results are illustrated in Fig. 4.9, where the position of the *i*-th probe is now sampled from a normal distribution centered on the true position of that probe, with a standard deviation Δx. The spread of the results is now correspondingly larger.

Fig. 4.10 shows the voltage standing wave profile along the line; the black circles represent the actual voltage sampled at the probe positions, the black lines are the actual profile, and the gray lines are the profiles reconstructed from the "erroneous" measurements.

Fig. 4.11 shows $\Delta|\Gamma|$, $\Delta\Phi(\Gamma)$ and ΔP_{CPL} (the standard deviations in $|\Gamma|$,

[3]It must be emphasized that the distribution of error Γ on Fig. 4.7 and similar figures is *not* uniform in the gray region, although it appears to be so because of the way chosen here to visualize the data. Density contours would reveal the true distribution but are not shown here for clarity.

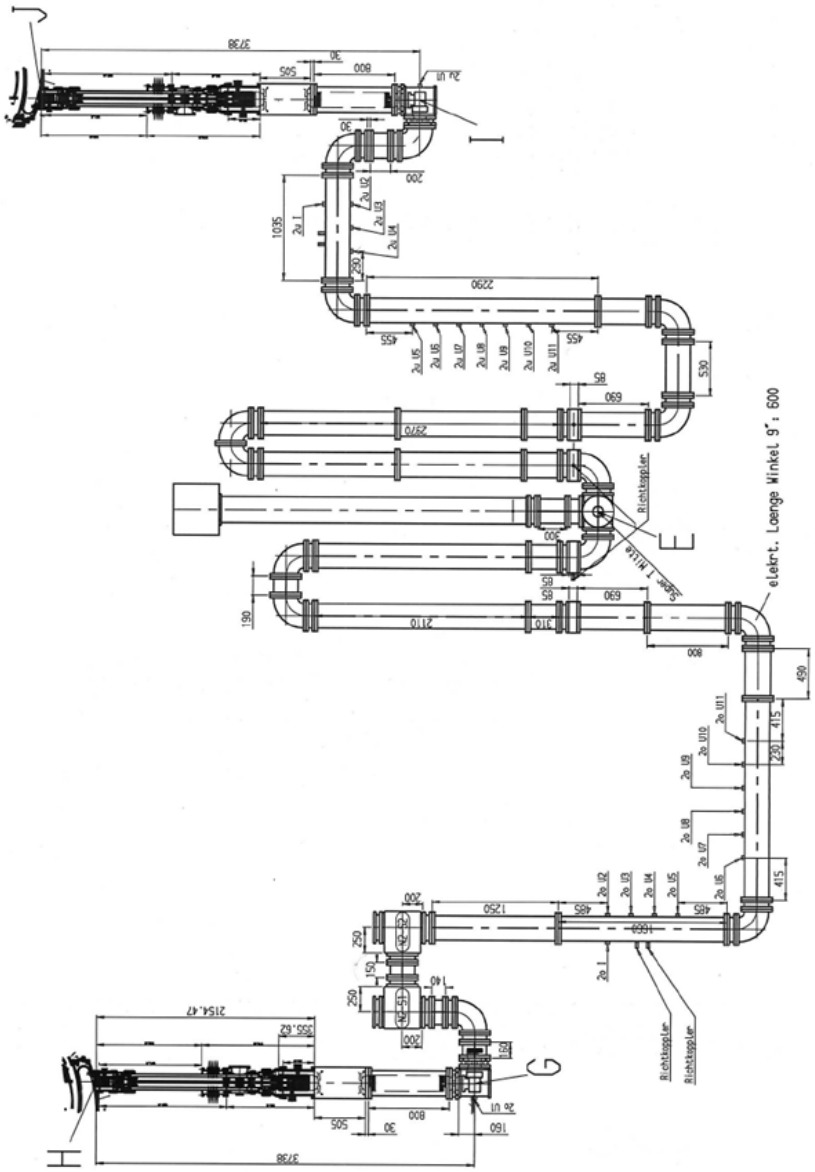


Figure 4.8: The two feeding lines of antenna 2. E refers to the T-section (with the antenna side stub on top), H and J are strap feeding points. Voltage probes are labeled 2oUX and 2uUX on the upper and lower lines resp.; except 2oU1 and 2uU1 they are distributed among two straight segments on each line, separated by an elbow and two ceramic spacers, making it difficult to precisely determine their relative positions. Schematic provided by G. Siegl.

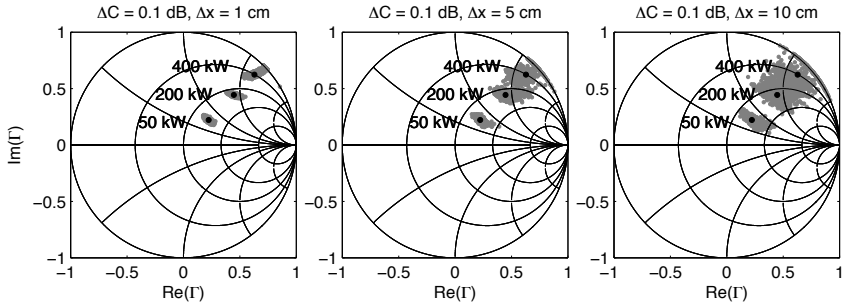


Figure 4.9: The effect of uncertainty in probe coupling factors (ΔC) and individual probe position (Δx) on Γ.

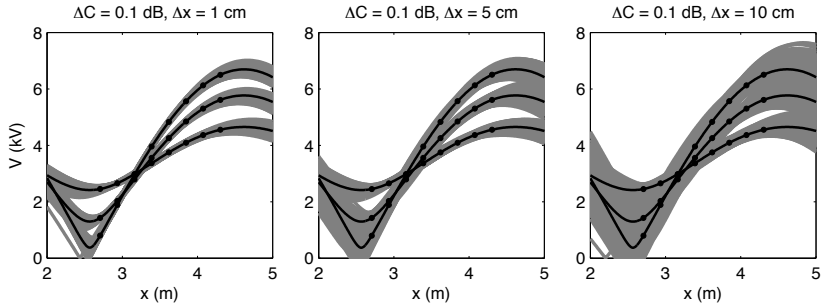


Figure 4.10: Voltage standing wave profile along the line, 8 probes with random variations in relative positions. Black circles represent the actual voltage sampled at the probe positions, black lines are the actual profiles, and gray lines are the profiles reconstructed from the "erroneous" measurements.

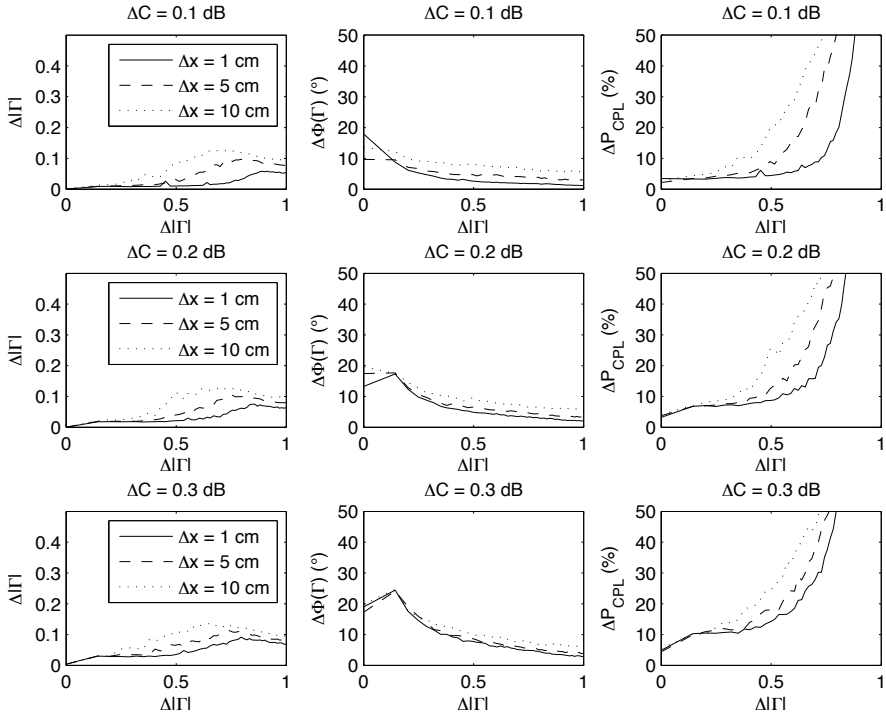


Figure 4.11: $\Delta|\Gamma|$, $\Delta\Phi(\Gamma)$ and ΔP_{CPL} as functions of $|\Gamma|$ for different values of (ΔC) and Δx, which now represents the uncertainty in the relative positions of the probes.

$\Phi(\Gamma)$ and P_{CPL}, resp.) as functions of $|\Gamma|$, for different values of ΔC and Δx.

The accuracy of this measurement method does not increase significantly by doubling the spatial resolution of the sampling. Fig. 4.12 shows the same measurements done with 16 probes located 11.5 cm from each other; it can be seen that the spread has not decreased significantly w. r. to Fig. 4.9. Doubling the resolution again offers some improvement but is not feasible with the equipment used on ASDEX Upgrade since the voltage probes have a diameter of ~ 6 cm.

The position of the array plays a role as well. Fig. 4.13 shows an array with 8 probes but displaced 1 m towards the load w. r. to Fig. 4.9, therefore centered roughly on the voltage minimum; note that the angular spread has decreased and the radial spread has, in contrast, increased. The corresponding profiles along the line are shown in Fig. 4.14.

Conversely, Fig. 4.15 shows measurements done with the same array shifted 1 m away from the load, therefore centered roughly on the voltage maximum: the angular spread has decreased, at the cost of a very large uncertainty in magnitude due to the difficulty in resolving the voltage minimum, as illustrated in Fig. 4.16

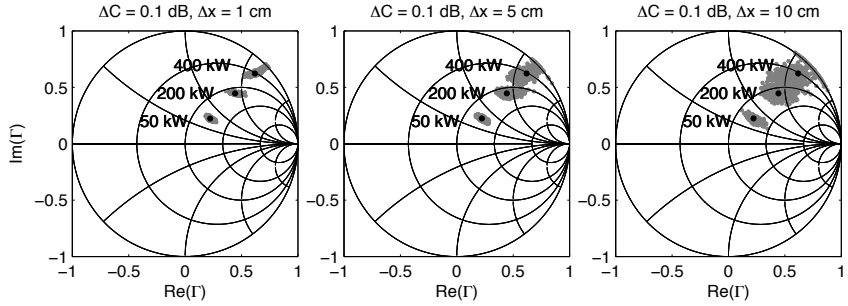


Figure 4.12: The effect of uncertainty in probe coupling factors (ΔC) and individual probe position (Δx) on Γ, 16 probes with a separation of 11.5 cm.

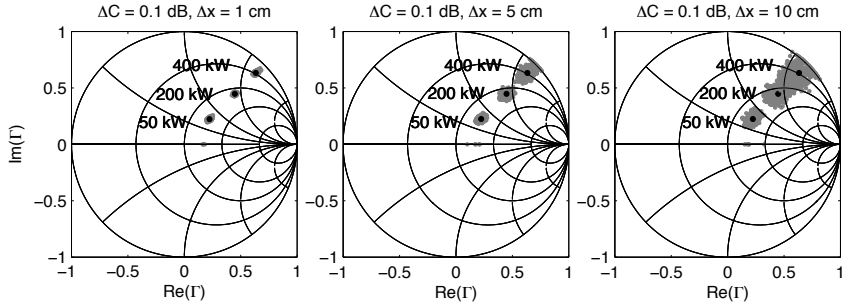


Figure 4.13: The effect of uncertainty in probe coupling factors (ΔC) and individual probe position (Δx) on Γ, 8 probes with a separation of 23 cm, roughly centered on voltage minimum. Points on the horizontal axis close to the center of the chart are cases where the fitting routine fails (see also Fig. (4.14)).

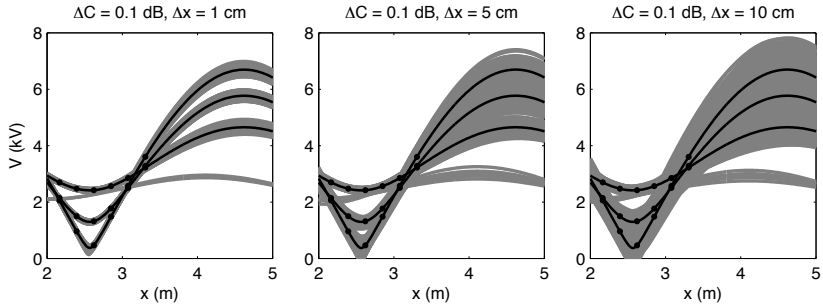


Figure 4.14: Voltage standing wave profile along the line, 8 probes with random variations in relative positions, centered roughly on the voltage minimum. Black circles represent the actual voltage sampled at the probe positions, black lines are the actual profiles, and gray lines are the profiles reconstructed from the "erroneous" measurements. Note the cases where the fitting routine fails altogether, visible as "flat" profiles (see also Fig. (4.13)).

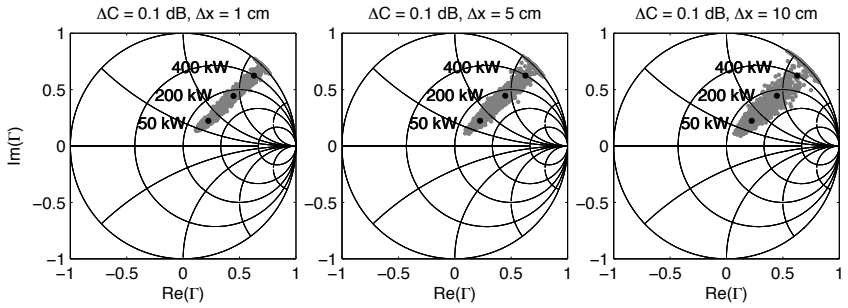


Figure 4.15: The effect of uncertainty in probe coupling factors (ΔC) and individual probe position (Δx) on Γ, 8 probes with a separation of 23 cm, roughly centered on voltage maximum.

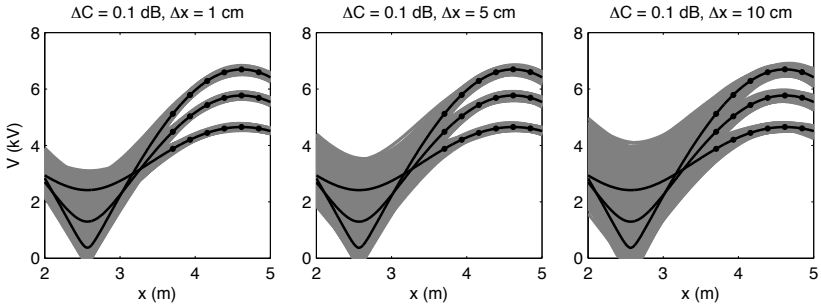


Figure 4.16: Voltage standing wave profile along the line, 8 probes with random variations in relative positions, centered roughly on the voltage maximum. Black circles represent the actual voltage sampled at the probe positions, black lines are the actual profiles, and gray lines are the profiles reconstructed from the "erroneous" measurements. Note the difficulty in resolving the voltage minimum, i. e., the results of the fit in gray can be significantly less "sharp" than the actual profiles, leading to the large radial spread on Fig. (4.15). This is in contrast with Figs. (4.10) and (4.14) - the closer the probes are to the minimum, the easier it is to resolve.

where the corresponding voltage profiles are shown.

4.4 Voltage and current probe pairs

Measuring the voltage amplitude, current amplitude and the phase difference between them at any point on the line by definition yields the input impedance at that point. Complementing the voltage probe described in the previous section, the current probe is inductively coupled to the line. It consists of a coil wrapped around a ferrite core, positioned in a slot in the outer conductor, that samples the

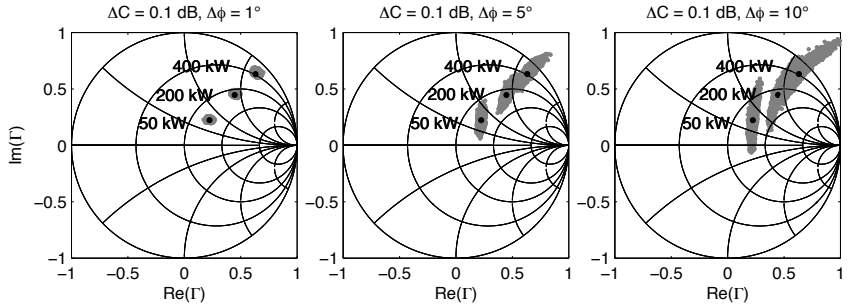


Figure 4.17: The effect of uncertainty in probe coupling factors (ΔC) and phase difference ($\Delta\phi$) on Γ. With a given uncertainty value, the measured Γ can occupy any point in the gray region, with the true value shown in black. $P_{FWD} = 500$ kW and P_{BWD} is indicated for each case. The phase difference between the reflected and forward waves is $45°$.

magnetic field inside the line. In its simplest form, the output voltage is given by

$$V_{out} = \frac{-j\omega M I_{in} R_1 R_2}{R_1 R_2 + j\omega L(R_1 + R_2)}, \tag{4.5}$$

where I_{in} is the current flowing on the line, L is the self-inductance of the coil, R_1 its internal resistance and R_2 the input impedance of the measuring device connected to probe output. M is a constant characterizing the magnetic flux through the coil.

Measuring input impedance with a voltage/current probe pair is advantageous on unmatched lines [40] since they are not sensitive to reflected power, and neither do they suffer from uncertainties associated to position measurements as the voltage probe array. They do, however, require very accurate measurement of the phase difference between the two signals.

This is illustrated in Fig. 4.17. The voltage and current probe coupling values were sampled at random from Gaussian distributions centered on -73 and -80 dB (typical values for ASDEX Upgrade probes on 25 Ω transmission lines) with standard deviations $\Delta C = 0.1$ dB. Error phase shift was sampled from a Gaussian distribution centered on $0°$ with a standard deviation of $\Delta\Phi = 1°$, $5°$ and $10°$, meaning that their intrinsic phase difference was taken to be zero. This would not be the actual case, per Eqs. (4.3) and (4.5), but it is not relevant in this example since it has no effect on the spread of the results (when dealing with actual measurements, however, it has to be taken into account).

Though Fig. 4.17 gives an intuitive understanding of how errors in probe coupling and phasing translate into data spread on the Smith chart, this behavior is further quantified in Fig. 4.18. The standard deviations of the probability distributions for the three main quantities of interest, $|\Gamma|$, $\Phi(\Gamma)$ and coupled power are shown as functions of $|\Gamma|$ for different values of $\Delta\phi$ and ΔC.

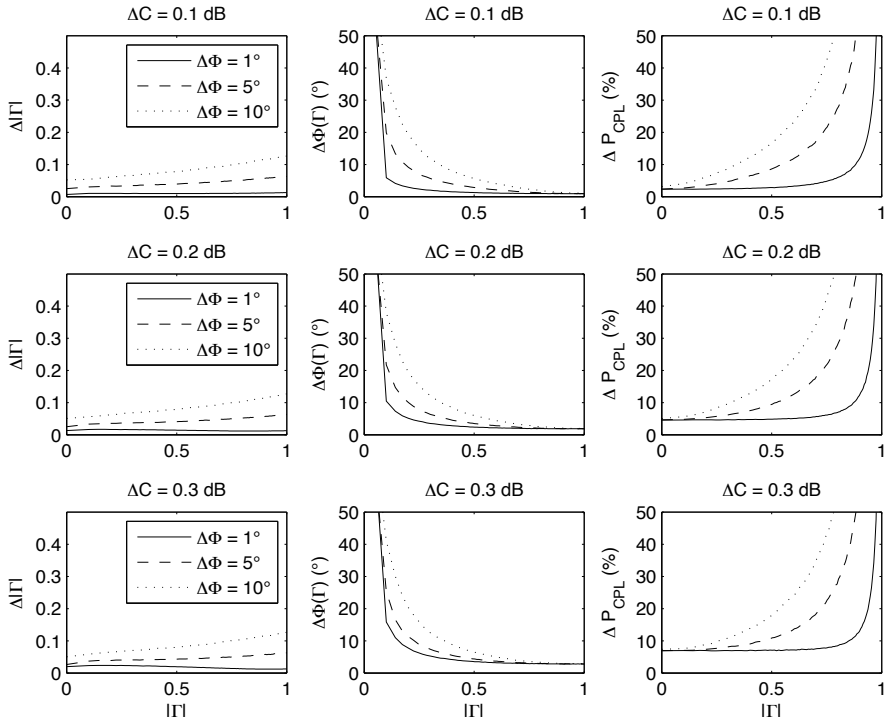


Figure 4.18: $\Delta|\Gamma|$, $\Delta\Phi(\Gamma)$ *and* ΔP_{CPL} *as functions of* $|\Gamma|$ *for different values of* (ΔC) *and* $\Delta\Phi$. *Note that measurement of* P_{CPL} *is especially sensitive to* $\Delta\Phi$.

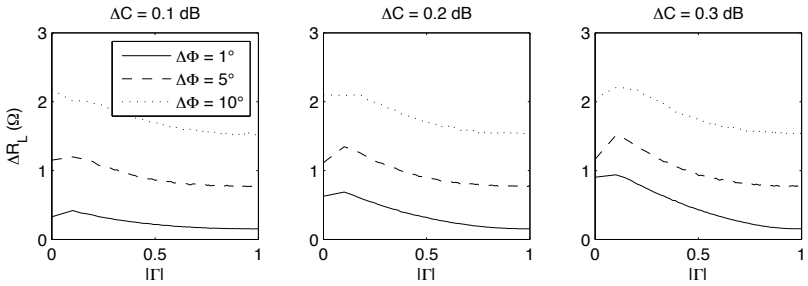


Figure 4.19: The effect of uncertainty in probe coupling factors (ΔC) and phase difference ($\Delta\phi$) on R_L. Note the very high sensitivity to $\Delta\phi$.

Fig. 4.18 clearly shows the very high sensitivity of the measurements to phase errors, especially in the case of P_{CPL}. Even with an error of 1° the impact on P_{CPL} is already considerable at high reflections, which will be usually the case of interest, since that is where directional couplers yield unreliable results. It is easy to see that this leads to practical difficulties since one needs to know the phase difference introduced by the cables connecting the probes to a detector. At a frequency of 30 MHz, the mechanical length of a coaxial cable corresponding to a phase shift of 1° is roughly 3 cm, and the electrical one is roughly 2 cm. In the ASDEX Upgrade case, the total length of these cables is on the order of 100 m, and the difficulty of measuring it with sufficient accuracy is further compounded by the fact that the cables themselves are composite. Finally, note that while the distributions for C and ϕ are Gaussian, the distributions for $|\Gamma|$, $\Phi(\Gamma)$ and coupled power are not, as it is clearly seen from in Fig. 4.17.

Finally, Figs. 4.19 and 4.20 show the impact of ΔC and $\Delta\Phi$ on R_L and V_{max} obtained from the voltage/current probe measurements. At high VSWR, the errors on V_{max} depend primarily on ΔC, whereas ΔR_L is extremely sensitive to phase errors and will constitute a significant percentage of the value of R_L, which is typically $1-3\ \Omega$ per strap during normal operation (see Sec. 4.6). Again, these results emphasize the need for very accurate knowledge of the phase shift introduced by external cables, as well as the probes themselves. Note that though position uncertainties play no role in the determination of the impedance at the measurement location, both for directional couplers and voltage/current probe pairs, as a rule the experimenter is interested in knowing those values at other locations, such as antenna input. In the case of ASDEX Upgrade, the voltage/current probe pairs are located significantly closer to the antenna ports ($\sim$ 3 m) than the directional couplers ($\sim$ 30 m), therefore gaining a significant reduction in the uncertainties associated with the geometry and composition of the ICRF transmission network.

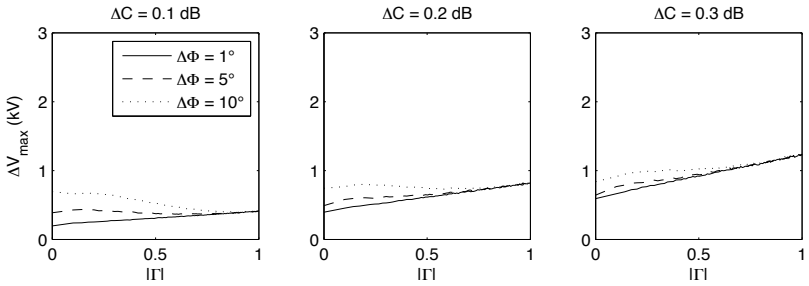


Figure 4.20: The effect of uncertainty in probe coupling factors (ΔC) and phase difference ($\Delta\phi$) on V_{max}.

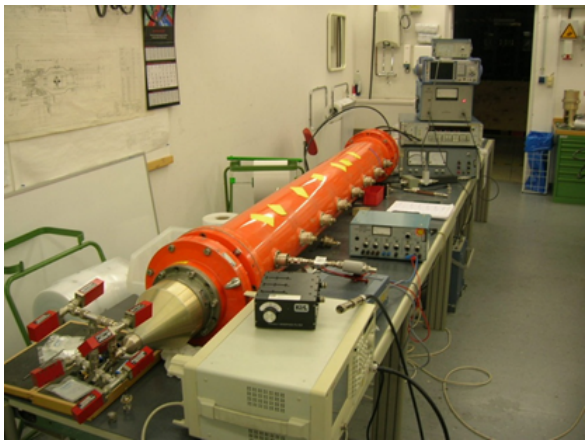


Figure 4.21: Low-power testbed.

4.5 Experimental comparison of measurement methods

Though the theoretical calculations shown above give a good idea of what to expect when using the three methods, their sources of error are quite different and a comparison of the three "on an equal footing" is not straightforward on that basis alone. Therefore it is worthwhile to see the results obtained when doing actual measurements, using the three methods, on a single transmission line and under the same conditions. The test stand assembled for this purpose is shown in Fig. 4.21.

The stand consisted of a straight 9" 50 Ω coaxial transmission line section with a length of 250 cm, with a ceramic spacer at each end. Two 50 Ω 9"-to-N adapter cones (at either end) provided the transition to the load at one side and the

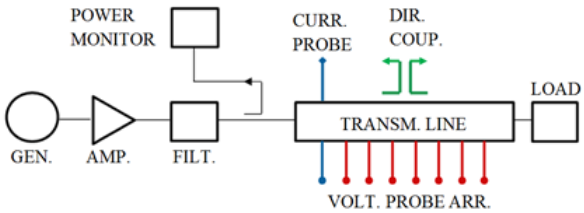


Figure 4.22: Low-power testbed (schematic).

signal source on the other. The line was fed by a Rohde & Schwarz SMH signal generator at ~ 0 dBm output power and a 30 dB amplifier; either a low-pass filter (when working at 30 MHz) or a bandpass filter (when working at 36.5 MHz) was used to suppress source harmonics. Furthermore, an 80 dB directional coupler served as power monitor. The measurement apparatus consisted of eight voltage probes mounted on the line with a spacing of 23 cm, one current probe and two directional couplers (sampling forward and reflected power) spaced 11 cm apart. This arrangement is shown schematically in Fig. 4.22. All the sensors were used to measure artificial load impedances of 50, 25,12.5 6.25 and 4.3 Ω[4], open line and short circuit termination. Data was measured and recorded with:

- Rohde & Schwarz ZVL network analyzer - for measurement of exact load impedances and characterization of amplifiers, filters and cables.
- Rohde & Schwarz ZPV vector analyzer to record readings from directional couplers and voltage/current probe pair.
- An RF voltmeter - to record readings from voltage probes.
- Spectrum analyzer observation of source harmonics.

The measurement procedure was the following:

1. Measure the exact impedance Z_L of each load and compute the reflection coefficient.
2. Measure the impedance at the sensor location.
3. Translate the measured impedance towards the load[5] and compute the measured reflection coefficient.

[4]These values are not exact; the real values were measured on the network analyzer, vary slightly with frequency and were found to have small imaginary parts.

[5]The translation distance between the sensor and the load was taken to be mechanical one, as the accuracy of the electrical length measurement by time-domain reflectometry was far too low with the available equipment.

All measurements were made at 30 and 36.5 MHz. The main results are summarized in Table 4.1. To exclude errors due to the separation of the forward and backward directional couplers, the same coupler was used in both configurations.

$\lvert\Gamma_L\rvert$	$\lvert\Gamma_{DC}\rvert$	$\lvert\Gamma_{VP}\rvert$	$\lvert\Gamma_{IV}\rvert$
0.00	0.01	-	0.00
1.00	-	0.91	-
1.00	1.01	0.75	0.99
0.83	0.84	0.72	0.83
0.77	0.77	0.70	0.77
0.59	0.59	0.58	0.59
0.33	0.33	0.33	0.33

(a) Measurement of $|\Gamma|$ using a directional coupler (DC), voltage probe array (VP) and voltage/current probe pair (IV).

$\Phi(\Gamma_L)$	$\Phi(\Gamma_{DC})$	$\Phi(\Gamma_{VP})$	$\Phi(\Gamma_{IV})$
$0.00°$	$-73.34°$	-	$0.00°$
$0.00°$	-	$0.00°$	-
$180.00°$	$174.26°$	$175.64°$	$172.01°$
$175.61°$	$168.16°$	$170.57°$	$167.07°$
$163.78°$	$155.06°$	$157.75°$	$155.28°$
$172.90°$	$164.86°$	$167.25°$	$164.06°$
$175.40°$	$168.16°$	$171.05°$	$166.08°$

(b) Measurement of the phase of Γ using a directional coupler (DC), voltage probe array (VP) and voltage/current probe pair (IV).

Table 4.1: Measurement results at 36.5 MHz. Lines 2 and 3, where $|\Gamma| = 1$, correspond to open and short, respectively.

The best accuracy is obtained when using the voltage/current probe pair, independent of VSWR. The directivity of the directional coupler was ~ 35 dB, errors in $|\Gamma|$ are in the range ≤ 0.04. The error when using the voltage probe array clearly increases with VSWR, and is in the range ≤ 0.25. The error when using the voltage/current probe pair is in the range ≤ 0.01. The last method clearly shows the highest accuracy in these experiments, although the directional coupler also performs well in this particular setup. Regarding phase it can be seen that, in all cases, the translated values are a few degrees off the expected values, and the error is systematic. This is attributed to an error in the measured length of the test line, probably due to the presence of a ceramic spacer and several low impedance transition sections. No measurements were done with directional couplers or voltage/current probes with the open line, as the vector analyzer gave unreliable readings in these conditions. Likewise, no measurements on a 50 Ω load were made with the voltage probe array, as the routine used to reconstruct the standing wave pattern produced erratic results. The above results also show that, even under relatively well-controlled conditions (straight 50 Ω line), the voltage probe array (as configured here) cannot be used for accurate impedance measurements.

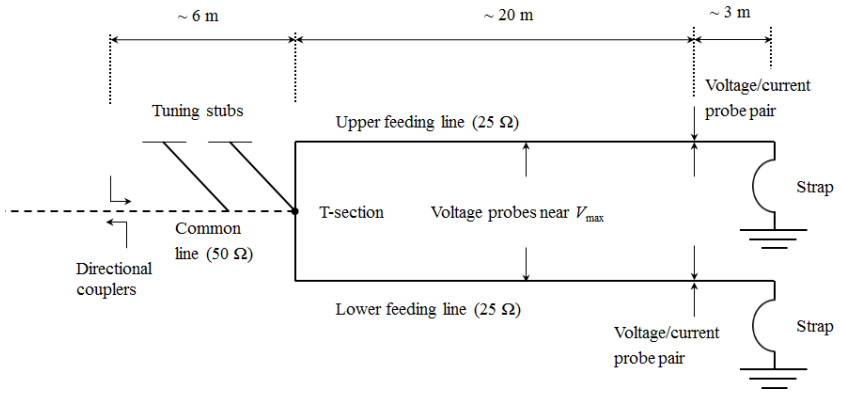


Figure 4.23: Antenna diagnostics on one (of four) ASDEX Upgrade transmission network. Lengths are approximate and different for each system. Not shown are the voltage probe arrays on each 25 Ω feeding line. Note that is the pre-2014 feeding configuration.

4.6 Standard measurement of coupled power, antenna impedance and loading resistance on ASDEX Upgrade

Until the recent implementation of voltage/current probe pairs to measure port input impedance, RF diagnostics routinely used to measure the antenna loading consisted (on each antenna) of

1. a pair of directional couplers (for forward and reflected power) located approx. 3 m behind the generator-side tuning stub, and

2. two voltage probes, one per feeding line, located near the voltage maximum (the measurement of V_{max} is relatively insensitive to errors in position of the order of ~ 10 cm due to its width).

This setup is shown in schematic form in Fig. 4.23.

Because the VSWR is rather low on the common feeding line during normal (matched) operation, $\lesssim 1.2$, this setup is expected to give an accurate measurement both of P_{CPL} and $|\Gamma|$, but not phase. With a directivity of 25 dB we would expect $\Delta|\Gamma| \simeq 0.06$, $\Delta\Phi(\Gamma) \simeq 35°$ and $\Delta P_{CPL} \simeq 2.6\%$; the phase error is quite considerable, in agreement with Figs. 4.3 and 4.4 for such a low reflected power. Therefore, while the measurement of coupled power can be considered quite reliable, the measurement of input impedance (at the location of the couplers) is not.

Furthermore, the input impedance *at the T-section*, Z_T, is obtained from the directional coupler measurements by translation through the matching network

L_{DC}	L_S	L_G	L_A
218 cm	295 cm	357.5 cm	217.3 cm

Table 4.2: Translation lengths and stub lengths (offset included), A3, AUGD 29110.

and subtraction of the two stub admittances. To illustrate the sensitivity of Z_T to translation length and stub position accuracy, we consider typical AUG data during matched operation: Γ on the common line of antenna 3, AUGD shot nr. 29110 between 1.82 and 1.83 s; this is an L-mode shot, which eliminates additional error sources due to Z_T leaving the matched region during ELMs. The frequency was f = 36.5 MHz. Only seven data points are shown for simplicity[6]. The average $|\Gamma|$ and $\Phi(\Gamma)$ during this time window were 0.14 and 122.7°. The measurements are then translated to the T-section through the matching network; the corresponding lengths and stub positions are shown in Fig. 4.24 and given in Table 4.2.

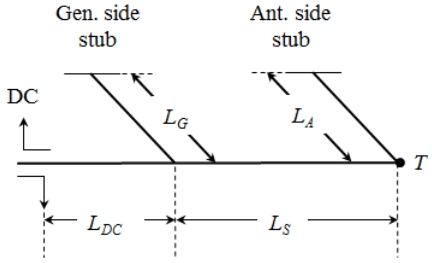


Figure 4.24: Translation lengths and stub lengths. DC = directional coupler.L_{DC} = distance from directional couplers to generator side stub, L_S = distance between stubs, L_G = total length of generator side stub, L_A = total length of antenna side stub.

To estimate the possible errors we assume a coupler directivity of 20, 30 and 40 dB as in section 4.2, and the four lengths sampled at random from normal distributions entered on the values in Tab. 4.2 with standard deviations of 1, 5 and 10 cm. The input impedance at the T-section is given by $Z_T = 1/Y_T$ with

$$Y_T = Y_2 - Y_{AS}, \tag{4.6}$$

$$Y_{GS} = f(Y_1 - Y_{GS}, L_S, \beta, Z_0), \tag{4.7}$$

$$Y_1 = f(Y_{DC}, L_{DC}, \beta, Z_0), \tag{4.8}$$

$$Y_{AS,GS} = \frac{1}{jZ_0 \tan \beta L_{A,G}}, \tag{4.9}$$

$$f(Y, L, \beta, Z_0) = \frac{1}{Z_0} \frac{YZ_0 - j \tan \beta L}{1 - jY_L Z_0 \tan \beta L} \tag{4.10}$$

[6]Here taken from the low-resolution ICP diagnostic group.

where $Z_0 = 50\ \Omega$ is the characteristic impedance of the common line and $\beta = 2\pi f/c$ is the propagation constant. Y_{AS} and Y_{GS} are the input admittances of the antenna and generator side stub resp., with L_A and L_G being their total lengths. L_{DC} is the distance from the directional couplers to the generator side stub, and L_S is the distance between stubs. The results of the calculations are shown in Fig. 4.25. The black circles close to the center of the chart are the actual values of Γ measured by the directional couplers at their location; Γ_T is in the upper right corner, with average $|\Gamma_T|$ and $\Phi(\Gamma_T)$ being 0.78 and 43° respectively. The gray points represent possible values of Γ_T with the given uncertainty assumptions. As can be seen from the figure, directivity does not have a major effect on the result distribution; in contrast, relatively small length errors (e. g. ~ 5 cm) impact Γ_T significantly, although this represents $\lesssim 3\%$ of the actual measured lengths as can be seen from Table 4.2). It must be borne in mind that this sensitivity imposes restrictions both on the comparison between diagnostics situated in different locations in the transmission network, and the comparison with the results of any code capable of computing Γ_T (in this case TOPICA, but this also holds for commercial packages such as MWS simulating the antenna in vacuum).

The coupled power, however, is not affected by this limitation (the main error source there is still the directivity), and hence the calculation of the loading resistance R_L will primarily be sensitive to the V_{max} measurements, whose accuracy will depend on knowledge of the voltage probe coupling factor as well as its position, the latter being rather tolerant to errors since the voltage profile changes slowly around the maximum. To illustrate this we compute R_L on a line with an antenna having $|\Gamma| \in [0.5, 1]$, $\Phi(\Gamma) = 45°$; the forward voltage is $V_{FWD} = 4.2 \times 10^4$ kV, chosen in such a way that with $|\Gamma| \sim 0.9$, the coupled power is about 800 kW, corresponding to the actual situation during shot 29110 during the time window given above. Again, sampling the probe coupling at random from a normal distribution centered around -73 dB with a standard deviation ΔC, and the probe position from a normal distribution centered on V_{max} with a standard deviation Δx, we find the results shown in Fig. 4.26, where the corresponding spread in R_L is given. It is evident that the measurement of R_L in this way is quite tolerant to errors in coupling and position, especially at high $|\Gamma|$, which is ~ 0.9 during normal operation. The values of the loading resistance itself, as well as of the voltage maximum, with $P_{FWD} = 4.2 \times 10^4$ kW, $\Delta C = 0.1$ dB and $\Delta x = 10$ cm is shown in Fig. 4.27. Error values are shown in gray. Note that the present example is characterized by low R_L ($\sim 1.5\ \Omega$) and high V_{max} (~ 28 kV).

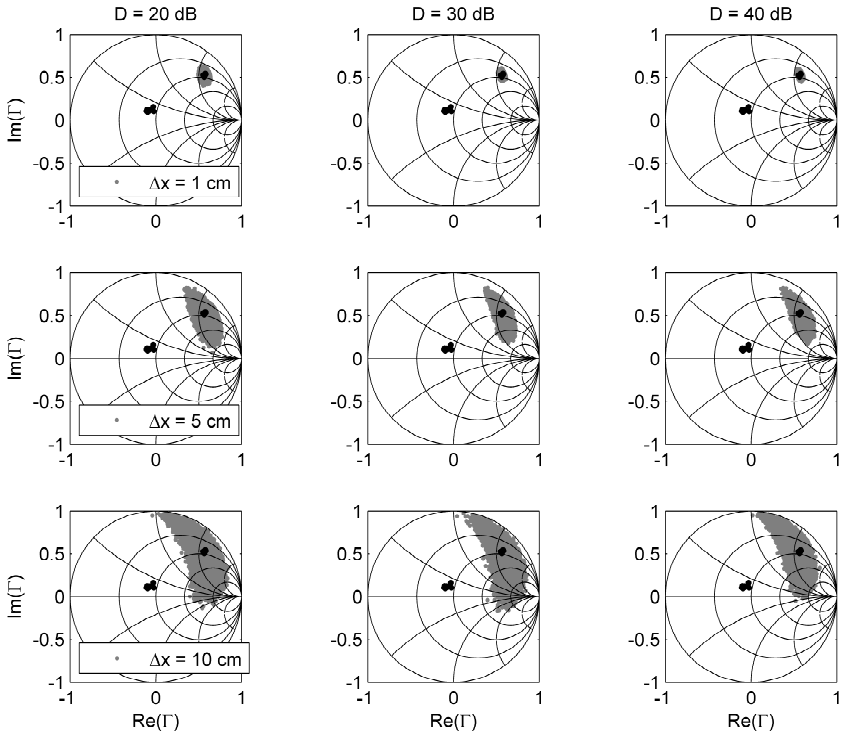


Figure 4.25: Sensitivity of Γ_T to errors in translation and stub length. The black circles near the center are the actual directional coupler measurements, whereas Γ_T itself is in the upper right corner. Note the very significant spread of the results for $\Delta x \geq 5$ cm.

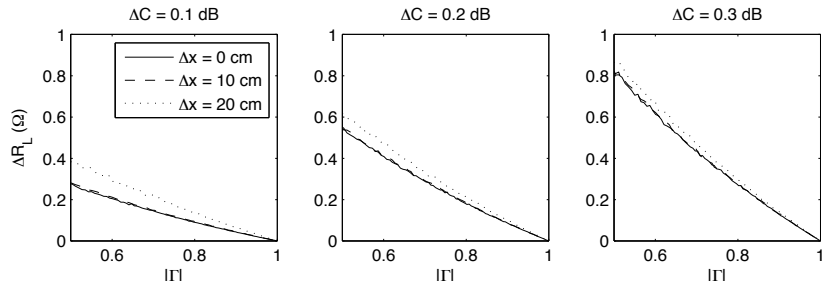


Figure 4.26: Standard deviation of the distribution of R_L, for different values of ΔC and Δx. The actual situation on ASDEX Upgrade corresponds to $|\Gamma| \sim 0.9$.

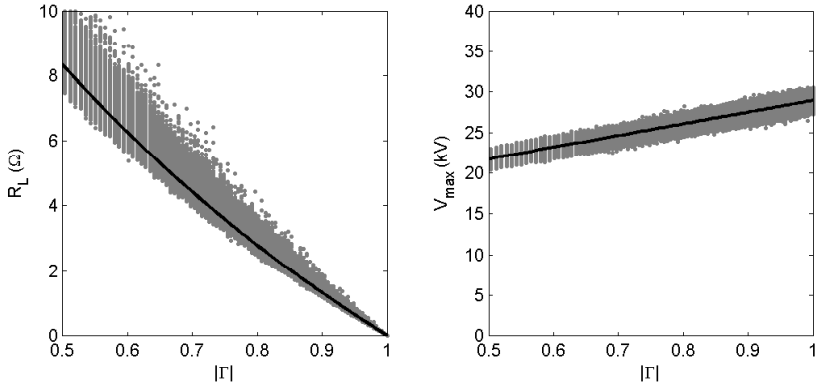


Figure 4.27: Loading resistance and voltage maximum, $V_{FWD} = 4.2 \times 10^4$ kV, $\Delta C = 0.1$ dB, $\Delta x = 10$ cm. Real values in black, error values in gray.

4.7 Determination of Z_T from Z_{inp} on each line on ASDEX Upgrade

If measurements of Z_{inp} at some point on each feeding line are available, accurate knowledge of the geometry of the transmission network is crucial for the determination of Z_T, both for matching and comparison with standard measurements. Obviously errors in probe coupling and phasing will also affect Z_T. Fig. 4.28 illustrates this. The reflection coefficients on the upper (Γ_U) and lower (Γ_L) line are time averages of shot nr. 29110, t = 1.82 - 1.83 s on Antenna 3. To obtain Γ_T we use the nominal line length values 16.959 m (upper) and 17.487 m (lower)[7]. Note that this is the distance between the probe location and the T-section, not the total length of a line from T-section to antenna input. As before, we have assumed a standard deviation in probe coupling and phasing, ΔC and $\Delta\phi$ respectively. The true Γ_T is shown in black, with the error values due to ΔC and $\Delta\phi$ plotted in gray. We now add the uncertainty in the length values; the line lengths are now sampled from normal distributions centered on the values quoted above and having standard deviations Δx. The result of this is shown in Fig. 4.29. Note that $\Delta x = 10$ cm amounts to $\sim 0.6\%$ of the total line length; however, even this "reasonable" uncertainty produces a very large spread of Γ_T over the Smith chart. For the purposes of comparing measurements obtained during an experiment with code results, this means that both results must be obtained at locations as close to each other as possible. For a code whose output is the scattering matrix of the antenna, the corresponding measurements should be done as near as possible to the plane at

[7]Electrical length, ± 20 cm, provided by H. Faugel on the basis of mechanical measurements. The error bars are due to the presence of two-way switches and a large number of ceramic spacers

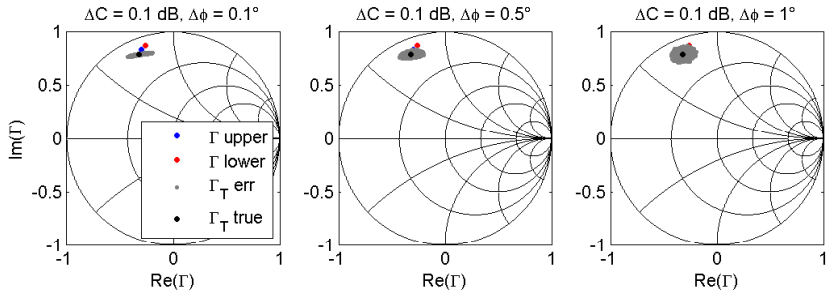


Figure 4.28: Sensitivity of Γ_T to ΔC and $\Delta\phi$ on the upper and lower lines. The error values of Γ_T are plotted in gray (10^6 runs), while the correct value is black. The error values of Γ_U and Γ_L are omitted for clarity.

which the **S**-matrix is defined, i. e. if the simulated antenna model only includes a few meters of transmission network behind the input ports, these results must be compared with measurements taken at the same locations on the feeding lines; otherwise errors of the order of 1% in the dimensions of the transmission network will completely invalidate the comparison[8] (see also the results of the preliminary comparison of TOPICA results with standard measurements on AUG).

4.8 Summary and conclusions

As stated in Sec. 4.5, a direct comparison of the three measurement methods on the grounds of theoretical error calculation is not straightforward, since they are sensitive to errors in different parameters, some of which may be easier to determine depending on the nature of the measurement. For instance, from the discussion above it is seen that if one just wants to know the total coupled power, directional coupler measurements on the matched section will have an accuracy of a few percent, provided the directivity is acceptable ($\gtrsim$ 30 dB, see Fig. 4.4); in contrast, the phase of Γ will have an error bar of tens of degrees (see same figure), and its translation through a matching network with modest length uncertainties (a few cm) will result in very large errors in Z_T, as shown in Fig. 4.25. Voltage probe arrays have the advantage of not depending on problematic phase shift measurements, instead relying on highly accurate knowledge of their positions with respect to the load/antenna input. Having the whole probe array located on a single uniform section of transmission line would mean that at least their relative positions are well known; then one would face the situation shown in Fig. 4.7 instead of that in Fig. 4.9, so that at least $|\Gamma|$ would have tolerable error bars

[8] Comparing coupled power only may not solve the problem, since then one needs to know accurately the input *complex* voltage, which again relies on detailed knowledge of the transmission network.

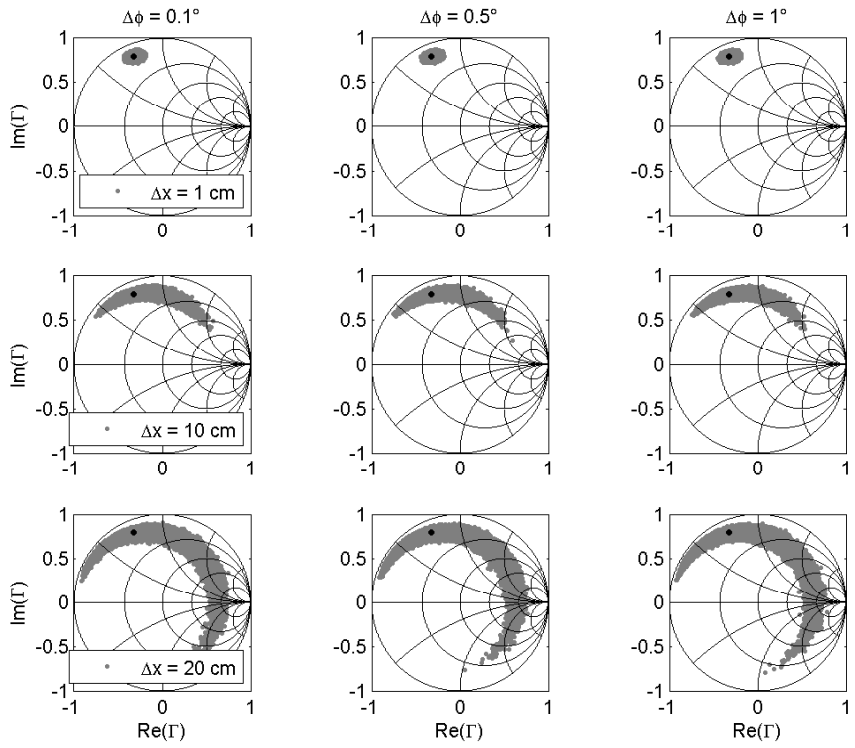


Figure 4.29: to ΔC, $\Delta\phi$ and Δx on the upper and lower lines. The error values of Γ_T are plotted in gray (10^6 runs), while the correct value is black. Γ_U and Γ_L are omitted for clarity.

(although not its phase). However, as stated, this is not the situation with the AUG probes. Additionally, because of the results shown in Sections 4.6 and 4.7, it is best to avoid translating results through large sections of the matching network as much as possible. Therefore we conclude that in this particular situation the use of voltage and current probe pairs to measure *input impedance*, rather than coupled power, is superior to the other two methods, in the sense that at least the $|\Gamma|$ of a given input port will not be sensitive to translation errors. Although the sensitivity to cable-dependent phase shifts remains a problem, this can be offset somewhat by comparing the coupled power computed from these measurements, to the one yielded by the directional couplers, which we consider to be reliable (see Sec. 4.6). Due to the same arguments of Sec. 4.7, however, the probe pairs are only meant to complement, and not replace, the standard diagnostics; it is obvious from Fig. 4.29 that an error bar of 20 cm on translations lengths makes it impossible to determine Z_T from the probe pair measurements.

5

Implementation of voltage and current probes on ASDEX Upgrade

5.1 Introduction

The arguments presented in Chapter 4, as well as the unsatisfactory results of a first TOPICA comparison study using standard diagnostics (see Chapter 8), stressed the need for a more detailed RF diagnostic set in the form of voltage and current probes on the feeding lines of each antenna. As stated in section 4.6, the probes already existed and were installed into the lines, but had been neither calibrated nor used. This chapter briefly describes the steps followed to calibrate the probes, study their sensitivity to several sources of error on test stands, and find a set of systematic correction factors which turned out to be necessary for their correct functioning.

For reference, voltage probes are labeled NUU00 on the lower line of the N-th antenna (N from 1 to 4) and NOU00 on the upper line. Similarly, current probes are labeled NUI00 on the lower line and NOI00 on the upper line.

5.2 Probe calibration

The probes had been originally built for the 50 Ω lines, and their coupling values on a 25 Ω line were not known. A 25 Ω calibration kit would have consisted of a short 25 Ω coaxial, with impedance matching sections to connect it to a 50 Ω network analyzer. Such a kit was not available and would have required considerable

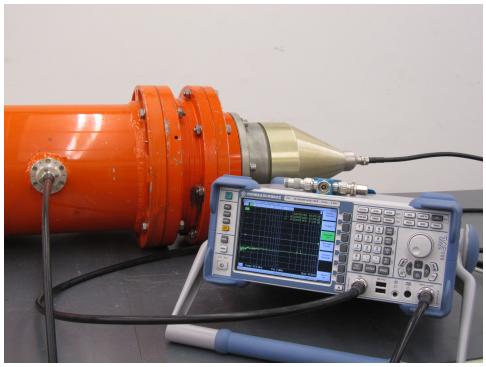


Figure 5.1: A photograph of the 50 Ω setup used for probe calibration, showing a portion of the 9" line with a mounted probe, adapter cone and network analyzer.

time to build; furthermore the matching pieces would have introduced additional sources of error. It was therefore decided that the coupling factors of the probes would be measured on the existing 50 Ω setup, and then recomputed for 25 Ω.

The calibration setup is shown in Fig. 5.1. It consists of the same straight 9" 50 Ω coaxial transmission line section described in section 4.5, with ports in the outer conductor to mount RF probes and directional couplers. A probe is inserted into one of the slots; the line is fed from port 1 of a Rohde & Schwarz ZVL network analyzer, with the probe output feeding port 2.

With the other end of the line terminated by a matched load, the voltage or current amplitude at the location of the probe is equal to that on the output of the network analyzer, and hence the transmission coefficient S_{21} is taken to be equal to the probe coupling C which, for a probe mounted on a powered transmission line, relates the voltage V_{line} and current I_{line} on the line at the location of the probe, to the voltage V_{out} measured on the probe output:

$$\begin{aligned} V_{line} &= \sqrt{R} \times 10^{\frac{V_{out}-C-30}{20}} \quad \text{(voltage probe)}, \\ I_{line} &= \frac{1}{\sqrt{R}} \times 10^{\frac{V_{out}-C-30}{20}} \quad \text{(current probe)}, \end{aligned} \tag{5.1}$$

where R is the input impedance of the measuring device connected to the probe output (in this case taken to be 50 Ω). The phase shift introduced by the cables was subsequently subtracted from the measurement results. All the voltage/current probes mounted closest to the antenna inputs (with indices 00 on all four systems) were characterized in this manner.

Fig. 5.2 shows a typical measurement result; the magnitude of S_{21} is given in dB and the phase in degrees. The first calibration produced the wavy traces depicted in blue on both graphs; although it was not realized at the time, it was

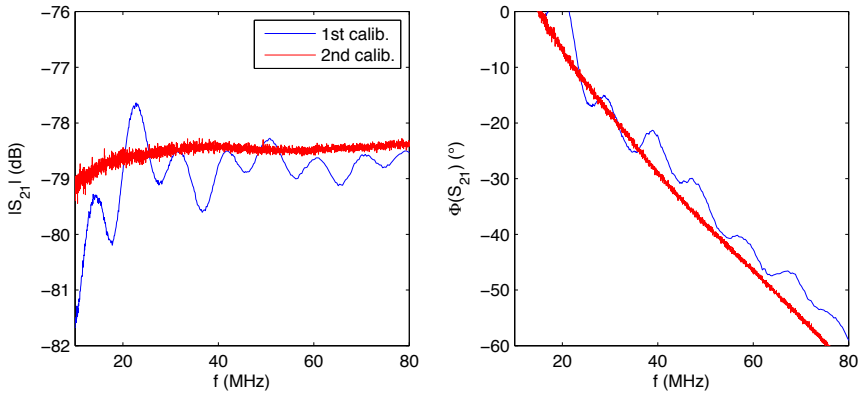


Figure 5.2: Typical calibration results on the 50 Ω setup. The wavelike variations in the first trace were found to be caused by multiple internal reflection in low quality cables, which was corrected in a subsequent calibration.

later discovered that these oscillations were caused by multiple internal reflections in faulty cables. This was corrected in a later calibration using high quality cables, which showed that probe coupling is roughly constant across the relevant frequency range, and is about -79 dB. This measurement is depicted in red.

Due to time constraints it was possible to unmount and recalibrate the probes of one system only, namely system 2[1]; however, having measured the curves for these probes, it was possible to reconstruct the equivalent curves for all the other probes. Figure 5.3 shows a close-up of the original calibration curves (smooth plots), both for magnitude and phase, for the voltage probes on systems 1 to 3 (results are identical for system 4 but are omitted here for clarity). The results of the recalibration with high quality cables of probes 2OU00 and 2UU00 are also shown (noisy lines). Since all the probes were measured with the same cables, the oscillations on all of them are the same, and the only difference is a systematic vertical shift of a few tenths of a dB. Therefore we assume that the correct curves of all probes will also be essentially identical to the two recalibrated probes, with the same relative shift. To avoid confusion, we denote the original (incorrect) curve by $\mathbf{C}_O$ and the recalibration result by $\mathbf{C}_R$. Then $\mathbf{C}_R(\text{2OU00})$ is taken as reference, smoothed by a moving average with a span of 50 points, and interpolated on the domain of $\mathbf{C}_O(\text{2OU00})$ (so that it is sampled on the same frequency base as the original curves); we call it $\mathbf{C}_R^{\text{int}}(\text{2OU00})$. Then the correct (reconstructed) curve

[1] It was, however, possible to recalibrate all the voltage probes with non-zero indices, i. e., the ones originally used for the reconstruction of the standing wave profile and measurement of V_{max}.

for, e. g., 1UU00 will be given by

$$\mathbf{C}_R^{\text{int}}(\text{1UU00}) = \frac{\mathbf{C}_R^{\text{int}}(\text{2OU00})}{\mathbf{C}_O(\text{2OU00})} \times \mathbf{C}_O(\text{1UU00}). \tag{5.2}$$

This is done separately for magnitude and phase for all probes. A portion of the reconstructed curves thus obtained is shown in Fig. 5.4; the curves for the current probes are not shown but the procedure is identical.

In order to use the $\mathbf{C}_R^{\text{int}}$ curves for RF measurements, the correction in coupling due to their use on 25 Ω lines had to be found. As stated in the beginning of this section, a 25 Ω calibration stand was not available, but the variation in coupling when transitioning to a 25 Ω line can be computed from simple physical models of the probes. The voltage probe is a capacitive divider; assuming a time variation $\propto \mathrm{e}^{j\omega t}$, the voltage ratio is given by[2]

$$\frac{V_{out}}{V_{in}} = \frac{j\omega C_1}{j\omega(C_1 + C_2) - 1/R}, \tag{5.3}$$

where V_{in} is the actual voltage on the line, V_{out} is the probe output voltage, C_1 is the capacitance between the probe and the inner conductor, C_2 is the internal capacitance of the probe and R is the input impedance of the device that the probe is connected to. Here $R = 50\ \Omega$ and $C_2 \simeq 2$ nF. C_1 is not known exactly, but assumed to be of the form $C_1 = kC_{50}$, where C_{50} is the capacitance per unit length of the 50 Ω line and k a geometrical constant. The coupling constants of eight probes selected at random were measured on the test line with the network analyzer; the averages were found to be -79.2 dB at 30 MHz and -79.1 dB at 36.5 MHz, average -79.15 dB. Inserting this number into the absolute value of Eq. (5.3), we get $C_1 \simeq 0.22$ pF. On the other hand, the capacitance per unit length of a coaxial line is given by

$$C = \frac{2\pi\epsilon_0}{\ln(b/a)}, \tag{5.4}$$

where a and b are the inner and outer conductor radii and $\epsilon_0 = 8.85 \times 10^{-12}$ F/m is the permittivity of free space. For the 50 Ω line $a = 50$ mm and $b = 115$ mm, hence $C_{50} = 6.6761 \times 10^{-11}$ F/m. Therefore $k \simeq 0.33$ m. The only thing that changes in the probe coupling when varying the line impedance is C_1, which will now be $C_1 = kC_{25} = 0.445$ pF with $a = 76$ mm. Since $C_2 \gg C_1$, this amounts to a factor of 2 in Eq. (5.3), or 4 when the voltages are squared; therefore the voltage probe coupling changes by 6 dB when the line impedance is changed from 50 to 25 Ω.

The current probe, on the other hand, is inductively coupled to the line; it consists of a coil wrapped around a ferrite core, positioned in a slot in the outer

[2]Note that in this instance only we use $\mathrm{e}^{j\omega t}$ to represent the change of a quantity with time, as is common in electrical engineering. Throughout the rest of this text, the "physics" convention $\mathrm{e}^{-j\omega t}$ is used instead.

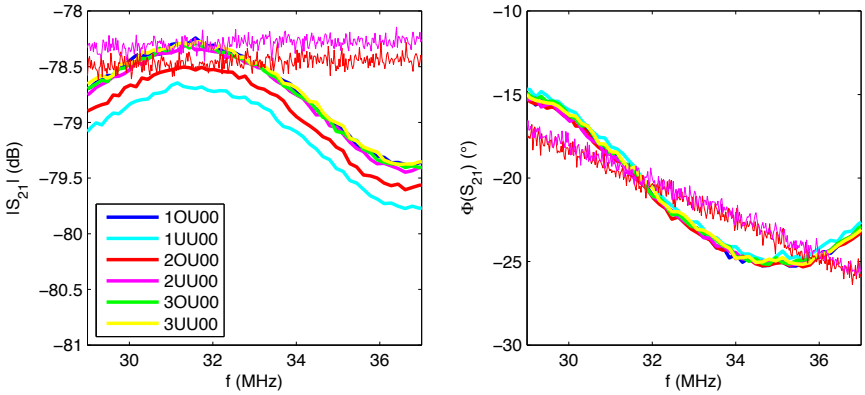


Figure 5.3: Close-up of the calibration curves for the voltage probes on systems 1-3. The original results (with the faulty cables) are displayed as smooth curves; the two noisier signals correspond to the recalibration of 2OU00 and 2UU00. The only difference between the original curves is a systematic vertical shift of a few tenths of a dB, since they were all calibrated using the same cables.

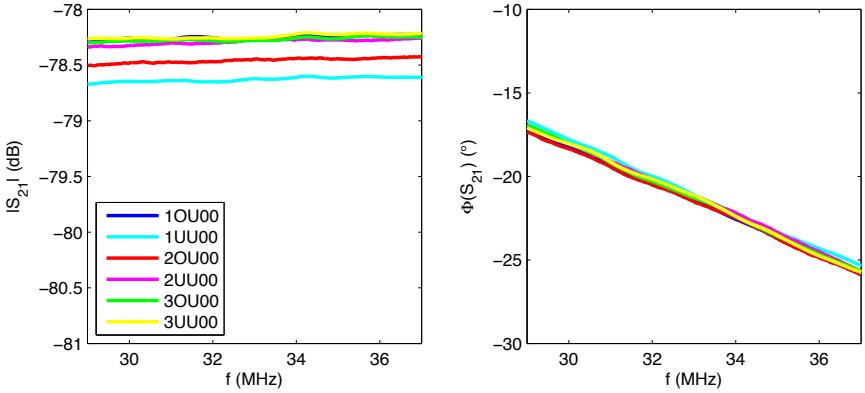


Figure 5.4: Close-up of the reconstructed calibration curves for the voltage probes on systems 1-3, displaying the same relative shift as the original curves.

conductor, that samples the magnetic field inside the line. If a current I_0 runs on the central conductor of the line, the output voltage of the probe will be given by

$$V_{out} = \frac{-j\omega M I_0 R_1 R_2}{R_1 R_2 + j\omega L(R_1 + R_2)}, \tag{5.5}$$

where $R_1 = 33\ \Omega$ is the internal resistance of the probe (measured), $R_2 = 50\ \Omega$ is the input impedance of the device to which the probe is connected, L is the coil inductance; $M = \mu N A/(2\pi b)$, N being the number of turns of the coil, A its transversal area and μ the permeability of the ferrite core. Since Eq. (5.5) is independent of a, the current probe coupling is not affected when the line impedance is changed. Note that at very high power, saturation of the ferrite core would be expected and hence relationship (5.5) would cease to be linear; however, the probes were specifically designed for the high-power environment of the AUG antenna lines, and therefore we do not expect the non-linear effects to be significant in this application.

Despite the simplicity of the calculations above, these results were later confirmed by the results taken on the 25 Ω line (see section 5.3.2), as well as simulations of a more detailed voltage probe model using HFSS[3].

5.3 Testbed measurements

In order to have an experimental observation of the capabilities and accuracy limits of the diagnostic system and identify possible error sources, a series of studies was carried out on three testbeds with varying conditions. These were:

1. A 50 Ω testbed, power in the range of ~ 1 kW
2. A 25 Ω testbed, power in the range of ~ 1 kW
3. A 25 Ω testbed, power in the range of ~ 10 kW

Broadly, the error sources considered were:

- Incorrect probe coupling change due to the transition to a 25 Ω line
- Incorrect RF detector calibration and sensitivity to noise
- Effect of DC breaks
- Effect of cable length uncertainty/phase errors

The main conclusions drawn on the basis of the test runs are summarized below.

[3]Franz Braun, personal communication.

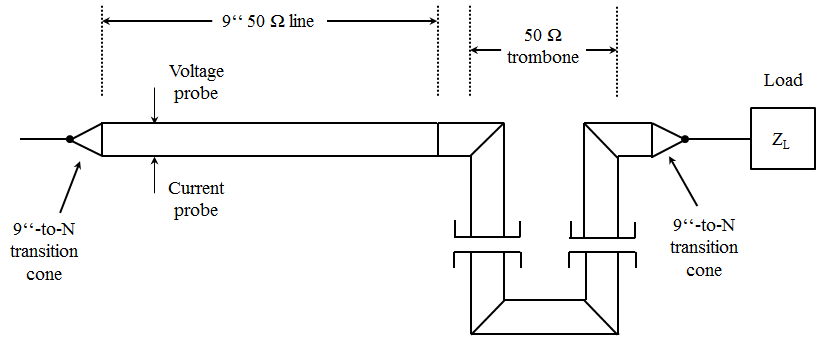


Figure 5.5: The 50 Ω test setup. The adjustable load consists of a fixed 50 Ω termination and a 50 Ω coaxial stub tuner, with a variable length between 0 and 70 cm.

5.3.1 Low power 50 Ω testbed

A 50 Ω testbed is the simplest setup in which the diagnostics can be tested. The test setup is shown schematically in Fig. (5.5). It is based on the straight 9” measurement section described in section 4.5. Only two probes were mounted, as indicated in the figure, with the other openings left unplugged, since their diameter ($\sim$ 6 cm) is very small compared to the signal wavelength ($\sim$ 10 m). At one end of the measurement section a 9”-to-N transition cone is mounted to connect it to a voltage source or network analyzer. The other end is connected to a trombone whose length can be varied by 2.5 m by means of an electric motor. The trombone is terminated by a second 9”-to-N transition cone, which is then connected to an adjustable load consisting of a fixed 50 Ω termination in series, and (through an N-to-BNC connector) to a 50 Ω parallel stub, with a length between 0 and 70 cm terminated in a short circuit. To cover as much of the Smith chart as possible, the length of the parallel stub can be set to 10, 30, 50 and 70 cm; then the trombone length is scanned while recording the data. Adding a 2.5 m cable between the load and the rightmost 9”-to-N transition section and repeating the procedure covers a significant area of the chart. The measurement procedure (for the three testbeds) is the following:

1. The network analyzer is connected to the line input; it is used to record the data while the trombone length is scanned with a fixed stub extension. This is done at four values of stub length; a 2.5 m cable is inserted between the load and the line output, and the procedure repeated. The results obtained are translated to the position of the probes; this is the reflection coefficient Γ_{NA}.

2. A voltage source and a 55 dB amplifier are connected at the line input, and the same measurements are now done with a pair of probes connected to an

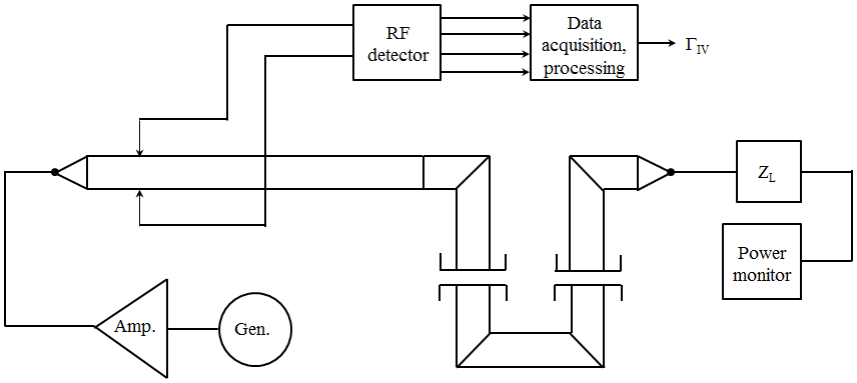


Figure 5.6: The 50 Ω test setup with voltage source, amplifier, RF detector/data acq. system and power monitor.

RF detector; a data acquisition system is used to read the output voltages; this is shown in Fig. 5.6. An RF voltmeter is connected to the output of the 50 Ω dummy load to monitor coupled power.

3. The raw data is processed, applying the necessary calibration factors to signal magnitude and phase. The reflection coefficient Γ_{IV} is obtained.

All measurements were done at 30.0 and 36.5 MHz; the forward power was in the range 1 - 1.5 kW (depending strongly on VSWR and the phase of the reflected power).

The results of Γ measurements by network analyzer during the trombone scan are shown in Fig. 5.7 for both frequencies. The four concentric "broken rings" correspond to parallel stub lengths of 10, 30, 50 and 70 cm (in order of descending radius). A small jump in amplitude can be observed on each ring, corresponding to the results obtained with and without the additional 2.5 m between load and line output. With the exception of the gap in each ring, the results cover the relevant regions of the Smith chart, as during normal ICRF operation on ASDEX Upgrade the reflection coefficients on the antenna feeding lines have magnitudes in the range $0.8 - 0.9$. Fig. 5.8 shows the corresponding measurements taken with voltage and current probes, in this case 3OU00 and 3OI00 using detector #1. To test the functioning of the system with long cables, the upper and longer line cables were connected together for a total length of ~ 200 m for each probe, from the testbed into the ASDEX Upgrade hall and looped back again. The source output power was 12 dBm; in order to avoid excessive heat loads on the cables and amplifier damage due to very high VSWR, power was pulsed with a period of 2 seconds and 50% duty cycle, which can be clearly seen in the probe results. For the results shown, no DC breaks were connected. During the course of the test

runs it was found that the amplifier output had a significant harmonic content, with the 2nd harmonic only 15 dB below the fundamental; this was believed to be a possible source of measurement error. A low-pass filter[4] was added to the amplifier output, suppressing all harmonics to below noise level; no difference in the results was observed but the filter was nonetheless used in all the measurements presented here. A manual phase correction of 39° (at 30 MHz) and 40° (at 36.5 MHz) between the two signals was added to compensate for the length difference between the cables connecting each probe to the detector. The results show good accuracy, with a maximum difference in $|\Gamma|$ of $\sim 5\%$ and a few degrees in phase. Around the $\Gamma = -1$ and $\Gamma = 1$ points, some distortion and gaps in the probe results can be observed. These correspond to regions of very low voltage ($\Gamma = -1$) and current ($\Gamma = 1$), so that the signals are outside of the measurement domain of the RF detector. To avoid damaging the amplifier by reflected power, it was not possible to increase the power level in this setup.

Note that probe results are slightly shifted to the left with respect to Γ_{NA}, more visible at 36.5 MHz. This is a consequence of either an incorrect attenuation value for a cable, an incorrect coupling value for a probe, or - more likely - a combination of both. Figure 5.9 shows the effect of adding ± 0.5 dB to the voltage probe coupling (conv. ∓ 0.5 dB to the current probe coupling); this amounts to under/overestimating the line voltage (or the opposite for current) and hence shifts the probe results right or left. Notice that a correction of $+0.5$ dB creates essentially absolute agreement between the two measurements. This is not surprising: the nominal accuracy of the ZVL NA transmission measurements (used for probe coupling), in the relevant frequency range and below 0 dBm is < 0.2 dB, while the corresponding reflection measurement accuracy (used for cable attenuation) is < 0.4 dB, about the range of the observed disagreement[5]. Conversely, Figure 5.10 shows the global effect of adding $\pm 7^\circ$ to the phase between the probes, Φ_{IV}: the result is roughly an upward or downward shift in the whole pattern. Here it must be stressed again that this is about 14 cm in equivalent electrical length, while each cable is around 200 m long.

Similar measurements were also done with the probes belonging to the upper line of antenna 3 (3OU00 and 3OI00) along with the corresponding detector (#2), as well as another pair of probes (unlabeled, not implemented on ASDEX Upgrade, and detector #24), producing essentially the same results. This confirmed that the calibration tables obtained as described in Section 5.2 were correct, along with the amplitude and phase calibration tables for the RF detectors[6]

[4] Kindly provided by Helmut Fünfgelder.

[5] Normally NA measurements were done at 10 dBm due to the very low probe coupling, so accuracy might have been below nominal.

[6] Kindly provided by Helmut Faugel.

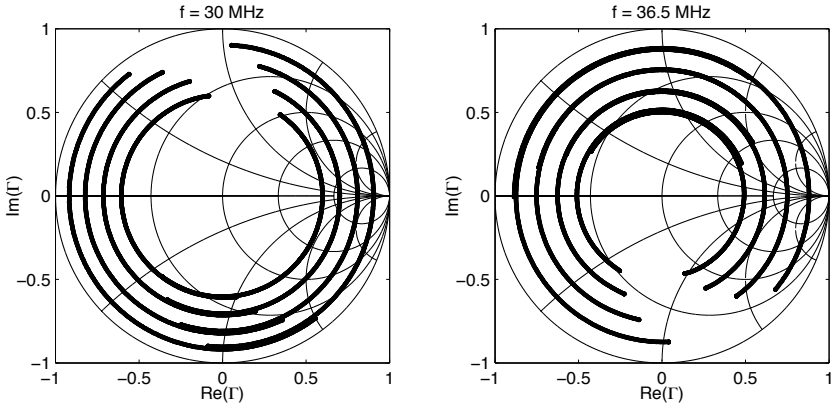


Figure 5.7: Measurements of Γ *by network analyzer during a trombone scan on the 50* Ω *testbed. The four concentric "broken rings" correspond to parallel stub lengths of 10, 30, 50 and 70 cm (in order of descending radius). The small amplitude jump is due to results obtained with and without the additional 2.5 m between load and line output.*

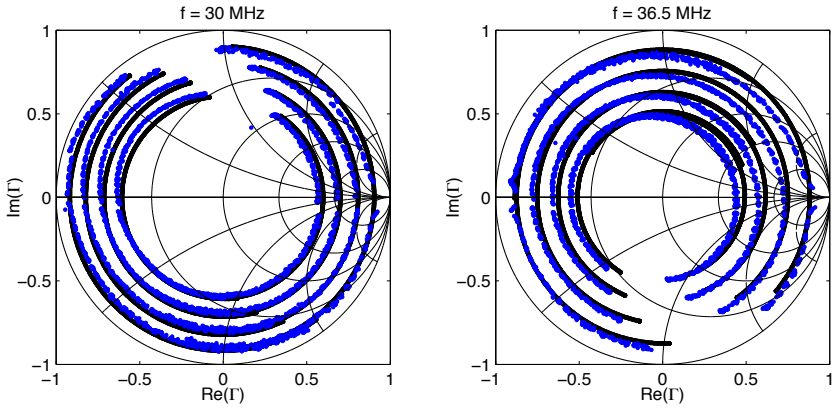


Figure 5.8: Measurements of Γ *by voltage and current probes during a trombone scan on the 50* Ω *testbed. No DC breaks. Bold black curves are NA measurements, blue dots are probe measurements.*

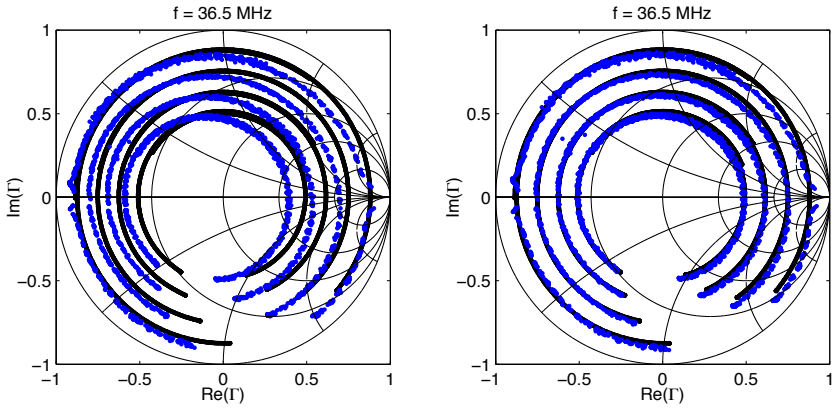


Figure 5.9: Effect of adding (left) or subtracting (right) 0.5 dB to the voltage probe coupling. Bold black curves are NA measurements, blue dots are probe measurements.

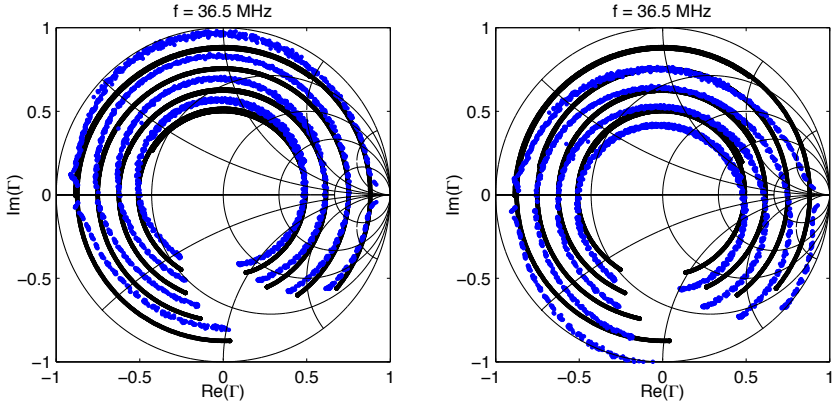


Figure 5.10: Effect of adding (left) or subtracting (right) 7° to Φ_{IV}. Bold black curves are NA measurements, blue dots are probe measurements.

5.3.2 Low power 25 Ω testbed

To convert the 50 Ω test setup to 25 Ω, the 100 mm internal conductor was switched by a 152 mm one and the adapter cones were also replaced; otherwise no changes were made. The same measurement procedure as described above was followed; in accordance with the results of section 5.2, the coupling values of all voltage probes were shifted by +6 dB. Figure 5.11 shows a typical measurement result, in this instance using probes 2UU00 and 2UI00 with detector #22. Source output power was 11 dBm. The measurements are now shifted due to the insertion of the 25 Ω section, but the agreement between the probes and NA is the same as reported above. It is noticeable from the pictures that a significantly higher level of noise is present; a specific explanation for this was not found, other than that it was not feasible to shield the test setup from the large amount of electric equipment and its effects were in many cases observed to be different from one day to another. Nonetheless, these results confirm that the coupling recomputation is correct.

Furthermore, an important aim in these runs was to determine the effect that the DC breaks might have on the measurements. To do this, the DC breaks were connected on the output of each probe as they are on the ASDEX Upgrade feeding lines. The results from this run, with no other conditions changed, are shown in Figure 5.12. Severe distortions of the signal are visible at both frequencies, while at 36.5 MHz the leftmost results are altogether shifted to the opposite side of the chart. This behavior was observed consistently on all probes and all DC breaks of systems 1, 2 and 3. In one case, two measurements with identical probes, breaks, cables and detector done several days apart produced markedly different results, both incorrect, indicating sensitivity to external interference[7]. Tests were also conducted with custom-built 10 nF DC breaks[8] (the default DC breaks having a capacitance of 1-3 nF), but no improvement was found. Measurements were then done with the DC breaks connected at the RF detector input inside the shielded ICRF control room, instead of at probe output. The results are shown in Figure 5.13 (measurements done using 2OU00, 2OI00 and detector #21). Although there is a relatively high amount of noise, it is clear that there is essentially no difference between the results with and without the DC breaks. The final tests involved the DC breaks again connected to the probe output ports, but now through 30 dB RF amplifiers with the aim of substantially increasing the signal-to-noise ratio. The measurements are shown in Figure 5.14. The results are again essentially the same with and without the breaks, indicating that the cause of the faulty results with DC breaks shown in Figure 5.12 is indeed the very low signal-to-noise ratio; notice also that noise is substantially decreased. The very severe distortion nonetheless indicates that the problem of external interference has been merely relocated to

[7] The testbed was positioned outside the ICRF control room, near continuously running electrical equipment.

[8] Kindly provided by Helmut Fünfgelder.

the amplifiers; however this is not a concern since no amplifiers are used when the probes are mounted on the ICRF feeding lines, where the power levels are ~ 30 dB higher than in these studies. From these measurements we conclude that the DC breaks should not significantly affect RF measurements on the lines.

The last issue to be addressed here is the phase change introduced by cables of different lengths connecting the voltage and current probes to the RF detector. In the above results this was corrected manually to match the NA measurements. Naturally this cannot be done while the probes are operating on the ICRF feeding lines (at least not unambiguously - see below); therefore the phase change introduced by each cable must be measured. For reference, the cables will be labeled in the same way as the probes, e. g. C2OU is the cable connecting probe 2OU00 to its RF detector, and C3UI is the cable connecting probe 3UI00 to its corresponding RF detector (this includes the extra cable length inside the ICRF control room). In principle the electrical length of each cable should be measured; but the resolution of the available time-domain reflectometer was limited to about 20 cm, clearly insufficient for the task at hand. The phase shift on each cable could be measured directly with the NA by connecting the cable between the two ports and then reading directly the phase of the transmission coefficient S_{21}. However, one end of each cable is located in the ICRF control room, and the other end at the probe on the feeding line, next to an antenna input port in the tokamak hall; physically extracting the cable was not feasible. However this is not necessary since only the phase difference between a pair of given cables is needed; each cable can be connected to a reference cable in the ASDEX Upgrade hall, which loops back into the control room and connected to the NA. After the phase shift of the two cables with the same reference is recorded, the results are subtracted and the reference canceled out. For example, the phase difference between voltage and current cables on the upper line of system 1 is

$$\begin{aligned} \Delta\Phi_O &= \Phi(\text{C1OU}) - \Phi(\text{C1OI}) \\ &= \Phi(\text{C1OU+C1UU}) - \Phi(\text{C1OI+C1UU}), \end{aligned} \tag{5.6}$$

where $\Phi(\text{C})$ is the phase of the transmission coefficient S_{21} of cable C. As stated at the beginning of this section, in all the conducted tests each voltage(current) probe output was connected to the detector through a composite cable, consisting of the upper line voltage(current) cable and the lower line voltage(current); therefore the necessary phase shifts here are $\Delta\Phi_O + \Delta\Phi_U$. Figures 5.15, 5.16 and 5.17 show the result of using these measured corrections for three probe/detector combinations. All measurements were done without DC breaks. It can be seen that the agreement with the NA results is very good in all cases (slightly better at 30 MHz); the slight shift of the probe results (blue) to the left with respect to the NA results (black) is due to coupling value error (this effect is shown in Figure 5.9). These results show that the diagnostic system, at least on the testbed, is completely character-

ized by the calibration curves of the probes and RF detectors, and the cable phase measurements. As shown below however, this not necessarily the case when the probes are mounted on the actual feeding lines.

5.3.3 Medium power 25 Ω testbed

The original aim was to conduct a final series of tests at high power (around 100 kW) to test the equipment in conditions closely resembling actual operation, in particular with DC breaks. One of the 2 MW RF generators had to be used as source for this, and there was a substantial risk of damage at high VSWR; hence the actual tests were by necessity limited to around 10 kW of input power and modest reflection (VSWR $\lesssim 5$, $\Gamma \lesssim 0.7$). The arrangement is similar to the low power testbed, except that the source is now the 2 MW generator, and the variable load consists of a 50 Ω water-cooled dummy load (normally used to dissipate reflected power due to ELMs) and a 9" parallel stub. A section of the 50 Ω line between the generator and the measurement section can be replaced by a 9"-to-N adapter, to which the NA can be connected to make the relevant measurements. The parallel stub length was set to two values only, 550 mm and 650 mm. The measurement procedure is as before: the NA is connected through the 9"-to-N adapter, and the trombone length is scanned for both stub settings. The adapter module is then removed and measurements done with the voltage/current probes at ~ 10 kW. No manual corrections are introduced (cable length is accounted for as described in the previous section). Figure 5.18 shows a typical result obtained during these runs, in this instance using probes 2UU00/2UI00/detector #21 (left) and 2OU00/2OI00/detector #22 (right). Measurements without DC breaks are shown in blue, while obtained with the DC breaks connected are plotted in red. The two results are essentially identical, save for a very small vertical displacement corresponding to a phase difference of $2^\circ - 3^\circ$; this is because the phase shift introduced by the cables was measured without the DC breaks, so they are expected to have a small effect. Nonetheless, the results again show that at high power levels, the DC breaks should not cause any major errors. Nonetheless, note that in this case the probe measurements do not agree with the NA results, displayed in black. The exact reason for this was not found; however, because this test setup is by necessity integrated into the ICRF transmission network - in contrast to the previous two testbeds - the portion of the line between the NA and the probe position includes several elbows, ceramic spacers and RF switches, significantly complicating the geometry of the line. The positions and lengths of these sections were measured by hand or approximated, and this can have a strong impact on the NA measurements since they had to be translated towards the probe position. Nonetheless, the measurements done with two different sensor combinations agree with each other; they were also replicated using the sensor set from the upper line of antenna 1 (not

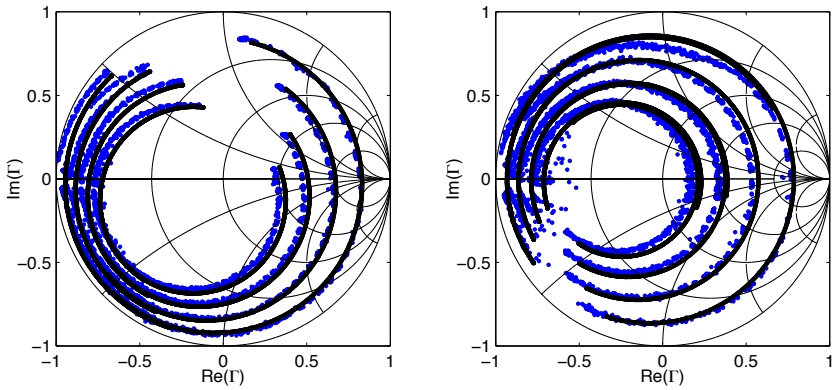


Figure 5.11: Measurements of Γ *by network analyzer and voltage/current probes during a trombone scan on the 25* Ω *testbed, no DC breaks. Bold black curves are NA measurements, blue dots are probe measurements.*

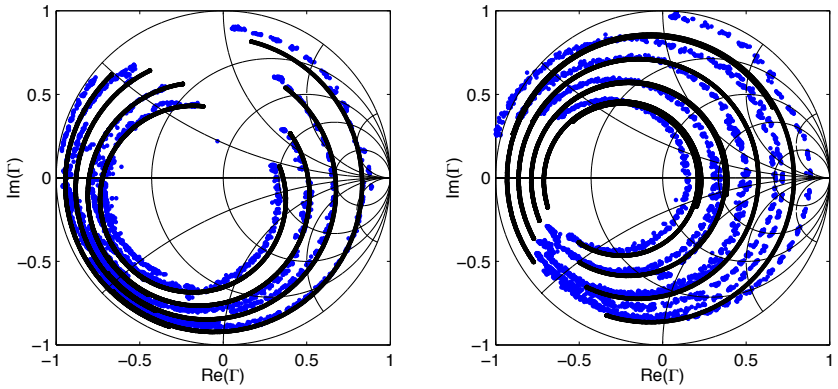


Figure 5.12: Measurements of Γ *by network analyzer and voltage/current probes during a trombone scan on the 25* Ω *testbed, with DC breaks connected at probe output. Notice the severe signal distortion. Bold black curves are NA measurements, blue dots are probe measurements.*

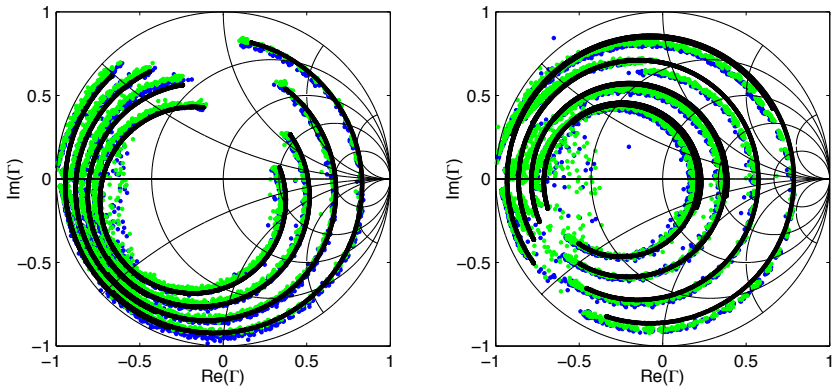


Figure 5.13: Measurements of Γ *by network analyzer and voltage/current probes during a trombone scan on the 25* Ω *testbed, without DC breaks (blue) and with DC breaks connected at RF detector input (green). There is a significant amount of noise but the results coincide. Bold black curves are NA measurements, blue and green dots are probe measurements.*

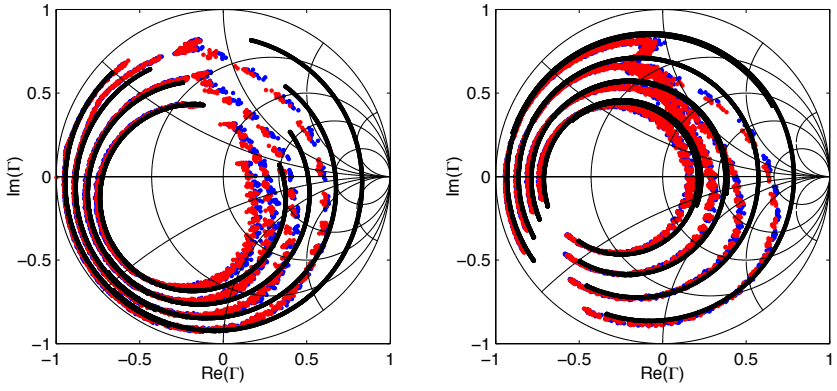


Figure 5.14: Measurements of Γ *by network analyzer and voltage/current probes during a trombone scan on the 25* Ω *testbed, with 30 dB RF amplifiers at probe output. Results without DC breaks (blue) and with DC breaks (red) are shown. There is a significant amount of distortion but the results coincide.Bold black curves are NA measurements, blue and red dots are probe measurements.*

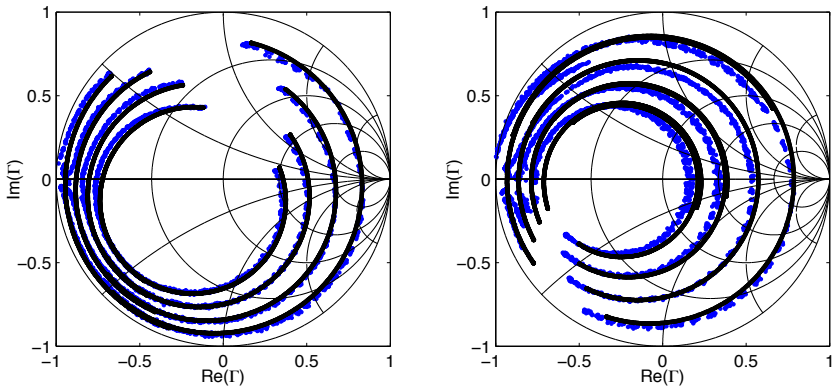


Figure 5.15: Γ measurements with probes 1OU00, 1OI00, detector #19, cables C1OU+C1UU and C1OI+C1UI. Bold black curves are NA measurements, blue dots are probe measurements.

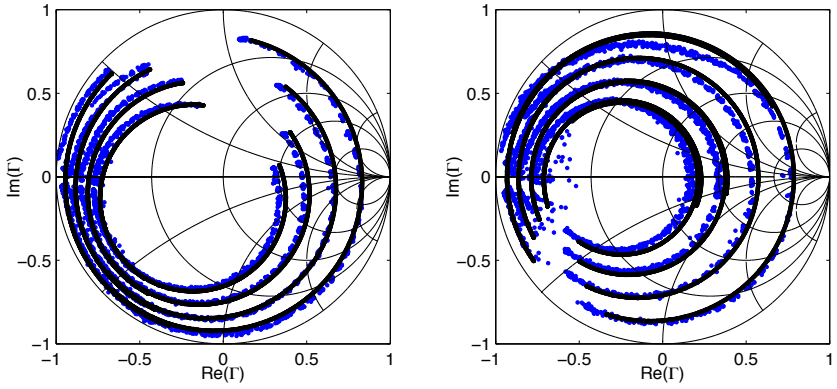


Figure 5.16: Γ measurements with probes 2UU00, 2UI00, detector #22, cables C2OU+C2UU and C2OI+C2UI. Bold black curves are NA measurements, blue dots are probe measurements.

shown here). Due to this, and the consistency shown in all previous tests, we conclude that there are no strong reasons to doubt the probe measurements in these runs.

5.4 RF measurements with voltage and current probes on ASDEX Upgrade

As the voltage and current probes were implemented on antennas 1-3, the data obtained during normal operation showed that, despite the observed agreement with independent measurements on the testbeds, the probe results disagreed significantly with the standard RF measurements. There are four quantities by which the probe results can be compared with the standard measurements for each antenna: the voltage maxima on each of the two lines, the impedance Z_T measured at the T-section, and the total coupled power. From the arguments presented in Chapter 4, Z_T is too unreliable for this purpose but voltage maxima and coupled power should be more robust. Coupled power is measured in the standard diagnostic set by directional couplers located behind the matching network (see Chapter 4, Fig. 4.23 for details), so it is separated from the point at which coupled power is measured by the probes by about 30 m of line length, on which some fraction is lost due to finite resistivity. In the low-loss approximation [3], the propagation constant $j\beta$ is to be replaced by $\gamma = \alpha + j\beta$, where $\alpha \simeq RZ_0/2$ accounts for losses and R is the resistance per unit length of the line. The coupled power measured at the T-section is related to the coupled power measured on the two feeding lines, at the location of the probes, by [3]

$$P_T = \frac{P_O\left(1-\left|\Gamma_O \mathrm{e}^{-2\gamma L_O}\right|^2\right)\mathrm{e}^{2\alpha L_O}}{1-\left|\Gamma_O\right|^2} + \frac{P_U\left(1-\left|\Gamma_U \mathrm{e}^{-2\gamma L_U}\right|^2\right)\mathrm{e}^{2\alpha L_U}}{1-\left|\Gamma_U\right|^2}, \quad (5.7)$$

where P_i is the coupled power measured at the probe location, Γ_i are the reflection coefficients (also at probe location), L_i is the line length from the probe location to the T-section and O, U denote upper and lower lines respectively. We use $R = 3 \times 10^{-3}$ Ω/m at 30 MHz and 6×10^{-3} Ω/m at 36.5 MHz[9]; with these values the power lost along a single feeding line is in the range 1%-2% of the power coupled on that line, but we still use expression (5.7) in what follows. Neglecting the power lost on the comparatively short stretch between the T-junction and the DCs, we would expect P_T to match the coupled power measured by the DCs (P_{DC}) at least within a few percent; however, this is not the case. We consider a database of all shots with ICRH starting from the 22nd of March 2013 (all probe signals integrated into ICS diagnostic) until the 25th of April (end of 2013 experimental campaign).

[9] Values measured by Helmut Faugel.

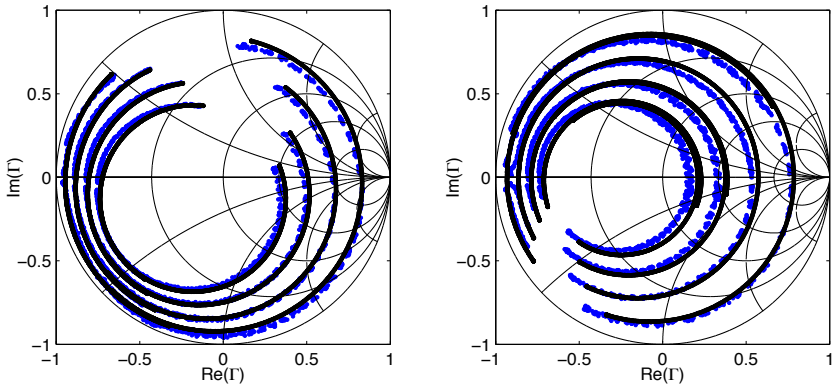


Figure 5.17: Γ measurements with probes 3OU00, 3OI00, detector #1, cables C3OU+C3UU and C3OI+C3UI. Bold black curves are NA measurements, blue dots are probe measurements.

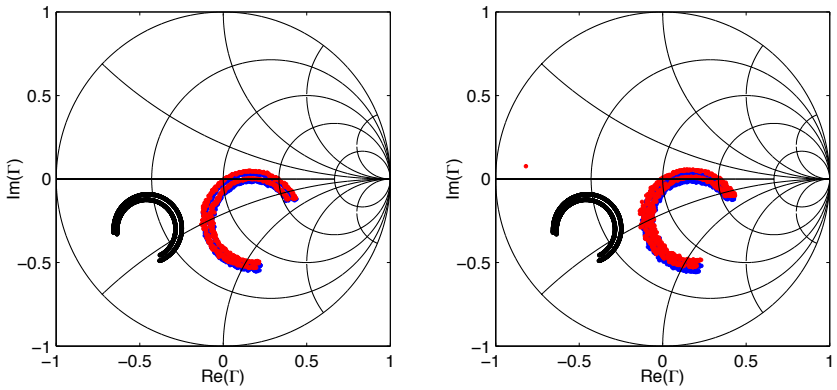


Figure 5.18: Γ measurements on the medium power 25 Ω testbed, with probes 2UU00, 2UI00, detector #21 (left), probes 2OU00, 2OI00, detector #22 (right). Measurements with DC breaks are shown in red, without DC breaks in blue. Aside from small phase difference (seen as a vertical shift), the two measurements agree with each other, but not with the NA measurements (shown in black). Bold black curves are NA measurements, blue and red dots are probe measurements.

A	$\tilde{\mathrm{P}}$	$\sigma\tilde{\mathrm{P}}$	$\tilde{\mathrm{V}}_U$	$\sigma\tilde{\mathrm{V}}_U$	$\tilde{\mathrm{V}}_L$	$\sigma\tilde{\mathrm{V}}_L$	$\tilde{\mathrm{R}}_U$	$\sigma\tilde{\mathrm{R}}_U$	$\tilde{\mathrm{R}}_L$	$\sigma\tilde{\mathrm{R}}_L$
1	0.54	0.15	1.09	0.10	1.07	0.14	0.57	0.29	0.47	0.32
2	0.65	0.12	1.06	0.12	0.96	0.05	0.74	0.27	0.57	0.23
3	0.73	0.11	1.37	0.19	1.36	0.38	0.49	0.11	0.30	0.15

Table 5.1: Voltage/current probe measurements of coupled power and V_{max} in comparison with standard measurements, averaged over all available shots in the 2013 experimental campaign, no corrections; σ is the standard deviation. U and L stand for upper and lower line, respectively.

This amounts to 28, 57 and 33 shots for antennas 1, 2 and 3 respectively. The data for each shot is ELM-synchronized, and the P_T and P_D averaged over the whole discharge are compared, as well as the height of the voltage maxima and the loading resistance of each strap. The results of this comparison, when no corrections are applied to the antennas, are summarized in Table (5.1), with

$$\tilde{\mathrm{P}} = \frac{\text{Coupled power measured by IV probes}}{\text{Coupled power measured by DC}},$$

$$\tilde{\mathrm{V}}_{U,L} = \frac{V_{max} \text{ computed from IV probes}}{V_{max} \text{ measured by standard probes}} \text{up./lw.},$$

$$\tilde{\mathrm{R}}_{U,L} = \frac{R_L \text{ computed from IV probes}}{R_L \text{ computed from standard diagnostics}} \text{up./lw.}$$

It can be seen that the coupled power computed from voltage and current probe measurements is, on average, substantially lower than that measured with the standard diagnostics, and in the case of antenna 3, V_{max} is substantially higher; R_L is correspondingly lower. As stated above, the reason for the discrepancy is unknown. A systematic search for the cause was not possible; instead we assume that there is a systematic average error in the phase between voltage and current signals - either in the length of the cables, for some reason not detected in the testbed runs, or introduced by some external interference. In order to find these systematic corrections, standard H-mode shots were selected from the database used above (based on the assumption that antenna matching was best during these shots, so that directivity errors were deemed to be low); phase corrections were then found for each antenna in each shot that, averaged over the discharge duration, minimized the difference between P_T and P_{DC} (more specifically, such that the difference became $< 0.1\%$ of P_{DC}.) Because two power values (one on each line) are compared with one, we imposed the additional constraint that the difference between the R_L computed from probe measurements on each line was also minimized. ELM synchronization was used in all cases.

The correction factors to be applied are taken to be the averages for each line over the whole series of selected shots. The values thus obtained are displayed in Tables 5.2 and 5.3, along with the standard deviation. Notice that, especially

Antenna	ϕ_C up.	$\sigma\phi_C$ up.	ϕ_C lw.	$\sigma\phi_C$ lw.
A1	$6.28°$	$1.48°$	$8.85°$	$3.56°$
A2	$1.48°$	$0.55°$	$7.71°$	$3.58°$
A3	$1.67°$	$0.26°$	$3.09°$	$0.43°$

Table 5.2: Phase correction factors at 30.0 MHz.

Antenna	ϕ_C up.	$\sigma\phi_C$ up.	ϕ_C lw.	$\sigma\phi_C$ lw.
A1	$-3.89°$	$0.16°$	$-5.48°$	$0.49°$
A2	$-3.00°$	$0.14°$	$-4.28°$	$0.31°$
A3	$-0.76°$	$0.36°$	$-3.60°$	$0.42°$

Table 5.3: Phase correction factors at 36.5 MHz.

in the case of antenna 3, they are fairly small in comparison with the corrections introduced manually to the first 50 Ω testbed results ($\sim 40°$, Section 5.3.1). Applying these constant correction factors to the database analyzed above results in a significantly better overall agreement in coupled power (notice also that the spread in F_P is decreased roughly by a factor of two); V_{max} is essentially insensitive to phase changes in this range, V_{min} changing instead. These results are shown in Table 5.4; these are the correction factors used for ASDEX Upgrade data analysis throughout this work, unless otherwise indicated. The standard deviation of each correction factor, together with the 0.6 dB accuracy of the NA measurements (probe coupling and cable attenuation, see Section 5.3.1), constitute the necessary input to compute the error bars for all RF measurements by the procedure outlined in Section 4.4.

The reason for the large discrepancy in V_{max} on antenna 3 is not known at the present. Because these V_{max} probes were recalibrated along with all others, it is unlikely that the coupling factor is incorrect. An error in probe position is also not likely, since the voltage maximum is relatively broad. The error could stem from an incorrect cable attenuation value; however, it was not possible to make the relevant NA measurement due to the system being in use at the time. Note that the R_L computed from the voltage/current probes on line 3 is almost a factor of 2

A	$\tilde{\mathrm{P}}$	$\sigma\tilde{\mathrm{P}}$	$\tilde{\mathrm{V}}_U$	$\sigma\tilde{\mathrm{V}}_U$	$\tilde{\mathrm{V}}_L$	$\sigma\tilde{\mathrm{V}}_L$	$\tilde{\mathrm{R}}_U$	$\sigma\tilde{\mathrm{R}}_U$	$\tilde{\mathrm{R}}_L$	$\sigma\tilde{\mathrm{R}}_L$
1	0.98	0.07	1.09	0.10	1.07	0.14	0.85	0.27	0.84	0.31
2	0.97	0.05	1.06	0.11	0.95	0.04	0.96	0.19	0.95	0.20
3	1.03	0.08	1.37	0.19	1.35	0.38	0.55	0.12	0.54	0.12

Table 5.4: Voltage/current probe measurements of coupled power and V_{max} in comparison with standard measurements, averaged over all available shots in the 2013 experimental campaign, with the corrections from Tables 5.2 and 5.3.

lower than that computed from standard measurements; in fact its absolute value is always lower than on lines 1 and 2. A detailed discussion of the possible reasons is found in section 8.3.

5.5 Summary and conclusions

Although the RF measurements obtained as described here are significantly more detailed than the standard ones, they have two main limitations in their present form. The first is the validity of P_{DC} as reference measurement when searching for phase corrections. Although directivity errors are expected to be low, differences in cable length (between forward and backward directional couplers) can have a more significant impact on the power measurement, thus casting doubt on the validity of the correction factors obtained.

The second issue is the assumption of equal R_L on both straps. Very similar, although not identical, loading would be expected on both straps due to their design; this is also consistent with TOPICA simulation results, in which the difference between the two straps is $\sim 0.2\ \Omega$ in the normal operating range, far lower than the variation in R_L due to changes in the plasma density. In any case, this constraint is imposed on the data only in a statistical sense, when averaging over a whole discharge, and it is neither expected nor observed for each individual measurement. Moreover, we are forced here to make *some* assumption. The alternative is to impose the constraint that the *coupled power* be equal on both lines, but this would be an even less realistic approach: identical coupled power would be expected only when the input impedance looking into both feeding lines from the T-junction is equal, but the geometrical complexity of the lines would make this very unlikely. Nonetheless, the consequences of such an approach are illustrated in Section 8.3 and will not be explored here for brevity, but the overall conclusion is that this gives rise to a significant difference in loading between the two straps; this is another reason to consider this assumption less likely than approximately equal loading.

6

Numerical modeling of ICRF antennas

6.1 General remarks

A variety of numerical codes have been developed in the last three decades with the aim of predicting the behavior of plasma-loaded antennas. The two codes mainly used in this work are FELICE (Finite ELement Ion Cyclotron Emulator) ([46], [47]) and TOPICA (TOrino Politecnico Ion Cyclotron Antenna) [18]. Both codes distinguish two different physical regions: the plasma column, and a vacuum region where the antenna itself is located. They are both based on the same physical plasma model, a multispecies finite-temperature plasma in slab approximation, i. e., a plasma with a "flat" surface that ignores all effects associated with the real toroidal geometry of a tokamak. Both codes compute the *plasma surface impedance matrix* $\mathbf{Z}_{surf}$, i. e., the ratio of electric and magnetic field components at the plasma-vacuum interface defined by

$$\begin{pmatrix} E_y \\ E_z \end{pmatrix} = \mathbf{Z}_{surf} \begin{pmatrix} H_y \\ H_z \end{pmatrix}, \tag{6.1}$$

which then serves as a boundary condition to compute the fields everywhere in the vacuum/antenna region, whence the relevant antenna parameters are determined (here y and z stand for poloidal and toroidal directions, respectively). Indeed, a modified version of FELICE constitutes the core of the module that computes $\mathbf{Z}_{surf}$ in TOPICA.

The main difference between the two codes is in their treatment of the antenna itself. The FELICE model is a simplified - but nevertheless three-dimensional - an-

tenna constituted by infinitely thin, flat conducting surfaces that also include radial feeders. The current distribution on the conductors can be either imposed (the so-called *forced EMF method*) or self-consistently determined (the *Ritz method*) [47]. During the time of this work, however, FELICE was being upgraded and the available version only allowed the forced current distribution, which is nonetheless still an acceptable approximation when the assumed current is a reasonable guess of the exact one [48]. The FELICE antenna description is flexible enough that a variety of configurations - feeder-to-short, push-pull, violin and even the "folded" ASDEX-like antennas - can be simulated. As part of the output, the radiation impedance defined in Chapter 3 is computed.

The TOPICA model, on the other hand, is fully three-dimensional, with the level of detail only limited by the size of the triangular mesh. Therefore the structure need not be "flat", but can be toroidally and poloidally curved as an actual physical antenna. Current distribution is always self-consistently determined; since multiport antennas can be modeled, the full **S**-matrix is computed as part of the output. The disadvantage, however, is that TOPICA usually requires rather long simulation times. Thus, FELICE and TOPICA can be used complementarily to study the behavior of a given antenna by running, e. g., parametric scans with FELICE and fine-tuning selected cases using TOPICA.

The following subsections briefly describe the FELICE and TOPICA codes.

6.1.1 FELICE

As mentioned above, FELICE is based on a plane-stratified model of the tokamak, with the static magnetic field in the z (toroidal) direction, and the plasma parameters varying in the x (radial) direction. Surfaces at $x = \text{const.}$ play the role of magnetic surfaces; vessel and plasma boundary also lie on such surfaces. In this simplified geometry the coordinates y and z are ignorable, and the wave fields can be decomposed in plane "partial waves"

$$\mathbf{E}(\mathbf{r},t) = \sum_{k_y}\sum_{k_z} \mathbf{E}(k_y,k_z;x)e^{i(k_y y + k_z z - \omega t)}; \tag{6.2}$$

$$\mathbf{B}(\mathbf{r},t) = \sum_{k_y}\sum_{k_z} \mathbf{B}(k_y,k_z;x)e^{i(k_y y + k_z z - \omega t)}. \tag{6.3}$$

which propagate independently of each other. Maxwell's equations thus reduce to a set of independent systems of ordinary differential equations for the amplitudes $\mathbf{E}(k_y,k_z;x)$ and $\mathbf{B}(k_y,k_z;x)$ of each partial wave. In vacuum these equations can be solved analytically, the corresponding Fourier components of the antenna currents acting as sources [47].

Antennas consist of thin straps parallel to the plasma boundary and the wall, and radial conductors connecting them to feeders and shorts. The currents on the

antenna elements are written as a superposition of transmission line modes with different propagation constants:

$$J(\eta) = \sum_k \alpha_k \left[J_{out}^{(k)} \cos\gamma_k(\eta - \eta_{out}) + K_{out}^{(k)} \frac{\sin\gamma_k(\eta - \eta_{out})}{\gamma_k} \right], \qquad (6.4)$$

where η is a coordinate along the strap, increasing from 0 at the feeder to the total length of the strap at the short. The propagation constants γ_k are chosen arbitrarily in the poloidal segments, while $\gamma = 1$ is assumed on the radial feeders as in a coaxial transmission line[1] [47]. The constants $J_{out}^{(k)}$ and $K_{out}^{(k)}$ are determined by continuity at each connection between radial and tangential segments; the coefficients α_k are determined by a variational procedure (the detailed description of the antenna is presented in [47]).

To describe the wave field in the plasma, FELICE uses the Swanson-Colestock-Kashuba (SCK) equations, valid to second order in the ratio of the Larmor radius to the wavelength - this is the *finite Larmor radius* (or FLR) approximation. The SCK model describes

- the cold plasma terms describing the fast and slow magnetosonic waves;
- cyclotron absorption at $\omega = 2\omega_{ci}$ (first harmonic);
- the Ion Berstein wave;
- the electron FLR contributions to the components ϵ_{yy} and ϵ_{yz} of the dielectric tensor.

[1] in FELICE lengths are measured in units of c/ω, so the γ_k are dimensionless.

For each partial wave in (6.2) and (6.3), the SCK wave equations are [47][2]

$$\begin{aligned}
0 = (n_y^2 + n_z^2 - S)E_x + \left(n_y \frac{\partial E_y}{\partial x} + DE_y\right) + \\
in_z \frac{\partial E_z}{\partial x} - \frac{\partial}{\partial x}\left(\sigma_2^i \frac{\partial E_x}{\partial x} - i\delta_2^i \frac{\partial E_y}{\partial x}\right) \\
+n_y^2\left(\sigma_2^i E_x - i\delta_2^i Ey\right) + \\
in_y\left[\frac{\partial}{\partial x}\left(i\delta_2^i E_x + \sigma_2^i E_y\right) - \left(i\delta_2^i \frac{\partial E_x}{\partial x} + \sigma_2^i \frac{\partial E_y}{\partial x}\right)\right] \\
+2in_y\lambda_0^e\left(\frac{\partial E_y}{\partial x} + in_y E_x\right) + in_y n_z \xi_0^e E_z, \qquad (6.5)
\end{aligned}$$

$$\begin{aligned}
0 = i\left(n_y \frac{\partial E_x}{\partial x} - DE_x\right) - \frac{\partial^2 E_x}{\partial x^2} + \left(n_z^2 - S\right)E_y - \\
n_y n_z E_z - \frac{\partial}{\partial x}\left(i\delta_2^i \frac{\partial E_x}{\partial x} + \sigma_2^i \frac{\partial E_y}{\partial x}\right) \\
+n_y^2\left(i\delta_2^i E_x + \sigma_2^i E_y\right) - \\
in_y\left[\frac{\partial}{\partial x}\left(\sigma_2 E_x - i\delta_2 E_y\right) - \left(\sigma_2^i \frac{\partial E_x}{\partial x} - i\delta_2^i \frac{\partial E_y}{\partial x}\right)\right] \\
-2\frac{\partial}{\partial x}\left[\lambda_0^e\left(\frac{\partial E_y}{\partial x} - in_y E_x\right)\right] - n_z \frac{\partial}{\partial x}\left(\xi_o^e E_z\right), \qquad (6.6)
\end{aligned}$$

$$\begin{aligned}
0 = in_z \frac{\partial E_x}{\partial x} - n_y n_z E_y - \frac{\partial^2 E_z}{\partial x^2} + \left(n_y^2 - P\right)E_z + \\
n_z \xi_0^e \left(\frac{\partial E_y}{\partial_x} - in_y E_x\right). \qquad (6.7)
\end{aligned}$$

Here $n_{y,z} = ck_{y,z}/\omega$, $\sigma_n^\alpha = \left(\lambda_{-n\alpha} + \lambda_{+n\alpha}\right)/2$, $\delta_n^\alpha = \left(\lambda_{-n\alpha} - \lambda_{+n\alpha}\right)/2$, with

$$\lambda_{n\alpha} = \frac{1}{2}\frac{\omega_{p\alpha}^2}{\omega_{c\alpha}^2}\frac{v_{th\alpha}^2}{c^2}\left(-x_{0\alpha} Z\left(x_{n\alpha}\right)\right), \; \xi_n^\alpha = \frac{1}{2}\frac{\omega_{p\alpha}^2}{\omega\omega_{c\alpha}^2}\frac{v_{th\alpha}^2}{c^2} x_{0\alpha} Z'\left(x_{n\alpha}\right), \qquad (6.8)$$

and $x_{n\alpha}$ and the Plasma Dispersion Function Z already defined in Chapter 2. The magnetic field is obtained from Faraday's law $\nabla \times \mathbf{E} = c^{-1}\partial\mathbf{B}/\partial t$:

$$B_x = n_y E_z - n_z E_y, \qquad (6.9)$$

$$B_y = i\left(\frac{\partial E_z}{\partial x} - in_z E_x\right), \qquad (6.10)$$

$$B_z = -i\left(\frac{\partial E_y}{\partial x} - in_y E_x\right). \qquad (6.11)$$

The fields everywhere are determined by first solving the SCK equations in the plasma (they are recast in the Galerkin weak-variational form and discretized with

[2] Gaussian units are used in [47] and hence also in the equations in this section. Throughout the remainder of this work SI units are used.

cubic Hermite finite elements) subject to boundary conditions. These can either be a conducting wall at the HFS of the slab, or *outward radiation conditions* at some point in the plasma, where it is assumed that the WKB approximation is valid, and that any power not reflected up to this point will be absorbed further inside [47]. Because the slab approximation overestimates the coherence between the launched and reflected waves [47], outward radiation conditions are preferable to the conducting wall conditions[3]; this is illustrated in detail in section 6.4.1. The plasma surface impedance obtained in this way, along with field continuity, is then used as boundary condition for the fields in the vacuum region. Once these are determined, the radiated power - and hence the antenna coupling resistance - is computed from Poynting's theorem. The entire procedure is explicitly shown in section 6.2.

6.1.2 TOPICA

As stated, TOPICA computes the full scattering/impedance/admittance matrix of a multiport antenna with complex realistic geometry, along with self-consistent distribution of currents on all conducting surfaces, and the radiated fields in front of the antenna on user-defined dedicated surfaces. Mathematical details are found in [18] and [49]; to summarize, TOPICA makes use of the equivalence theorem of electrodynamics to separate the physical domain of the problem into two regions, the plasma column and a vacuum region containing the antenna structure, which is assumed to consist of perfectly conducting surfaces. TOPICA solves the system of equations

$$\chi_C \left(\mathbf{E}_1^p + \mathbf{E}_1^s\right)|_{tan} = \widehat{\mathbf{n}} \times \left(\chi_P \mathbf{M}_P + \chi_A \mathbf{M}_{A-}\right), \tag{6.12}$$

$$\chi_A \left(\mathbf{H_1^p} + \mathbf{H_1^s} - \mathbf{H_2^s}\right)|_{tan} = 0, \tag{6.13}$$

where

- the subscripts 1 and 2 denote fields in the antenna and plasma region, respectively;
- the superscripts *p* and *s* denote respectively the *primary* fields, radiated by the sources $\mathbf{M}_P$, and the *scattered* fields, produced by equivalent sources $\mathbf{J}_C$ and $\mathbf{M}_{A-}$, where $\mathbf{J}_C$ are the surface currents on the metallic conductors and $\mathbf{M}_{A-}$ are magnetic currents defined on the boundary separating the two regions (termed *aperture*) according to the equivalence principle;
- the characteristic functions χ_β are defined as

$$\chi_\beta(\mathbf{r}) = \begin{cases} 1, & \text{if } \mathbf{r} \in S_\beta, \\ 0, & \text{if } \mathbf{r} \notin S_\beta \end{cases} \tag{6.14}$$

[3] Marco Brambilla and Roberto Bilato, personal communication.

and $\beta = A$ (aperture), C (conducting surface) or P (open feeder surface where the sources $\mathbf{M}_P$ are defined).

By writing the scattered fields $\mathbf{E}_1^s$, $\mathbf{H}_1^s$ and $\mathbf{H}_2^s$ in terms of their sources $\mathbf{J}_C$ and $\mathbf{M}_{A-}$ and Green's functions $\mathbf{G}$ (free space) and $\mathbf{G}_P$ (plasma region), the coupled integro-differential equations become

$$-jZ_0k_0\chi_C\int_{S_C} d^2r'\mathbf{G}(R)\cdot\mathbf{J}_C|_{tan} - \chi_c p.v.\int_{S_A} d^2r'\nabla\Phi\times\mathbf{M}_{A-}|_{tan} - \frac{1}{2}\hat{\mathbf{n}}\times\mathbf{M}_{A-}\chi_A = -\chi_C\mathbf{E}_1^p|_{tan} + \hat{\mathbf{n}}\times\mathbf{M}_P\chi_P, \quad (6.15)$$

$$\chi_A p.v.\int_{S_C} d^2r'\nabla\Phi\times\mathbf{J}_C|_{tan} - \frac{1}{2}\hat{\mathbf{n}}\times\mathbf{J}_C\chi_A - j\frac{k_0}{Z_0}\chi_A\int_{S_A} d^2r'\mathbf{G}\cdot\mathbf{M}_{A-}|_{tan} - \chi_A\hat{\mathbf{n}}\times\int_{S_A} d^2r'\mathbf{G}_P\cdot\mathbf{M}_{A-}\times\hat{\mathbf{n}} = -\chi_A\mathbf{H}_1^p|_{tan}, \quad (6.16)$$

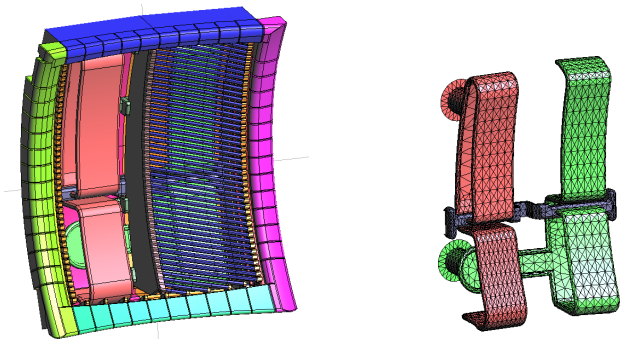
with Φ being the Helmholtz function

$$\Phi(R) = \frac{e^{-jk_0R}}{4\pi R}, \quad (6.17)$$

$R = |\mathbf{r} - \mathbf{r}'|$ and $\mathbf{r}'$, $\mathbf{r}$ indicate source and observation points, respectively [18]; $Z_0 = (\mu_0/\epsilon_0)^{1/2}$ and $k_0 = \omega(\epsilon_0\mu_0)^{1/2}$ are the vacuum impedance and wavenumber, respectively. Note that all the plasma effects appear only through the tensor $\mathbf{G}_P$; this in turn is computed by TOPICA from the plasma surface impedance, which is the output of a suitably modified version of the FELICE code (see above). The details of the mathematical procedure are found in [18] and [49].

The physical model of the antenna structure, which is needed as input, consists of a 3-D mesh with triangular cells, which is directly importable from commercial CAD packages and can therefore describe an antenna to a very high degree of geometrical complexity, with no need to make any assumptions, such as infinitely thin and straight radiating straps. An example of such an antenna model is shown in Fig. 6.1.

Together with this model, the user defines the driving frequency and the *feeding scheme*, that is, the amplitude and relative phasing of the source voltages on all input ports of the antenna. The FELICE module of the code requires the kinetic plasma profiles, namely density and temperature profiles of the plasma species. As stated above, the output of TOPICA consists of self-consistent current distributions on all conducting surfaces, electric and magnetic field distributions on user-defined surfaces and, of main interest for coupling properties, global parameters such as the scattering, impedance and admittance matrices of the antenna. All directly measurable quantities - coupled power, input reflection coefficients,



(a) Full antenna structure, Faraday screen bars removed on right.

(b) Triangular mesh generated on the basis of the model, showing radiating straps (with their supports) and feeders only.

Figure 6.1: The complex model of an ASDEX Upgrade two-strap antenna, produced in GiD. The triangular mesh on the right is used is used as TOPICA input.

loading resistance of each strap and so on - are computed from these matrices by a suitable transmission line model of the feeding network connected to the antenna. Because of the errors that may be introduced by uncertainties in knowledge about that network, it is advantageous to compare the code results with measurements taken as close to the antenna input as possible.

6.1.3 Rsolver

A third code, Rsolver (for *resistance solver*) was written for the present work, with the aim of using it for running a large number of simulations, when FELICE was not yet available. Rsolver makes use of a cold multispecies plasma model in slab approximation, includes the fast wave branch only, and has a current distribution imposed on an infinitely thin two-dimensional multistrap antenna. Although FELICE became available again at about the same time as Rsolver was finished and was used for most of the subsequent numerical work, Rsolver is still useful for several reasons:

1. Due to it simplicity, it is somewhat more robust than both FELICE and TOPICA[4].

2. Running simulations in parallel with the hot-plasma FELICE, it can highlight situations where the cold plasma approximation may not be sufficiently

[4]FELICE occasionally produces unreliable results when very low density plasma is present in front of the antenna, due to the finite temperature model it uses. When used in conjunction with TOPICA, the user always defines a boundary close to the antenna where the low density plasma is replaced by a vacuum layer [50].

accurate or, conversely, show that it is indeed sufficiently accurate for most cases.

3. Many procedures in Rsolver, such as the determination of $\mathbf{Z_S}$ and the subsequent calculation of R_{rad}, follow the same methods as the much more complex FELICE, thereby providing valuable insight into the internal workings of more complex codes.

For these reasons, it is worth outlining the mathematical model used in Rsolver. It must also be noted that this code very closely resembles the fast code ANTITER II recently used by Messiaen *et al.* for an extensive study of antenna coupling behavior, specifically an ITER-like model, with a wide range of analytical density profiles as approximations of expected ITER profiles [22] (more on which below). ANTITER II has also been used jointly with TOPICA in another study of ITER antenna behavior, this time as function of varying frequency and strap phasing [51]. The equations describing the field components of the FW in the plasma are identical in Rsolver and ANTITER II; however the antenna model is somewhat different - and more flexible - in ANTITER II, where it is described as an array of boxes recessed in a metal wall with each box being excited by a thin radiating strap [51]. In Rsolver, as shown below, the antenna is considered to be "protruding" from the vessel wall and not housed in a cavity.

6.2 Computing the coupling resistance of a simple flat antenna: the Rsolver code

6.2.1 Fields in the plasma

The physical model of the plasma-facing antenna is shown in Fig. 6.2. It consists of N rectangular straps (radial feeders have been neglected) oriented along the $y-z$ plane in a vacuum region, with a metallic wall on the left and a plasma on the right, which is uniform along y and z but not along x. The $n-$th strap is fed with some phasing ϕ_n relative to the first strap.

A spectral ansatz is used by assuming that the fields everywhere have the form

$$\mathbf{E}(\mathbf{r},t) = \sum_{k_y}\sum_{k_z} \mathbf{E}(k_y,k_z;x)e^{i(k_y y + k_z z - \omega t)}, \tag{6.18}$$

$$\mathbf{B}(\mathbf{r},t) = \sum_{k_y}\sum_{k_z} \mathbf{B}(k_y,k_z;x)e^{i(k_y y + k_z z - \omega t)} \tag{6.19}$$

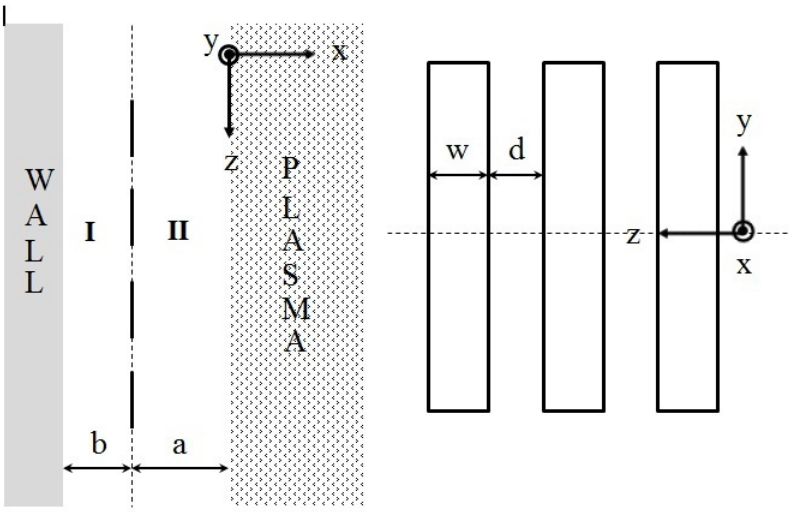


Figure 6.2: Antenna model. Straps shown on right.

as in FELICE (Eqs. (6.2) and (6.3)). The Maxwell equations are

$$\nabla \times \mathbf{E} = -\frac{\partial \mathbf{B}}{\partial t}, \tag{6.20}$$

$$\nabla \times \mathbf{B} = \mu_0 \mathbf{J} + \frac{1}{c^2}\frac{\partial \mathbf{E}}{\partial t}. \tag{6.21}$$

With $\mathbf{J} = i\omega\epsilon_0(\mathbf{I} - \epsilon)$ (6.21) can be written as

$$\nabla \times \mathbf{B} = -\frac{i\omega}{c^2}\epsilon \cdot \mathbf{E}, \tag{6.22}$$

where ϵ is the plasma dielectric tensor in the usual Stix notation (see Chapter 2)

$$\epsilon = \begin{bmatrix} S & -iD & 0 \\ iD & S & 0 \\ 0 & 0 & P \end{bmatrix}. \tag{6.23}$$

Then the Maxwell equations are written as

$$k_y E_z - k_z E_y = \omega B_x, \tag{6.24}$$

$$k_z E_x + i\frac{\mathrm{d}E_z}{\mathrm{d}x} = \omega B_y, \tag{6.25}$$

$$k_y E_x + i\frac{\mathrm{d}E_y}{\mathrm{d}x} = -\omega B_z, \tag{6.26}$$

$$k_y B_z - k_z B_y = -\frac{\omega}{c^2}(SE_x - iDE_y), \tag{6.27}$$

$$k_z B_x + i\frac{\mathrm{d}B_z}{\mathrm{d}x} = -\frac{\omega}{c^2}(iDE_x + SE_y), \tag{6.28}$$

$$k_y B_x + i\frac{\mathrm{d}B_y}{\mathrm{d}x} = \frac{\omega}{c^2}(PE_z). \tag{6.29}$$

We assume $P \to \infty$ (i.e. negligible electron inertia), which implies $E_z \to 0$. This assumption allows us to remove E_z from eqs. (6.24) - (6.29), which then reduce to

$$k_z E_y = -\omega B_x, \tag{6.30}$$

$$k_z E_x = \omega B_y, \tag{6.31}$$

$$i\frac{\mathrm{d}E_y}{\mathrm{d}x} = -k_y E_x - \omega B_z, \tag{6.32}$$

$$k_z B_y = k_y B_z + \frac{\omega}{c^2}(SE_x - iDE_y), \tag{6.33}$$

$$i\frac{\mathrm{d}B_z}{\mathrm{d}x} = -k_z B_x - \frac{\omega}{c^2}(iDE_x + SE_y), \tag{6.34}$$

$$k_y B_x = -i\frac{\mathrm{d}B_y}{\mathrm{d}x}. \tag{6.35}$$

From Eqs. (6.30) - (6.35) we can obtain two coupled first-order differential equations for the components E_y and B_z of the fast magnetosonic wave:

$$\frac{\mathrm{d}}{\mathrm{d}x}(i\omega B_z) = Fk_y(i\omega B_z) - k_\perp^2 E_y, \tag{6.36}$$

$$\frac{\mathrm{d}}{\mathrm{d}x}E_y = \left(1 - \frac{k_y^2}{G}\right) i\omega B_z - Fk_y E_y, \tag{6.37}$$

with

$$F = \frac{k_o^2 D}{G}, \tag{6.38}$$

$$G = k_o^2 S - k_z^2, \tag{6.39}$$

$$k_\perp^2 = k_o^2 S - k_z^2 - Fk_o^2 D, \tag{6.40}$$

$$k_o = \frac{\omega}{c}. \tag{6.41}$$

Eqs. (6.36) and (6.37), as stated, are equivalent to Eqs. (1) in [22].

The integration is started at a point $x = 0$ inside the plasma with outward radiation conditions, where the WKB approximation is locally valid and

$$E_y(x) = E_0 e^{-ik_x x}. \tag{6.42}$$

Then $E_y(x = 0) = E_0$, and from (6.36)

$$i\omega B_z(x = 0) = -k_\perp^2 E_0(-ik_x - Fk_y)^{-1}, \tag{6.43}$$

where $k_x = \sqrt{k_\perp^2 - k_y^2}$ and F and $k_\perp$ are evaluated at $x = 0$. With these initial conditions, Eqs. (6.36) and (6.37) are solved numerically advancing towards the antenna, up to the plasma surface at $x = x_{surf}$ (this corresponds to the interface between region II and the plasma in Fig. 6.2), to obtain the surface impedance

$$Z_{surf} = \frac{E_y(x = x_{surf})}{\omega B_z(x = x_{surf})}. \tag{6.44}$$

For the special case of a uniform plasma of constant density, with a uniform background magnetic field, the (normalized) electric field inside the plasma can simply be written as $E_y = e^{-ik_x x}$, with $k_x = \sqrt{k_\perp^2(x = 0) - k_y^2}$ as before. The wave magnetic field B_z and the surface impedance matrix are then easily obtained from Eqs. (6.37) and (6.44) respectively.

6.2.2 Fields in the vacuum region

In the vacuum region, the x-components of the fields can be eliminated to obtain equations in terms of y- and z-components only. Taking Eqs. (6.26) and (6.27) and recalling that $S \to 1$ and $D \to 0$ in vacuum, we obtain

$$\frac{\mathrm{d}E_y}{\mathrm{d}x} = i\omega\left(1 - \frac{k_y^2}{k_0^2}\right)B_z + i\omega\frac{k_y k_z}{k_0^2}B_y. \tag{6.45}$$

Taking Eqs. (6.25) and (6.27),

$$\frac{\mathrm{d}E_z}{\mathrm{d}x} = -i\omega\left(1 - \frac{k_z^2}{k_0^2}\right)B_y - i\omega\frac{k_y k_z}{k_0^2}B_z. \tag{6.46}$$

Taking Eqs. (6.29) and (6.24),

$$\frac{\mathrm{d}B_y}{\mathrm{d}x} = -\frac{i\omega}{c^2}\left(1 - \frac{k_y^2}{k_0^2}\right)E_z - \frac{i\omega}{c^2}\frac{k_y k_z}{k_0^2}E_y. \tag{6.47}$$

Finally from Eqs. (6.28) and (6.24),

$$\frac{\mathrm{d}B_z}{\mathrm{d}x} = \frac{i\omega}{c^2}\left(1 - \frac{k_z^2}{k_0^2}\right)E_y + \frac{i\omega}{c^2}\frac{k_y k_z}{k_0^2}E_z. \tag{6.48}$$

Eqs. (6.45) - (6.48) can be written somewhat more compactly in matrix form as

$$\frac{\mathrm{d}}{\mathrm{d}x}\begin{pmatrix} E_y \\ E_z \end{pmatrix} = \frac{1}{k_0^2}\begin{pmatrix} k_y k_z & k_0^2 - k_y^2 \\ -(k_0^2 - k_z^2) & -k_y k_z \end{pmatrix}\begin{pmatrix} i\omega B_y \\ i\omega B_z \end{pmatrix}, \tag{6.49}$$

$$\frac{\mathrm{d}}{\mathrm{d}x}\begin{pmatrix} B_y \\ B_z \end{pmatrix} = \frac{1}{k_0^2}\begin{pmatrix} k_y k_z & k_0^2 - k_y^2 \\ -(k_0^2 - k_z^2) & -k_y k_z \end{pmatrix}\begin{pmatrix} -i\omega E_y/c^2 \\ -i\omega E_z/c^2 \end{pmatrix}. \tag{6.50}$$

Furthermore, we take the derivative of Eq. (6.45) with respect to x; substituting (6.47) and (6.48) and rearranging, we obtain the Helmholtz equation for E_y

$$\frac{\mathrm{d}^2 E_y}{\mathrm{d}x^2} = -\kappa^2 E_y, \tag{6.51}$$

$$\kappa^2 = \left[\frac{(k_0^2 - k_y^2)(k_0^2 - k_z^2) - k_y^2 k_z^2}{k_0^2}\right]. \tag{6.52}$$

This has the solution

$$E_y(x) = \alpha e^{i\kappa x} + \beta e^{-i\kappa x}. \tag{6.53}$$

Similarly, starting with Eq. (6.46) we arrive at

$$E_z(x) = \gamma e^{i\kappa x} + \delta e^{-i\kappa x}. \tag{6.54}$$

Substituting Eqs. (6.53) and (6.54) into Eq. (6.47), we get

$$\frac{\mathrm{d}B_y}{\mathrm{d}x} = -\frac{i}{\omega}\left[k_y k_z \alpha + (k_0^2 - k_y^2)\gamma\right] e^{i\kappa x} - \frac{i}{\omega}\left[k_y k_z \beta + (k_0^2 - k_y^2)\delta\right] e^{-i\kappa x}. \tag{6.55}$$

Integrating with respect to x and eliminating the constant, we obtain the expression for B_y:

$$B_y(x) = -\frac{1}{\omega\kappa}\left[k_y k_z \alpha + (k_0^2 - k_y^2)\gamma\right] e^{i\kappa x} + \frac{1}{\omega\kappa}\left[k_y k_z \beta + (k_0^2 - k_y^2)\delta\right] e^{-i\kappa x}. \tag{6.56}$$

Similarly from (6.48),

$$B_z(x) = \frac{1}{\omega\kappa}\left[k_y k_z \gamma + (k_0^2 - k_z^2)\alpha\right] e^{i\kappa x} - \frac{1}{\omega\kappa}\left[k_y k_z \delta + (k_0^2 - k_z^2)\beta\right] e^{-i\kappa x}. \tag{6.57}$$

The constants α, β, γ, δ are determined in regions I and II of Fig. 6.2 (between wall and strap array, and between plasma and strap array respectively) by imposing the following boundary conditions: at the wall ($x = x_{surf} + a + b$) the tangential electric field is zero ($E_{zI} = 0$, $E_{yI} = 0$); at the strap ($x = x_{surf} + a$) the electric field is continuous, while the magnetic field has a discontinuity ($B_{zII} - B_{zI} = -\mu_0 j_y(k_y, k_z)$, $B_{yII} - B_{yI} = 0$, $E_{yII} - E_{yI} = 0$, $E_{zII} - E_{zI} = 0$); at the plasma surface ($x = x_{surf}$), $E_{zI} = 0$ and $E_{yII}/\omega B_{zII} = Z_{surf}$. Here $j_y(k_y, k_z)$ is the corresponding Fourier component of the strap current (see next section).

Once the fields in the vacuum region are completely known, we impose continuity of E_y and B_z at the plasma surface to determine the fields in the plasma:

$$E_{yII} = \eta E_{y,plasma}, \tag{6.58}$$

$$B_{zII} = \theta B_{z,plasma}, \tag{6.59}$$

where $E_{y,plasma}$ and $B_{z,plasma}$ are the values determined in the previous section and η, θ are constants.

6.2.3 Finding the coupling resistance

The antenna current is localized at the plane $x = x_{surf} + a$; with *N* radiating straps, the general form is

$$j(y,z) = J_0 \sum_{n=1}^{N} e^{i\phi_n} \Theta_n(z) \Upsilon(y), \tag{6.60}$$

where $\phi_n = (n-1)\Delta\phi$, $\Theta_n(z) = 1$ if $L_n \leq z \leq U_n$ and 0 otherwise, with

$$L_n = (d/2 + w/2) + (n-1)(d+w) - w/2, \tag{6.61}$$

$$U_n = (d/2 + w/2) + (n-1)(d+w) + w/2, \tag{6.62}$$

and $\Upsilon(y) = 1$ if $-h/2 \leq y \leq h/2$ and 0 otherwise. Here w is the width of the straps, h is their height and d is the separation between the straps. J_0 is the current amplitude at the short (the current distribution is approximately uniform along the poloidal direction due to the folded strap design of the ASDEX Upgrade antenna, see [37]). The Fourier transform of the current is then

$$j_y(k_y,k_z) = \frac{J_0}{T_z T_y} \sum_{n=1}^{N} e^{i\phi_n} \int_{L_n}^{U_n} \Theta_n(z) e^{-ik_z z} \mathrm{d}z \int_{-h/2}^{h/2} \Upsilon(y) e^{-ik_y y} \mathrm{d}y; \tag{6.63}$$

as a periodic boundary condition for the electric field components, we use a box of length $T_z = 2\pi R'$ and width $T_y = 2y_{vert}$, with $R' = R + x_{surf}$ (R being the tokamak major radius) and y_{vert} the vertical "radius" of the vessel. The integral over z can be written as

$$\int_{L_n}^{U_n} \Theta_n(z) e^{-ik_z z} \mathrm{d}z = e^{-ik_z(d/2+w/2+(n-1)(d+w))} \int_{-w/2}^{w/2} e^{-ik_z z} \mathrm{d}z \tag{6.64}$$

$$= e^{-ik_z(d/2+w/2+(n-1)(d+w))} w \,\mathrm{sinc}\left(\frac{k_z w}{2}\right). \tag{6.65}$$

Likewise for y

$$\int_{-h/2}^{h/2} \Upsilon(y) e^{-ik_y y} \mathrm{d}y = h \,\mathrm{sinc}\left(\frac{k_y h}{2}\right). \tag{6.66}$$

The complete expression is

$$j_y(k_y,k_z)=\frac{J_0}{T_zT_y}\sum_n e^{i\phi_n-ik_z(d_z/2+w/2+(n-1)(d_z+w))}w\,\mathrm{sinc}\left(\frac{k_zw}{2}\right) \times h\,\mathrm{sinc}\left(\frac{k_yh}{2}\right). \quad (6.67)$$

To obtain the eight constants $\alpha, \beta, \gamma, \delta$ (each one in the two regions) this expression is used in the boundary conditions in the previous section; the expressions of the constants are omitted here for brevity. The power is then given by

$$P=-\frac{1}{2}\int \mathbf{E}\cdot\mathbf{j}^*\mathrm{d}V. \quad (6.68)$$

Using the periodic boundary conditions specified above for the electric field components, substituting the expressions for electric field and current into Eq. (6.68) we get

$$\begin{aligned} P &= -\frac{1}{2}\sum_{n_y}\sum_{n_z}\sum_{m_y}\sum_{m_z}E_{yA}(k_y,k_z)j_y^*(k_y,k_z)\times \\ &\int_0^{2\pi R'}\int_0^{2y_{vert}} e^{in_y\pi y/y_{vert}}e^{im_y\pi y/y_{vert}}e^{in_z z/R'}e^{im_z z/R'}\mathrm{d}y\mathrm{d}z \\ &= -\frac{1}{2}(2\pi R')(2y_{vert})\sum_{k_y}\sum_{k_z}E_{yA}(k_y,k_z)j_y^*(k_y,k_z) \\ &= -\frac{1}{2}(2\pi R')(2y_{vert})\sum_{k_y}\sum_{k_z}\left(\alpha_I e^{-i\kappa(x_{surf}+a)}+\beta_I e^{i\kappa(x_{surf}+a)}\right)j_y^*(k_y,k_z) \end{aligned} \quad (6.69)$$

where we have used Eq. (6.53). We equate the expression (6.69) to the radiated power in terms of radiation impedance as defined in Chapter 3,

$$P=\frac{1}{2}(R_C+iX_{rad})I_S^2, \quad (6.70)$$

with $I_S = J_0$ is by definition the current amplitude at the short (note that we have written R_C instead of R_{rad}). The coupling resistance of the antenna is then

$$R_C=\frac{2\mathrm{Re}[P]}{J_0^2}. \quad (6.71)$$

It is important to recall that the *coupling resistance* computed both by FELICE and Rsolver is *not* the same thing as the *loading resistance* measured in an experiment, and neither is the same as the *real part of the input impedance* (see Chapter 3).

6.3 Code implementation

The code is implemented in MATLAB. Equations (6.36) and (6.37) are solved numerically using the ode45 algorithm, based on an explicit Runge-Kutta (4,5) formula, the Dormand-Price pair [52]. The parameters specifying the model of an "AUG-like" antenna are given in Table 6.1.

Parameter	Value
Major radius R_t	165 cm
Plasma surface position x_{surf}	55 cm
Vertical dim. of vessel y_{vert}	70 cm
Min. n_y, max. n_y	-7, 7
Min. n_z, max. n_z	-40, 40
Strap number *N*	2
Strap height *h*	96.4 cm
Strap width *w*	18 cm
Strap separation *d*	20 cm
Strap-to-plasma dist. *a*	4.6 cm
Strap-to-wall dist. *b*	21 cm
Strap current amplitude J_0	1 A
Strap phasing $\Delta\phi$	(0, π)

Table 6.1: Parameters used in the Rsolver code for an "AUG-like" antenna simulation.

The antenna current spectrum is given by

$$k_y = \frac{n_y \pi}{y_{vert}}, \tag{6.72}$$

$$k_z = \frac{n_z}{R_t + x_{surf}} \tag{6.73}$$

with $n_{y,z}$ integer numbers between the minimum and maximum given in Table 6.1. Fig. 6.3 shows the antenna current and coupled power spectra at 30 and 36.5 MHz (at $k_y = 0$), along with the input electron density profile used to obtain the spectra. The current spectra peak at $k_z = 7.727$ m^{-1}. The corresponding R-cutoff densities are at $n_e \simeq 0.44 \times 10^{19}$ m^{-3} (at 30 MHz) and 0.34×10^{19} m^{-3} (36.5 MHz) in a deuterium plasma with 5% H minority. It is clear from the figure that the range of values of toroidal refractive index $n_z \in [-40, 40]$ does not "cut off" any relevant portions of the coupled power spectrum. In this example and in general, input density profiles are obtained from IDA (see Section 8.1) and interpolated, giving a radial resolution of 0.55 mm (1000 points over the range $x \in [0, 55]$ cm); sensitivity tests showed that increasing the resolution further did not produce changes in the results. Adopting these values results in typical running times of about one minute on a Windows-based commercial PC with 8 GB RAM and 2.40 GHz CPU (the code was not optimized for speed), in comparison with FELICE

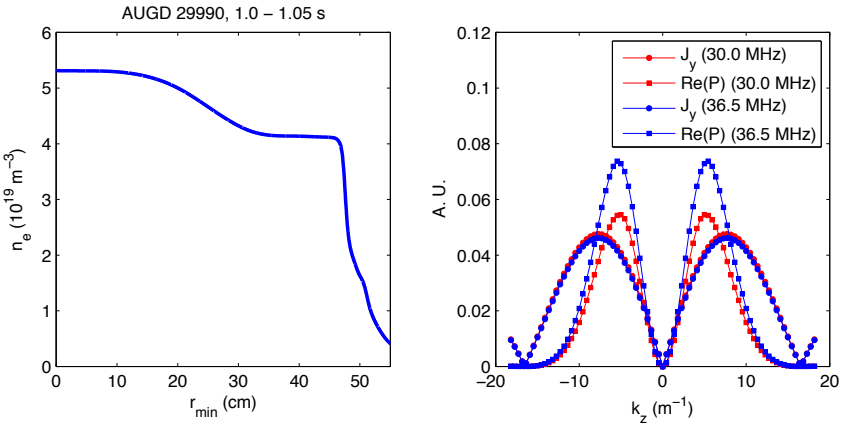


Figure 6.3: Current (J_y) and coupled power (P) spectra for the AUG-like antenna model, at 30.0 and 36.5 MHz (right) with $k_y = 0$. The J_y spectra peak at $k_z = 7.727\ m^{-1}$, the P spectra at 5 and 5.455 m^{-1} respectively. The input electron density profile is plotted on the left; note that in this example, the edge density is above cutoff.

runs, at similar resolution, of a few seconds on the Linux cluster at IPP Garching[5].

Rsolver has been extensively tested against FELICE, where the same parameters of Table 6.1 were used in the hot plasma code. The FELICE runs additionally require electron and ion temperature profiles, which are again obtained from IDA; however, given certain constraints, temperature effects play no role in coupling (see below). Fig. 6.4 shows 1242 simulation results, where the same plasma n_e profile, plasma composition, frequency, etc. was used to compute a coupling resistance by both codes. The plasma density and temperature profiles were reconstructed by IDA from shots 29822, 29823, 29833 and 29863, and averaging over 10 ms after ELM synchronization, ensuring a wide variability of the density profile, as can be seen from the range of R_C values in the figure. The integration length was 30 cm inside the plasma for all cases (see below). The proportionality constant and offset are different for the two operating frequencies; as yet the reason for this has not been found, but it is clear that the results from both codes are proportional to one another over a reasonable range of values (the proportionality constants are 0.18 at 30 MHz and 0.24 at 36.5 MHz). The black diagonal line, indicating 1:1 correspondence, is given for reference.

[5]Although this version of the code is enough for the purposes of this work, further developments are possible. To increase computation speed it would be desirable to write the code in Fortran; a further step would be to include a self-consistent current distribution such as implemented in FELICE, along with proper treatment of radial feeders.

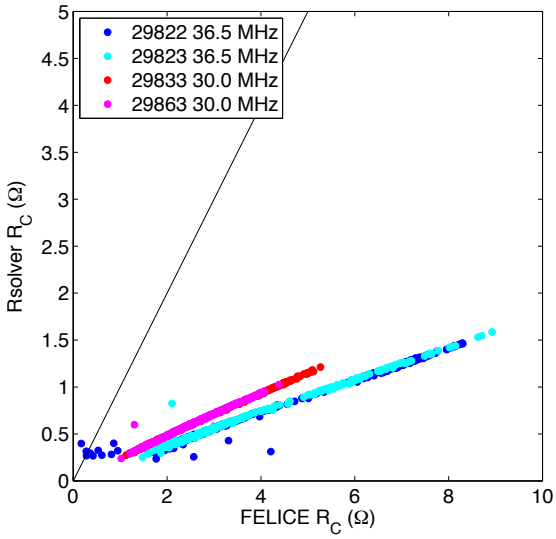


Figure 6.4: Relation of coupling resistance computed by FELICE and Rsolver, for the same profiles and parameters. Although the proportionality factor and offset are different for the two frequencies, the results are clearly proportional to one another. 1242 simulation points are shown.

6.4 Code applicability and validity domain

In this section we briefly describe the conditions and constraints that define the situations where the codes are applicable and produce valid results. From the point of view of the plasma, the slab model is a major constraint: it forces the user to work with a toroidally and poloidally featureless plasma, which is not true in real experiments due to a) the plasma shape, especially at high triangularity, and b) local three-dimensional density variations, as might be the case with ELMs. Recent work indicates that these variations may be significant for coupling calculations [53]. This is apart from wave behavior resulting from real tokamak geometry[6]. The second consideration is the assumption that the n_e profile used as input is actually the profile seen by the antenna during operation. This assumption may *not* be justified for several reasons:

1. The plasma may not be toroidally uniform, as is the case when magnetic perturbation fields are applied;

2. As mentioned above, the density profile is usually supplied by IDA, and the

[6]This would be the next step in antenna modeling; specifically in the case of TOPICA, the intention has been expressed in the past to interface it, for example, with the significantly more sophisticated full-wave ICRF code TORIC [18]

reconstruction is based on diagnostics situated in different sections of the torus;

3. During operation, the antenna itself modifies the density profile in front of it (see for example [54], [55], [56]).

Addressing these issues lies outside the scope of the present work. Nevertheless, despite these limitations, the slab model captures quite well a broad range of density variations and their effects on the antenna. Finally, the antenna model itself, besides having a drastically simplified geometry, is not, strictly speaking, treated as a microwave network with input ports; no scattering matrix or input impedance can be computed (this is only possible with a self-consistent current distribution).

6.4.1 Integration length

The integration length is the distance from the plasma surface at which the outward radiation conditions given by Eqs. (6.42) and (6.43) are imposed. The WKB approximation must be valid at that point and therefore it cannot be close to a resonance layer; it must also lie sufficiently far in the plasma so as not to exclude portions of the density profile which are relevant for the calculation of R_C.

Figure 6.5 illustrates the effect of different choices of integration length in FELICE on simulation results (the parameter is called "alengr" in the FELICE input file). Shot nr. 29514 was simulated at 30.0 MHz and 5% H in a D plasma with $B_0 = 2$ T, with n_e and T_e profiles averaged over 50 ms windows. The results correspond to integration lengths of 30, 50 and 70 cm from the plasma surface, along with a case where the FW equations are integrated through the whole plasma slab (of thickness 110 cm, i. e. twice the plasma radius) with a perfectly conducting wall on the high field side. In the upper section it is clearly seen that the 30 and 50 cm cases are essentially identical; the next case (70 cm) is significantly different from the previous two and very similar with the case where the conducting wall boundary condition is imposed. The lower section shows the same results superimposed on loading resistance measurements of the four antennas during the same shot[7]. Note that, in accordance with the definitions in Chapter 3 the results of the code are labeled *coupling resistance* R_C and the results of the measurement are labeled *loading resistance* R_L. The results with 30 and 50 cm are clearly in much better agreement with the experiment.

The details of this qualitative "jump" in R_C become explicit if several points of plot are chosen, and the corresponding R_C is evaluated as a function of the integration length. The results are shown in Fig. 6.6. The computed coupling resistance shows a discontinuity when the ion-ion cutoff is included in the integration region. Intuitively it would be expected that the computed R_C would be

[7] These were obtained with standard diagnostics - directional couplers and V_{max} probes - no recalibration correction.

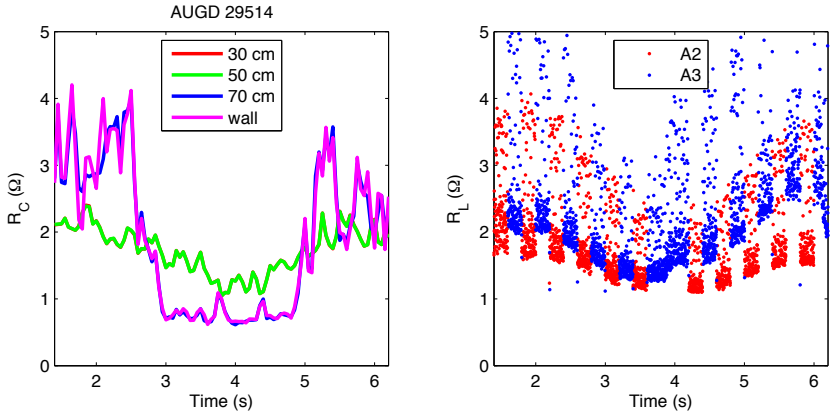


Figure 6.5: R_C computed by FELICE with different values of integration length ("alengr"), 30, 50 and 70 cm; the last case is the result of integration through the whole plasma slab (thickness is twice the minor radius) with a conducting wall at the HFS ($f_0 = 30$ MHz, 2 T on axis, 5% H in D, n_e and T_e profiles averaged over 50 ms windows). The results with 30 and 50 cm are essentially identical (red line hidden by green); the results with 70 cm and conducting wall are also very similar. The two groups are qualitatively different from one another. On the right the R_L measurements for the same shot are shown, antennas 2 and 3; the results with 30 and 50 cm clearly show a better qualitative agreement with the measurements. The difference in loading on the two antennas in the second half of the time interval shown here is due to local density profile modification by gas injection.

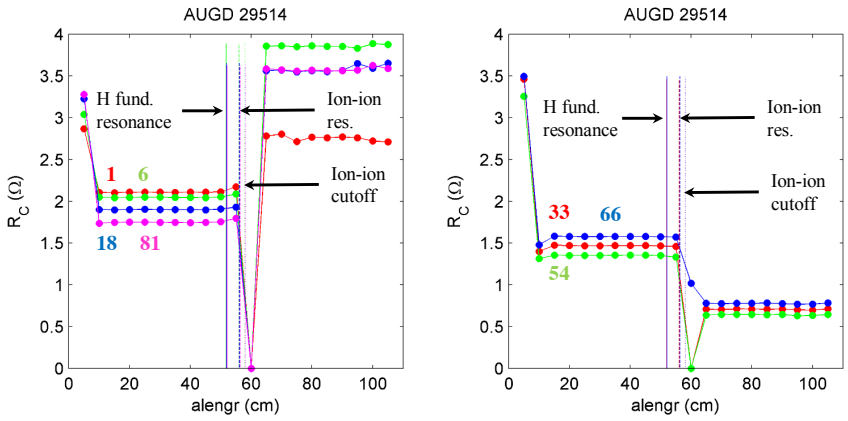


Figure 6.6: Several representative cases from Fig. 6.5, R_C plotted as function of integration length. The value of R_C is essentially constant throughout the plasma slab, with a jump happening when the ion-ion cutoff layer is included in the integration region.

closer to its experimental value when the whole plasma, including the absorption and ion-ion cutoff regions, is taken into account and bounded by a conducting surface on the HFS (however, this is emphatically *not* true for the cold plasma code; there the boundary conditions must be imposed before the absorption layer by default). On the other hand, the slab model may be too simple if FW reflection from the ion-ion cutoff layer is to be included, and some assumptions behind it become invalid - such as the decoupling of toroidal and poloidal modes (Eqs. (6.18) and (6.19)) - hence giving incorrect results. More specifically, the slab geometry overestimates the Q factor of resonance cavities such as that between cutoff and plasma surface. By limiting the integration interval, this overestimation is partially compensated[8]. Imposing outward radiation conditions before the absorption/cutoff layers evidently yields more reasonable results; throughout the present work alengr = 30 cm is used. From Fig. 6.6 it may seem that even half of that value would be enough, but this reserve ensures that enough plasma depth is taken into account even at large antenna-plasma separation, e. g. during R_{sep} scans. An integration length of 30 cm is also the value commonly used for TOPICA simulations and has been found by extensive testing to be an appropriate choice [50].

This explains, at least partially, why the cold plasma model is enough for coupling calculations, at least in the slab plasma approximation - the FW equations are usually not integrated far enough into the plasma for finite temperature effects to become important.

[8] Marco Brambilla and Roberto Bilato, personal communication.

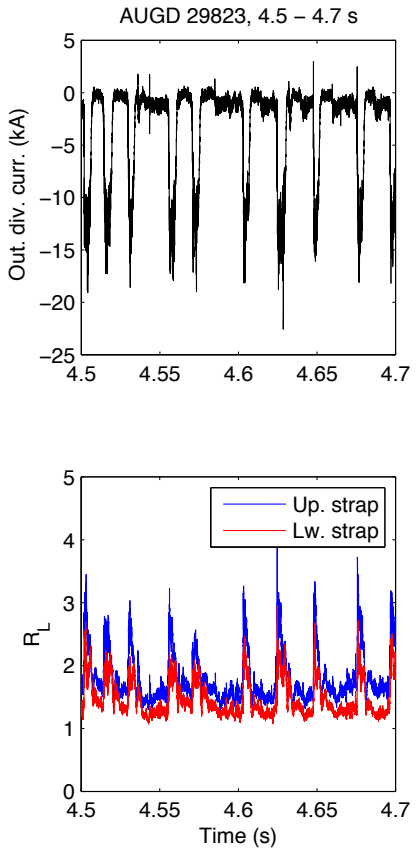


Figure 6.7: The effect of ELMs on strap R_L.

6.4.2 Averaging of the n_e profile

Notice that in most H-mode shots ELMs will significantly alter the density profile, and the strap R_L can double during an ELM. This is illustrated in Fig. 6.7, showing the behavior of the outer divertor current signal and the loading on both straps of antenna 1 during 0.5 s of H-mode shot 29823.

Naturally this will be reflected in the profile reconstruction; averaging density profiles over different time windows can result in different values for R_C, and it is not immediately obvious *which* time windows are most appropriate for ELM synchronization. After a significant number of simulations it was found that, as a rule, it is not possible to find time windows such that the simulation will reproduce the relatively "constant" loading between ELMs. For example, Fig. 6.8 shows the outer divertor current signal for the time window $t = 1.5 - 4$ s in shot 29823,

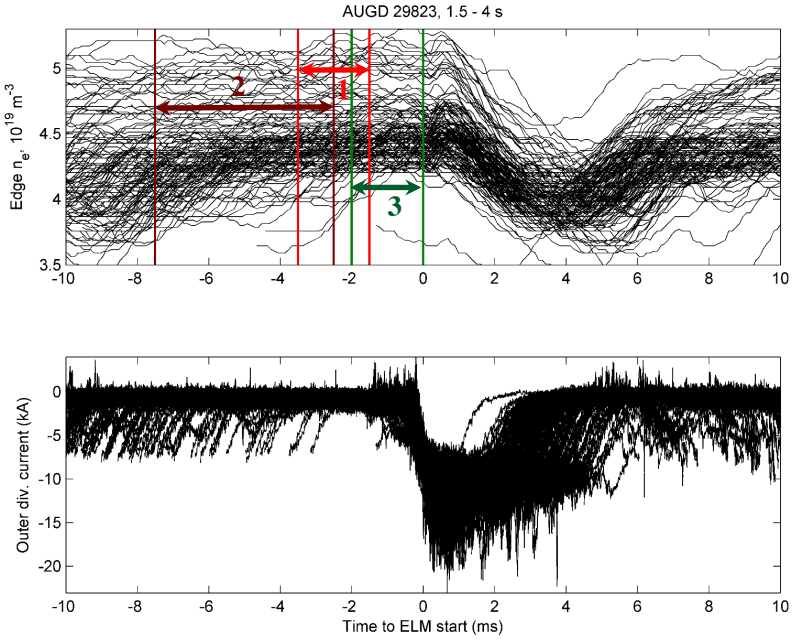


Figure 6.8: Line-integrated pedestal density (top) and outer divertor current (bottom) during ELMs, shot 29823 (172 ELMs); three different time windows for ELM synchronization are shown.

along with the corresponding pedestal top density (line-integrated) measured by DCN interferometer. The "start" time t_{start} of an ELM is defined as the moment at which the divertor current signal crosses the arbitrary value 7 kA[9]; both signals are plotted from $t_{start} - 10$ ms to $t_{start} + 10$ ms; 172 ELMs are shown. It can be seen from the figure that this is, at least roughly, an appropriate definition as the density drop occurs about 1 ms after $t = 0$. Several time windows for ELM synchronization are then selected, which are also shown: case 1 with $t \in [-3.5, -1.5]$ ms, case 2 with $t \in [-7.5, -2.5]$ ms and case 3 with $t \in [-2.0, 0.0]$ ms. Note that on the basis of this signal alone, one would expect the best results with case 3, since the density signal is most "stable" in that window.

For each time window, average n_e and T_e profiles are taken and used to compute R_C. Fig. 6.9 shows the results with cases 1, 2 and 3, along with the result from averaging the profiles on 50 ms windows regardless of ELMs. It is clear that the selected time windows reproduce only approximately the slowly changing loading observed experimentally between ELMs, the changes being caused in this case by separatrix scans ($2 - 3$ and $4 - 5$ seconds approximately) and a global

[9]It was found by trial and error that this is a good value in the sense that it neither picks up too many inter-ELM oscillations nor ignores moderate ELMs.

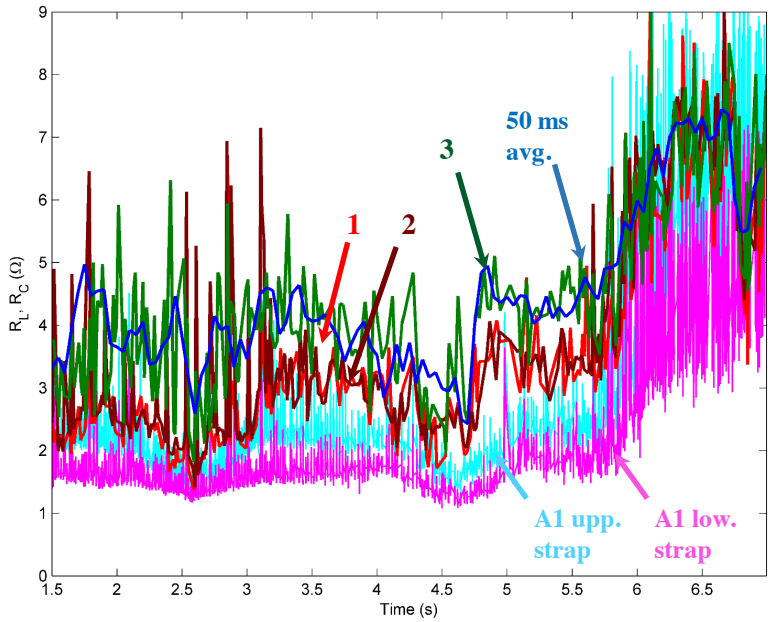


Figure 6.9: R_C computed by FELICE corresponding to cases 1, 2 and 3, and with averages over 50 ms windows without ELM synchronization, plotted on top of the experimentally observed R_L on both straps of antenna 1 (voltage and current probe data). Selecting these time windows for ELM sync. reproduces only approximately a "stable" R_C as would be expected between ELMs, that is, changing only on time scales of ~ 1 second due to separatrix scans ($2-3$ and $4-5$ seconds approximately) and a global density increase at ~ 5.75 seconds.

density increase at ~ 5.75 seconds (see Chapter 7). Cases 1 and 2 show a somewhat more stable behavior, in that R_C oscillates less during the first half of the discharge than the other two cases, but the overall trend is only slightly better than the one produced by using 50 ms averages. The same behavior can be observed in many shots on shorter time scales, even at the maximum time resolution of the IDA profiles, i. e., 1 ms. Fig. 6.10 shows a short time window ($3.4-3.9$ s) from shot nr. 29822. The measured R_L for both straps is plotted, as well as simulation results corresponding to the same ELM synchronization windows as above, and the results of taking every profile available. It can be clearly seen that, while the measured loading between ELMs stays constant over the whole time window, the computed R_C does not - in fact it is lower by $\sim 1\ \Omega$ in the right half of the figure. Naturally the ELM-synchronized results replicate this behavior, although it is not as obvious for case 3. The conclusion is that, at least from the point of view of antenna simulation, in situations like these, the time resolution of the IDA reconstruction may not be enough (even though the time between ELM starts is

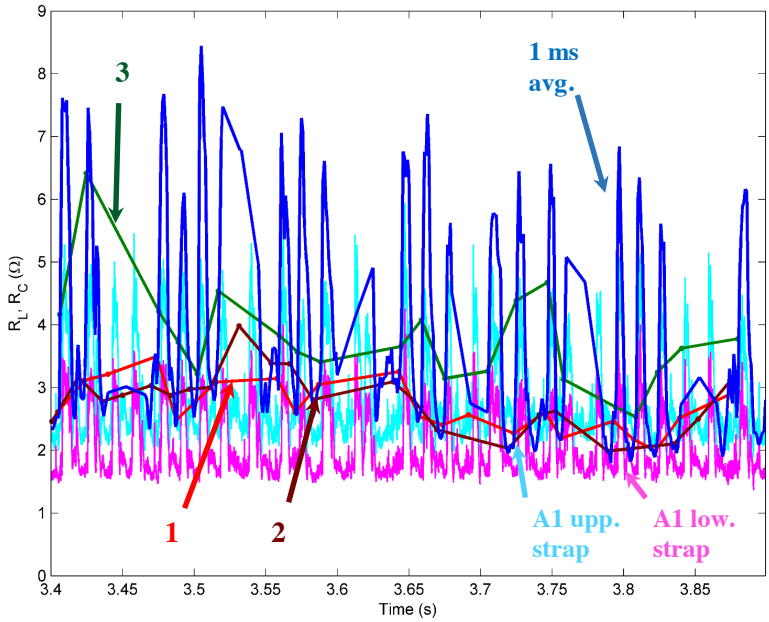


Figure 6.10: R_C computed by FELICE corresponding to cases 1, 2 and 3, and with all available IDA profiles (1 ms resolution), plotted on top of the experimentally observed R_L on both straps of antenna 1 (voltage and current probe data). While the measured loading is constant between ELMs over the whole time window, the calculated R_C is not, due to fluctuations in the reconstructed density profile. This can be seen even when all profiles are used; R_C is lower by $\sim 1\ \Omega$ in the right half of the figure. Note also the gaps where no IDA data is available at the required time resolution, clearly visible around ~ 3.45, 3.525, 3.6, 3.7, 3.775 and 3.85 s.

$\sim 10 - 20$ ms in this example): the reconstructed profiles used in fact do not necessarily "stabilize" between ELMs.

6.4.3 Hydrogen concentration

As stated in Section 6.4.1, the resonance and cutoff layers (except for the R-cutoff) typically lie well outside the integration domain. The calculated coupling resistance is therefore relatively insensitive to the hydrogen concentration in the situations considered here. This is illustrated in Fig. 6.11, which shows R_C calculated with Rsolver for a number of different density profiles taken from shot 29823, ELM-synchonized and averaged over 200 ms. The main species is deuterium, with the hydrogen fraction indicated in the legend. It is seen that R_C is essentially unaffected by changes in the H fraction in a wide domain, and the variation in resistance due to the density profile is far more significant. Among the TOPICA

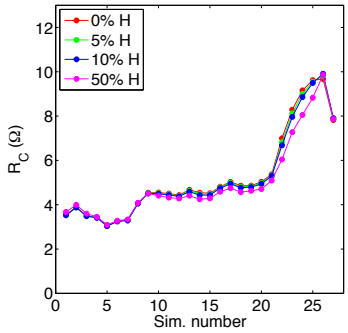


Figure 6.11: R_C computed with Rsolver, using the same sequence of density profiles with different H concentration. The variation in loading due to the H fraction are significantly smaller than those due to density changes.

simulation results discussed in Section 8.3, there are two sets of runs using density data from shots 29110 and 29113, part of an experiment series on mode conversion heating, with 15% and 47% H concentration respectively. No significant effects are observed, indicating that this lack of sensitivity is not merely an artifact of the cold plasma model implemented in Rsolver.

6.5 Summary

Throughout this chapter we have attempted to discuss some general issues relevant for coupling calculations using the numerical codes available for this study. Two main limitations of the fast codes are 1) the unknown degree of correspondence between the input density profile (in this cases provided by IDA) and the actual profile seen by the antenna during operation, and 2) forced current distribution on the antenna straps, making it impossible to compute scattering parameters, loading resistance and/or actual coupled power. Therefore only trends in coupling can be studied in this way. As mentioned, this is a fundamental limitation in Rsolver but only a temporary one with FELICE. In TOPICA, only the density profile is an issue. A third limitation, inherent in all codes, is the slab plasma model that does not account for effects arising from the three-dimensional geometry of the plasma torus. The shape of the plasma facing the antenna can be accounted for to some extent by changing the aperture shape in the antenna model[10], but the difficulties related to the overestimation of the Q value of the resonant cavity still remain. More detailed modeling by necessity must rely on 2D full-wave codes such as TORIC [57] or AORSA [58].

[10]Daniele Milanesio, personal communication.

7

Experimental studies of antenna coupling on ASDEX Upgrade

7.1 Introduction

In order to improve antenna coupling it is necessary to introduce changes to the electron density profile, either globally or locally. Besides from the obvious solution of displacing the separatrix position, in order to shift the R-cutoff closer to the antenna and decrease the width of the evanescence region, altering the properties of the SOL by puffing neutral gas close to the antenna location has been investigated on several tokamaks. The effect of changes in the magnetic surface shape on antenna behavior has also been studied on JET and ASDEX Upgrade (see section 7.3). These alternative methods of loading improvement are important in view of the requirements of machine protection and plasma scenario limitations on ITER [26].

7.2 Neutral gas injection

The injection of neutral gas into the plasma edge in order to change the SOL properties and bring the fast wave cutoff closer to the antenna has been studied on JET, TEXTOR, ASDEX Upgrade, Tore Supra and DIII-D. The JET study [17] investigated the effects of gas injection from different locations including divertor, midplane and top of the tokamak, whereby midplane injection was found to

be significantly more efficient. Improvement in coupling on all antennas was observed, independently of whether the antennas were magnetically connected to the injection location, suggesting global changes in the SOL density; however, the strongest improvement was observed on the antenna closest to the location of the gas injection modules.

Two TEXTOR studies have been reported. The first one used D plasma [24] with a rather high H concentration ($\sim 17\%$) and D injection, with the second using He plasma [23] and He injection. In the first study three gas valves at different toroidal and poloidal locations were used; although an increase in antenna coupling was observed[1], no significant differences were found regarding injection location, again indicating global changes in SOL density. The second study used a single valve located 1.7 m from the antenna and magnetically connected to it; antenna loading was seen to increase only as an effect of central plasma density increase, but no difference was observed in antenna behavior between discharges with and without gas injection [23]. Furthermore, both studies observed evidence of global fast wave eigenmodes, manifested as characteristic peaks in antenna loading resistance and self-inductance, possibly due to poor absorption of the fast wave in the plasma.

Two ASDEX Upgrade studies have also been reported so far, investigating the use of local gas injection in L- [25] and H-modes [26], with special emphasis on distinguishing local effects. In the first study it was observed that, for a given injection rate, coupling is increased more significantly on the antenna closest to the injection location, in agreement with the JET study cited above. More specifically, the authors introduce an antenna-valve distance defined as

$$\rho = \left(\frac{1}{|\Phi_{\text{ant}} - \Phi_{\text{valve}}|_{\text{clockw.}}} + \frac{1}{|\Phi_{\text{ant}} - \Phi_{\text{valve}}|_{\text{counter-clockw.}}} \right)^{-1}, \qquad (7.1)$$

with Φ being the toroidal angle. By deducing the R-cutoff position from Li-beam density measurements, and calculating the expected change in R_C due to this R-cutoff shift alone based on the analytical model

$$\frac{\Delta R_C}{R_{C_ref}} = \left(\mathrm{e}^{\beta k_\parallel \Delta L_C} - 1 \right), \qquad (7.2)$$

the change in antenna coupling due to global SOL density variation is estimated and compared with the actual change in R_C (here L_C is the antenna-cutoff distance; the analytical model is proposed in [59]). It is found far from a given antenna ($\rho \sim 1.5$) the change in coupling is consistent with global density increase in the SOL, while at lower separation ($\rho \sim 0.8$ and lower) local SOL changes, not measurable by Li-beam, must be invoked. The second ASDEX Upgrade study, as mentioned, extended the investigation for H-mode discharges and replicated the

[1] Only one ICRF antenna was used in both studies.

results previously observed in L-mode; specifically, changes in loading of more than 25% when switching from a remote to a nearby injection valve are reported. In contrast to the L-mode results, however, it was found that the side at which the valve is located toroidally with respect to a given antenna - upstream or downstream of the SOL parallel plasma flow - can play an important role. It is also reported that gas injection is accompanied by a decrease in tungsten influx from the limiters and its effective sputtering yield, at least when the midplane valve with radially retracted injectors is used [26].

During experiments in DIII-D [27] it was found that injecting D at a rate of 10^{22} el/s led to a sixfold increase in the loading resistance of the adjacent antenna; however a somewhat lower increase in the coupling of the other antenna, remote and not connected magnetically, was also observed suggesting global SOL changes as part of the mechanism. In Tore Supra experiments, no difference regarding the use of injection location was observed [27]. Taken together, these experiments indicate that the loading increase mechanism has a global and a local part, and their proportion is a function of field line geometry relative to injection valve and antenna, parallel transport, connection lengths, cross-field transport enhancement by turbulence and ELMs and other factors [27].

7.3 Plasma triangularity

Changing the plasma triangularity in order to improve coupling has been investigated on JET [28] and ASDEX Upgrade [29]. The JET study carried out dedicated discharges using four different shape configurations with a wide range of triangularity values, namely lower triangularity δ_L varied between 0.21 to 0.44 and upper triangularity δ_U between 0.23 and 0.48. It was found that the best coupling is achieved with a plasma shape matching the antenna curvature. Furthermore, the authors investigate the dependence of antenna loading on three radial antenna-plasma distances, namely ROG (radial outer gap in the equatorial midplane), GAP3 (wall-to-separatrix gap above antenna) and GAP4 (wall-to-separatrix gap at the lower vertical limit of the antenna). The experimental data is best described by an exponential function where the ROG is by far the most important parameter. The ASDEX Upgrade study referred to above is focused more on the antenna behavior during ELM events under high triangularity conditions; however, two L-mode discharges are studied in detail in order to separate out the changes of antenna coupling which are not directly related to ELM size [29]. The two L-mode shots differ significantly in δ_L, with a value of 0.27 for the shot where the separatrix shape matches well the poloidal profile of the antenna, and 0.41 where they are markedly different. When plotted versus the average antenna-separatrix distance (calculated by integrating along the vertical antenna extension), antenna loading is higher at *higher* triangularity; moreover, the electron density profile

Shot nr.	I_P	q_{95}	n_0	B_0	P_T	P_{IC}	f
29822	0.8	5.493	7.56	-2.488	9.861	3.598	36.5
29823	0.8	5.457	8.13	-2.489	10.024	3.616	36.5
29833	0.8	4.392	8.58	-2.000	8.140	3.104	30.0

Table 7.1: Global parameters of the March 2013 discharges. I_P is plasma current (in MA), n_0 is central electron density (flattop end) in 10^{19} m^{-3}, B_0 is the toroidal field (in T), P_T (in MW) is the sum of NBI, ICRH (P_{IC}, maximum from standard diagnostics) and ECRH heating power, and f is the antenna operating frequency in MHz.

in the SOL was found to be higher in the high δ_L case, possibly attributed to a stronger plasma-wall interaction [29]. Another explanation could be that because the line lengths are longer, so there is *less* interaction with the wall and the density is not "scraped off" by it[2].

In order to complement and extend these studies to the H-mode regime, several dedicated discharges were carried out on ASDEX Upgrade, divided into two runs: one in March 2013 using the pre-2014 ICRF system configuration (shots 29822, 29823 and 29833), and the other in April 2014 in the framework of the MST1 campaign using the post-2014 configuration (shots 30629, 30630 an 30631).

Figure 7.1 shows the variation of two plasma parameters, separatrix position R_{sep} and upper triangularity δ_U throughout the discharge, used in 29822, 29823 and 29833; it can be seen that δ_U was varied between about 0.1 and 0.32, with three constant intervals at ~ 0.1, 0.2 and 0.3 roughly one second long and an R_{sep} scan in each interval. The lower triangularity δ_L (not shown) was kept constant at 0.45. All discharges used deuterium and were done in lower single null configuration. Some global parameters are shown in Table 7.1. Fueling was by midplane and divertor valves at 9×10^{21} s^{-1} (29822), 7×10^{21} s^{-1} (29823) and 14×10^{21} s^{-1} (29833).

Figure 7.2 shows the evolution of various plasma and antenna parameters during shot 29822 in more detail. Time traces of $|\Gamma|$, $\Phi(\Gamma)$ and R_L measured on the upper and lower lines of each antenna are also shown. Note that all RF quantities shown in this chapter have been calculated from voltage and current probe signals, therefore allowing the measurement of the input impedance of each antenna port, which had not previously been possible.

The RF signals have been ELM-synchronized, so that only the data between 3.5 and 1.5 ms before the start of each ELM are shown from 1.5 s until 6 s. For $t > 6$ s no ELM synchronization is applied; it can be clearly seen on the R_{sep} trace that type I ELMs stop at this point and are replaced by type II ELMs with a significantly higher frequency (see below). Moreover, an increase and decrease in loading when the separatrix is moved away from and back towards the LFS are

[2] J.-M. Noterdaeme, personal communication.

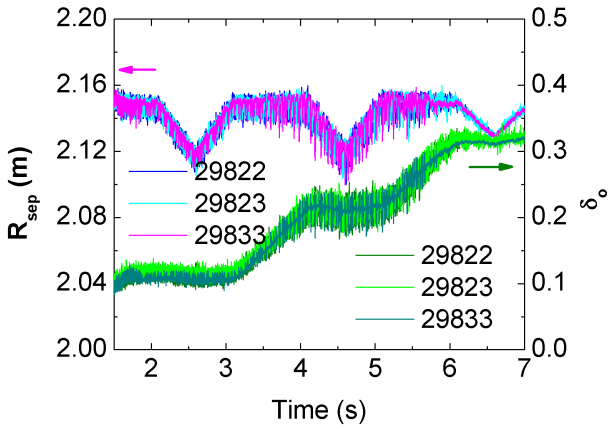


Figure 7.1: Time traces of separatrix position R_{sep} and upper triangularity in shots 29822, 29823 and 29833.

visible in the intervals between 2 and 3 and between 4 and 5 seconds, with the phase of Γ showing a similar response. Notably, between 5.5 and 6 seconds the loading resistance grows significantly and remains very high during the last second, although the effects of the last R_{sep} scan are still visible. $\Phi(\Gamma)$ also increases during this time interval, albeit after a small drop after 6 s. In addition, magnetic perturbation coils (B-coils) were switched on between 1.7 and 2 s, but no visible effect is present.

Figure 7.3 shows the corresponding time traces for shot 29823, where essentially the same features can be seen as in the previous shot. Again, the main feature of the discharge is the significant increase in antenna coupling after about 6 seconds. Changes in coupling due to R_{sep} scans are also visible. B-coils are also on between 1.7 and 2 seconds. Finally, the time traces for shot 29833 are displayed in Figure 7.4. Notice that $\Phi(\Gamma)$ on all antennas has been shifted due to the different operating frequency. Note that in this shot magnetic perturbation coils were switched on between 1.7 and 3.6 seconds, a significantly longer time than in the previous two cases, and their effect is visible as a decrease in ELM strength during that interval.

The loading resistance of the antennas on each strap is plotted versus upper triangularity, for the three discharges considered here, in Figure 7.5. Each point corresponds to an average over 10 ms after ELM synchronization. In all three shots R_L increases at higher values of δ_U, in a qualitatively consistent manner. The features seen on each plot right after $\delta_U = 0.1$, 0.2 and 0.3 correspond to changes in loading due to R_{sep} scans. The "bump" in R_L right after $\delta_U \approx 0.1$ in shot 29833 is consistent with a rapid density increase seen by the DCN interferometer (see Fig. 7.7).

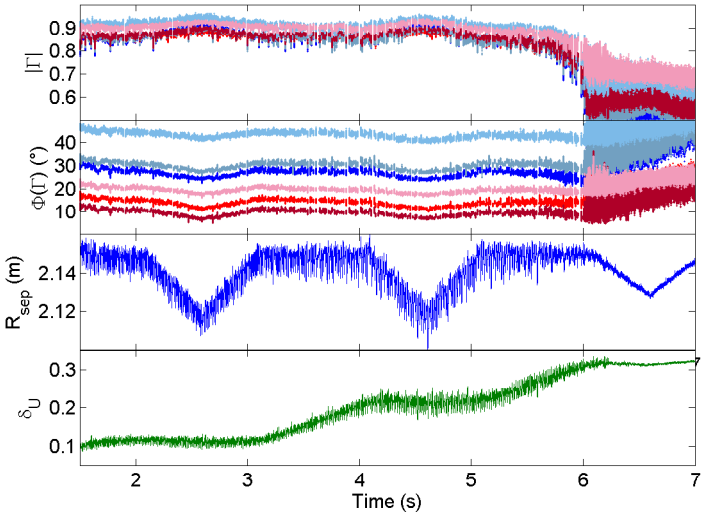


Figure 7.2: Shot 29822, time traces of RF measurements on antennas 1, 2 and 3 along with separatrix position R_{sep} and upper triangularity δ_U. Antenna coupling increases significantly from $t \simeq 6$ s on; coupling changes due to R_{sep} scans are also visible between 2-3 and 4-5 seconds. Each time trace displays the behavior of an individual strap (six in total), but the legend is omitted here and in similar figures for clarity; see Fig. 7.5.

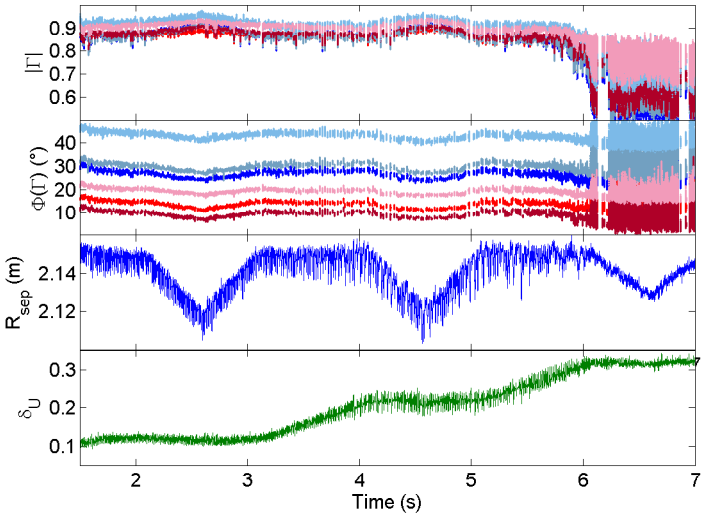


Figure 7.3: Shot 29823, time traces of RF measurements on antennas 1, 2 and 3 along with separatrix position R_{sep} and upper triangularity δ_U. Antenna coupling increases significantly from $t \simeq 6$ s on; coupling changes due to R_{sep} scans are also visible between 2-3 and 4-5 seconds.

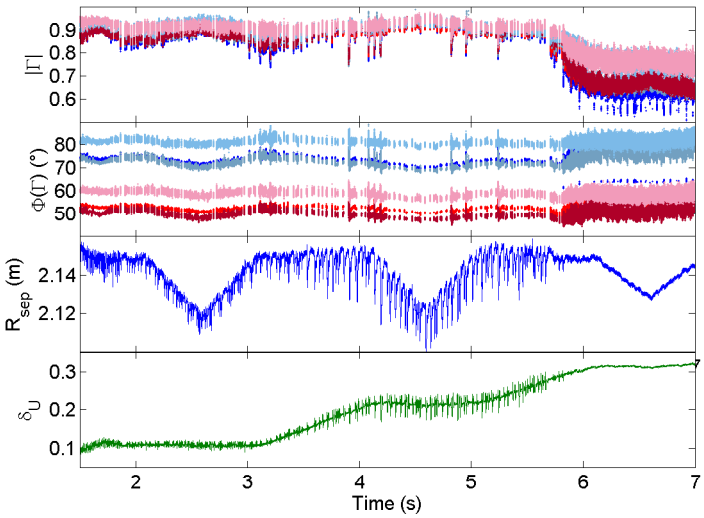


Figure 7.4: Shot 29833, time traces of RF measurements on antennas 1, 2 and 3 along with separatrix position R_{sep} and upper triangularity δ_U. Antenna coupling increases significantly from $t \simeq 6$ s on.

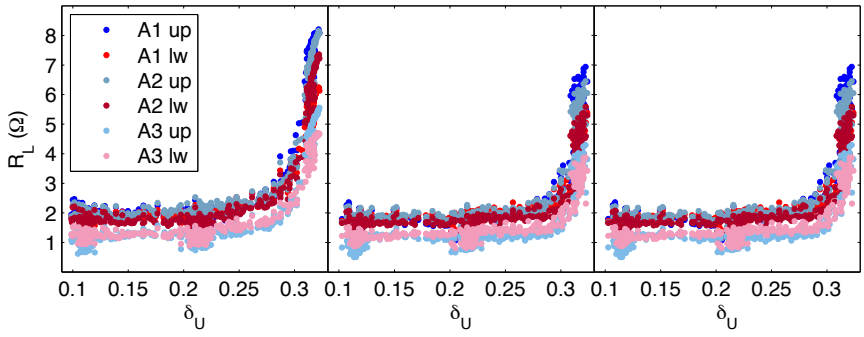


Figure 7.5: Antenna loading resistance versus upper triangularity in shots 29822, 29823 and 29833 (left to right). The small increase in R_L right after $\delta_U \approx 0.1$ in shot 29833 is consistent with a rapid density increase seen by the DCN interferometer.

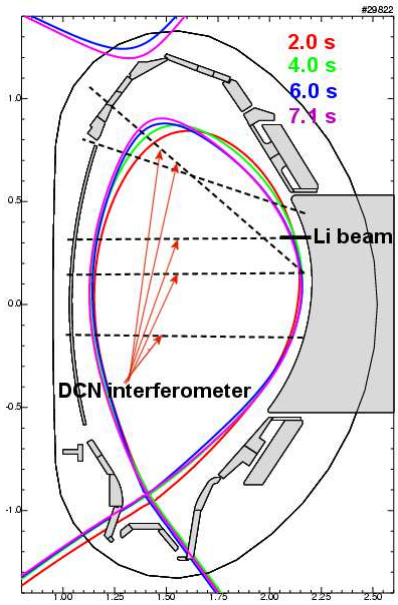


Figure 7.6: Magnetic surface shape for several time points in shot 29822. Note that the plasma shape stays largely constant in front of the antenna, with the changes mostly taking place at the top of the plasma column. The poloidal positions of the density diagnostics are also shown.

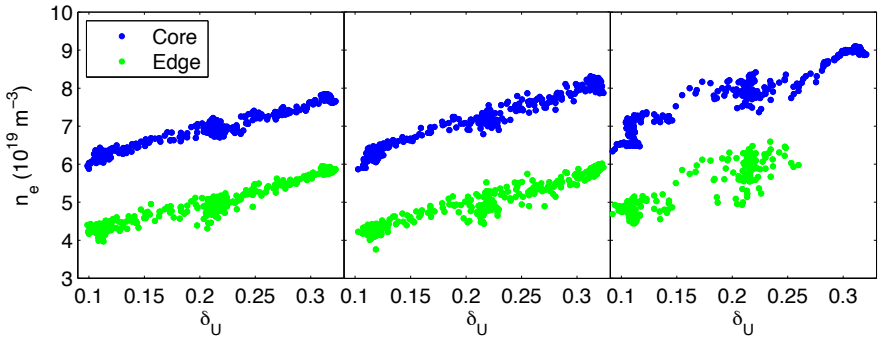


Figure 7.7: DCN density signals, core and edge, in shots 29822, 29823 and 29833 (left to right). Only a portion of the edge density signal for shot 29833 is available.

It must be kept in mind that, unlike in the JET [28] and previous ASDEX Upgrade [29] studies, the increase in triangularity performed during these shots does not lead to a substantial change in the shape of the last closed flux surface directly in front of the antenna; the changes are mainly confined to the top of the plasma column. That the magnetic geometry does not change substantially in front of the antennas can already be seen in Fig. 7.1: between 2 and 3 seconds δ_U increases from 0.2 to 0.3 but R_{sep} stays constant. Nonetheless, the evolution of the LCFS in shot 29822 is also shown in Fig. 7.6. At $t = 2$, 4 and 6 seconds R_{sep} is at about the same position as this is immediately before each scan, and $t = 7$ seconds is almost at the end of the last scan. As noted, the plasma surface in front of the antennas remains largely unchanged. In spite of this, the electron density does change substantially throughout the discharge. Fig. 7.7 shows DCN interferometer density measurements (average, assuming 1 m chord length) on axis and pedestal top, ELM-synchronized and averaged over 10 ms intervals. As can be seen, the density measurements are proportional to δ_U. Note that these are the time traces obtained after fringe jump correction[3], and a portion of the second half of shot 29833 is not available. The effects of the R_{sep} scans are again visible right after $\delta_U = 0.1$, 0.2 and 0.3.

The increase in density seen in Fig. 7.7 is consistent with confinement improvement that has been observed at ASDEX Upgrade in high δ discharges [60]. Confinement and transport studies in AUG have found that the energy confinement time τ_{th} normalized by the IPB98(y) ELMy H-mode τ scaling, for a given value of density, is increased at higher δ [61]; improved confinement in turn allows a higher density to be reached at the same gas injection rate, which is consistent with the n_e increase in Fig. 7.7. In our case $\tau_{th}/\tau_{\text{IPB98(y,2)}} \approx 0.8$ is observed at $\delta_U \approx 0.1$, and ~ 1 at $\delta_U \approx 0.3$. Note that a density increase can also take place at high δ

[3] Kindly provided by Dr. A. Mlynek.

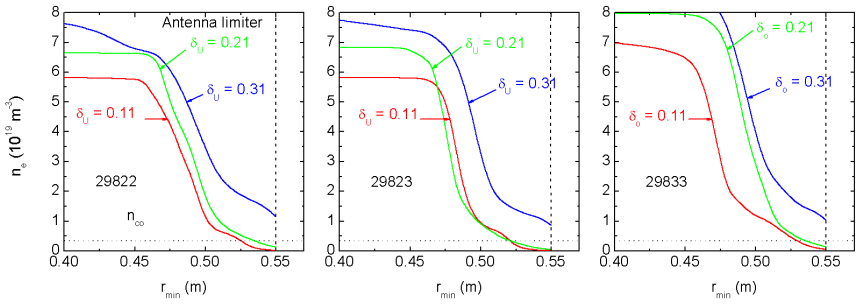


Figure 7.8: Density profiles at constant δ_U, averaged over 0.5 s after ELM synchronization.

due to reduced divertor pumping, when the strike points do not fit well into the divertor [60]; however Figure 7.6 shows that this is not the case in these shots.

The qualitative change in antenna behavior after about 6 seconds in all three shots is consistent with a transition into a type II ELMy regime, characterized by low amplitude, high frequency ELMs, that occurs in highly shaped plasmas at high collisionality or large edge safety factor [62]; this regime has been observed in ASDEX Upgrade, DIII-D and JET [63]. In fact the relevant global parameters in 29822 and 29823 around 6 seconds ($q_{95} \sim 5.5$, $\delta_U \sim 0.3$ and plasma elongation $\kappa \sim 1.6$ as well as I_P and B_0 in Table 7.1) are very close to those quoted for the dedicated type II ELMy discharges on ASDEX Upgrade [62]. At this point the configuration is very close to double null, with the distance ΔX_P between the separatrix and the upper X-point being ~ 1 cm, also consistent with [62] and [64]. Because of the high frequency, ELM synchronization is not possible in this regime. Although ELM strength is reduced, a variation in R_L of $1 - 2\ \Omega$ is still observed, significantly larger than the variation of the ELM-synchronized signal, as can be seen from Figs. 7.2-7.4. Therefore the average R_L in Fig. 7.5 corresponding to $\delta_U \approx 0.3$ and higher is overestimated with respect to its baseline value; in fact this can be seen for shots 29822 and 29823, as a discontinuity in R_L after $\delta_U \sim 0.3$. The same is true for the n_e profiles measured by Li beam[4], which in this context is relevant for numerical simulation since, as a consequence, the input profiles will have a higher SOL density and calculated coupling will be correspondingly affected. Representative n_e profiles (IDA) at different values of δ_U are shown in Fig. 7.21; these were obtained averaging all available ELM-synchronized profiles in the intervals $2 \lesssim t \lesssim 2.5$ s, $4 \lesssim t \lesssim 4.5$ s and $6 \lesssim t \lesssim 6.5$ s in each shot, corresponding to the duration of the inward R_{sep} motion at constant δ_U. Note that operation in this regime is interesting for ITER, since the peak power load on the divertor target plates due to type II ELMs is substantially reduced [62].

[4]E. Wolfrum, personal communication.

Shot nr.	I_P	q_{95}	n_0	B_0	P_T	P_{IC}	f
30629	0.8	5.440	8.06	-2.503	8.153	1.794	36.5
30630	0.8	5.443	7.6	-2.506	8.213	1.829	36.5
30631	0.8	5.513	8.44	-2.507	7.725	1.247	36.5

Table 7.2: Global parameters of the April 2014 discharges. I_P is plasma current (in MA), n_0 is central electron density (flattop end) in 10^{19} m^{-3}, B_0 is the toroidal field (in T), P_T (in MW) is the sum of NBI, ICRH (P_{IC}, maximum from standard diagnostics) and ECRH heating power, and f is the antenna operating frequency in MHz.

However, the transition into the type II ELMy regime alone does not account for the coupling increase observed at $t \gtrsim 6$ seconds and the marked rise in SOL density as evidenced by the Li beam measurements in Fig. 7.8. This becomes evident with the results of the second experimental run in April 2014, during which a markedly different antenna behavior was recorded. The global parameters for these shots are summarized in Table 7.2. Besides from the somewhat lower heating power, the setup is very similar to 29822 and 29823. Shots 30629 and 30631 were fueled from divertor valves at 10^{22} s^{-1}, whereas shot 30630 was fueled from a midplane valve at 5×10^{21} s^{-1}.

Fig. 7.9 shows the time traces for shot 30629. The general scheme is the same as in the previous three shots, namely an increase of δ_U from ~ 0.1 to ~ 0.3, with R_{sep} scans at constant δ_U. Note the antennas are now powered pairwise (A1-A3, A2-A4) in one second intervals and the discharge is one second longer. As previously observed, upon reaching $\delta_U \approx 0.3$ around $t \approx 6.5$ seconds there is a transition into a type II ELMy regime but, in contrast to 29822 - 29833, only a rather moderate increase in R_L of about 0.5 Ω is recorded at $t \gtrsim 7.5$ seconds (compare with Figs. 7.2 - 7.4). This small increase in loading was observed consistently in the three discharges under consideration. This is shown explicitly in Fig. 7.10, where R_L is plotted versus δ_U; the same procedure was used here to obtain the data points as in Fig. 7.5.

There are several notable features in these results. Shot 30629 was the only "well-behaved" one, in the sense that $\tau_{th}/\tau_{\text{IPB98(y,2)}} \sim 0.9$ at $\delta_U \approx 0.1$ and increases to ~ 1 at $\delta_U \approx 0.3$, as in 29822 - 29833. A small increase in R_L begins around $\delta_U \approx 0.25$; there is a total change of about 0.5 to 1 Ω as evidenced from the difference in the lower boundaries of the small clusters right after $\delta_U = 0.2$ and 0.3 produced by the R_{sep} scans. A similar effect is seen at high δ_U in 30630, evident mostly for antennas 1 and 2. The sharp spike in R_L at the right is not an effect of triangularity; it is simultaneous with an abrupt drop in confinement around 7.5 seconds, with a corresponding density increase in the SOL, due to excessive tungsten accumulation in the plasma[5]. The same confinement drop occurs

[5] V. Bobkov, personal communication.

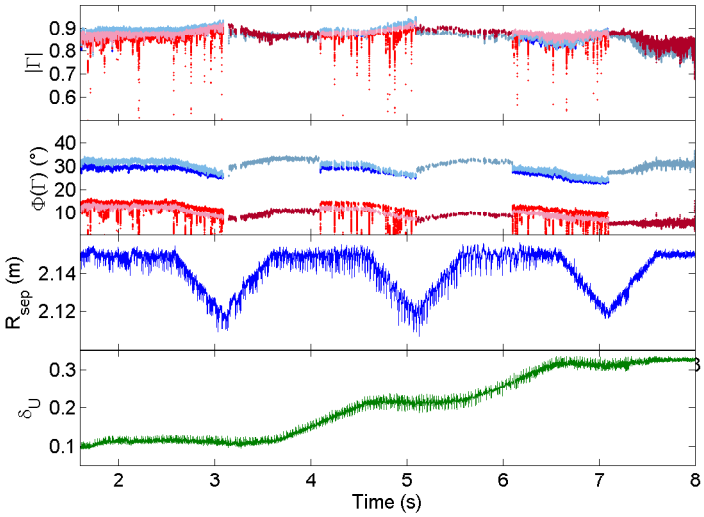


Figure 7.9: Shot 30629, time traces of RF measurements on antennas 1, 2 and 3 along with separatrix position R_{sep} and upper triangularity δ_U. Note that the increase in coupling is significantly smaller than in shots 29822 - 29833.

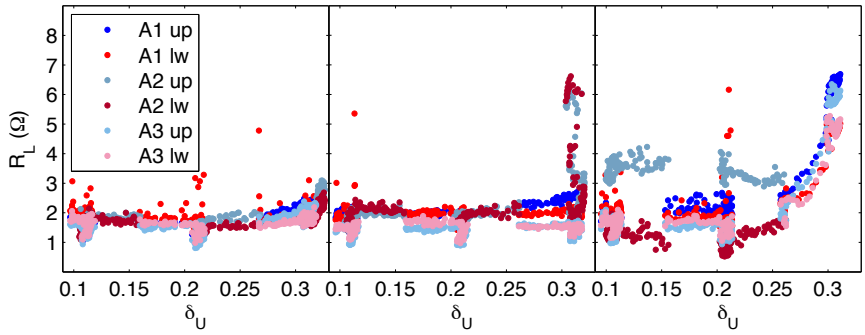


Figure 7.10: Antenna loading resistance versus upper triangularity in shots 30629, 30630 and 30631 (left to right).

at $t \gtrsim 6$ seconds in 30631 and is responsible for the increase in R_L starting around $\delta_U \approx 0.25$. Note that the two straps of antenna 2 record a very different loading, in stark contrast to all other shots; the reason for this is likely connected to the fact that A2 was operated with a phasing of $(0, \pi/2)$ during this shot, as opposed to the normal $(0, \pi)$ operation.

The situation is made somewhat clearer by examining the neutral particle flux density Γ_0^{main}, which is known to be related to the square of an effective scrape-off layer density [65]. Fig. 7.11 shows the time traces of the recorded loading on antenna 1 (averaged over the two straps for clarity) and the neutral flux density measured by an ionization gauge located in the main chamber midplane, from 5 to 7 seconds in the six shots analyzed here. All data points are ELM-synchronized and averaged over 5 ms intervals. $\delta_U \approx 0.3$ in all the intervals shown, but it is clear that Γ_0^{main} is substantially different from shot to shot, and there is in fact a strong correlation, as expected, between this quantity and the antenna resistance. In fact, the antenna behavior becomes at least qualitatively consistent in all six discharges when plotted versus Γ_0^{main}, as shown in Fig. 7.12. In 29833, the small cluster of data points around $\Gamma_0^{\text{main}} \approx 10^{21}$ m^{-2}s^{-1}, $R_L \approx 1\ \Omega$ is due to a slight increase in SOL density during the R_{sep} scan between 4 and 5 seconds, hence the low coupling. Around 6.5 seconds in shot 30631 the edge density measured by the DCN interferometer begins to decrease, possibly accounting for the decreasing loading at high neutral flux density.

The reason for the large SOL density increase in 29822 - 29823 and 30631 is not clear. Triangularity variations can affect gas recycling through changes in the connection length of the magnetic field lines in the SOL [29]; however this does not reveal the cause of such large differences in recycling when triangularity is essentially the same in all discharges. In the absence of this increased plasma-wall interaction, in the range of δ_U investigated here we expect the improvement in coupling be similar to that observed towards the end of discharge 30629, i. e. about 1 - 0.5 Ω.

We conclude this section with a few remarks about the simulation results for these shots. The coupling resistance R_C computed with FELICE using the available IDA profiles for discharges 29822 - 29833[6] (ELM-synchronized where applicable, otherwise averaged over 10 ms) shows good qualitative agreement with the experimental results (however there is also a large spread in the numerical results); this is shown in Fig. 7.13. Note that on each plot the data points are very roughly grouped into two clusters, at low and high resistance. The low R cluster is due to the fact that during most of the time during each shot R_L remains in the range $1 - 2\ \Omega$ (see Fig. 7.5). Upon transition into the type II ELMy regime ELM synchronization stops, with $\delta_U \approx$ const., and R_L stays in a constant range, falling into the $R_L \gtrsim 4\ \Omega$ cluster; because the transition is fast, there are relatively few

[6] No IDA profiles are available after about 6 second for the remaining three shots.

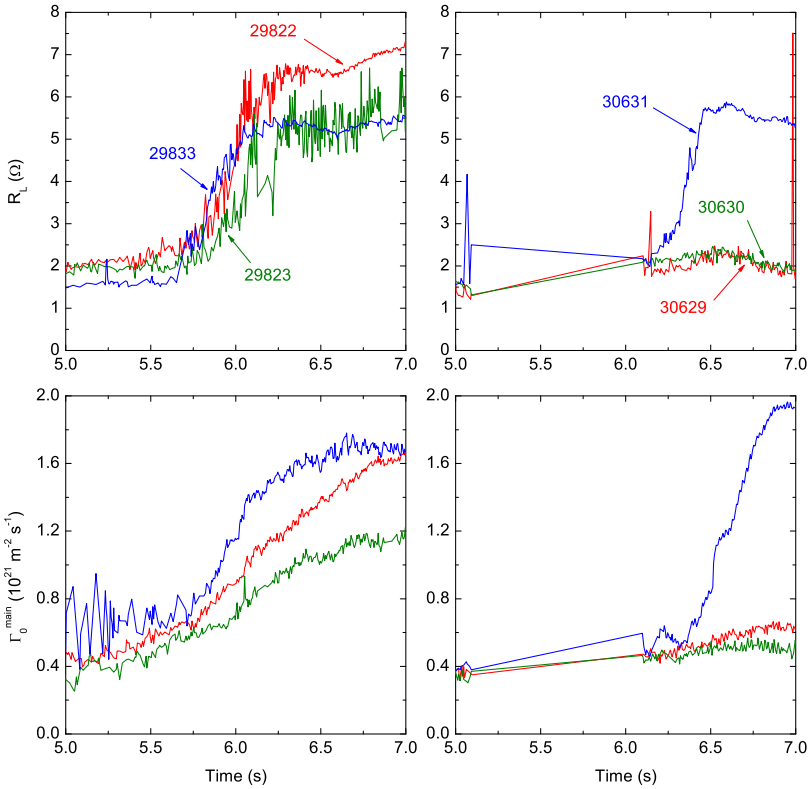


Figure 7.11: R_L on antenna 1 (averaged over the two straps) and main chamber neutral flux density versus time, 5 to 7 seconds in all shots. It can be seen that R_L increases only in those shots where Γ_0^{main} also increases.

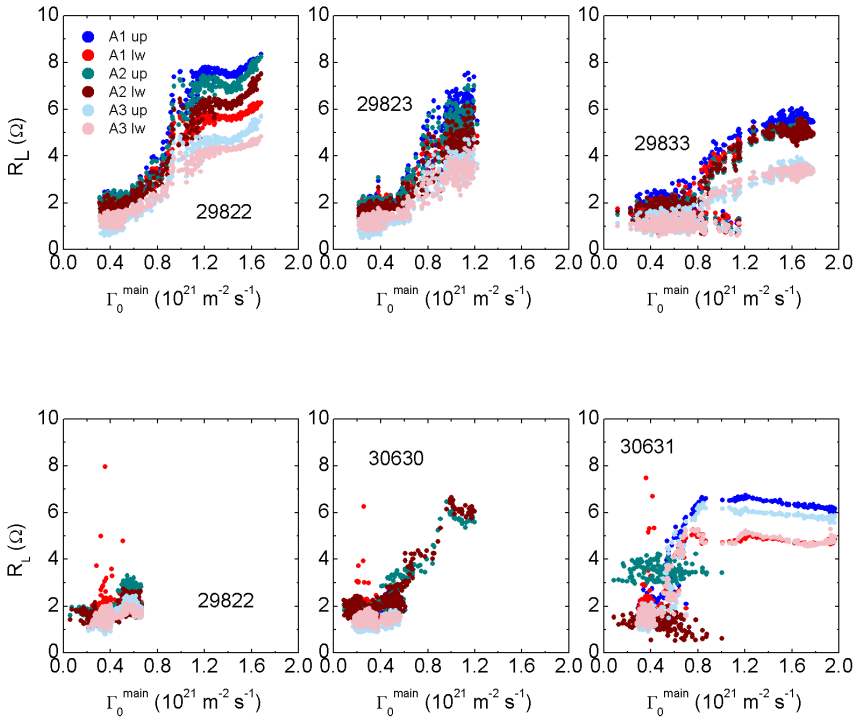


Figure 7.12: Antenna loading resistance versus main chamber neutral flux density Γ_0^{main}, all shots. A clear correlation is seen between R_L and Γ_0^{main}.

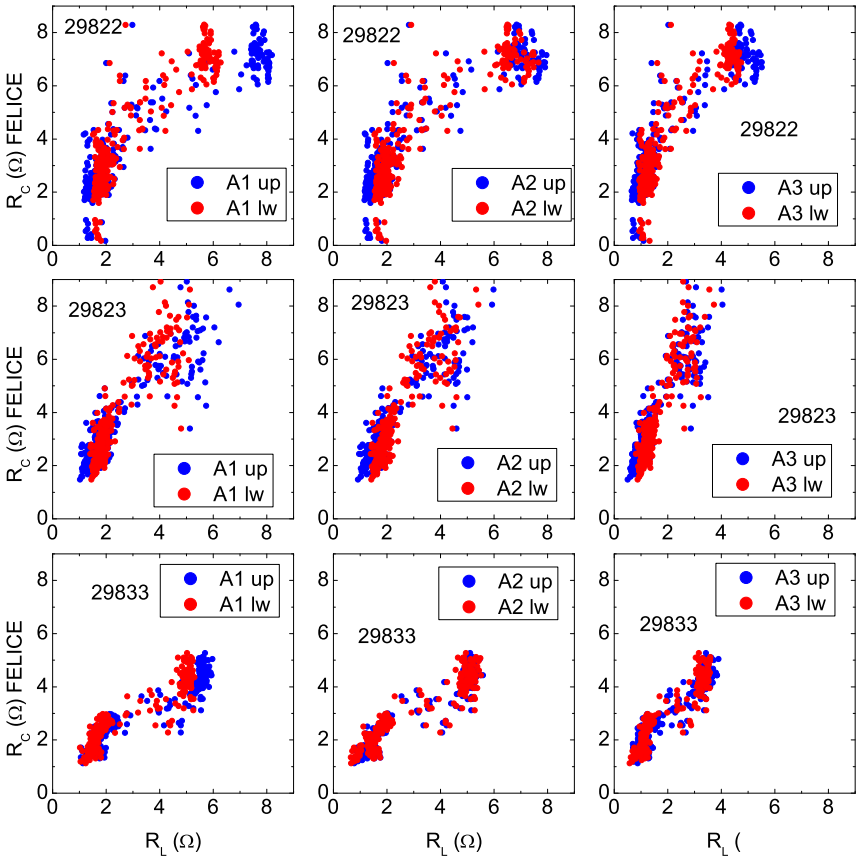


Figure 7.13: R_C computed with FELICE vs. R_L measured during shots 29822, 29823 and 29833. There is qualitative agreement between the simulated and the measured data, but a large spread can be seen in the code results as well.

R_L values in between.

The experimental and calculated values are also shown as a function of time (shot 29823 only) in Fig. 7.14, where it is seen that the variation in calculated R_C is substantially higher than in measured R_L even when ELM synchronization is applied; naturally it is even higher with no synchronization in the type II ELMy phase ($t \gtrsim 5$ s). This highlights once again one of the fundamental problems with numerical simulation of ICRF antennas, namely that of obtaining a density profile which is representative of the one in fact present in front of the antenna during a given time window.

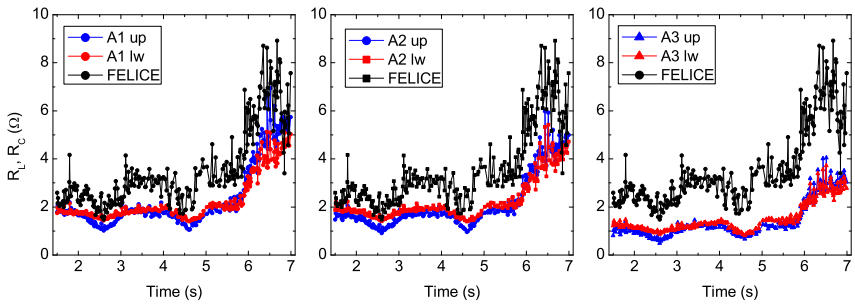


Figure 7.14: R_C computed with FELICE and R_L measured in shot 29823 as function of time.

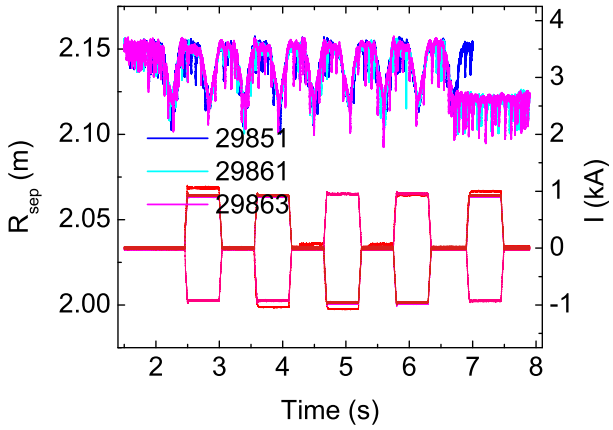


Figure 7.15: Time traces of separatrix position R_{sep} in shots 29851, 29861 and 29863, and B-coil current during shot 29861 (only one shot is displayed as the setup was virtually identical in all discharges).

7.4 Magnetic perturbation fields

The effects of non-axisymmetric magnetic perturbation fields on plasma density and temperature profiles on ASDEX Upgrade had been first reported in [66] in the context of an ELM mitigation study. Although no significant edge density changes were described, it was observed that, on a time scale of $0.5 - 1$ seconds after coil switch-on, a small decrease in density gradient and a small increase in pedestal top density occur. ELM mitigation is normally observed on ASDEX Upgrade with MPs with toroidal mode numbers $n = 1$, 2, 4 above a density threshold $n_e/n_{GW} \approx 0.65$, with n not related to a narrow resonance with the edge safety factor [67].

Three successful discharges were carried out in March 2013 to study the effect

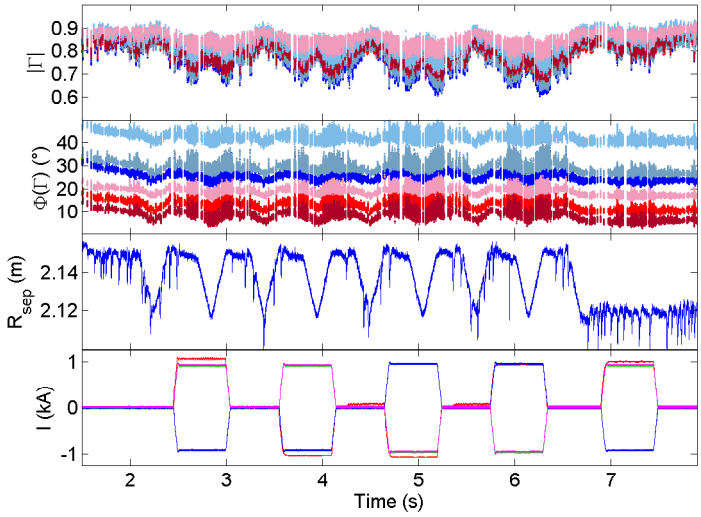


Figure 7.16: Shot 29861, time traces of RF measurements on antennas 1, 2 and 3 along with separatrix position R_{sep} and B-coil current (four current traces are shown in different colors). ELM reduction is observed when the B-coils are switched on, with the exception of the last interval.

of MPs on antenna behavior. Figure 7.15 shows the setup of the three dedicated shots. The B-coils are switched on for 0.5 second intervals, introducing a perturbation field with $n = 2$, with the phase being shifted by $\pi/2$ each time. During each on and off interval, the LCFS is moved ~ 3 cm away from the antenna and then returned to its original position.

The evolution of RF parameters during a typical discharge is displayed in Figure (7.16) (only one shot is shown since the antenna behavior was nearly identical in the other two discharges). Several important features can be seen. First of all, essentially complete ELM suppression occurs when the coils are switched on, with the exception of the last window; however type I ELMs are replaced by low intensity, high frequency ELMs, which can be seen most clearly on the phase signal. Because of their low intensity and high frequency, ELM synchronization is not possible and hence the RF signals tend to be noisy during the intervals when the B-coils are on. Second, baseline loading on all antennas improves during MPs (see below). Third, improvement does not appear to depend on the phase of the perturbing field. These features were observed consistently in all three shots.

The degree to which antenna loading changed during MPs is displayed more explicitly in Fig. 7.17, which shows the loading resistance R_L versus separatrix position R_{sep}, with and without magnetic perturbations (the "on" and "off" intervals are arbitrarily defined here by the coil current crossing 0.5 kA). All values were obtained after ELM synchronization and averaging over 5 ms intervals. It

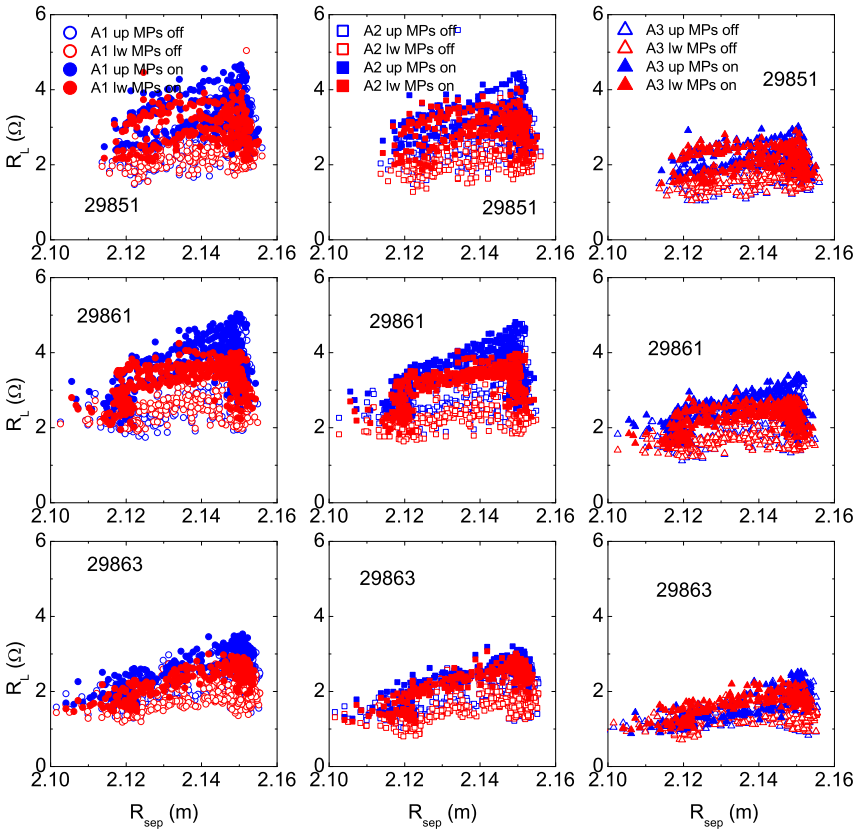


Figure 7.17: Antenna loading resistance as a function of R_{sep} in shots 29851, 29861 and 29863, with and without magnetic perturbations.

can be clearly seen that R_L is about $30\% - 50\%$ higher while the B-coils are on, for the whole range of separatrix movement. Note that, besides from the increase in R_L that occurs when R_{sep} is moved toward the antenna (larger values), there are two vertically elongated clusters of points at the low and high boundaries of the R_{sep} range, i. e. around $R_{sep} \approx 2.12$ m and 2.15 m. The cluster on the lower boundary is present because during the last time interval with MP coils on in shots 29861 and 29863 ($7 \lesssim t \lesssim 7.5$ s), R_{sep} stays constant at its lower value; the high frequency ELM activity leads to large variations in R_L, clearly seen in Fig. 7.15. Accordingly, this cluster is not present in the data from shot 29851. The cluster at the high boundary is due to the fact that R_{sep} scan actually begins about 200 ms after the MP coils are switched on. During this time R_L increases due to the MPs, again leading to a vertical variation at constant R_{sep}.

This evolution of R_L as a function of time after coil switch-on and switch-off

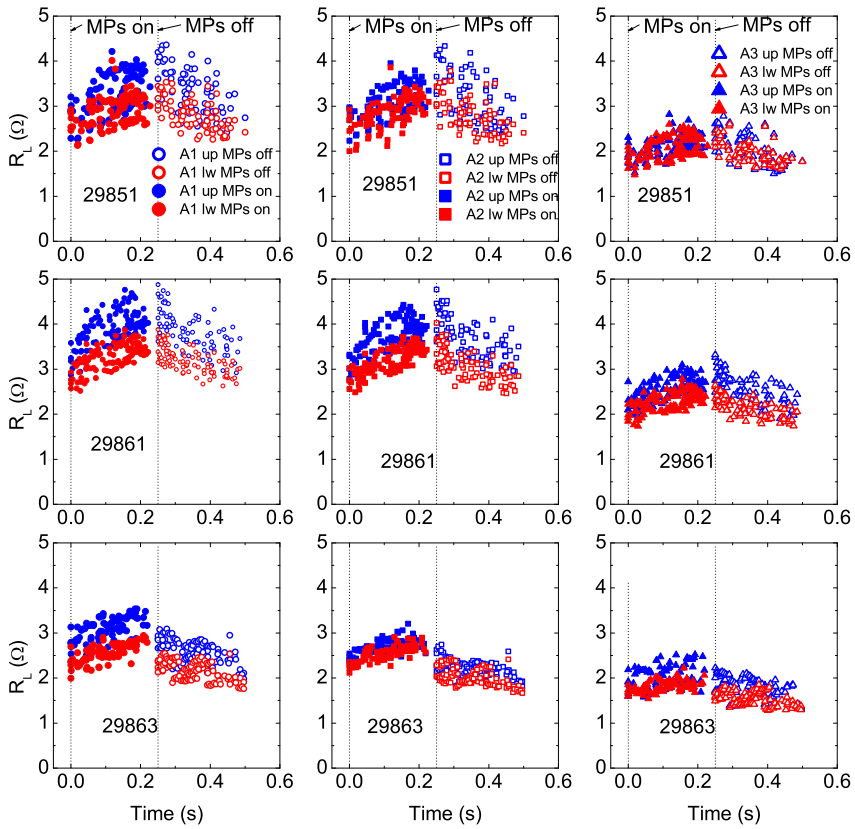


Figure 7.18: Antenna loading resistance as a function of time in shots 29851, 29861 and 29863, at R_{sep} = const., with and without magnetic perturbations.

is illustrated in Fig. 7.18. The points are only taken from the 200 ms intervals before each R_{sep} scan, to separate the effects of the LCFS displacement. Note the time position at which the coils are turned off are displaced by 250 ms for clarity. We observe a linear increase in R_L beginning immediately after the coils are switched on, amounting to about 0.5 Ω during 200 ms. Each cluster of points is taken from four intervals within each shot, corresponding roughly to $2.5 \lesssim t \lesssim 2.7$ s, $3.6 \lesssim t \lesssim 3.8$ s, $4.7 \lesssim t \lesssim 4.9$ s and $5.8 \lesssim t \lesssim 6$ s. The vertical spread of the data points is also due to the fact that the average resistance increases slightly throughout each shot. After the coils are switched off, R_L decreases at about the same rate and reaches its initial value after 200 ms, at least in shots 29851 and 29861; the situation is somewhat different in 29863, where R_L at the end of each R_{sep} scan is slightly lower than before the scan.

Although the effect of the MPs on antenna resistance is relatively clear, it is

not straightforward to relate this variation to changes in the density profile. On one hand, the perturbation field introduces a toroidal asymmetry into the equilibrium, meaning that the assumption that the measured profile corresponds to the profile actually in front of a given antenna is probably invalid; on the other hand, the high frequency ELMs occurring in the intervals where the type I ELMs are mitigated make it difficult to accurately measure the n_e profile at all. This means that we do not expect the results of any numerical code to closely reproduce the measured loading. As an illustration, Fig. 7.19 shows the relation between FELICE calculations and the experimental results for the three shots discussed above. All input plasma profiles are ELM-synchronized where possible, and averaged over 10 ms otherwise. While a general proportionality is observed, the scatter is significant, indicating large variations both in the measured R_L and the IDA n_e profiles. That the calculated resistance behaves at least consistently with measurements can also be seen in Fig. 7.20, where the FELICE results are plotted vs. R_{sep} with the MPs on and off; note, however, that a clear dependence of R_C on R_{sep} can be observed only for shot 29863, in contrast to the experimental data in Fig. 7.17. The increase in average R_C is 1.1, 0.60 and 0.27 Ω, corresponding to 28%, 14% and 11% of the value without MPs, in shots 29851, 29861 and 29863 respectively. Finally, because of the large fluctuations, it is difficult to resolve the changes in the n_e profile itself; averaging the available density profiles over the whole discharge does not improve the situation significantly. Fig. 7.21 shows these averages with the MPs on and off. The change seen in each case is minimal, although in all shots the pedestal gradient is slightly decreased when the B-coils are switched on, which would be qualitatively consistent both with previous observations [66] and the recorded increase in coupling.

7.5 Summary

Several dedicated discharges have been carried out on ASDEX Upgrade to investigate the behavior of the antenna at high triangularity and with non-axisymmetric magnetic perturbations. The triangularity experiments reported here differ from the previous studies in ASDEX Upgrade [29] and JET [28] in that the plasma shape does not change significantly in front of the antenna; however, a moderate improvement in loading resistance (0.5 to 1 Ω) is still observed after the plasma enters a type II ELMy regime. This effect seems to be independent of a much larger increase in coupling (of a few Ω) that is related to a drastic increase in SOL density, as evidenced by Li beam n_e and main chamber neutral flux density measurements, and is possibly caused by a higher plasma-wall interaction.

The effect of non-axisymmetric magnetic perturbations appears to be clearer in all the shots analyzed here. In addition to the beneficial effects of ELM mitigation, baseline loading on all antennas is observed to rise steadily when the MPs are

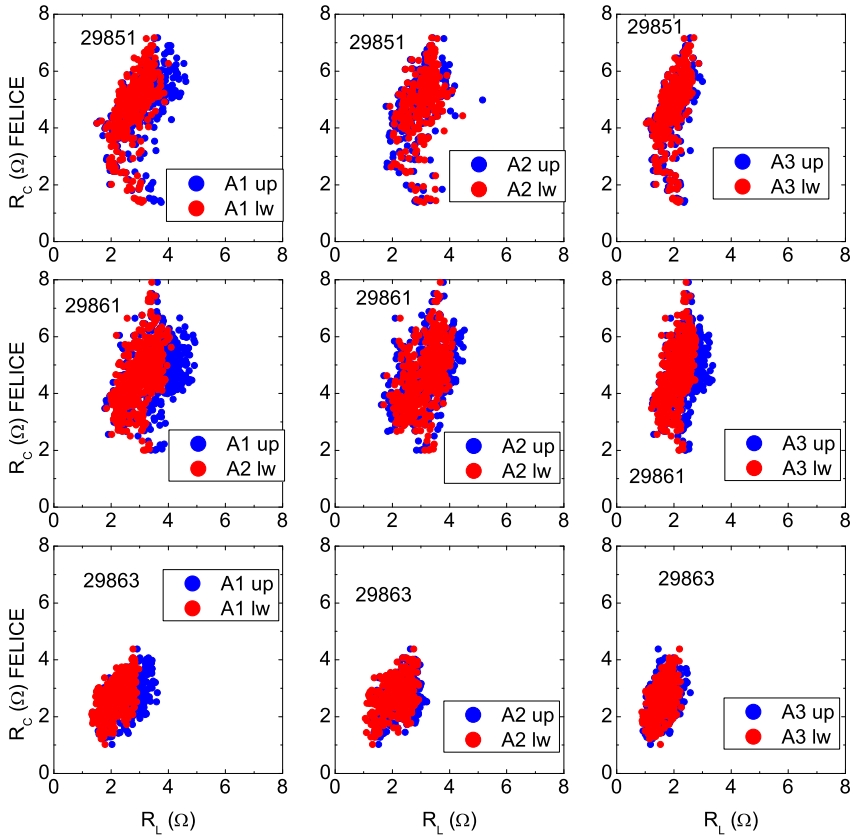


Figure 7.19: R_C computed with FELICE vs. R_L measured during shots 29851, 29861 and 29863. Notice the significant scatter.

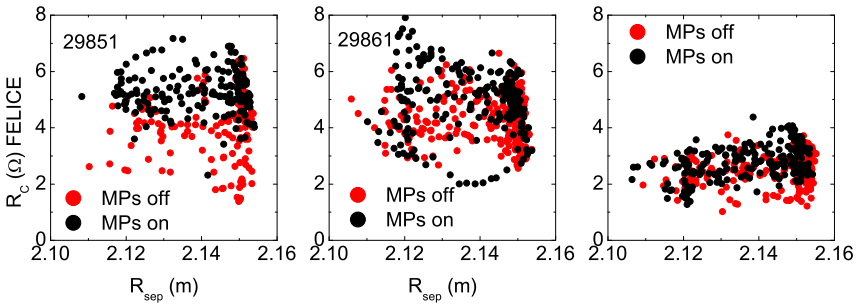


Figure 7.20: R_C computed with FELICE vs. R_{sep}, with and without MPs, for shots 29851, 29861 and 29863.

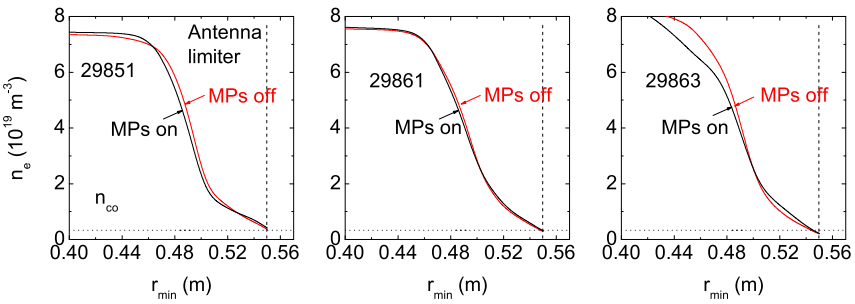


Figure 7.21: Density profiles with and without MPs, averaged over the entire shot.

switched on, and return to its normal value when the coils are switched off. The improvement in coupling also corresponds to about 0.5 - 1 Ω and has been consistently observed on all antennas. Because of fast density fluctuations, however, it is not straightforward to relate this improvement to specific changes in the electron density profile, except in a very general way consistent with previously reported results [66].

8

Comparison of TOPICA results with experimental data on ASDEX Upgrade

8.1 Introduction

In recent years, TOPICA has been extensively tested against experimental results obtained on Alcator C-Mod [18], Tore Supra [19], DIII-D [20] and JET [21]; it is not straightforward to directly compare the results of these studies, since they differ in the quantities being compared: coupling resistance per unit length in Tore Supra, effective conductance in JET, complex voltage reflection coefficient in Alcator C-Mod, and loading resistance in DIII-D. In addition, two other studies investigated the performance of both the baseline and the wide limiter antenna at ASDEX Upgrade in terms of coupling and RF potentials, namely [68] and [69], but no comparisons with experimental data are quoted. In the other studies, the agreement with experiment has usually been rather good. The Alcator C-Mod study reported $< 10\%$ agreement in $|\Gamma|$ and $< 10^\circ$ in the phase of Γ (in many cases better, see [18] for details); the JET and Tore Supra both report TOPICA results well within the measurement error bars (the latter was different from standard antenna studies in that it focused on computing certain antenna parameters from fixed reflection coefficients on the feeding ports, see [19] for details). The DIII-D study reported very good absolute agreement, especially in H-mode [20].

ASDEX Upgrade is advantageous for such a study because of the availability of detailed measurements and reconstruction of the electron density and temperature profiles, thereby reducing one of the possible error sources. For all the

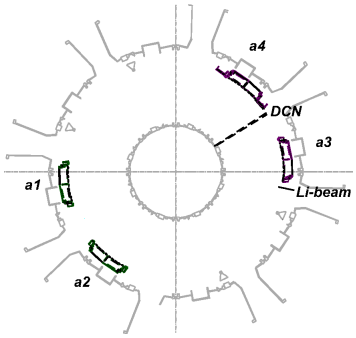


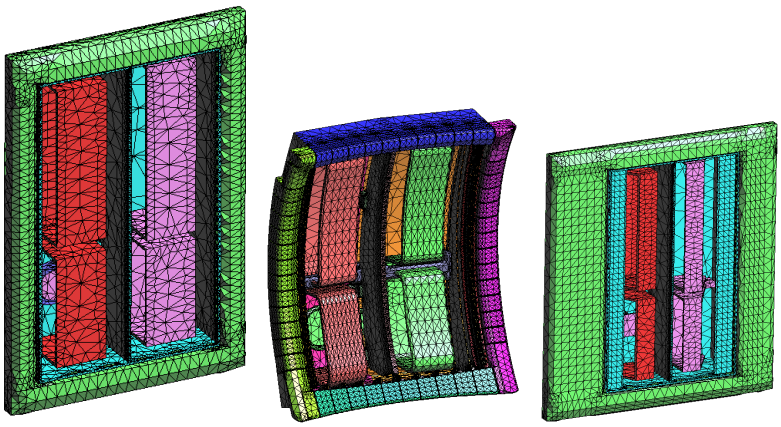
Figure 8.1: Position of the density diagnostics used for profile reconstruction by IDA, as well as the four ICRF antennas.

simulation runs, electron density (n_e) and temperature (T_e) profiles were obtained from Integrated Data Analysis (IDA) files [70][1]. Electron density is measured in the core and pedestal top via DCN interferometer and at the edge/SOL by Lithium beam emission spectroscopy; electron temperature is measured by electron cyclotron emission. The toroidal positions of these diagnostics, as well as the four ICRF antennas, are shown in Fig. (8.1) (note that the density diagnostics are closest to antenna 3, located in sector 10.) Point-wise profiles along the whole plasma radius are reconstructed via Bayesian analysis [70] and are available with a time resolution of 1 ms; the resolution of the density profile in the edge region is 5 mm (densities up to 0.8×10^{20} m^{-3} are accessible by Lithium beam [70]).

Because of the large fluctuations in density due to ELMs in H-mode discharges, all input profiles were ELM-synchronized where applicable. The outer divertor current was taken as indicator of ELM activity and the time interval used for synchronization was between 3.5 and 1.5 ms before each ELM event (the impact of different choices of synchronization intervals is discussed in Chapter 6). For each shot, time windows ranging from 10 to 200 ms were selected; all the n_e and T_e profiles available in ELM-synchronized intervals within each window were averaged into one density and one temperature profile and used as input; likewise only experimental data within the same intervals was averaged and used for comparison. The n_e and T_e profiles are cut at $R_{maj} = 2.2$ m, which is the radial position of the antenna limiters at the midplane.

As it is shown below, the availability of accurate RF diagnostics is also an essential requisite for a meaningful comparison. Two studies were carried out in the context of the present work, one using experimental data from the standard diagnostics, and one making use of voltage/current probe measurements implemented later.

[1] Kindly provided by Dr. R. Fischer.



(a) Baseline flat. (b) Baseline curved. (c) Wide limiter flat.

Figure 8.2: Antenna models for TOPICA input. The Faraday screen bars have been removed on all models for clarity.

8.2 First comparison

Two discharges were chosen for the first TOPICA study, 25634 and 25654. Both are L-mode discharges from a series of shots dedicated to study loading improvement by local gas injection [25], with a significant variation in R_L in both, with $B_0 = 2$ T and $f = 30$ MHz. Due to operation in L-mode, no ELM synchronization was applied to the input profiles; n_e and T_e were simply averaged over the time window specified for each simulation point[2]. A plasma composition of 1.5% H, 98.5% D was used in these simulations, the average of the values reported in [25].

Three antenna models were used to simulate shot 25634: a flat and a curved model of the two-strap baseline antenna, and a flat model of the wide limiter antenna 4. These models are shown in Fig. 8.2. In all cases the feeding scheme was $(0, \pi)$ with an amplitude of 1 V on both ports. Here and in all simulations, all free parameters (both in input profile preparation and in the actual runs - e. g., replacement of a thin layer of low-density plasma for the correct functioning of the FELICE module and the selection of the hot-cold transition wavenumber [18]) were set to the values recommended in the TOPICA manual [50]. In all cases, outward radiation conditions were imposed at 30 cm from the plasma surface.

In order to speed up computation, only a small portion of the transmission network ($\sim$ 15 cm of each feeding line; it was verified that this distance from

[2]However, some indications of ELMs were observed in these discharges due to proximity to the H-mode power threshold [25].

any discontinuity is enough to assume that the electric field inside the coaxial line recalls the ideal TEM feeding distribution adopted in TOPICA[3]) is included in the TOPICA model; the 2×2 scattering matrix $\mathbf{S}$, which constitutes the relevant part of the TOPICA output, is used instead to compute the quantities of interest. The $\mathbf{S}$-matrix is computed on the input ports of the upper and lower strap, labeled here as ports 1 and 2 respectively. With the standard setup, the T-section is the closest point to the antenna where the input impedance is accessible for measurement; therefore this is also the quantity to be computed from the scattering matrix. The relevant sections of the transmission network are shown in Fig. 3.3, section 3.2. The $\mathbf{S}$-matrix translated to the T-section is

$$\mathbf{S}' = \mathbf{\Theta S \Theta}, \tag{8.1}$$

where

$$\mathbf{\Theta} = \begin{bmatrix} e^{-j\beta l_1} & 0 \\ 0 & e^{-j\beta l_2} \end{bmatrix}, \tag{8.2}$$

$\beta = 2\pi f/c$, and l_1, l_2 are the distances to the T-section along the lower and upper lines respectively. From (8.1) the impedance and admittance matrices at the T-section are

$$\mathbf{Z} = Z_{0I} \left(\mathbf{I} + \mathbf{S}'\right) \left(\mathbf{I} - \mathbf{S}'\right)^{-1}, \tag{8.3}$$

$$\mathbf{Y} = \mathbf{Z}^{-1}, \tag{8.4}$$

with $Z_{0I} = 25\ \Omega$ the characteristic impedance of the feeding lines and $\mathbf{I}$ being the unit matrix. From $\mathbf{Y}$ the voltage reflection coefficient looking into the T-section from the generator side is given by

$$\Gamma_T = \frac{1 - Z_{0C}(Y_{11} + Y_{12} + Y_{11} + Y_{22})}{1 + Z_{0C}(Y_{11} + Y_{12} + Y_{11} + Y_{22})}, \tag{8.5}$$

where $Z_{0C} = 50\ \Omega$ is now the characteristic impedance of the common line. Since the directional couplers are located behind the matching network, Γ_T should be translated further through the tuning stubs towards the generator; here the opposite is done, i. e., the reflection coefficient measured at the coupler location is translated towards the T-section as described in Chapter 4. As discussed therein, the reflection coefficients thus computed are very sensitive to errors in translation length.

The results of the comparison with the flat baseline and the flat wide limiter models is shown in Figs. 8.3 (antennas 1 and 3) and 8.4 (antennas 2 and 4). $\Delta\Phi$ is the phase difference between the TOPICA results and the measurements, i. e. $\Delta\Phi = \Phi(\text{TOPICA}) - \Phi(\text{measured})$. It can be seen that

[3]Daniele Milanesio and Riccardo Maggiora, personal communication.

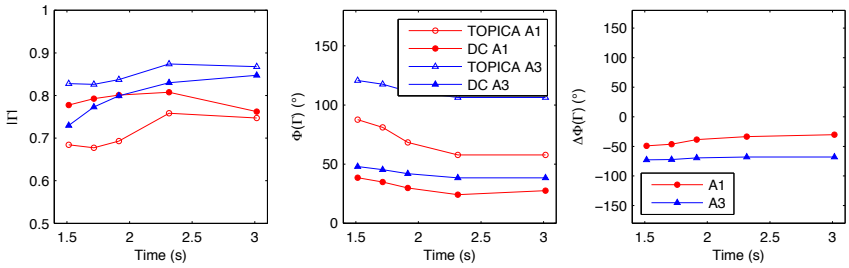


Figure 8.3: Computed and measured reflection coefficients for antennas 1 and 3, shot 25634, flat baseline model. $\Delta\Phi$ is the phase difference between simulation and measurement for each point. Large differences in $|\Gamma|$ are observed, and the trend agreement is only partial.

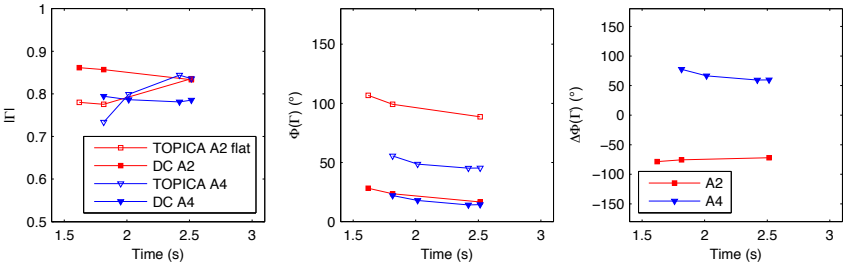


Figure 8.4: Computed and measured reflection coefficients for antennas 2 and 4, shot 25634, flat baseline and flat wide limiter models. $\Delta\Phi$ is the phase difference between simulation and measurement for each point. Large differences in $|\Gamma|$ are observed, and the there is no agreement in trend.

- relatively large differences in $|\Gamma_T|$ exist between the simulation and the measurement (up to $\sim 11\%$);
- the differences in $|\Gamma_T|$ change significantly from point to point, for example on antenna 1 (from $\sim 11\%$ down to $\sim 1\%$);
- no agreement in trend exists for antennas 2 and 4; not clear for antennas 1 and 3;
- agreement in the trend of $\Phi(\Gamma_T)$ exists for all antennas, with roughly systematic differences ranging from $\sim 30°$ (antenna 1) to $\sim 80°$ (antenna 2).

As stated, results of the calculations with the fully curved antenna model exist for this shot; these are shown in Figs. 8.5 (antennas 1 and 3) and 8.6 (antenna 2).

It is immediately noticeable that $|\Gamma_T|$ computed for all antennas using this model is substantially higher than with the flat model, leading to very large dif-

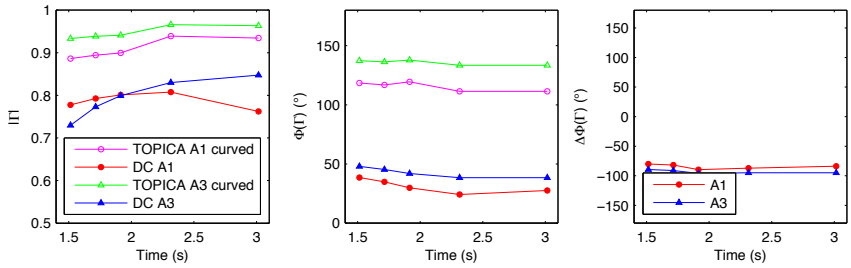


Figure 8.5: Computed and measured reflection coefficients for antennas 1 and 3, shot 25634, curved baseline model. There is substantial difference with the results of the flat baseline model, and here the agreement is significantly worse.

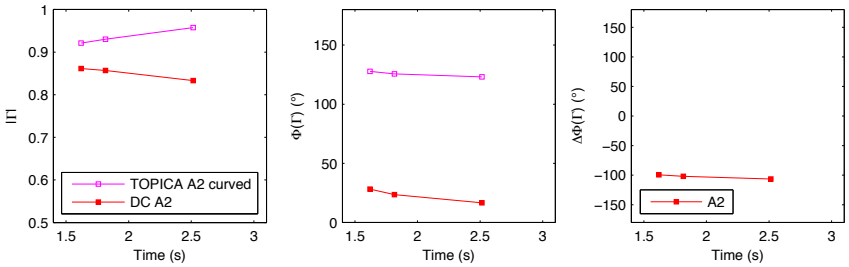


Figure 8.6: Computed and measured reflection coefficients for antenna 2, shot 25634, curved baseline model. There is substantial difference with the results of the flat baseline model.

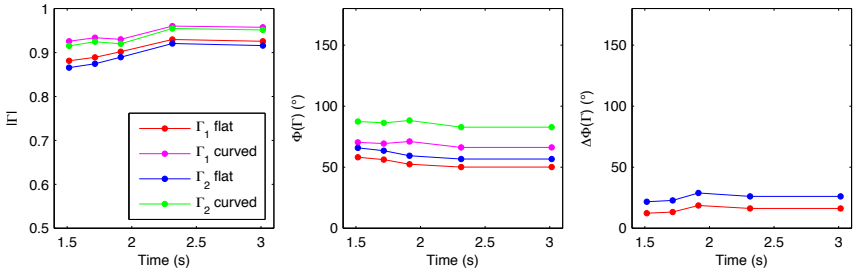


Figure 8.7: Individual reflection coefficients for the two baseline antenna models. With the convention adopted here the indices 1 and 2 correspond to the lower and upper lines, respectively. Very little difference is seen between the two in terms of $|\Gamma|$.

ferences with measurement - up to 20% in the case of antenna 3. There is also a substantial shift in $\Phi(\Gamma_T)$ (a few tens of degrees) with respect to the flat model results. Although some variation between the two models is expected, such a large difference in loading - given by $|\Gamma_T|$ - is not. However, it can be easily seen that these differences stem mostly from the way in which Γ_T is computed (Eqs. (8.1) - (8.5)) and not from the models. Although the individual voltage reflection coefficients on both lines depend on all the terms of $\mathbf{S}'$ (and hence again on the lengths of those lines), because the off-diagonal terms of $\mathbf{S}$ for the models considered here are small compared to the diagonal terms, a good approximation is

$$\Gamma_i \simeq S_{ii}. \tag{8.6}$$

The results thus obtained for the two antenna models are displayed in Fig. 8.7.

It is evident that the difference in coupling is very small - in this case the changes in $|\Gamma_T|$ are less than 2%, although phase differences in the range $20° - 30°$ exist; therefore we conclude that the large variations in $|\Gamma_T|$ in Figs. 8.3-8.4 and 8.5-8.6 are indeed due to the imprecise knowledge of the transmission network geometry. These results again confirm that calculating Γ or input impedance far from the antenna input ports can lead to very large inaccuracies in the characterization of the antenna[4].

The results for shot 25654 are shown in Figs. 8.8 and 8.9. A smaller number of simulation points is available here, but the overall conclusions are the same as in the previous case. Moderate differences in coupling between the code and the measurements exist (up to 6%), changing significantly from point to point, and no agreement in trend is observed for any antenna. The differences in phase are roughly constant and similar to what was obtained for shot 25634.

[4]Error bars are not shown in Figs. 8.3-8.6 because they require a specific assumption on measurement errors, i. e. coupler directivity, line lengths, stub positions and so on, which are in this case not known. However, a good indication of the confidence limits under varying assumptions is illustrated in Fig. 4.25.

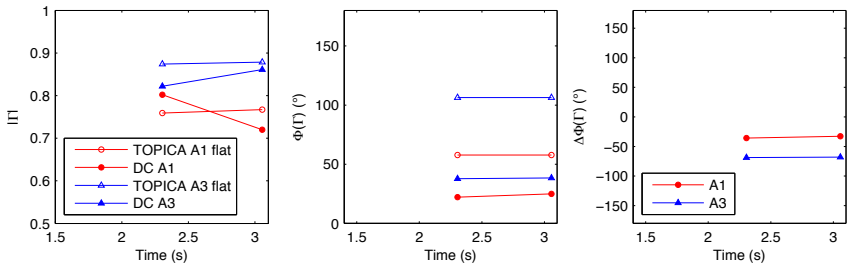


Figure 8.8: Computed and measured reflection coefficients for antennas 1 and 3, shot 25654, flat baseline model. No agreement in trend is observed.

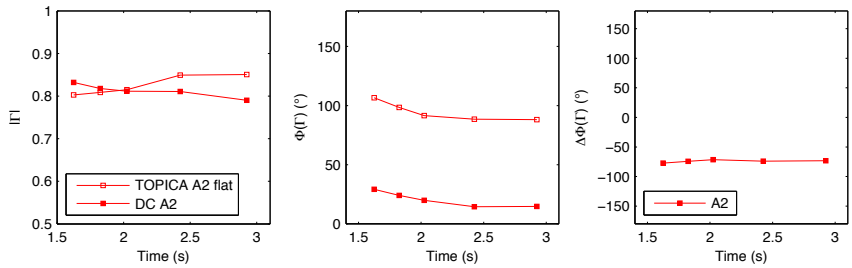


Figure 8.9: Computed and measured reflection coefficients for antenna 2, shot 25654, flat baseline model. No agreement in trend is observed.

Shot nr.	B_0 (T)	f (MHz)	RF data	Remarks
29093	2	30.0	A3	L-mode with neutral gas injection
29110	2.5	36.5	A3	L-mode with 15% H, 85% D
29113	2.5	36.5	A3	L-mode with 47% H, 53% D
29822	2.5	36.5	A1, 2, 3	H-mode with strong δ_o variation
29823	2.5	36.5	A1, 2, 3	H-mode with strong δ_o variation
29833	2	30.0	A1, 2, 3	H-mode with strong δ_o variation
29990	2.5	36.5	A2, 3	H-mode with ELM suppression

Table 8.1: ASDEX Upgrade discharges used in this study; δ_o is upper triangularity.

Because of the very significant uncertainties incurred in all quantities - measured and simulated - while translating scattering matrices along networks of unknown length, it is clear that a meaningful comparison must involve results both computed and measured as close as possible to the antenna ports. This point has already been established in Chapter 4, and the results presented here confirm the conclusions reached there. Such a comparison became possible after the implementation of the voltage/current probe pairs on the antenna feeding lines, and the results are presented in the next section.

8.3 Second comparison

The numbers and main characteristics of the discharges during which profiles and RF measurements were recorded are summarized in table 8.1. Unless stated otherwise, plasma composition was taken to be 1.5% H, 98.5% D. These numbers were based on shots 25634 and 25654 used in the first comparison; although this is somewhat lower than the usual H concentration in ASDEX Upgrade ($\sim 5\%$), sensitivity tests showed that varying the H content from 0% to 10% had virtually no effect on the results (see Chapter 6). For shot 29990, no A1 RF data is available.

In this study, only the curved baseline antenna model (shown in Fig. (8.2b)) is used. Instead of computing Γ_T, the lower and upper reflection coefficients Γ_1 and Γ_2 were used in this study. It must be stressed, once again, that the TOPICA **S**-matrix is computed ~ 15 cm from antenna input, while the RF probes are located ~ 3 m away; both measured and computed quantities are translated towards antenna input. Due to the difficulties with length measurements, some disagreement in phase is to be expected; however, unlike in the procedure used above, this will not affect the magnitude of the reflection coefficients because Γ_T is not used.

To obtain the reflection coefficients on both ports, the scattering matrix should be first translated towards the antenna input:

$$\mathbf{S}' = \mathbf{\Theta S \Theta}, \tag{8.7}$$

where

$$\mathbf{\Theta} = \begin{bmatrix} e^{j\beta l_1} & 0 \\ 0 & e^{j\beta l_2} \end{bmatrix}, \tag{8.8}$$

$\beta = 2\pi f/c$, and l_1, l_2 are the distances to the input ports along the lower and upper lines respectively. By the definition of the scattering matrix,

$$\overrightarrow{V}^- = \mathbf{S}'\overrightarrow{V}^+, \tag{8.9}$$

where $\overrightarrow{V}^+ = \left[V_1^+ \; V_2^+\right]^{\mathrm{T}}$ is the vector containing the incident voltage waves and $\overrightarrow{V}^- = \left[V_1^- \; V_2^-\right]^{\mathrm{T}}$ is the vector containing the scattered waves for ports 1 and 2 respectively. The reflection coefficients are then

$$\Gamma_i = \frac{V_i^-}{V_i^+}. \tag{8.10}$$

The incident waves have the same phase; their amplitudes have no effect on the scattering matrix[5]. Note that these are active reflection coefficients, because both ports are fed simultaneously. We note also the TOPICA assumes that all antenna surfaces are perfect conductors and does not take resistive losses into account.

Regarding the measurement side, we recall that the voltage/current probe pairs provide information on input impedance Z_{inp}, voltage reflection coefficient Γ, loading resistance R_L and coupled power P_{cpl} on each individual line by measuring the RMS voltage and current magnitudes (V and I resp.) at the same point on the line and the phase θ between them, giving

$$Z_{inp} = \frac{V}{I}e^{j\theta} \quad \Gamma = \frac{Z_{inp} - Z_0}{Z_{inp} + Z_0} \quad R_L = \frac{Z_0}{VSWR} \quad P_{cpl} = VI\cos\theta \tag{8.11}$$

with $VSWR = (1 + |\Gamma|) / (1 - |\Gamma|)$. Since the voltage/current probes are located some 3 m from strap input, reflection coefficients measured at their location were translated towards the antenna input (i. e. the same plane where $\mathbf{S}'$ is defined) in order to carry out the comparison at the same reference plane as the TOPICA results.

The results of the comparison with data from shot 29093 are shown in Fig. 8.10 (only data for antenna 3 are available for shots 29093, 29110 and 29113 as no probes had been implemented on the other systems). Only the reflection coefficient is shown for clarity here for each shot; the loading resistance R_L of each strap computed with TOPICA, for all the studied cases, is plotted versus the corresponding measured values in Fig. 8.28 at the end of this section. The increase and subsequent decrease in $|\Gamma|$ correspond to a scan in separatrix position, which is shown in Fig. 8.11.

[5]The values $\overrightarrow{V}^+ = [1\ 1]^{\mathrm{T}}$ are used here.

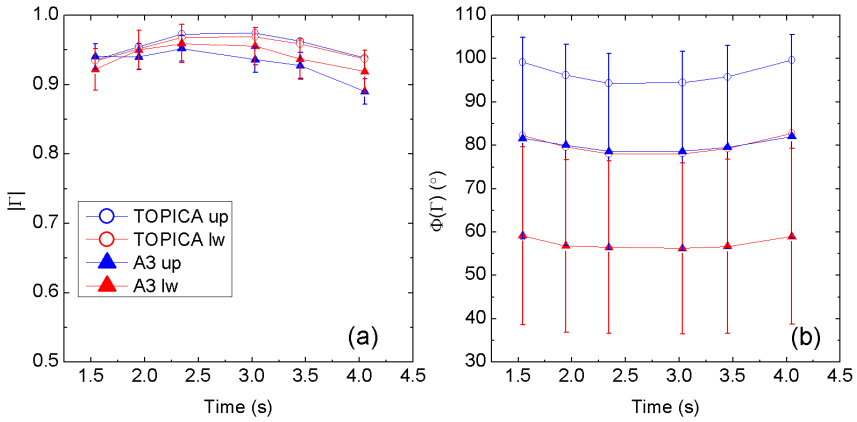


Figure 8.10: Magnitude (a) and phase (b) of Γ*, shot 29093, antenna 3. The increase and subsequent decrease in* $|\Gamma|$ *correspond to a scan in separatrix position, which is shown in Fig. 8.11.*

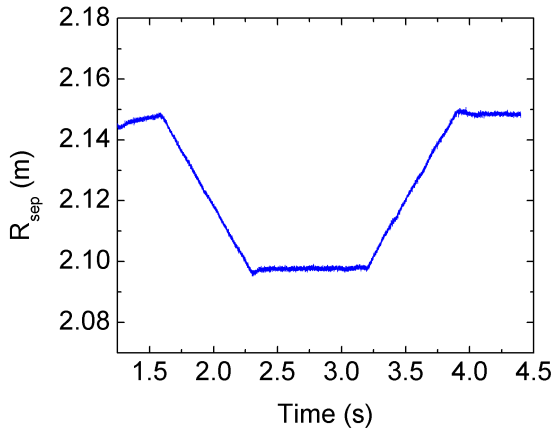


Figure 8.11: Separatrix position time trace, shot nr. 29093.

The agreement in antenna coupling - here given by $|\Gamma|$ - is very good: the average of the relative difference

$$\frac{\Delta|\Gamma|}{|\Gamma|} = 100 \times \left| \frac{|\Gamma|_{TOPICA} - |\Gamma|_{meas}}{|\Gamma|_{meas}} \right| \tag{8.12}$$

is 2.9% for the upper line and 1.4% for the lower line.

It can also be seen that there is a relatively large (but roughly constant) difference in phase between the simulated and measured results, i. e. $\Delta\Phi = \Phi(\text{TOPICA}) - \Phi(\text{measured})$; the average values are 17° and 23° (upper and lower lines respectively). If caused by an error in line length, at 30 MHz they correspond to equivalent lengths of 23 and 31 cm. Since the length of the lines between the probe location and the antenna port is around 3 m, this amounts to an error on the order of 10% of that length. Furthermore, we note that the line section between the probe pair location and the antenna input port is highly non-uniform due to the presence of the vacuum feedthrough and the transition to the strap, making it difficult to accurately measure the line length between the probes and the antenna input. This is therefore a plausible cause of the observed discrepancy in $\Phi(\Gamma)$.

Figs. 8.12 and 8.13 show the results from shots 29110 and 29113. In contrast to the other shots presented here, no significant variation in coupling is seen because no changes were introduced in the plasma (no separatrix shift, for instance); the data was included in the study because of the non-standard plasma composition (see table 8.1). Relative errors in coupling are in the same range as in 29093. The average $\Delta\Phi$ values are 26°, 33° (s. 29110, corresponding to 30 and 38 cm at 36.5 MHz) and 26°, 32° (29113, corresp. to 26 and 37 cm), which is reasonably close to the differences seen in 29093, thereby increasing the likelihood that they are indeed due to a length error.

Shots 29822, 29823 and 29833 were part of a series to test antenna behavior with changing upper plasma triangularity δ_o; therefore the variation in density - hence in antenna loading - is much more significant than in the previous shots. Fig. 8.14 shows the time traces of the separatrix position R_{sep} and upper triangularity δ_o. Three R_{sep} scans were performed (roughly between 2-3, 4-5 and 6-7 s). Lower triangularity (not shown) δ_u stays at ~ 0.45 while δ_o changes from ~ 0.1 to ~ 0.32.

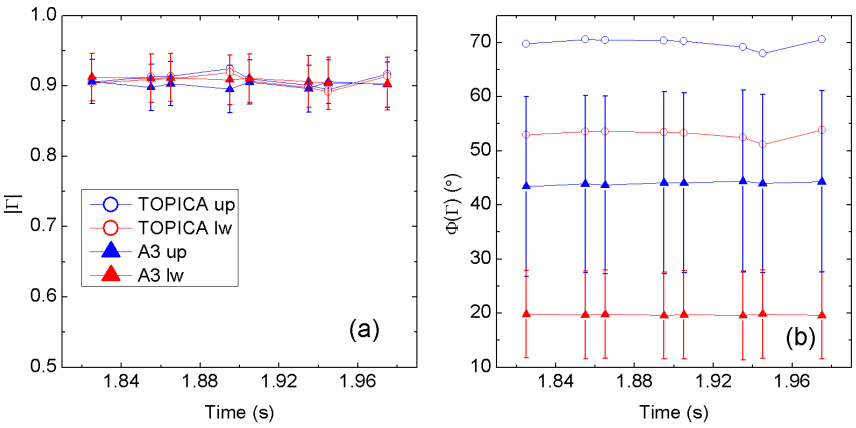


Figure 8.12: Magnitude (a) and phase (b) of Γ*, shot 29110, antenna 3.*

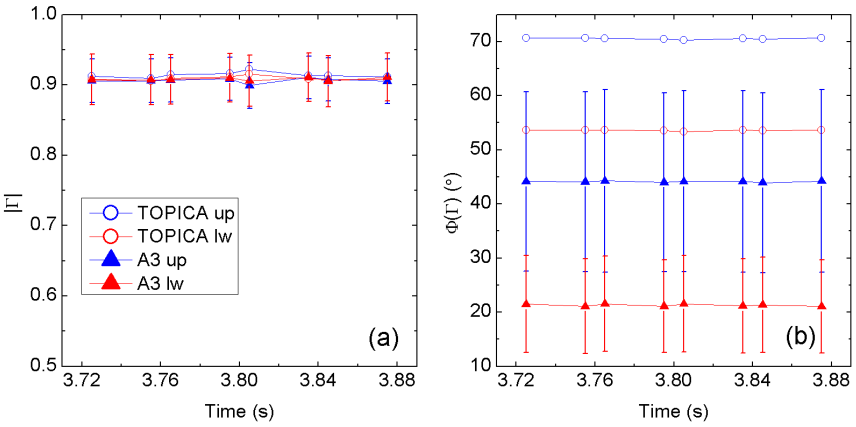


Figure 8.13: Magnitude (a) and phase (b) of Γ*, shot 29113, antenna 3.*

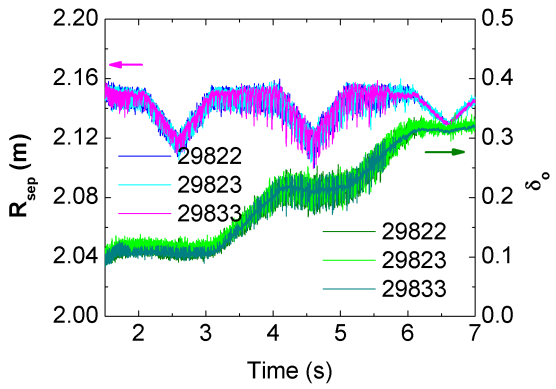


Figure 8.14: Time traces of separatrix position R_{sep} and upper triangularity in shots 29822, 29823 and 29833.

In addition to antenna 3, data from antennas 1 and 2 had become available. Figs. 8.15, 8.16 and 8.17 show the time variation of the measurements and simulation results during shot 29822 for antennas 1, 2 and 3 respectively. Noticeable in the measurement time traces (and somewhat less in the simulation results) are two of the three R_{sep} scans (roughly between $2-3$ and $4-5$ s) and a significant decrease in $|\Gamma|$ around ~ 5.5 s, where $\delta_o \simeq 0.29$.

From Figs. 8.15, 8.16 and 8.17 it is evident that the data from antennas 1 and 2 agree less with the code results than antenna 3. For antenna 1, the average relative errors in $|\Gamma|$ are 9.3% and 6.5% (upper and lower line resp.), and for antenna 2 9.0% and 6.8% (in contrast, on antenna 3 the corresponding numbers are 2.2% and 1.8%). Nonetheless the code follows fairly well the general trend in loading throughout the discharge, with the exception of the anomalous downward peak roughly between 5.1 and 5.7 s noticeable on both magnitude and phase plots, with no similar peak being observed on any of the antennas. The other major discrepancy, as stated, is observed from ~ 6 s to the end of the discharge. A possible explanation for this divergence could be that the high δ_o conditions observed in this interval lie outside the validity domain of the slab plasma geometry used in TOPICA; however, Fig. 8.14 shows that δ_o was the same for all shots, and as shown below, the discrepancy is much smaller in the results of shot 29823. Furthermore, changes in plasma shape are illustrated for shot 29822 in Fig. 8.21, along with the poloidal positions of the diagnostics used for density profile reconstruction, i. e. the DCN interferometer and the Lithium beam. From Fig. 8.21, it can be seen that there is no substantial change in plasma shape at midplane from 6 to 7 seconds, despite the large variations in coupling observed in the same time interval shown in Figs. 8.15, 8.16 and 8.17 (the observations are similar for shot 29823 and not illustrated here for brevity). We therefore conclude that the discrepancies between measurements and TOPICA results seen at high δ_o in these shots

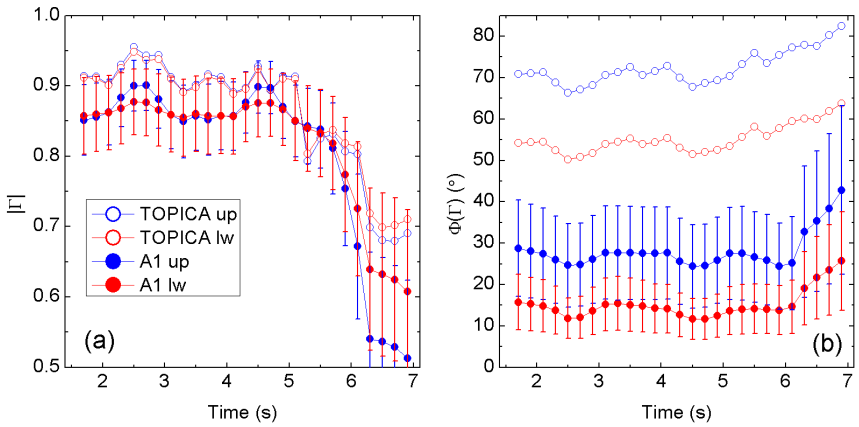


Figure 8.15: Magnitude (a) and phase (b) of Γ*, shot 29822, antenna 1. The average relative errors in* $|\Gamma|$ *are 9.3% and 6.5% (upper and lower line respectively).*

are at least *not* due to the use of the FELICE slab approximation to simulate highly shaped plasmas. See Fig. 8.22 below for further discussion.

Notably, the phase differences also increase somewhat towards the end of the discharge, although not as drastically as the loading.

The comparison results from shot 29823 are shown in Figs. 8.18, 8.19 and 8.20 for antennas 1 and 3 respectively. The conclusion again is that the code shows remarkable agreement with antenna 3, even after 6 s at high δ_o: the average $\Delta|\Gamma|/|\Gamma|$ is 1.8% and 1.6%, on the upper and lower lines. For antennas 1 and 2 the corresponding numbers are 5.7%, 5.4% and 5.5%, 3.3% respectively - which is significantly better than in shot 29822 - and the code reproduces well the main trend in loading. The situation is less clear where the phase of Γ is concerned. In both shots, the phase of each reflection coefficient calculated with TOPICA increases visibly after ~ 5 s (this is much clearer in shot 29822); on the other hand, the phase of the measured Γ increases in 29822 but actually decreases somewhat in 29823, leading to an overall increase in $\Delta\Phi$ throughout the discharge.

As stated above, the discrepancy in $|\Gamma|$ towards the end of the discharge is lower for 29823 than for 29822, although the value of δ_o is the same, and magnetic equilibrium reconstruction indicates that changes in the plasma shape mostly occur in the upper part of the plasma and not in front of the antenna (see Fig. 8.21). A global density rise is however associated with the δ_o increase; to illustrate this, eight representative density profiles used as FELICE input are shown in Fig. 8.22, four from shot 29822 and four from shot 29823 (the profiles were obtained as described in section 8.1). The radial position of the antenna limiter and the fast wave cutoff ($\sim 3 \times 10^{18}$ m^{-3}) are also shown. In the last two cases of each shot, where $|\Gamma|$ is significantly decreased, the edge density is well above cutoff.

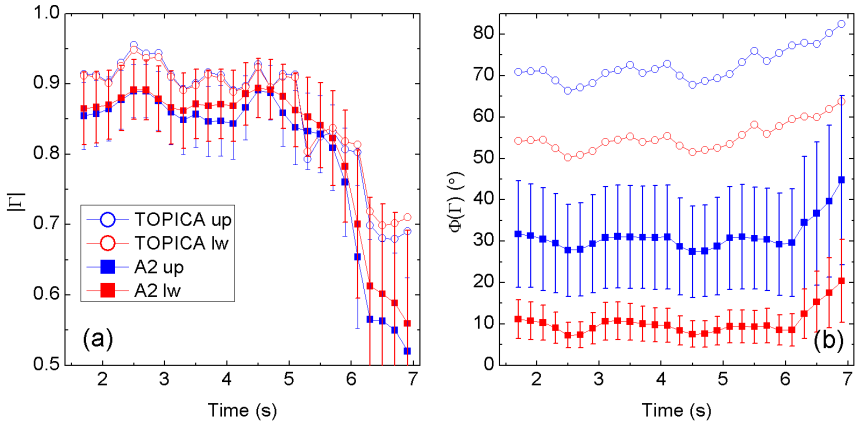


Figure 8.16: Magnitude (a) and phase (b) of Γ*, shot 29822, antenna 2. The average relative errors in* $|\Gamma|$ *are 9.0% and 6.8% (upper and lower line respectively).*

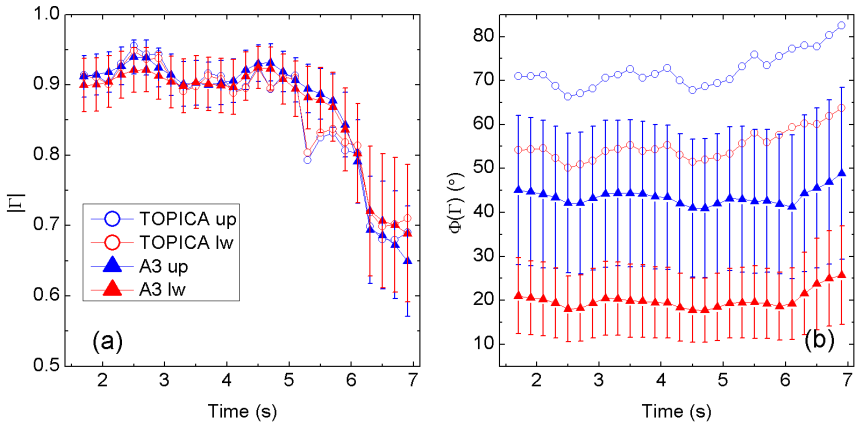


Figure 8.17: Magnitude (a) and phase (b) of Γ*, shot 29822, antenna 3. Excellent agreement is seen in* $|\Gamma|$*, with the exception of the downward 'spike' around* ~ 5 *seconds. The average relative errors in* $|\Gamma|$ *are 2.2% and 1.8% (upper and lower line respectively).*

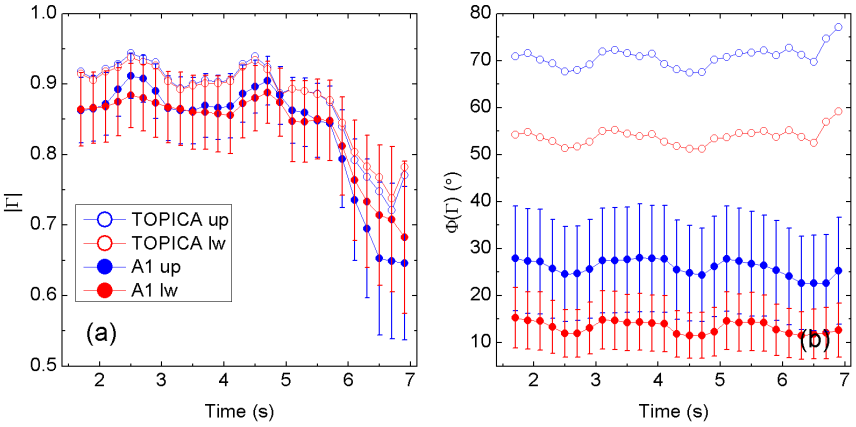


Figure 8.18: Magnitude (a) and phase (b) of Γ, shot 29823, antenna 1. The average relative errors in |Γ| are 5.7%, 5.4% (upper and lower line respectively).

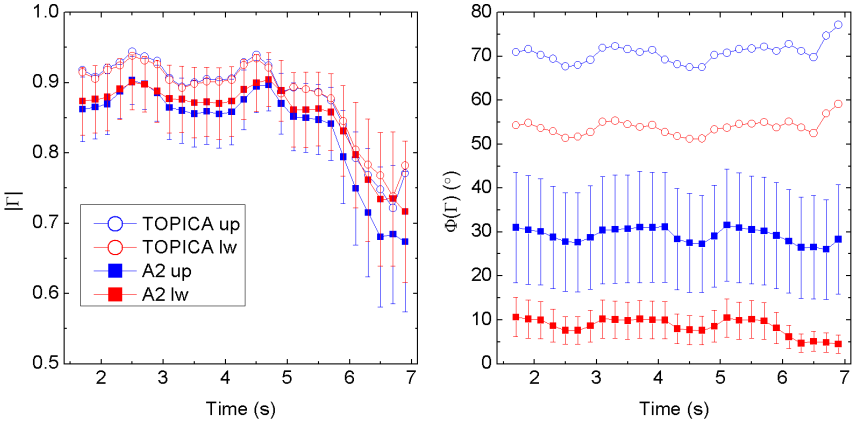


Figure 8.19: Magnitude (a) and phase (b) of Γ, shot 29823, antenna 2. The average relative errors in |Γ| are 5.5%, 3.3% (upper and lower line respectively).

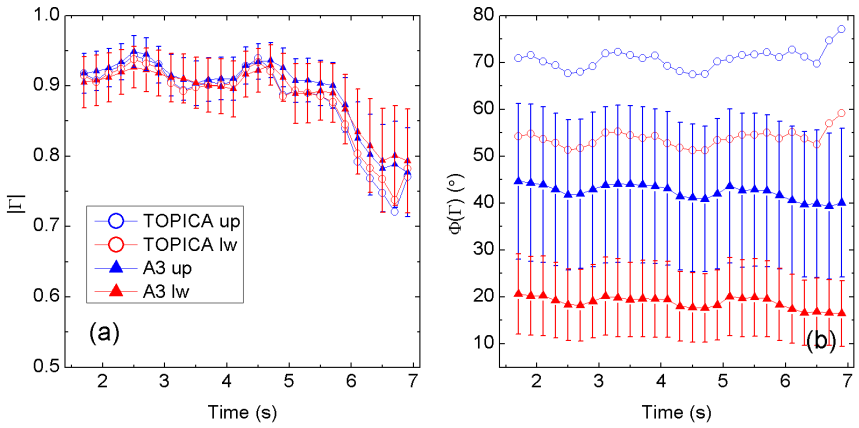


Figure 8.20: Magnitude (a) and phase (b) of Γ, shot 29823, antenna 3. Excellent agreement is seen in $|\Gamma|$ throughout the entire discharge. The average relative errors in $|\Gamma|$ are 1.8% and 1.6% (upper and lower line respectively).

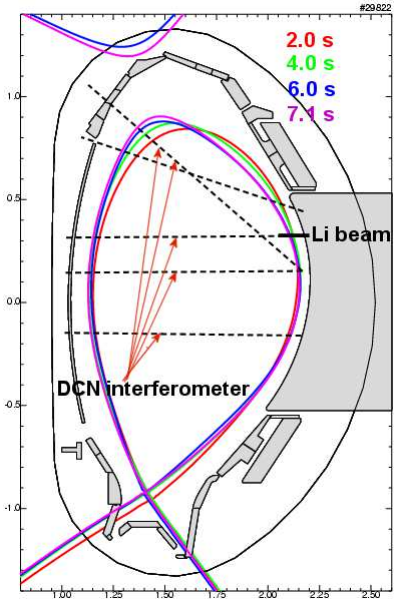


Figure 8.21: Variations in separatrix shape at several times during shot 29822; it can be seen that the changes are mostly confined to the upper part of the plasma and do not occur in front of the antenna. The poloidal location of the diagnostics used for the reconstruction of the density profile is also shown.

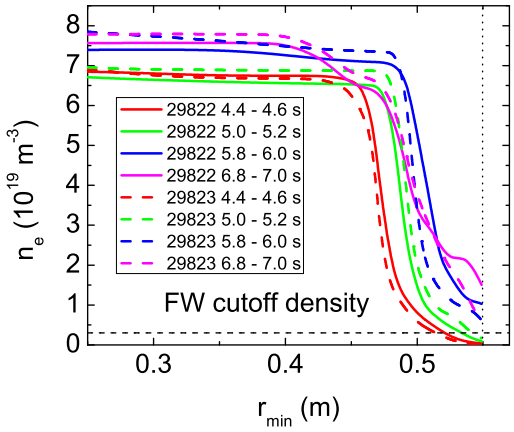


Figure 8.22: IDA reconstruction of four representative n_e profiles from shots 29822 and 29823, used in FELICE. All profiles are ELM-synchronized and averaged over the indicated time window. The radial position of the antenna limiter and the approximate fast wave cutoff density ($\sim 3 \times 10^{18}$ m^{-3}) are also shown. Note that in the last two cases in both shots, the edge n_e is significantly above cutoff density. This causes an abrupt change in density at the aperture of the antenna cavity, since TOPICA assumes there is no plasma in the cavity; this in turn leads to a possible overestimation of $|\Gamma|$ at high δ_o.

TOPICA assumes that no plasma is present in the antenna box, which therefore results in an abrupt change in n_e from zero to some relatively high value, which is expected to degrade coupling (this is shown with an analytical model in [59]. However, in reality the density is nonzero inside the antenna cavity, decreasing the gradient and also allowing the fast wave to propagate; therefore under these conditions the measured $|\Gamma|$ is expected to be lower than calculated. This is consistent with the observation that the edge n_e at 5.8 and 6.8 seconds is significantly lower in 29823 than in 29822, with a corresponding better agreement between TOPICA and experiment (the same argument applies to shot 29833). Because of the restrictions of the TOPICA model, extending the n_e profile closer to the antenna would require removing the limiter, thereby reducing the geometrical accuracy of the comparison. Nonetheless this hypothesis is to be tested in further work.

In shot 29833 the same procedure was followed as in 29822-29823 (δ_o increase and R_{sep} scans, as shown in figure 8.14) but with a central field of 2 T and with an operating frequency of 30 MHz. The data from all antennas follow the same general trend as before. The results of the comparison are shown in Figs. 8.23, 8.24 and 8.25. $\Delta|\Gamma|/|\Gamma|$ is in the same range as in previous shots. The agreement is again very good for antenna 3; however a large decrease in loading is seen on antennas 1 and 2 roughly from 3.3 to 4.5 s, which diverges significantly from the code results (in fact this behavior is also seen on antenna 3, as figure 8.25 shows,

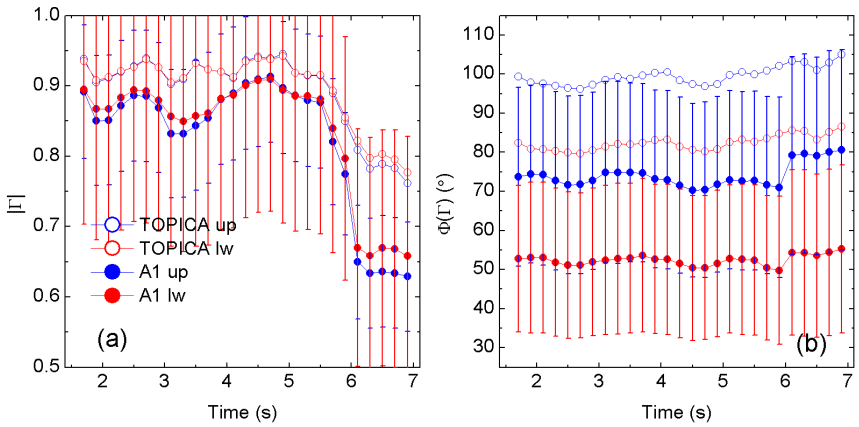


Figure 8.23: Magnitude (a) and phase (b) of Γ*, shot 29833, antenna 1. Agreement is similar to that observed in shots 29822 and 29823.*

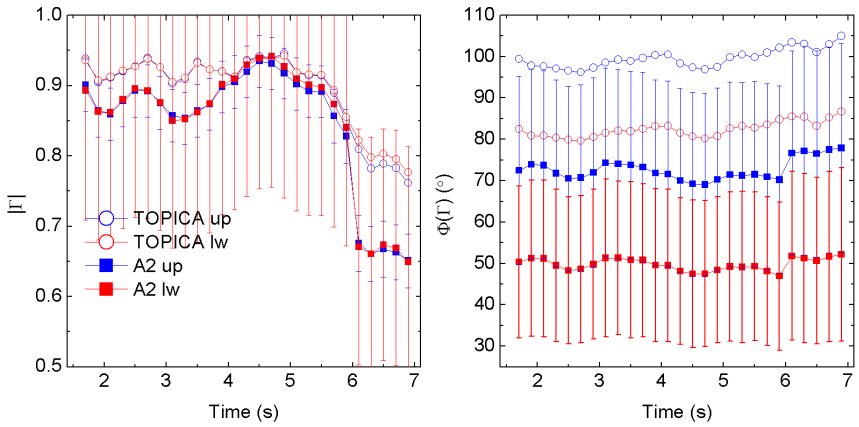


Figure 8.24: Magnitude (a) and phase (b) of Γ*, shot 29833, antenna 2. Agreement is similar to that observed in shots 29822 and 29823.*

but it is less drastic and so the errors on $|\Gamma|$ are still very small).

We remark again at this point that the significant coupling improvement towards the end of shots 29822, 29823 and 29833 is strongly correlated with the neutral flux density measured by an ionization gauge located in the main chamber midplane (see Chapter 7 for details).

Finally, the results for shot 29990 are shown in Figs. 8.26 and 8.27. Once again the code reproduces very well the overall trend in loading, although the variation is not as high as in other shots.

Although the complex voltage reflection coefficient Γ is well suited for a de-

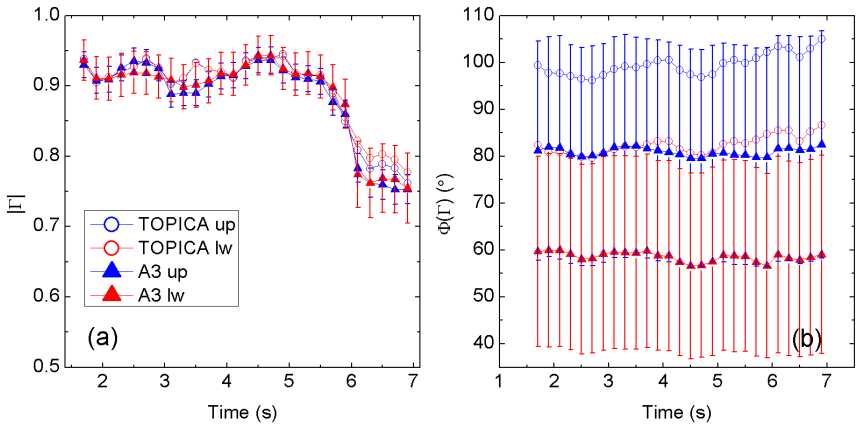


Figure 8.25: Magnitude (a) and phase (b) of Γ*, shot 29833, antenna 3. Agreement is similar to that observed in shots 29822 and 29823.*

tailed antenna study, in the sense that comparing a complex quantity can reveal more information than, e. g., loading resistance R_L which is a function of $|\Gamma|$, R_L is much more frequently used as a figure of merit for antenna coupling properties. The calculated loading for all shots (obtained from equation 8.11), as function of measured loading, is shown in Fig. 8.28. It is evident that the agreement with antenna 3 is very good, while a substantially higher (than predicted) loading is observed on antennas 1 and 2. Note that approximately the same R_L is measured on both, which would be expected because they are located next to each other and therefore must face the same plasma. It is also worth noting that, because of the usually very high VSWR on the feeding lines during normal operation, even moderate differences in $|\Gamma|$ mean rather large relative differences in R_L. This is seen from equations 8.11, using $\rho = |\Gamma|$:

$$\frac{\partial R_L}{\partial \rho} = -\frac{2Z_0}{(1+\rho)^2} \Rightarrow \frac{\Delta R_L}{R_L} = -\frac{2\Delta\rho}{1-\rho^2} \tag{8.13}$$

for small $\Delta\rho$ and ΔR_L. For example, in shot 29823, for antenna 1 the average $\Delta|\Gamma|/|\Gamma|$ values are found to be 5.7% and 5.4% on the upper and lower lines, respectively, which translate into relative errors in R_L of 30% and 31% respectively.

The differences between measurements and simulation results, for all shots, are summarized in Fig. 8.29. Each point is the average over the whole corresponding shot. $\Delta\Phi$ is given in centimeters as equivalent mechanical length. As stated at the end of the last section, regarding coupling the simulation results show excellent agreement with the experimental data from antenna 3, and good agreement with antennas 1 and 2. While the trend is correct, antennas 1 and 2 exhibit a substantially higher loading than computed by the code, almost by a factor of 2 at

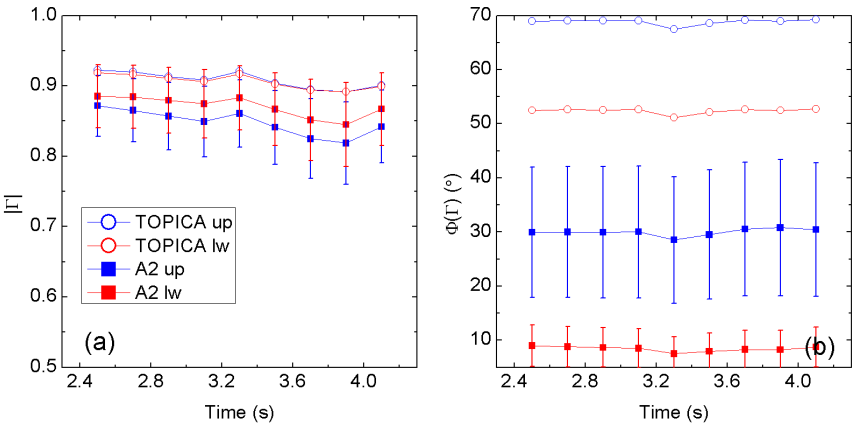


Figure 8.26: Magnitude (a) and phase (b) of Γ*, shot 29990, antenna 2.*

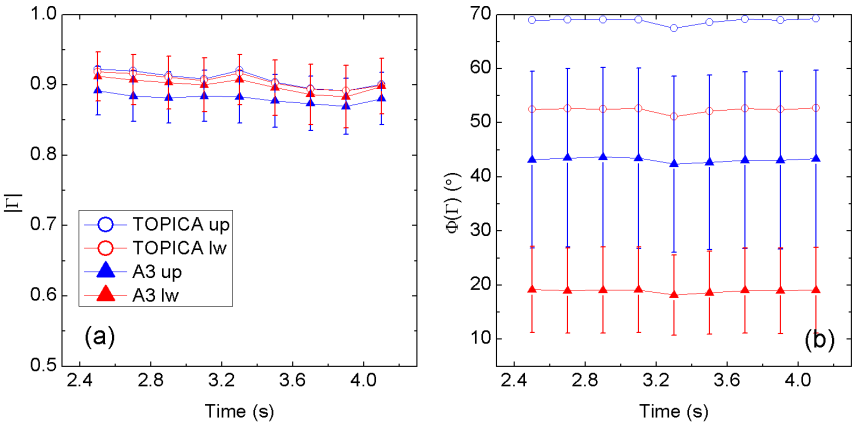


Figure 8.27: Magnitude (a) and phase (b) of Γ*, shot 29990, antenna 3.*

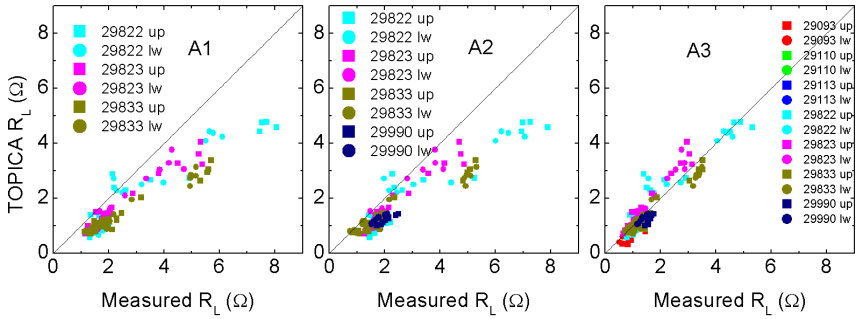


Figure 8.28: Results for all shots, antennas 1, 2 and 3. The agreement with antenna 3 is very good, while a substantially higher (than predicted) loading is observed on antennas 1 and 2. Because of the usually very high VSWR on the feeding lines during normal operation, even moderate differences in $|\Gamma|$ mean rather large relative differences in R_L.

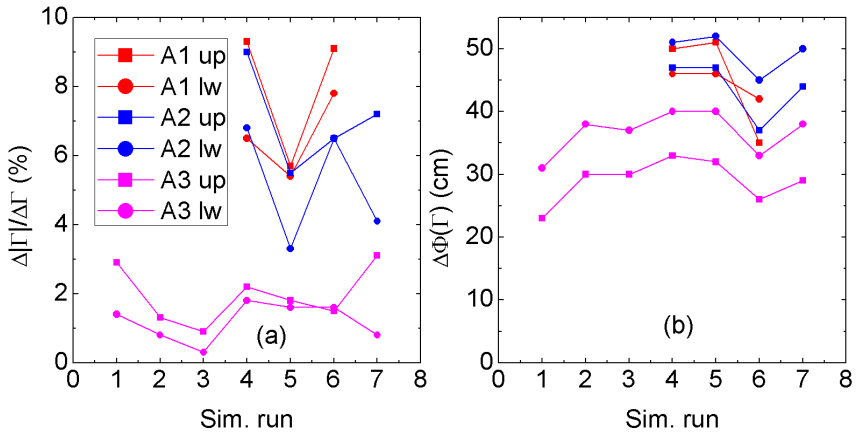


Figure 8.29: Overall differences between measurement and simulation results. $\Delta\Phi$ is given in centimeters as equivalent mechanical length; the horizontal axis indicates the shot number from 29093 (1) to 29990 (7).

high R_L. For all antennas, the disagreement becomes larger at high δ_o. Regarding phase, it can be seen that $\Delta\Phi$ varies only by a few centimeters from shot to shot, therefore making it likely that this discrepancy is caused by a systematic error in line length measurement.

The reason for the large differences in loading for the three antennas is still unknown; several hypotheses can be invoked as possible explanations, but a clear reason has not yet been found. First, the diagnostic Lithium beam that measures the edge n_e profile is located in sector 9, in close proximity to antenna 3 (sector 10) and far from antennas 1 and 2 (sectors 2 and 4 resp., essentially on the opposite side

of the torus); on the other hand there is no strong reason to believe that the plasma had any significant toroidal asymmetry. Magnetic perturbation coils were switched on from 1.15 until 4.10 seconds in shot 29990, encompassing almost the whole time window during which plasma profiles and RF data were measured; however, this would not explain the differences between the antennas seen in 29822, 29823 and 29833, as MP coils were on only from 1.7 to 2 seconds in shots 29822 and 29823, and from 1.7 to 3.6 s in 29833. In any case, a factor of ~ 2 is too high to be explained by MPs alone, since their effect on antenna behavior has also been studied on ASDEX Upgrade [71], [72] and less significant effects were reported.

Second, as stated in Chapter 5, at this point correction factors in the phase difference between voltage and current signals still have to be introduced to match the total coupled power to that measured by directional couplers; therefore the measurements depend directly on another diagnostic system. With this in view, it can be argued that it might not be correct to impose the condition of equal loading resistance on the two radiating straps to obtain the correction factors. The effects of relaxing this constraint can be seen, for example, by requiring that the *coupled power* be equal instead. Strictly speaking, this would be expected if the loading resistances were equal *and* the feeding lines were also equal in length, but given the geometrical complexity of the transmission network the latter is unlikely to be exactly fulfilled; nonetheless it is a useful alternative to look at. With the correction factors thus obtained, one may recompute the measurement result, e. g., for antennas 1 and 2 in shot 29822. The result is shown in Fig. 8.30 (only $|\Gamma|$ is plotted). Comparing figure 8.30 with figures 8.15 and 8.16, one can see that there is a substantial difference in coupling between the two antennas, which would be unexpected since, as stated above, antennas 1 and 2 are located next to each other and should be facing the same plasma. There is also a significant difference between the two straps on antenna 1, indicating that the assumption of equal loading is probably more realistic. In any case, averaging the $|\Gamma|$ on both lines gives roughly the results shown in Figs. 8.15 and 8.16; therefore it is unlikely that the assumption of equal loading is the reason for the observed discrepancy[6].

A third reason for the higher loading observed on antennas 1 and 2 could be a systematic error in the radial position of the antenna, since the same radial position was used in TOPICA for all antennas. As an estimate of this error, we can use the expression

$$R_L \propto P_0 \exp(-1.1 k_{\|} L_c) \tag{8.14}$$

proposed in [59], with $k_{\|}$ being the peak of the antenna current spectrum (in the case of ASDEX Upgrade $\simeq 7.7\ \mathrm{m}^{-1}$) and L_c the distance from the plasma surface to the R-cutoff. An increase of R_L by a factor of 2 - roughly the difference in

[6]The real situation is likely somewhere between the two extremes; however, in order to make no assumptions it is required that the voltage/current probes be made completely independent of the standard RF diagnostics.

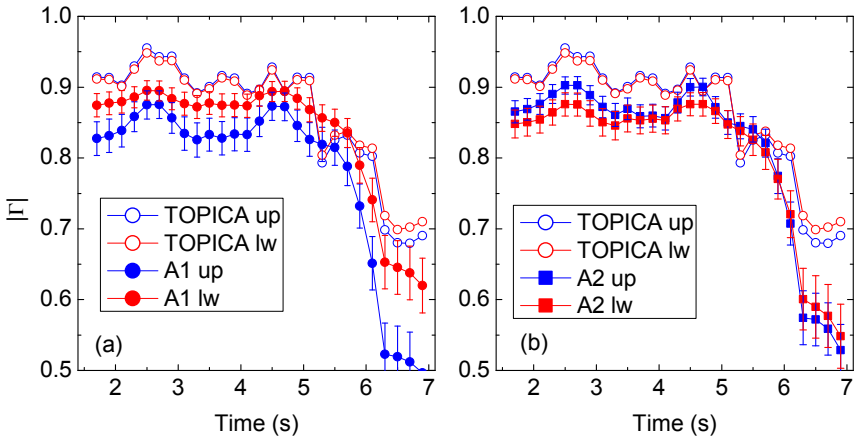


Figure 8.30: Magnitude of Γ*, antennas 1 (a) and 2 (b), shot 29822, using correction factors calculated with the constraint of equal coupled power on both lines. There are substantial differences in coupling between the two antennas, as well as between the two straps of antenna 1.*

loading between antennas 1 and 3 seen from Fig. 8.28 - would correspond to a radial shift of about 8 cm, a rather large difference. (Naturally such a large uncertainty in measurement would also cast doubt on the results of antenna 3.)

8.4 Conclusions

For the reasons outlined above, none of these hypotheses offers a clear explanation for the observed differences in the behavior of the antennas, and further analysis is needed. As the absolute comparison of TOPICA results with measured impedances depends crucially on the reliability of the RF diagnostics, subsequent work will be focused on finding the reason for the phase correction factors described in Chapter 5, with the aim of making the voltage/current probes fully independent from the standard diagnostics. Nonetheless, the use of the probes in this study - as well as making measurements much closer to the antenna, without the additional complexities of the transmission network - shows a significant improvement over the results of the first TOPICA comparison (where directional couplers and voltage probe arrays were used) and therefore places smaller error bars on the code results, which are given by $\Delta|\Gamma|$ and $\Delta\Phi(\Gamma)$ in Fig. 8.29.

Because the results of the comparisons presented in this chapter are not unambiguous, it is difficult to draw a definitive conclusion about the accuracy of TOPICA results. The difference in $|\Gamma|$, for instance, between the code predictions and the measurements does not exceed 10% on antennas 1 and 2 (which is consis-

tent with all the previous studies) while for antenna 3 it is always below 4%, and in most cases actually in the range of $1\% - 2\%$, which - given the level of detail involved in this study - is significantly better than previously found. On the basis of these results alone it is difficult to defend the proposition that the RF measurements on antenna 3 are closer to the truth than antennas 1 and 2. Nonetheless, as stated above, it is encouraging that the best results come from the antenna which is a) closest to the locations at which density measurements are taken, and b) the only one with - at this moment - a fully independent diagnostic set. Essentially, this study shows that for a meaningful antenna code test it is indispensable to have

1. accurate and detailed RF diagnostics *as close to the antenna as possible*, and
2. accurate and detailed density measurements, *again as close to the antenna as possible.*

This is especially relevant in view of the fact that the RF fields may modify the density profile in the immediate vicinity of a powered antenna. The availability of such direct density measurements, or lack thereof, puts a rather severe constraint on any code study. Unfortunately measurements of this kind were not available at the time of the present work.

It must also be kept in mind that, as stated above, small errors in $|\Gamma|$ may result in very large errors in R_L, and hence in coupled power, under conditions of near total reflection as is the case on the feeding lines of the ASDEX Upgrade antennas. It is seen in the results shown above that, in this case, differences of $5\% - 10\%$ in $|\Gamma|$ can translate into differences of $50\% - 100\%$ - or even higher - in coupled power.

9

Estimating ICRF power coupling from the plasma density profile

9.1 Introduction

The previous chapter showed the results of a detailed test of TOPICA simulation results versus experimental data measured on ASDEX Upgrade with a recently implemented diagnostic suite based on voltage and current probes. With respect to power coupling only, the main results are given in Fig. 8.28; that is, based on the analysis presented here, the difference between the predicted and measured loading resistance R_L. We are now interested in determining which conclusions, if any, can be drawn regarding the goal of coupling 20 MW per antenna to the ITER plasma, and the relationship of this goal to the plasma density profile, using the modeling tools we have available.

Several caveats must be kept in mind at this point. The first is that the results of the comparison as presented here are far from conclusive. Although possible reasons for the large difference in measured loading, between the three antennas, have been discussed at the end of Section 8.3, their verification requires a much more extensive analysis outside of the scope of this work. Because of this, it is difficult to estimate error bars for the TOPICA results. For the purposes of the present discussion, because we deal with coupled power only, we will consider that the error bars on R_L computed by TOPICA will be the average of the difference

$$\Delta R_L = |R_{TOPICA} - R_{measr.}| \tag{9.1}$$

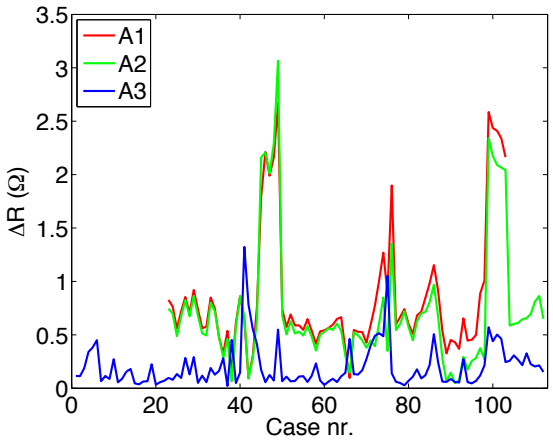


Figure 9.1: Absolute error of the R_L computed by TOPICA, according to Eq. (9.1). All simulated shots are shown. For each antenna the values are the average over the two straps.

	A1	A2	A3
ΔR_L (Ω)	0.61	0.52	0.18

Table 9.1: Absolute error of the results computed by TOPICA, averaged over all simulated shots excepting the abnormally high density cases.

over all the cases presented in Section 8.3, excluding those with abnormally high density at the antenna limiter (such as those shown in Fig. 8.22). These differences are illustrated in Fig. 9.1, where the values for each antenna are averages over both straps. The mean values are shown in Table 9.1. Because the reasons for the differences between the R_L measured on the three antennas are not fully clear, we will consider the ΔR_L thus estimated for antennas 1 and 3 to be the worst and best cases, respectively. However, it is evident from Fig. 8.28 that in the case of A1 and A2 there is a large systematic component to the difference, while with A3 it is mostly random. Since we later use ΔR_L as if it were the standard deviation of a distribution, to compute the resulting uncertainty for ITER results, this distinction must be kept in mind.

The second caveat is that the RF measurements presented here are themselves not unambiguous, given the correction factors introduced as described in Section 5.4. To make this diagnostic system fully independent, the reason for these corrections must be found and accounted for in the signal processing.

The third caveat is that, as stated before, the main quantity of interest is not R_L but the scattering matrix $\mathbf{S}$, because power distribution depends strongly on the geometry of the transmission network, especially for multiport launchers such

as the ITER antenna (note that the **S**-matrix by definition implies a self-consistent calculation of the currents on the launcher). We are nonetheless, at least in the case of ASDEX Upgrade studied here, forced to work with R_L because the available information on the transmission network is not accurate enough (see discussion in Sections 3.2 and 4.7).

Because of these factors, any conclusions reached here will have a necessarily reduced validity and should be interpreted with due caution.

The influence of the projected density profile on ICRF power coupling on ITER has already been studied extensively using TOPICA [51] and the fast code ANTITER II [22]. In particular, in [22] the density profile is assumed to have an approximate analytical description, namely constant core density and a double exponential approximating the edge and SOL (the approximation itself being based on the "Sc2 short 17" profile provided by the ITER organization). The detailed parametric study therein identifies three features having the crucial effect on coupling: the distance from the antenna to the cutoff density n_{CO}, the distance between n_{CO} and an "optimum density" n_{MAX}, and the density gradient (more precisely, decay length) between n_{MAX} and the constant core density; n_{MAX} is defined as the height of a flat density profile, separated from the antenna by a vacuum layer, at which coupling is maximized. Note also that in this study, as well as in [51], the figure of merit is the mean conductance of the triplet feeding lines, defined by

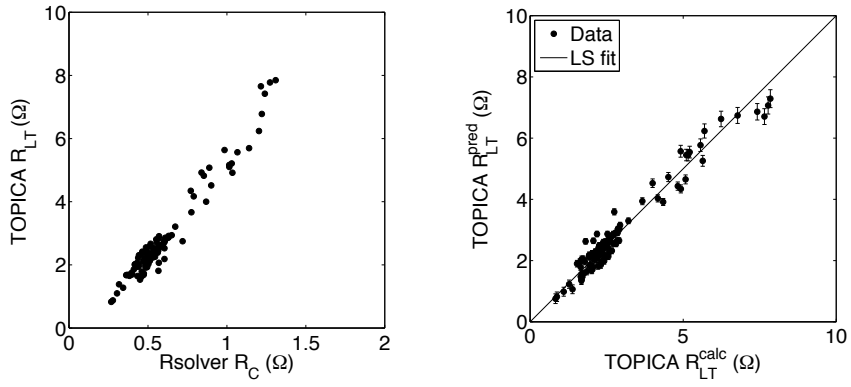
$$G_{\mathrm{min3}} = \frac{2(P_{\mathrm{TOT}}/8)}{|V_{\mathrm{max}}|^2} \tag{9.2}$$

where P_{TOT} is the total coupled power and $|V_{\mathrm{max}}|$ is the voltage stand-off on the line feeding the triplet [22].

Because the IDA profiles available on ASDEX Upgrade are themselves the result of a complex fitting procedure, an analytical characterization is neither suitable nor desirable in our case. Instead we adopt a statistical approach by building a database, consisting of a large number of IDA density profiles measured on ASDEX Upgrade, and the corresponding antenna resistance computed by code for each profile. The aim is then to see whether it is possible to derive an empirical formula for antenna resistance - and hence coupled power - in terms of a few suitable parameters of the density profile.

9.2 Estimation of coupled power from fast code results

As stated above, the coupled power would be ideally computed by a code with a self-consistent current description, in our case TOPICA. However the computational costs preclude the use of TOPICA for such a statistical analysis; hence



(a) R_{LT} computed by TOPICA versus R_C computed by Rsolver, all available cases.

(b) R_{LT} estimated from R_C versus R_{LT} computed by TOPICA.

Figure 9.2: Relationship between TOPICA and Rsolver results, ASDEX Upgrade antenna.

we are forced to rely on fast codes. The problem now is that the fast codes available for this study - Rsolver and FELICE in the forced EMF mode - cannot by themselves predict coupled power. We recall from Sections 3.2 and 6.2.3 that the quantity actually computed by the codes is the *coupling resistance* R_C, defined by

$$R_C = \frac{2P_{cpl}}{|I_S|^2}, \tag{9.3}$$

with I_S being the current at the strap short. It cannot be computed given V_{max} on the feeding line, because to do so would require knowing the complex reflection coefficient at the strap input, which can only be found via self-consistent current distribution; I_S is an imposed parameter which is canceled out when calculating R_C (see Section 6.2.3 for details). Therefore within this model it is not possible a find a relation between R_C and R_L, since it depends strongly on antenna geometry, and hence not possible to predict coupled power from R_C alone.

However, we may estimate the relationship of R_C to R_L for a given antenna by comparing a number of fast code results with the corresponding TOPICA output. Such a comparison is possible for the ASDEX Upgrade antenna due to the large number of TOPICA results already available and discussed in Chapter 8. This is shown in Fig. 9.2a, which displays the total loading resistance R_{LT} (the sum of the loading resistances of both straps) calculated by TOPICA in all available cases, versus R_C calculated by Rsolver using the same input profiles and the "AUG-like" antenna model described in Section 6.3. From these data it is possible to derive an empirical formula to predict R_{LT} from the fast code results; fitting a simple linear model to the data by the standard least squares method results in

$$R_{LT}^{pred} = A + BR_C, \tag{9.4}$$

with $A = -0.92 \pm 0.08$ and $B = 6.3 \pm 0.1$. A plot of R_{LT}^{pred} versus R_{LT} is shown in Fig. 9.2b[1]. Note that error bars, corresponding to a $\pm 3\sigma$ confidence interval, are also shown on the plot, here and in all subsequent figures.

This automatically gives the expression

$$P_{cpl}^{pred} = \frac{(A + BR_C)\overline{V_{max}^2}}{2Z_0^2}, \tag{9.5}$$

which can be interpreted as an estimate of the maximum power coupled by the ASDEX Upgrade antenna, with $\overline{V_{max}^2}$ being the average voltage stand-off on the two feeding lines, *as calculated by TOPICA*; it is *not*, by itself, an estimate of actual coupled power measured in an experiment. Another limitation inherent in this analysis is that relatively few data points are available at higher coupling. Note also that we have used only Rsolver results in the database, but the same analysis can be done using FELICE, since it was already shown in Chapter 6 that there is a linear relationship between the results of the two codes[2].

9.3 Dependence of R_C on the density profile

Having obtained an approximate expression for maximum coupled power in terms of the coupling resistance R_C calculated by a fast code, we would like to know if a similar approximate expression can be obtained for R_C in terms of some parameters describing the density profile. Note that the analysis below is restricted to empirical features of the density profile, together with parameters related to fast wave propagation (such as toroidal magnetic field and antenna frequency). An empirical study of antenna resistance in terms of *global* plasma parameters - plasma current, heating power, etc. - in this particular case using Tore Supra data, can be found in [73]. On the other hand, studying the influence of the global parameters on the shape of the density profile itself is outside the scope of this work. Furthermore, here we consider only ELM-synchronized profiles, and exclude all cases with $n_e \geq n_{co}$ everywhere. The database considered here consists of 718 density profiles, resulting from IDA reconstruction of density measurements during H-mode shots 29822, 29823 and 29833, and L-mode shot 29093. In this instance R_C is always calculated at 36.5 MHz, regardless of the actual operating frequency during each shot[3].

[1] Note that for the same antenna $R_L \simeq R_C |I_S|^2 / |I_{max}|^2$ if the ohmic losses are low, as seen from Eqs. (3.35) and (3.37), providing a justification for the linear model. Strictly speaking the constant term should be zero, but it is included here since R_C and R_L are computed by codes with different antenna and plasma models.

[2] However, this has been obtained with FELICE in forced EMF mode only; when available, the self-consistent current description should be used instead, presumably leading to more accurate results.

[3] A more correct way to proceed would be to derive approximate expressions for R_C at both frequencies. For brevity we work here with one frequency only; 36.5 MHz is much more commonly used during AUG operation than 30 MHz, hence the choice.

We select the following parameters, which are unrelated to any particular choice of analytical shape for the profile:

- edge density n_{edge}, giving a measure of pedestal height and arbitrarily defined here as the density at the radial position where $|\nabla^2 n_e| > 3 \times 10^{22}$ m^{-5} when going from the plasma core towards the edge;
- limiter density n_{lim}, i. e., density at the plasma surface[4];
- distance d_{co} to the cutoff density n_{co}, where $c^2 k_\parallel^2/\omega^2 = R$ with $k_\parallel = 7.7$ m^{-1};
- the density gradient ∇n_e at the cutoff position, ∇_{co};
- maximum of ∇n_e, ∇_{max}[5];
- minimum of ∇n_e, ∇_{min};
- an "effective" gradient

$$\nabla_{eff} = \frac{n_{edge} - n_{co}}{r_{edge} - r_{co}}. \tag{9.6}$$

- the distance d_{min} between n_{co} and ∇_{min}, in the region between n_{edge} and n_{co}.

When building the database, since densities are of order 10^{20}, all density and gradient values are divided by this scaling factor so that the order of magnitude is closer to that of d_{co} (which is given in meters).

Fig. 9.3 shows a few typical L- and H-mode density profiles, along with some of the parameters defined above. d_{min} was included as a way of characterizing the density "bump" in the SOL of the H-mode, more visible in the H-mode profiles; for almost all L-mode profiles, $d_{min} = 0$.

To get a feeling for the relative relevance of each one of these parameters, we first fit a linear scaling of the form

$$R_C^{pred} = \overrightarrow{\mathrm{A}}\,\overrightarrow{\mathrm{X}}^{\mathrm{T}}, \tag{9.7}$$

with $\overrightarrow{\mathrm{A}} = [a_0 \ \ldots \ a_8]$ and

$$\overrightarrow{\mathrm{X}} = [1 \ \nabla_{eff} \ \nabla_{max} \ \nabla_{min} \ d_{co} \ \nabla_{co} \ d_{min} \ n_{edge} \ n_{lim}]\,; \tag{9.8}$$

the results of the fit are summarized in Table 9.2 and the fit is illustrated in Fig 9.4a.

[4]We recall from Chapter 6 that the plasma surface is defined at $r = r_{min}$, at the interface between the plasma slab and the antenna 'cavity' in vacuum.

[5]These gradients are taken in the pedestal.

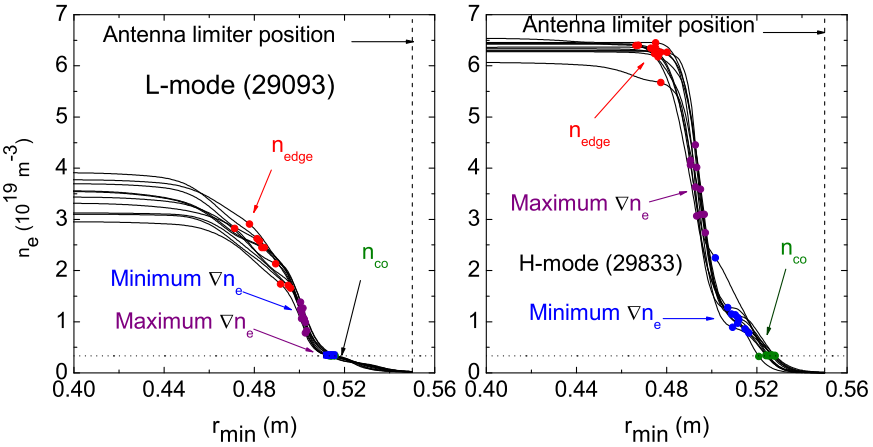


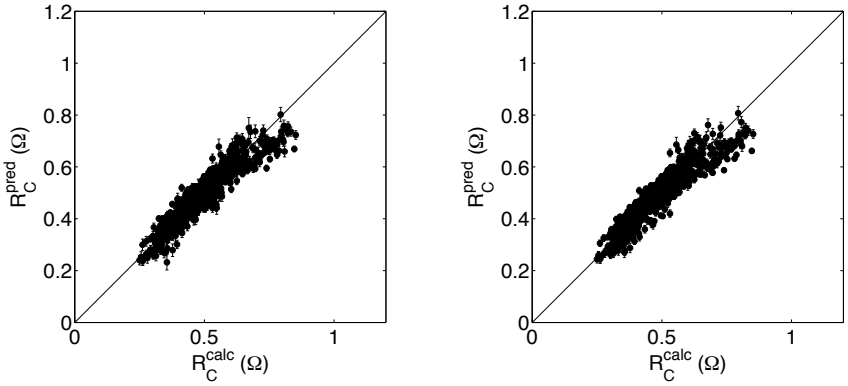
Figure 9.3: Typical electron density profiles at ASDEX Upgrade and some associated parameters. On the L-mode profiles, the minimum ∇n_e point coincides with the cutoff position.

	μ	σ	t	p-value
a_0 (1)	0.81	0.01	56.083	2.4608×10^{-261}
a_1 (∇_{eff})	-0.028	0.002	-17.2	1.3951×10^{-55}
a_2 (∇_{max})	-0.0018	0.0003	-6.6764	4.9836×10^{-11}
a_3 (∇_{min})	0.008	0.002	4.2921	2.019×10^{-5}
a_4 (d_{co})	-4.7	0.1	-35.077	2.006×10^{-156}
a_5 (∇_{co})	0.000	0.001	-0.15256	0.87879
a_6 (d_{min})	2.6	0.2	11.706	4.8819×10^{-29}
a_7 (n_{edge})	0.134	0.002	5.9947	3.2615×10^{-9}
a_8 (n_{lim})	0.28	0.04	7.3412	5.8858×10^{-13}

Table 9.2: Results of fitting Eq. (9.7) with the parameters in (9.8) to the database; for each parameter, μ is the estimated value, σ is the standard deviation and t denotes the t-statistic. The parameter corresponding to each coefficient is indicated in parenthesis.

	μ	σ	t	p-value
$a_0\ (1)$	0.85	0.01	62.913	3.3115×10^{-291}
$a_1\ (\nabla_{eff})$	-0.022	0.001	-16.135	4.5696×10^{-50}
$a_2\ (\nabla_{max})$	-0.0021	0.003	-7.5738	1.1417×10^{-13}
$a_3\ (d_{co})$	-4.8	0.13	-36.183	8.8833×10^{-163}
$a_4\ (d_{min})$	2.9	0.2	14.241	1.2573×10^{-40}
$a_5\ (n_{lim})$	0.38	0.03	10.842	1.9551×10^{-25}

Table 9.3: Results of fitting Eq. (9.7) with the parameters in (9.9) to the database; for each parameter, μ is the estimated value, σ is the standard deviation and t denotes the t-statistic. The parameter corresponding to each coefficient is indicated in parenthesis.



(a) With all parameters (Eq. (9.8)).

(b) With ∇_{eff}, d_{co}, d_{min}, n_{edge} and n_{lim}.

Figure 9.4: R_C predicted with the linear model of Eq. (9.7) versus the calculated R_C.

	μ	σ	t	p-value
b_0 (1)	1.05	0.03	34.155	2.6×10^{-151}
b_1 (∇_{eff})	-0.061	0.003	-19.979	1.2×10^{-70}
b_2 (∇_{max})	-0.0036	0.0005	-7.4797	2.2×10^{-13}
b_3 (∇_{min})	0.016	0.003	4.7589	2.4×10^{-6}
b_4 (d_{co})	-11.5	0.3	-37.589	3.5×10^{-170}
b_5 (∇_{co})	-0.006	0.002	-2.6856	0.007
b_6 (d_{min})	4.7	0.4	13.182	1.3×10^{-35}
b_7 (n_{edge})	0.029	0.004	6.9146	1.1×10^{-11}
b_8 (n_{lim})	0.09	0.06	1.446	0.1

Table 9.4: Results of fitting Eq. (9.10) to the database; for each parameter, μ is the estimated value, σ is the standard deviation and t denotes the t-statistic. The parameter corresponding to each coefficient is indicated in parenthesis.

From the p-values in Table 9.2, it is seen that the most relevant parameters in this model are d_{co}, ∇_{eff}, d_{min} and the additive constant a_0. The normalized root mean square error (NRMS) is 7.1%. Removing the three least relevant parameters - ∇_{min}, ∇_{co} and n_{edge} - from the fit, and leaving

$$\overrightarrow{\mathrm{X}} = [1 \; \nabla_{max} \; \nabla_{eff} \; d_{co} \; d_{min} \; n_{lim}] \,, \tag{9.9}$$

produces the results shown in Fig. 9.4b with $\mathrm{NRMS} = 7.4\%$; the statistical values are shown in Table 9.3.

Theoretically, we expect R_C to decay exponentially with d_{co}, so it is worth looking at an exponential model of the form

$$R_C^{pred} = b_0 \exp(b_1 \nabla_{eff} + b_2 \nabla_{max} + b_3 \nabla_{min} + b_4 d_{co} + b_5 \nabla_{co} \ldots + b_6 d_{min} + b_7 n_{edge} + b_8 n_{lim}). \tag{9.10}$$

Fitting the exponential model to the database results in the values given in Table 9.4, and the relationship between predicted and calculated R_C is given in Fig. 9.5a. The resulting NRMS is 6.5%, therefore better (but only slightly) than the linear model. Eliminating the three least significant parameter from the model results in

$$R_C^{pred} = b_0 \exp\left(b_1 \nabla_{eff} + b_2 \nabla_{max} + b_3 d_{co} + b_4 d_{min} + b_5 n_{edge}\right). \tag{9.11}$$

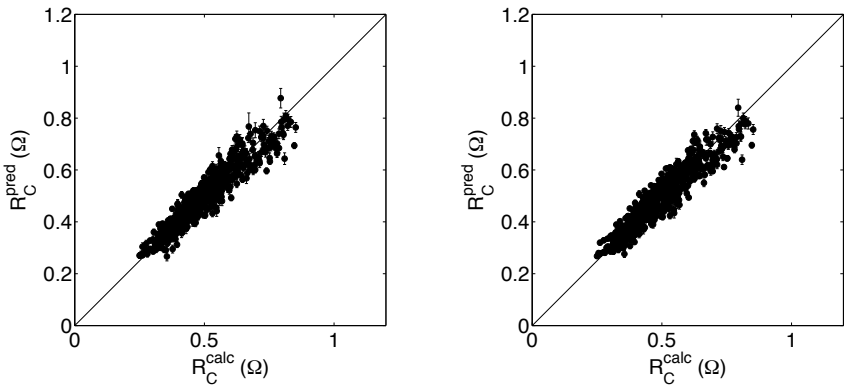
The results are summarized in Table 9.5 and Fig. 9.5b, with NRMS = 6.7%.

9.4 TOPICA simulations of the ITER antenna

Each one of the two ITER ICRF antennas is expected to couple 20 MW to the plasma in the frequency band $40 - 55$ MHz. The launcher is an array of 4 toroidal

	μ	σ	t	p-value
b_0 (1)	1.06	0.03	37.101	8.3×10^{-168}
b_1 (∇_{eff})	-0.064	0.003	-21.966	7.5×10^{-82}
b_2 (∇_{max})	-0.0040	0.0005	-8.0535	3.4×10^{-15}
b_3 (d_{co})	-11.5	0.2	-49.414	4.8×10^{-231}
b_4 (d_{min})	3.9	0.3	11.327	1.9×10^{-27}
b_5 (n_{edge})	0.0036	0.004	9.0623	1.2×10^{-18}

Table 9.5: Results of fitting Eq. (9.11) to the database; for each parameter, μ is the estimated value, σ is the standard deviation and t denotes the t-statistic. The parameter corresponding to each coefficient is indicated in parenthesis.



(a) Exponential model (Eq. (9.10)) with all parameters.

(b) Exponential model (Eq. (9.10)) with ∇_{eff}, ∇_{max}, d_{co}, d_{min} and n_{edge}.

Figure 9.5: R_C predicted with the exponential model versus the calculated R_C.

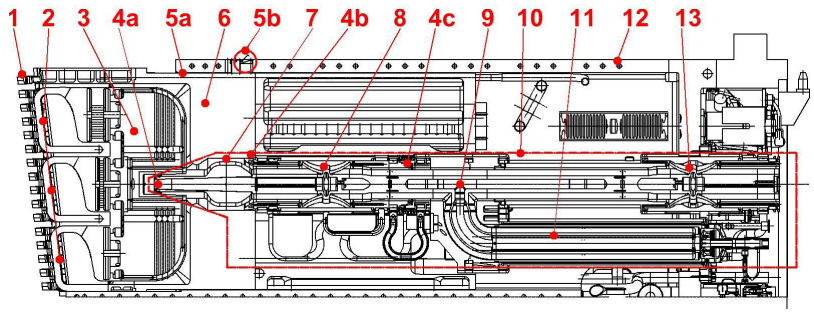


Figure 9.6: Section through one of the eight triplets of straps and feeding vacuum transmission line, showing some relevant components. (1) Faraday screen, (2) RF current straps, (3) four-port junction, (10) removable vacuum transmission line (RVTL), (11) service stub, (13) rear vacuum window (VCW). Figure reproduced from [4].

by 6 poloidal current straps [4], grouped into eight strap triplets. Each triplet is fed by a passive four-port junction (4PJ) with a characteristic impedance of 15 Ω, then connected to a 20 Ω feeding line, into which a 15 Ω service stub (SS) is inserted in parallel, at a distance $\sim \lambda_{mid-band}/4$ from the 4PJ [51]. The main components of one of the eight triplets are illustrated in Fig. 9.6, and the launcher is described in detail in [51], [21] and [4].

From the point of view of the antenna structure, the launcher is subject to the following constraints, specified by the ITER Organization and the CYCLE Consortium [4]:

- E-field less than 2 kV/mm parallel to the magnetic field in the torus vacuum areas and magnitude less than 3 kV/mm everywhere and voltages less than 45 kV;

- currents less than 2 kA through RF contacts, with the highest current density (5 kA/m) between RVTL and 4PJ inner conductors.

Extensive studies indicate [4] that constraints imposed on different parts of the antenna structure - including the transmission lines, stubs, etc. - become dominant at different points throughout the ITER frequency domain. This means that it is not possible to compute a single representative quantity and use it for the whole domain to estimate coupled power given a single constraint; for example at a given frequency the voltage stand-off V_{max} on a line feeding a triplet, in Eq. (9.2), may be below the maximum allowed value, but the electric field elsewhere may exceed the allowed range. This is illustrated in Fig. 9.7. Each colored line in the top image represents the maximum coupled power given a single constraint, as function of frequency, with $(0, \pi, 0, \pi)$ toroidal and $(0, -\pi/2)$ poloidal phasing, resulting from the "Low density SOL" case provided by IO. In order to obey all constraints,

coupled power must stay below the minimum of all the curves. Note that this minimum is given by different curves on different portions of the frequency domain.

For this reason, in addition to the need to run separate TOPICA simulations for multiple frequency points, a full analysis of the ITER antenna over the whole frequency domain lies outside the scope of this work; we restrict the analysis to a single frequency point, namely midband - 47.5 MHz - where the relevant constraints are the voltages on the 4PJ, movable transmission line (MTL) behind the rear VCW and the line between the 4PJ and the SS insertion point, all approximately equal to 45 kV. At this point therefore - *and this point only* - we can use the $G_{\min 3}$ defined by Eq. (9.2) as a figure of merit for power coupling capacity. For the same reason we use one toroidal phasing only - $(0, \pi, 0, \pi)$ - and one plasma composition only, namely 50% D - 50% T.

The ITER antenna used as TOPICA input is shown from the front and back in Fig. 9.8. The Faraday screen rods have been removed from the front, to display the 6×4 radiating strap array. Comparing with Fig. 9.6, it can be seen that only the antenna "front face" is included in the model. TOPICA therefore calculates the 24×24 **S**-matrix corresponding to the 6×4 feeder array. The 4×4 **S**-matrix of the 4PJ is produced separately by a CST-MWS simulation [4] and then integrated with the TOPICA matrix (see below), yielding an 8×8 scattering matrix characterizing the system of eight triplets fed by eight transmission lines.

Furthermore, we select twelve plasma density profiles for the simulations. Two of these are simply the "High density SOL" and "Low density SOL" cases provided by IO. Because no other ITER profiles exist, we use ten ASDEX Upgrade profiles, artificially scaled to put them into the ITER-relevant range. The profiles were selected from those used for the second TOPICA study - see Chapter 8 - in particular, from shot 29823, corresponding to the time windows $1.6 - 1.8$, $1.8-2.0$, $2.2-2.4$, $2.6-2.8$, $3.0-3.2$, $3.4-3.6$, $3.8-4.0$, $4.2-4.4$, $4.6-4.8$ and $5.0-5.2$ seconds, thus avoiding the atypical cases towards the end of the discharge with very high edge density.

As stated above, some operations must be performed on the 24×24 **S**-matrix $\mathbf{S}_{ant}$ of the antenna front face calculated by TOPICA to produce meaningful results. These operations are 1) translating the $\mathbf{S}_{ant}$ reference plane to take into account the different lengths of the transmission lines joining the strap array to the 4PJ; 2) integrating the resulting matrix with the 4PJ matrix $\mathbf{S}_{4PJ}$; 3) including the effect of a series inductance from the RF contact between the 4PJ and the VTL; 4) translating the results through a length of VTL and adding the parallel service stub. From these results, $G_{\min 3}$ and maximum coupled power can be computed. These steps are described below.

The TOPICA matrices as produced by the code have their straps numbered as

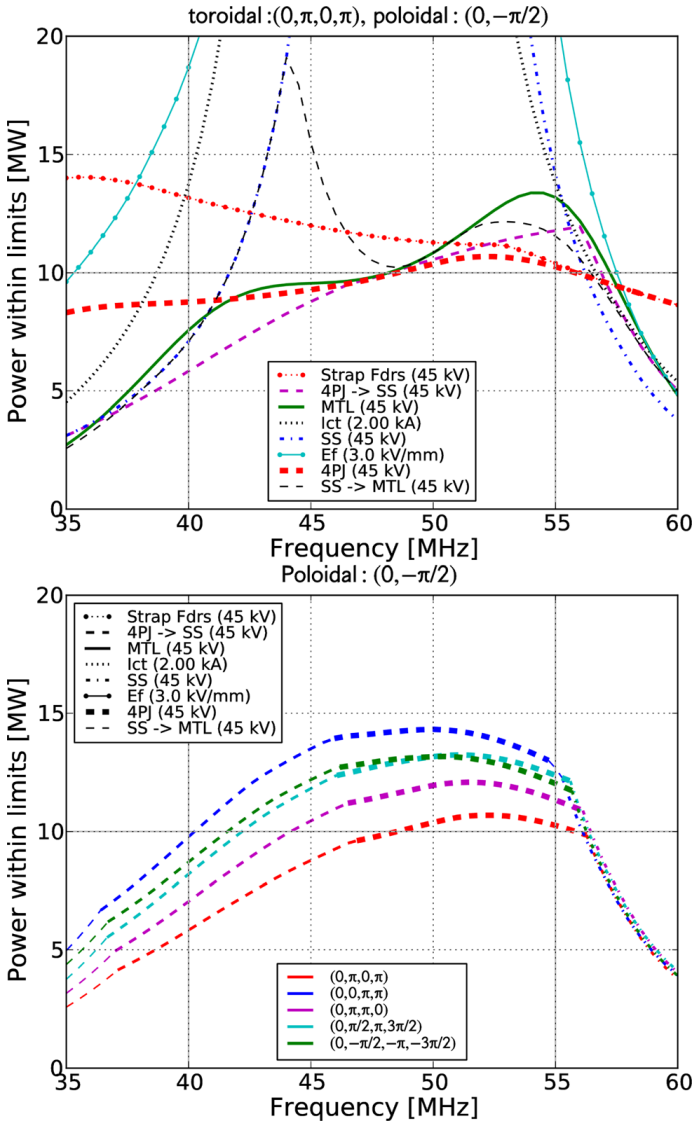
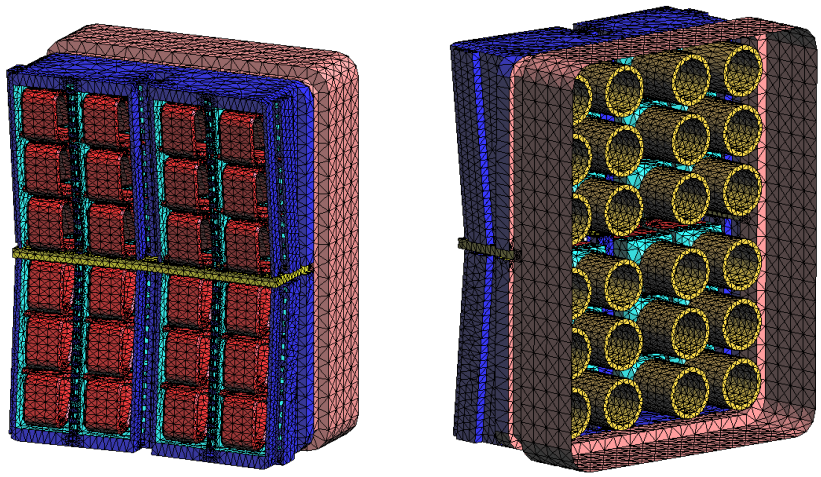


Figure 9.7: Coupled power per ITER launcher, given maximum values for voltage and/or electric field in different parts of the structure. In order to fulfill all requirements, the coupled power must stay below the minimum of all curves throughout the frequency range. The density profile used here is the "Low density SOL" case provided by IO. Figure reproduced from [4].



(a) Front, showing the 6×4 strap array grouped into eight triplets. Faraday screen bars removed for clarity.

(b) Back, showing the strap feeders.

Figure 9.8: The ITER ICRF antenna model used in TOPICA.

follows, when viewed from the back, i. e., looking towards the plasma:

$$\begin{bmatrix} 4 & 3 & 2 & 1 \\ 8 & 7 & 6 & 5 \\ 12 & 11 & 10 & 9 \\ 16 & 15 & 14 & 13 \\ 20 & 19 & 18 & 17 \\ 24 & 23 & 22 & 21 \end{bmatrix}. \tag{9.12}$$

In order to be consistent with the labeling convention used below for the integration of the 4PJ matrices (this is the convention used in [51] and [4]) they have been re-labeled[6] in the following way:

$$\begin{bmatrix} 1 & 7 & 13 & 19 \\ 2 & 8 & 14 & 20 \\ 3 & 9 & 15 & 21 \\ 4 & 10 & 16 & 22 \\ 5 & 11 & 17 & 23 \\ 6 & 12 & 18 & 24 \end{bmatrix} \tag{9.13}$$

The scattering matrix $\mathbf{S}$ is computed by TOPICA with a reference impedance $Z_{ref} = 12.63\ \Omega$ at 47.5 MHz and $(0, \pi, 0, \pi)$ phasing, as stated in the TOPICA input files. In all cases, outward radiations conditions were imposed at 50 cm from

[6] Script kindly provided by Daniele Milanesio.

the aperture. Note that the array shown above does *not* have the correct dimensions of the TOPICA scattering matrix and is only given for visual reference.

To de-embed the scattering matrix it must be first shifted by a distance $d_1 = 418.8$ mm towards the plasma, and then - also towards the plasma - by the individual distances given in mm by

$$d_2 = \begin{bmatrix} 100 & 82 & 82 & 100 \\ 62 & 44 & 44 & 62 \\ 25 & 7 & 7 & 25 \\ 18 & 0 & 0 & 18 \\ 45 & 27 & 27 & 45 \\ 71 & 53 & 53 & 71 \end{bmatrix}, \tag{9.14}$$

according to the labeling convention shown in (9.13) (we again note that array d_2 does not have the dimensions of the scattering matrix and is only shown for visual reference).

As described in Ch. 3, the matrix **S** is translated by

$$\mathbf{S'} = \mathbf{DSD}$$

$$= \begin{bmatrix} e^{j\beta l_1} & 0 & \cdots & 0 \\ 0 & e^{j\beta l_2} & \cdots & 0 \\ \vdots & \vdots & \ddots & \vdots \\ 0 & 0 & \cdots & e^{j\beta l_{24}} \end{bmatrix} \begin{bmatrix} S_{1,1} & S_{1,2} & \cdots & S_{1,24} \\ S_{2,1} & S_{2,2} & \cdots & S_{2,24} \\ \vdots & \vdots & \ddots & \vdots \\ S_{24,1} & S_{24,2} & \cdots & S_{24,24} \end{bmatrix} \cdots$$

$$\times \begin{bmatrix} e^{j\beta l_1} & 0 & \cdots & 0 \\ 0 & e^{j\beta l_2} & \cdots & 0 \\ \vdots & \vdots & \ddots & \vdots \\ 0 & 0 & \cdots & e^{j\beta l_{24}} \end{bmatrix} \tag{9.15}$$

where the lengths l_i are positive when going towards the plasma and negative when going towards the generator. We assume that all lengths are on transmission lines with the same $Z_{ref} = 12.63\ \Omega$ as the matrix. Here $\beta = 2\pi f/c$, with $c =$ speed of light in vacuum.

Finally, one has to account for small differences in feeder length connecting the 4PJ to the strap array; therefore the matrix is shifted again, this time towards the generator, by the distances (in mm)

$$d_3 = \begin{bmatrix} 75.7 & 75.7 & 75.7 & 75.7 \\ 37.8 & 37.8 & 37.8 & 37.8 \\ 0 & 0 & 0 & 0 \\ 0 & 0 & 0 & 0 \\ 26.7 & 26.7 & 26.7 & 26.7 \\ 53.5 & 53.5 & 53.5 & 53.5 \end{bmatrix}, \tag{9.16}$$

the array having the same labeling convention as d_2. We assume again translation along 12.63 Ω lines.

The matrix resulting after these translations (we refer to it as $\mathbf{S}'$) has to be renormalized to $Z_{ref} = 20\ \Omega$ before integrating the 4PJ matrices. The new scattering matrix will be given by

$$\mathbf{S}_{20} = \left[\mathbf{S}'\mathbf{N} + \mathbf{P}\right]^{-1}\left[\mathbf{S}'\mathbf{P} + \mathbf{N}\right], \tag{9.17}$$

with

$$\mathbf{P} = \frac{1}{2}\left(\frac{12.6\ \Omega}{20.0\ \Omega} + 1\right)\mathbf{1}, \quad \mathbf{N} = \frac{1}{2}\left(\frac{12.6\ \Omega}{20.0\ \Omega} - 1\right)\mathbf{1}. \tag{9.18}$$

Here and in what follows, $\mathbf{1}$ denotes a unitary matrix of the necessary dimensions (24×24 in this case).

Now we incorporate the 4PJ matrices, from which some feeder lengths must first be removed. We re-normalize the 4PJ matrix from $20\ \Omega$ to $12.6\ \Omega$, so

$$\mathbf{S_{4PJ}} = \left[\mathbf{S_{4PJ}}\mathbf{N} + \mathbf{P}\right]^{-1}\left[\mathbf{S_{4PJ}}\mathbf{P} + \mathbf{N}\right], \tag{9.19}$$

with

$$\mathbf{P} = \frac{1}{2}\left(\frac{20.0\ \Omega}{12.6\ \Omega} + 1\right)\mathbf{1}, \quad \mathbf{N} = \frac{1}{2}\left(\frac{20.0\ \Omega}{12.6\ \Omega} - 1\right)\mathbf{1}. \tag{9.20}$$

.

The translation lengths are given by

$$L = [0\ 26.7\ 53.5\ 0]\ \text{mm}. \tag{9.21}$$

The 4PJ matrix is translated:

$$\begin{aligned}\mathbf{S_{4PJ}} &= \mathbf{L}\mathbf{S_{4PJ}}\mathbf{L} \\ &= \begin{bmatrix} 1 & 0 & 0 & 0 \\ 0 & e^{j\beta L_2} & 0 & 0 \\ 0 & 0 & e^{j\beta L_3} & 0 \\ 0 & 0 & 0 & 1 \end{bmatrix} \begin{bmatrix} S_{11} & S_{12} & S_{13} & S_{14} \\ S_{21} & S_{22} & S_{23} & S_{24} \\ S_{31} & S_{32} & S_{33} & S_{34} \\ S_{41} & S_{42} & S_{43} & S_{44} \end{bmatrix} \cdots \\ &\quad \times \begin{bmatrix} 1 & 0 & 0 & 0 \\ 0 & e^{j\beta L_2} & 0 & 0 \\ 0 & 0 & e^{j\beta L_3} & 0 \\ 0 & 0 & 0 & 1 \end{bmatrix}.\end{aligned} \tag{9.22}$$

After this the 4PJ matrix is renormalized back to $20\ \Omega$, by

$$\mathbf{S_{4PJ}} = \left[\mathbf{S_{4PJ}}\mathbf{N} + \mathbf{P}\right]^{-1}\left[\mathbf{S_{4PJ}}\mathbf{P} + \mathbf{N}\right], \tag{9.23}$$

with

$$\mathbf{P} = \frac{1}{2}\left(\frac{12.6\ \Omega}{20.0\ \Omega} + 1\right)\mathbf{1}, \quad \mathbf{N} = \frac{1}{2}\left(\frac{12.6\ \Omega}{20.0\ \Omega} - 1\right)\mathbf{1}. \tag{9.24}$$

The matrix given here actually corresponds to a 4PJ below mid-plane, so for the strap triplets above the mid-plane the indices 1 and 3 in the 4PJ S-matrix are swapped; the resulting matrix is referred to as $\mathbf{S^F_{4PJ}}$. This is,

$$\mathbf{S_{4PJ}} = \begin{bmatrix} S_{11} & S_{12} & S_{13} & S_{14} \\ S_{21} & S_{22} & S_{23} & S_{24} \\ S_{31} & S_{32} & S_{33} & S_{34} \\ S_{41} & S_{42} & S_{43} & S_{44} \end{bmatrix}, \quad \mathbf{S^F_{4PJ}} = \begin{bmatrix} S_{33} & S_{32} & S_{31} & S_{34} \\ S_{23} & S_{22} & S_{21} & S_{24} \\ S_{13} & S_{12} & S_{11} & S_{14} \\ S_{43} & S_{42} & S_{41} & S_{44} \end{bmatrix}. \tag{9.25}$$

The connection and port labeling for the integration of the matrices is shown in Fig. 9.9; we follow the procedure in [74]. The incoming (voltage) wave on port i is labeled a_i and the scattered wave is labeled b_i, with

$$\begin{aligned} a_j &= \frac{1}{2}\left(V_j + Z_0 I_j\right) \equiv V_j^+, \\ b_j &= \frac{1}{2}\left(V_j - Z_0 I_j\right) \equiv V_j^-, \end{aligned} \tag{9.26}$$

where V_j and I_j are the total voltages and currents at port j fed by a transmission line with characteristic impedance Z_0 (see Eqs. (3.19)). Then the scattering matrix can be written as

$$\overrightarrow{b} = \mathbf{S}\overrightarrow{a}. \tag{9.27}$$

We define the 56×56 block-diagonal matrix $\mathbf{S_B}$ as

$$\begin{aligned} \overrightarrow{b} &= \mathbf{S_B}\overrightarrow{a}, \\ \overrightarrow{b} &= [b_1\ b_2\ \cdots\ b_{56}]^{\mathrm{T}}, \\ \overrightarrow{a} &= [a_1\ a_2\ \cdots\ a_{56}]^{\mathrm{T}}, \\ \mathbf{S_B} &= \begin{bmatrix} \mathbf{S_{20}} & \mathbf{0} & \mathbf{0} & \cdots & \mathbf{0} \\ \mathbf{0} & \mathbf{S^F_{4PJ}} & \mathbf{0} & \cdots & \mathbf{0} \\ \mathbf{0} & \mathbf{0} & \mathbf{S_{4PJ}} & \cdots & \mathbf{0} \\ \vdots & \vdots & \vdots & \ddots & \vdots \\ \mathbf{0} & \mathbf{0} & \mathbf{0} & \cdots & \mathbf{S_{4PJ}} \end{bmatrix}. \end{aligned} \tag{9.28}$$

Following the paper, we define the permutation matrix $\mathbf{P}$ such that

$$\overrightarrow{a} = \mathbf{P}\begin{bmatrix} \overrightarrow{a}_{cop} \\ \overrightarrow{a}_{inc} \end{bmatrix}. \tag{9.29}$$

Here $\overrightarrow{a}_{inc}$ contains all the waves incident on the ports not connected to any other part of the system, in other words

$$\overrightarrow{a}_{inc} = [a_{28}\ a_{32}\ a_{36}\ a_{40}\ a_{44}\ a_{48}\ a_{52}\ a_{56}]^{\mathrm{T}}. \tag{9.30}$$

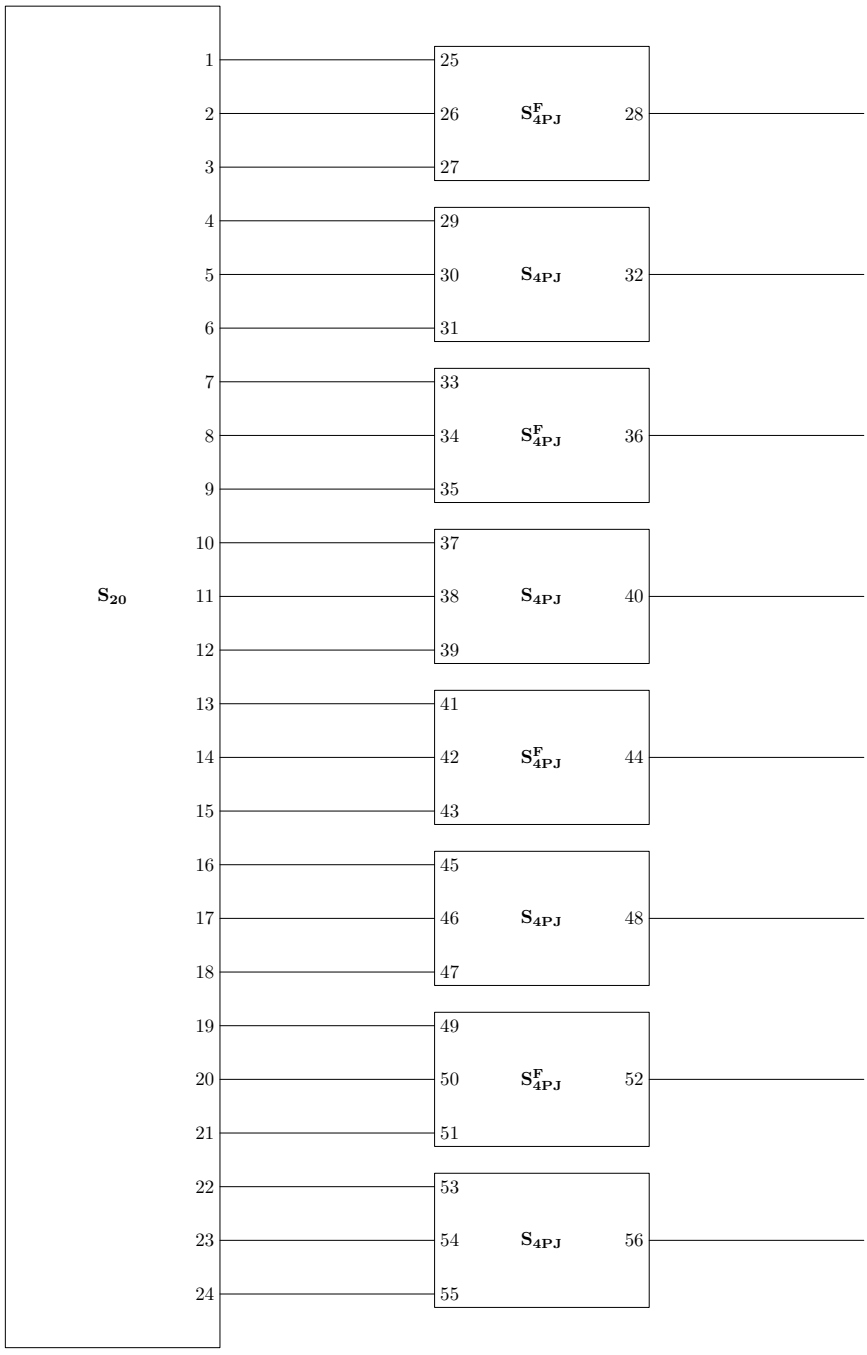


Figure 9.9: Port labeling for the integration of the $\mathbf{S_{20}}$ *and 4-port junction matrices.*

The vector $\overrightarrow{a}_{cop}$ contains the waves incident on all the other ports, in ascending order:

$$\overrightarrow{a}_{cop} = [a_1 \ \ldots \ a_{24} \ a_{25} \ a_{26} \ a_{27} \ a_{29} \ a_{30} \ a_{31} \ \ldots \ a_{53} \ a_{54} \ a_{55}]^{\mathrm{T}}. \tag{9.31}$$

Next we define a second permutation matrix $\mathbf{F}$, which expresses the relationship between the waves scattered from one port in the composite system and incident on another (see Fig. 9.9):

$$\begin{bmatrix} a_1 \\ a_2 \\ \vdots \\ a_{25} \\ a_{26} \\ a_{27} \\ b_{28} \\ \vdots \\ a_{53} \\ a_{54} \\ a_{55} \\ b_{56} \end{bmatrix} = \mathbf{F} \begin{bmatrix} b_1 \\ b_2 \\ \vdots \\ b_{25} \\ b_{26} \\ b_{27} \\ b_{28} \\ \vdots \\ b_{53} \\ b_{54} \\ b_{55} \\ b_{56} \end{bmatrix} \tag{9.32}$$

From Fig. 9.9, we see that $a_1 = b_{25}$, $a_2 = b_{26}$ and so on. All signals scattered from the external ports are unaffected.

The scattered signals are then re-ordered in the same way as the incident ones, per Eq. (9.29). The resulting vector is expressed by

$$\begin{bmatrix} \overrightarrow{a}_{cop} \\ \overrightarrow{b}_{sct} \end{bmatrix} = \mathbf{P}^{-1}\mathbf{F}\,\overrightarrow{b}, \tag{9.33}$$

with

$$\overrightarrow{b}_{sct} = [b_{28} \ b_{32} \ b_{36} \ b_{40} \ b_{44} \ b_{48} \ b_{52} \ b_{56}]^{\mathrm{T}} \tag{9.34}$$

being the vector containing the waves scattered from the "external" ports. Combining Eqs. (9.28), (9.29) and (9.33), we obtain

$$\begin{bmatrix} \overrightarrow{a}_{cop} \\ \overrightarrow{b}_{sct} \end{bmatrix} = \mathbf{P}^{-1}\mathbf{F}\mathbf{S}_{\mathbf{B}}\mathbf{P} \begin{bmatrix} \overrightarrow{a}_{cop} \\ \overrightarrow{a}_{inc} \end{bmatrix}, \tag{9.35}$$

where the matrix $\mathbf{G} = \mathbf{P}^{-1}\mathbf{F}\mathbf{S}_{\mathbf{B}}\mathbf{P}$ describes the composite system. $\mathbf{G}$ can be split into four blocks $\mathbf{G_{ij}}$ corresponding to the dimensions of $\overrightarrow{a}_{cop}$ (48×1), $\overrightarrow{a}_{inc}$ (8×1) and $\overrightarrow{b}_{sct}$ (8×1). We have

$$\overrightarrow{a}_{cop} = \mathbf{G}_{11}\,\overrightarrow{a}_{cop} + \mathbf{G}_{12}\,\overrightarrow{a}_{inc}, \tag{9.36}$$

$$\overrightarrow{b}_{sct} = \mathbf{G}_{21}\,\overrightarrow{a}_{cop} + \mathbf{G}_{22}\,\overrightarrow{a}_{inc}. \tag{9.37}$$

From these two equations we obtain

$$\overrightarrow{b}_{sct} = \left[\mathbf{G}_{21}\left[\mathbf{1} - \mathbf{G}_{11}\right]^{-1}\mathbf{G}_{12} + \mathbf{G}_{22}\right]\overrightarrow{a}_{inc}, \tag{9.38}$$

where the matrix

$$\mathbf{S_{TOT}} = \mathbf{G}_{21}\left[\mathbf{1} - \mathbf{G}_{11}\right]^{-1}\mathbf{G}_{12} + \mathbf{G}_{22} \tag{9.39}$$

is the 8×8 scattering matrix of the system composed by the strap array and the eight four-port junctions. Note that $\mathbf{S_{TOT}}$ is defined with $Z_{ref} = 20\,\Omega$. It follows from Fig. 9.9 that the eight input ports are labeled

$$\begin{bmatrix} 1 & 3 & 5 & 7 \\ 2 & 4 & 6 & 8 \end{bmatrix}, \tag{9.40}$$

again when viewed from the back, i. e., looking towards the plasma.

Furthermore, the effect of the $L = 1.7$ nH series inductance is included by defining an additional 2×2 S-matrix:

$$\mathbf{S_L} = \begin{bmatrix} Z/\xi & 2Z_0/\xi \\ 2Z_0/\xi & Z/\xi \end{bmatrix}, \tag{9.41}$$

with $\xi = 2Z_{ref} + Z$, $Z = j\omega L$ and Z_{ref} = 20 Ω. Eight of these matrices are also incorporated into $\mathbf{S_{TOT}}$ using the same procedure; the resulting matrix is called $\mathbf{S^L_{TOT}}$ and we note that it's still defined with reference to 20 Ω.

The service stubs are located a distance $d = 1.229$ m behind the 4PJ port on each feeding line, so we must again translate $\mathbf{S^L_{TOT}}$ by this distance towards the generator:

$$\begin{aligned} \mathbf{S^L_{TOT}} &= \mathbf{D}\mathbf{S^L_{TOT}}\mathbf{D} \\ &= \begin{bmatrix} e^{-j\beta d} & \cdots & 0 \\ \vdots & \ddots & \vdots \\ 0 & \cdots & e^{-j\beta d} \end{bmatrix} \begin{bmatrix} S^{\mathrm{L}}_{\mathrm{TOT}(11)} & \cdots & 0 \\ \vdots & \ddots & \vdots \\ 0 & \cdots & S^{\mathrm{L}}_{\mathrm{TOT}(88)} \end{bmatrix} \cdots \\ &\qquad \times \begin{bmatrix} e^{-j\beta d} & \cdots & 0 \\ \vdots & \ddots & \vdots \\ 0 & \cdots & e^{-j\beta d} \end{bmatrix} \end{aligned} \tag{9.42}$$

(the distances d are the same on each line). The service stub is also incorporated via its own 2×2 scattering matrix. The stub is essentially equivalent to the input impedance of a short-circuited line of length L_{SS} and chacateristic impedance Z_{0S} inserted in parallel between the two ports of a short section of the RVTL, so we define its scattering matrix, similarly to Eq. 9.41, as

$$\mathbf{S_{ST}} = \begin{bmatrix} -Z_0/\zeta & 2Z_{ST}/\zeta \\ 2Z_{ST}/\zeta & -Z_0/\zeta \end{bmatrix}, \tag{9.43}$$

with $\zeta = 2Z_{ST} + Z_{0S}$, $Z_{ST} = jZ_{0S}\tan\beta L_{SS}$, $Z_{0S} = 15\ \Omega$, $Z_0 = 20\ \Omega$ and $L_{SS} = 1.5779$ m being the total length of the stub (a quarter wavelength at ITER midband). Eight $\mathbf{S_{ST}}$ matrices are again incorporated into $\mathbf{S^L_{TOT}}$ by the procedure described above, and the resulting matrix $\mathbf{S^{ST}_{TOT}}$ now represents the full system, consisting of the strap array, four-port junctions, RF contacts and vacuum transmission lines up to and including the service stubs. Note that $\mathbf{S^{ST}_{TOT}}$ is still defined with a reference impedance of $20\ \Omega$.

Because G_{min3} is defined on the $20\ \Omega$ transmission line section behind the service stub, we can now say something about the power coupling capacity of the antenna. From Eqs. (9.26) and (9.27), we have

$$\overrightarrow{V}^- = \mathbf{S^{ST}_{TOT}}\overrightarrow{V}^+, \tag{9.44}$$

where $\overrightarrow{V}^+ = \left[V_1^+\ V_2^+ \cdots V_8^+\right]^{\mathrm{T}}$ is the vector containing the excitation voltage, i. e. the voltage waves incident on the eight ports of the system, and $\overrightarrow{V}^- = \left[V_1^-\ V_2^- \cdots V_8^-\right]^{\mathrm{T}}$ is the vector containing the corresponding scattered waves. The $(0, \pi, 0, \pi)$ toroidal and $(0, -\pi/2)$ poloidal phasing assumed here mean that the incident wave vector will be

$$\overrightarrow{V}^+ = [1,\ -j,\ -1,\ j,\ 1,\ -j,\ -1,\ j]^{\mathrm{T}}, \tag{9.45}$$

where all voltages are of amplitude 1. From the definition of the scattering matrix, the voltage reflection coefficients on each line will be given by

$$\Gamma_i = \frac{V_i^-}{V_i^+}. \tag{9.46}$$

Note that these are active reflection coefficients, since all the ports are driven simultaneously. Then the VSWR and G_{min3} will be defined on each line by

$$\mathrm{VSWR}_i = \frac{1 + |\Gamma_i|}{1 - |\Gamma_i|}, \quad G_{min3,i} = \frac{1}{Z_0 \mathrm{VSWR}_i}, \tag{9.47}$$

and the maximum power coupled by the antenna is

$$P_{CPL} = \frac{1}{2} V_{max}^2 \sum_{i=1}^{8} G_{min3,i}, \tag{9.48}$$

where $V_{max} = 45$ kV is the voltage stand-off on the transmission line behind the service stub.

The maximum coupled power calculated in this way, along with the n_e profiles used in this study, is shown in Fig. 9.10. The horizontal dashed line indicates the cutoff density corresponding to a $k_\parallel \simeq 8.5\ \mathrm{m}^{-1}$, which is where the maximum is located in the nominal power spectrum at $(0, \pi, 0, \pi)$ toroidal phasing. Only the

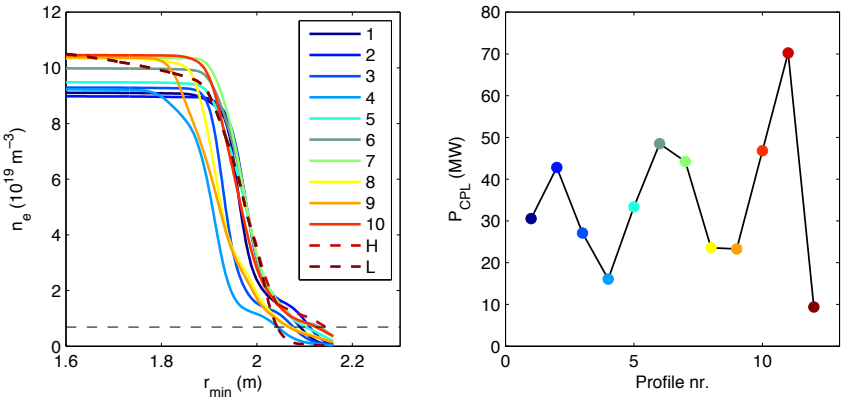


Figure 9.10: Electron density profiles used for the ITER simulations and the corresponding maximum coupled power. Profiles 1 to 10 are the ten rescaled ASDEX Upgrade profiles, while H and L (11 and 12 on the right) are the 'High' and 'Low' density cases provided by IO. The horizontal dashed line indicates the cutoff density corresponding to $k_{\|} \simeq 8.5\ m^{-1}$.

outer 56 cm of the plasma is shown in all cases since, as stated above, outward radiation conditions were imposed 50 cm from the antenna aperture. From the figure it is evident that the 'High' profile allows the most power to be coupled, which would be expected from looking at the corresponding density profiles; in the 'High' case, the cutoff density is closest to the antenna. Profiles 'Low' and number 4 produce a similar amount of coupled power, both below the minimum ITER requirement, having the largest antenna-cutoff distance; note that this is despite the two profiles being significantly different for $n_e > n_{co}$.

We recall that, in Section 9.1, the error bars on the R_L computed with TOPICA were estimated *on the basis of the available RF measurements* as $0.18 - 0.61\ \Omega$ (best - worst cases, respectively). To see what this means for the ITER case, we write the coupled power as usual in terms of the loading resistance:

$$P_{CPL} = \frac{1}{2Z_0^2} V_{max}^2 \sum_{i=1}^{8} R_{L,i}. \tag{9.49}$$

Using $V_{max} = 45$ kV and $Z_0 = 20\ \Omega$ and writing $C = V_{max}^2/2Z_0^2$ we see that, for the whole array the uncertainty in coupled power would be

$$\Delta P_{CPL} \simeq \sqrt{8C^2 \left(\Delta R_L\right)^2}, \tag{9.50}$$

that is 1.3 - 4.4 MW (best - worst cases respectively), i. e. 6.5% and 22% of the required 20 MW per antenna. As already stated, however, ΔR_L is mostly random only in the former case, so the estimate for the latter is not to be taken too seriously.

9.5 Rsolver simulations of the ITER antenna

Continuing with the procedure outlined for the ASDEX Upgrade antenna in Section 9.2, we now compute the coupling resistance R_C for an equivalent "ITER-like" antenna using the fast code Rsolver, for the same density profiles as used above. In close analogy of the AUG-like antenna description from Section 6.2.3, we model the ITER antenna as a two-dimensional array of N horizontal $\times$ M vertical uniform current sheets, with width w, horizontal gap d_z, height h and vertical gap d_y. The current is given by

$$j(y,z) = J_0 \sum_{n=1}^{N} e^{i\phi_n} \Theta_n(z) \sum_{m=1}^{M} e^{i\psi_m} \Upsilon_m(y). \tag{9.51}$$

Here the horizontal term is $\Theta_n(z) = 1$ if $L_{nz} \leq z \leq U_{nz}$ and 0 otherwise, with

$$L_{nz} = (d_z/2 + w/2) + (n-1)(d_z + w) - w/2, \tag{9.52}$$

$$U_{nz} = (d_z/2 + w/2) + (n-1)(d_z + w) + w/2, \tag{9.53}$$

with the toroidal phasing given by $\phi_n = (n-1)\pi$. Correspondingly, the vertical term is $\Upsilon_m(y) = 1$ if $L_{ny} \leq y \leq U_{ny}$ and 0 otherwise, with

$$L_{ny} = (d_y/2 + h/2) + (m-1)(d_y + h) - h/2, \tag{9.54}$$

$$U_{ny} = (d_y/2 + h/2) + (m-1)(d_y + h) + h/2, \tag{9.55}$$

and the poloidal phasing being $\psi_m = 1$ if $m \leq M/2$ and $\psi_m = \pi/2$ otherwise. The current spectrum is then given by

$$j_y(k_y, k_z) = \frac{J_0}{L_z} \sum_n \exp[i\phi_n - ik_z\,(d_z/2 + w/2 + (n-1)(d_z + w))] w \,\mathrm{sinc}\left(\frac{k_z w}{2}\right) \ldots \times \frac{1}{L_y} \sum_m \exp[i\psi_m - ik_y\,(d_y/2 + h/2 + (m-1)(d_y + h))] h \,\mathrm{sinc}\left(\frac{k_y h}{2}\right) \tag{9.56}$$

with $L_z = 2\pi\,(R_t + x_{surf})$ and $L_y = 2y_{vert}$. The parameters specifying the model of the "ITER-like" antenna are given in Table 9.6.

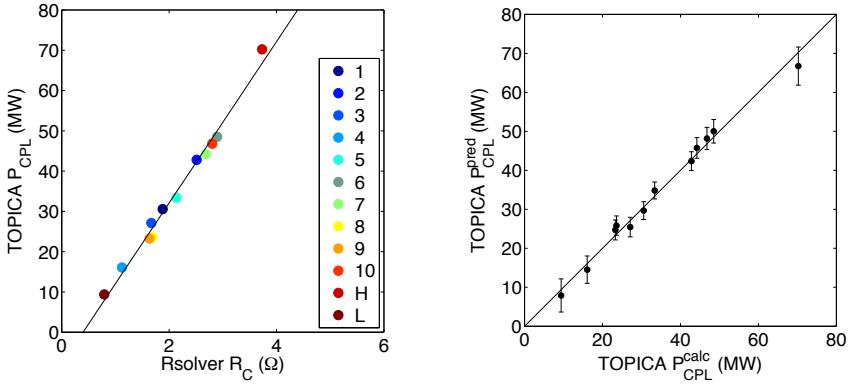
Figure 9.11a shows the coupled power computed with TOPICA versus the coupling resistance R_C calculated with Rsolver. The results are clearly proportional to one another. According to the procedure in Section 9.2, we fit a linear model of the form

$$P_{CPL}^{pred} = A + BR_C, \tag{9.57}$$

with $A = -7.9633 \pm 1.57$ and $B = 20.027 \pm 0.69103$. P_{CPL}^{pred} is plotted versus P_{CPL} computed by TOPICA in Figure 9.11b.

Parameter	Value
Major radius R_t	620 cm
Plasma surface position x_{surf}	216 cm
Vertical dim. of vessel y_{vert}	300 cm
Min. n, max. n	-80, 80
Min. m, max. m	-7, 7
Horiz. number *N*	6
Vert. number *M*	4
Strap height *h*	30 cm
Strap width *w*	21 cm
Horiz. gap d_z	15 cm
Vert. gap d_y	2.3 cm
Strap-to-plasma dist. *a*	6 cm
Strap-to-wall dist. *b*	11 cm
Strap current amplitude J_0	1 A

Table 9.6: Parameters used in the Rsolver code for an ITER-like antenna simulation.



(a) P_{CPL} computed by TOPICA versus R_C computed by Rsolver, all available cases.

(b) P_{CPL} estimated from R_C versus P_{CPL} computed by TOPICA.

Figure 9.11: Relationship between TOPICA and Rsolver results, ITER antenna.

Having deduced an empirical relationship between the coupled power, computed by TOPICA, and R_C computed by Rsolver, we can again build a large database of "ITER-like" density profiles with an associated R_C for each one. The profiles will actually be the same ones that were used in section 9.3 for the AUG analysis, but scaled by the same factors as those used in the TOPICA simulations above, i. e. a factor 4 along r and a factor 1.6057 in density; naturally the vessel parameters are those of ITER (see Table 9.6), with $B_0 = 5.2$ T and a species concentration of 50% D - 50% T. All profiles are sampled at 1000 radial points, i. e. they have a radial resolution of 2.16 mm. Outward radiation conditions were imposed at 30 cm from plasma surface[7]. The selected density parameters are the same as in the AUG case. All the cases with $R_C \geq 3.5\,\Omega$ have been excluded from the database. At least in the domain of density profiles in this study, this restriction is not especially strong since, with the exception of the 'High' case provided by IO, R_C falls into this range, as can be seen in Fig. 9.11a.

We study here only an exponential model and omit the linear one for brevity. By trial and error it was found that a model that produces relatively reliable results is given by

$$R_C^{pred} = b_0 \exp\left(b_1 \nabla_{eff} + b_2 d_{co} + b_3 \nabla_{co} + b_4 d_{min} + b_5 n_{lim}\right). \qquad (9.58)$$

We are naturally interested in seeing how well this model (or any other) reproduces the TOPICA results shown in Fig. 9.10. Fig. 9.12a shows the resulting scaling of R_C, when only the profiles from shot 29823 are included in the database, which we do at first because the ten scaled profiles used in TOPICA above were extracted from this particular shot. The NRMS is 7.7%. Fig. 9.12b shows the results of applying this scaling, together with Eq. (9.57) to the TOPICA results, i. e. the model is

$$P_{CPL}^{pred} = b_6 + b_0 \exp\left(b_1 \nabla_{eff} + b_2 d_{co} + b_3 \nabla_{co} + b_4 d_{min} + b_5 n_{lim}\right). \qquad (9.59)$$

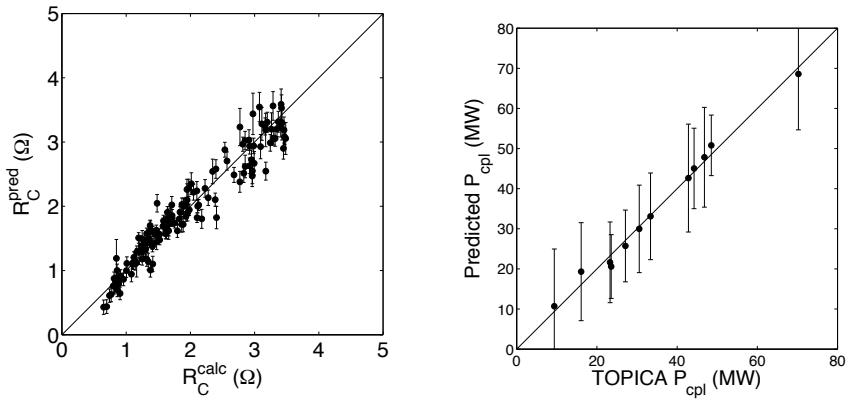
The resulting NRMS is 24.2%. Although the trend is rather well reproduced, given the simplicity of Rsolver, the error bars are considerable. The fit coefficients are given in Table 9.7.

Further including shots 29822 and 29833 into the database yields the R_C scaling shown in Fig. 9.13a, with an NRMS of 7.6%. The corresponding P_{CPL} scaling is the same since the model has not changed.

Looking at the p-values listed in Table 9.8, we see that ∇_{co}, d_{min} and n_{lim} are far less relevant than ∇_{eff} and d_{co}. The simplest model to try is then

$$R_C^{pred} = b_0 \exp\left(b_1 \nabla_{eff} + b_2 d_{co}\right). \qquad (9.60)$$

[7] Although TOPICA simulations used 50 cm, it was determined that decreasing the length until 30 cm had no effect on the results in Rsolver.

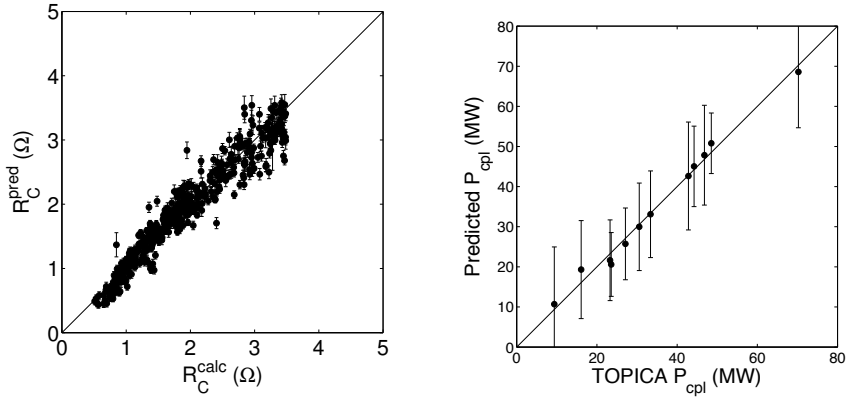


(a) Rsolver R_C scaling. (b) TOPICA P_{CPL} scaling.

Figure 9.12: Exponential model, shot 29823 only.

	μ	σ	t	p-value
b_0 (1)	5.2	0.5	9.9192	9.4×10^{-18}
b_1 (∇_{eff})	-0.05	0.02	-2.5712	0.01
b_2 (d_{co})	-10.1	0.6	-18.014	10^{-37}
b_3 (∇_{co})	-0.05	0.02	-2.764	7×10^{-3}
b_4 (d_{min})	0.6	0.3	1.864	0.06
b_5 (n_{lim})	-0.1	0.1	-0.9	0.4

Table 9.7: Results of fitting Eq. (9.58) to the database, profiles from shot 29823 only; for each parameter, μ is the estimated value, σ is the standard deviation and t denotes the t-statistic.

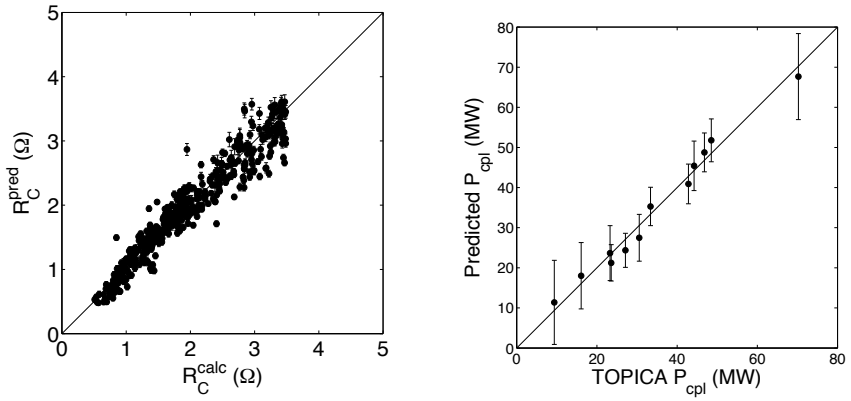


(a) Rsolver R_C scaling. (b) TOPICA P_{CPL} scaling.

Figure 9.13: Exponential model, shots 29822, 29823 and 29833.

	μ	σ	t	p-value
b_0 (1)	5.0	0.3	18.693	5.6×10^{-57}
b_1 (∇_{eff})	-0.049	0.009	-5.3635	1.4×10^{-7}
b_2 (d_{co})	-10.0	0.3	-37.708	5.7×10^{-136}
b_3 (∇_{co})	-0.02	0.01	-1.994	0.05
b_4 (d_{min})	0.1	0.2	0.51538	0.6
b_5 (n_{lim})	-0.12	0.04	-2.8081	0.005

Table 9.8: Results of fitting Eq. (9.58) to the database, profiles from shots 29822, 29823 and 29833; for each parameter, μ is the estimated value, σ is the standard deviation and t denotes the t-statistic.



(a) Rsolver R_C scaling.

(b) TOPICA P_{CPL} scaling.

Figure 9.14: Simplest exponential model, shots 29822, 29823 and 29833.

The R_C scaling thus obtained is shown in Fig. 9.14a. With an NRMS of 7.7%, there is surprisingly little change with respect to the model given by Eq. 9.58, considering that further simplification already leads to the well known (analytical) exponential decay formula for the coupling resistance. The coefficients obtained from the fit are listed in Table 9.9. The corresponding P_{CPL} scaling,

$$P_{CPL}^{pred} = b_3 + b_0 \exp\left(b_1 \nabla_{eff} + b_2 d_{co}\right), \tag{9.61}$$

is shown in Fig. 9.14b, giving an NRMS of 23.9%, not far from the previous model (in fact slightly better). Note that, as expected, in all the models used here d_{co} is invariably the most important parameter.

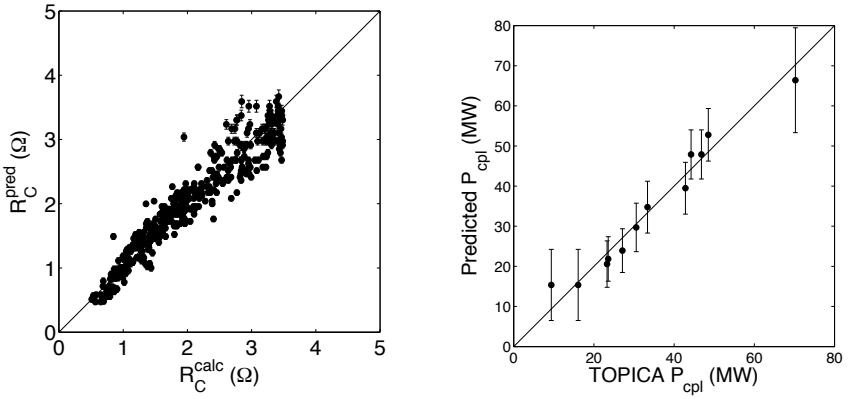
Finally, we can compare the above results with the analytical model

$$R_C^{pred} = b_0 \exp\left(b_1 d_{co}\right). \tag{9.62}$$

The R_C scaling is shown in Fig. 9.15a, with an NRMS of 8.1%, which is again a surprisingly small change with respect to the previous model, considering that we

	μ	σ	t	p-value
b_0 (1)	4.7	0.1	31.417	5.5×10^{-112}
b_1 (∇_{eff})	-0.053	0.008	-7.0251	8.8×10^{-12}
b_2 (d_{co})	-9.5	0.2	-57.209	1.6×10^{-199}

Table 9.9: Results of fitting Eq. (9.60) to the database, profiles from shots 29822, 29823 and 29833; for each parameter, μ is the estimated value, σ is the standard deviation and t denotes the t-statistic.



(a) Rsolver R_C scaling.

(b) TOPICA P_{CPL} scaling.

Figure 9.15: Analytical model, shots 29822, 29823 and 29833.

are now down to a single parameter. The corresponding P_{CPL} scaling,

$$P_{CPL}^{pred} = b_2 + b_0 \exp\left(b_1 d_{co}\right). \tag{9.63}$$

is shown in Fig. 9.15b with an NRMS of 24.3%.

Note that the P_{CPL} corresponding to 'High' IO profile is predicted with a significantly larger error, compared to the other profiles. This might suggest that analyzing the ITER antenna with density profiles derived from AUG data, even though properly rescaled and used in an 'ITER-like' vessel (see Table 9.6) is not the best choice; the weight of each parameter may be different if the database contained 'proper' ITER profiles, improving the predictions for the two outlying cases. However, we are by necessity limited to AUG data since, as already stated, no other ITER profiles are available.

All the results shown above make use of the ordinary method of least squares. However, the regression analysis for the ITER case (with the exponential model given by Eq. (9.58)) was repeated using an advanced regression method called 'geodesic least squares regression' (GLS) [75]. This technique minimizes the difference between the so-called 'modeled' and 'observed' probability distributions

	b_0 (1)	b_1 (∇_{eff})	b_2 (d_{co})	b_3 (∇_{co})	b_4 (d_{min})	b_5 (n_{lim})
μ	5.35	0.57	-3.75	-0.37	13.65	1.27

Table 9.10: Results of fitting Eq. (9.58) to the database, profiles from shots 29822, 29823 and 29833, using the geodesic least squares method.

of the response variable (here coupled power). The modeled distribution is obtained if all assumptions regarding the regression model are considered to be correct. It was calculated by assuming Gaussian distributions on all regression variables, with standard deviations calculated according to standard Gaussian error propagation. Hence, the GLS method intrinsically takes into account the uncertainties on the response *and* predictor variables. The observed distribution, here also considered to be Gaussian, is centered on the exact 'measurement values' of the coupled power (the ones calculated by TOPICA), while the standard deviation is estimated from the data. Hence, this distribution is minimally dependent on any assumptions regarding the regression model. GLS uses the Rao geodesic distance to minimize the discrepancy between the modeled and observed distributions. As a result, it is considerably more robust with respect to ordinary least squares (OLS). The regression coefficients using the exponential regression model (9.58), obtained by GLS, are given in Table 9.10[8]. Note that the values of the coefficients differ from those obtained with OLS. Unfortunately, presently it is not possible to provide error bars on these estimates, since GLS in its current form is based on an optimization procedure (this is part of future developments of the method). The plot of the regressed power versus the power calculated by TOPICA is shown in Fig. 9.16. The error bars are the ones expected on the *individual* experimental values of the coupled power under the regression model, and they are considerably larger than the ones provided for OLS, as in the case of GLS they take into account also the uncertainty on the predictor variables. Error bars on *predicted* values of the coupled power are likely to be somewhat smaller, but this cannot be shown with the present analysis.

Any one of the models given by Eqs. (9.59), (9.61) and (9.63) yields an estimate *of the power coupling capability of the ITER launcher facing a 50% D - 50% T plasma with* $B_0 = 5.2$ *T, as would be computed by TOPICA for a frequency of 47.5 MHz, toroidal and poloidal phasing of* $(0, \pi, 0, \pi)$ *and* $(0, -\pi/2)$ *respectively, and a maximum voltage of 45 kV on the RVTL.* We must bear in mind that such a model, if valid at all, applies only in these conditions and will not make any meaningful predictions for another plasma or antenna parameters (frequency, phasing, etc.). As such, this is a rather strong restriction, since D-T operation is only expected to start in 2027. However, to make more general predictions it would be necessary to run TOPICA simulations for each plasma composition and antenna

[8]Results kindly provided by G. Verdoolaege.

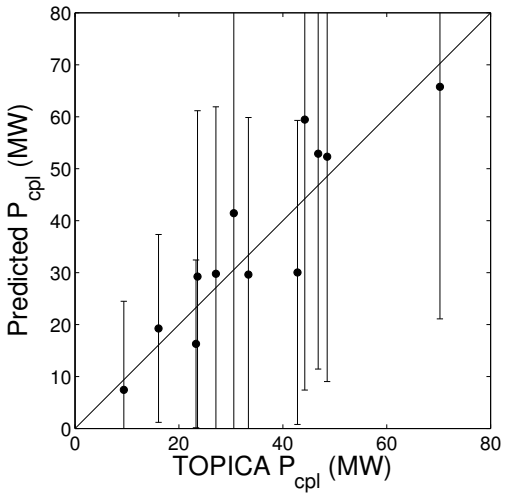


Figure 9.16: Exponential model with geodesical least squares, shots 29822, 29823 and 29833. The error bars are significantly larger than with ordinary least squares, because GLS takes into account the uncertainty on the predictor variables.

Case	∇_{eff} $\left(10^{20}\ \mathrm{m}^{-4}\right)$	d_{co} (m)
High	3.1372	0.0151
Low	4.8839	0.1168

Table 9.11: Selected parameters for the 'High' and 'Low' density cases.

operational regime separately; due to the computational cost this lies outside the scope of the present work.

We now consider the power estimates we can make with the simplest 'non-analytical' model, that is Eq. (9.61). There are only two projected ITER density profiles - the 'High' and 'Low' cases - but we can still at least get a rough idea of the expected behavior. The parameters ∇_{eff} and d_{co} for the two cases are summarized in Table 9.11.

The resulting coupled power 'map' as function of these two parameters is shown in Fig. 9.17. As expected from the values in Table 9.9, the change in coupled power with d_{co} within the operational space is far stronger than the corresponding variation with ∇_{eff}, which in practice means that it is not possible to compensate for the negative effects of an increase in evanescence length by introducing changes to the effective density gradient as defined here. Very broadly speaking, according to the model the evanescence length must be between 8 and 11 cm for the ITER antenna to couple 20 MW (maximum and minimum effective gradient, respectively), and between 12 and 15 cm to couple 10 MW (likewise).

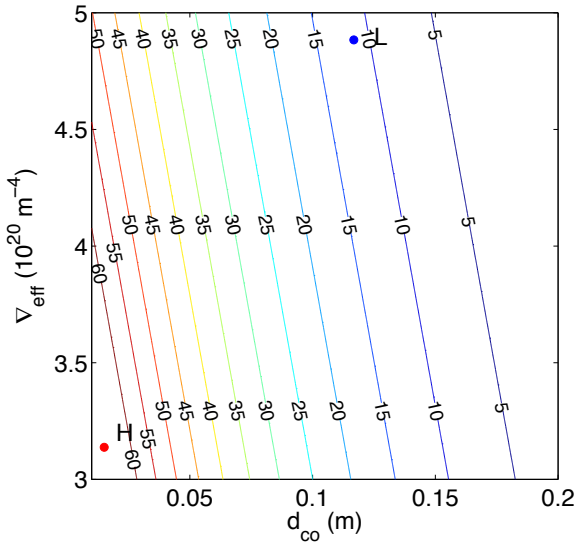


Figure 9.17: Power coupled by the ITER launcher (in MW) as function of ∇_{eff} and d_{co} computed with Eq. (9.61). The predicted values for the 'High' and 'Low' cases are indicated on the plot.

9.6 Summary

Several conclusions can be drawn from the results presented in the previous section. The rather simple scaling models that we have studied here certainly reproduce the right trend where projected coupled power is concerned. Their ultimate usefulness is, however, limited by several factors. In the first place, we have seen that the two actual ITER cases have predicted values which are rather far from those computed by TOPICA. In the 'High' case this is not so critical since, as stated above, the projected power level (either from TOPICA or from a scaling model) is much higher than the minimum ITER requirement. In the 'Low' case, it is much more problematic because the TOPICA result is about 10 MW while the scaling gives 16 MW, an important difference. This is an issue that could conceivably be solved by running Rsolver with a large database of ITER profiles, which however are not at present available. The available results, for the moment, show error bars which are very large compared to the actual power values, especially at lower coupled power (10 - 20 MW) where the antenna is expected to operate; the uncertainties are clearly too high to be able to make any reasonable predictions. Presumably the accuracy of the model will improved when used with other modeled (or measured) ITER profiles.

Secondly, the specific form of the scaling models used - the exponential and, in the AUG case, linear dependencies - were defined *a priori*. The justification for

the former is the well-known exponential dependence of R_C on the evanescence length obtained by analytical methods, but there is no particular reason to extend this to the remaining parameters; the linear model was chosen solely because of its simplicity and robustness. An unexplored functional relationship may well offer better agreement. A related issue is the choice of the relevant density parameters themselves. Besides from the choice of the evanescence length d_{co}, which is justified on theoretical grounds, these parameters were chosen from a more or less qualitative picture of what a 'typical' AUG density profile should look like. In order to rigorously justify these choices, or select more relevant - but less superficial - parameters, we must start from the physics relevant to the formation of the density shape and not those of the fast wave propagation. However, this also involves the modeling of the density profile itself, which unfortunately lies outside the scope of the present work.

Because of these reasons it is unclear how useful these results are to the prediction of the actual coupled power on ITER. However, the relationship obtained between the results of TOPICA and those of Rsolver indicates that, once the proportionality has been obtained for a given set of antenna operating parameters, Rsolver will give a reliable estimate of the projected coupled power to within a few percent of error for a plasma density profile. Extensive statistical or parametric studies for which TOPICA is not well suited due to computational cost will then yield 'real-world' numbers as opposed to the R_C of an oversimplified antenna, which - as we have seen in Chapter 3 - is not readily related to actual measurements. Note that this emphatically does *not* mean that running TOPICA or an equivalent sophisticated code becomes unnecessary. The derivation of equation (9.57), as we have seen, required extensive transformations of the antenna S-parameters, meaning that if the operating frequency, phasing, or transmission network geometry is changed, the numerical values in Eq. (9.57) become invalid and must be re-derived again on the basis of TOPICA results. What our conclusion *does* mean, however, is that if only the plasma density profile is changed and only the *total* coupled power is required, without further details such as differences in voltage distribution between the feeding lines, then an Rsolver run and Eq. (9.57) are sufficient instead of a full TOPICA simulation[9]. Although this cannot be used for real-time improvement of antenna coupling, at least we see that the method can be used for quick estimation of coupled power on a shot-to-shot basis, provided the density profiles are known beforehand.

[9]Naturally this also applies to any other fast code, particularly FELICE, when used with an ITER-like antenna model; presumably the inclusion of self-consistent current distribution calculation will yield more accurate results.

10
Summary and conclusions

Throughout this work we have attempted to progress, in a logically structured way, from a broad basis of experimental measurement methods and numerical simulations of ICRF antennas towards specific predictions regarding the performance of the ITER launcher, given certain conditions. More specifically, in Chapter 4 we argue that voltage and current probes possess distinct advantages over directional couplers and voltage probe arrays for impedance measurements, at least in the specific case of the ASDEX Upgrade ICRH system. Chapter 5 then describes how this diagnostic set was calibrated, its performance studied on testbeds under different conditions, and finally implemented for operational measurements. Chapter 7 then presents the observations made using the diagnostic set, and so on. The development of this work, however, was significantly less linear. The original aim was a) to carry out an extensive and unambiguous comparison between TOPICA results and the already existing database of RF measurements on ASDEX Upgrade, b) to determine which features of the density profile were most relevant for antenna coupling, c) to determine the set of density profiles which would allow the ITER antenna to couple the required 20 MW and d) to determine whether this set of profiles was accessible on ITER, using the B2-EIRENE edge modeling code.

The result of objective a) is the first AUG-TOPICA study presented in detail in section 8.2. The results obtained from this study were, obviously, significantly worse than expected, especially when compared with the results reported in, e. g., [18] on Alcator C-Mod. These results motivated a search for potential error sources and the testbed comparison between impedance measurement methods reported in [24], and ultimately led to the calibration, testing and implementation

of the voltage and current probes, a necessary work that was not foreseen in the original plan and that occupied a significant part of the total duration of this thesis. All subsequent work with B2-EIRENE was then excluded, partially because of these difficulties and partially because the independent validation of a second, highly complex, numerical code would have been outside the scope of this thesis.

Furthermore, as already reported in Chapter 5, testbed observations showed a very good agreement between measurements taken with voltage / current probes and those done with a network analyzer. By the time that the discrepancies in coupled power measurements had been discovered and characterized, the probes were already in operation and the test stands had been dismantled. Rebuilding them and running further tests on the probes would have required considerable additional time. Furthermore, high power tests needed to be carried out; judging by the measurements done at the medium power test stand (see section 5.3.3), it was far from clear how to reach power levels of ~ 100 kW at the very high operation-relevant VSWR values without damaging the ICRF generators. Hence, despite the very clear improvement in the second AUG-TOPICA study, a degree of uncertainty remains in the ICRF measurements. Because this necessitated the cross-calibration of the probes with directional couplers - although in conditions where the obvious disadvantages would be minimized - this AUG-TOPICA comparison is not as unambiguous as originally intended. Therefore the first obvious step for subsequent work is to find the source for these discrepancies in probe measurements and either eliminate them, if they are indeed related to the probes (or other diagnostic equipment, e. g. cables, RF detectors, etc.), or account for them when calculating the relevant RF quantities from the raw probe data if they are caused by an external source that cannot be eliminated. The aim is to make the probes a fully independent diagnostic set, as originally intended.

Nonetheless, the testbed runs have yielded much valuable information about probe operation and their limits of accuracy. In particular, accuracy of a few percent in $|\Gamma|$ and a few degrees in phase have been demonstrated at high VSWR, and one relevant source of error has been found, namely the sensitivity of the DC breaks to fields produced by external sources. The calibration tables that have been obtained for $Z_0 = 25\ \Omega$ are fully suitable for using the probes during routine operation of the ICRF system on ASDEX Upgrade.

Besides the RF measurement issues, another important source of uncertainty in the comparison is the density profile used as TOPICA input. As explained in section 8.1, density is not actually measured in front of any antenna, as illustrated in Fig. 8.1. In order to account for the possible changes in the density profile due to the antenna fields themselves, it was proposed to install a microwave reflectometer between the straps of one antenna to have direct measurements of the density profile *in situ*; however, this was not carried out within the time frame of the present work. On the other hand, at the present time there are no provisions

in TOPICA to account for self-consistent profile modification; hence this effect is not quantified in any way and its impact on ITER performance is not evaluated. At the time of writing, a follow-up thesis is ongoing, with the aim of calculating the density profile in front of the antenna (Wei Zhang, IPP Garching). The reflectometer will become available in the near future and this will an important next step for any work attempting to make detailed predictions for the ITER antenna[1].

Despite these shortcomings - both from the RF and density measurement sides - it is evident that the second TOPICA comparison, carried out using voltage/current probes, shows a clear improvement over the first one, using the standard diagnostic set, for the following reasons:

1. The reflection coefficients measured close to the input ports of each antenna are much more convenient to compare with the TOPICA results than the Γ_T (refl. coeff. at the T-section) used in the previous study, since they a) offer more information and b) they do not depend on the properties of the long transmission network from antenna port to T-section, which are not known well enough. The sensitivity of these results to uncertainties in line length has already been illustrated in Chapter 4.

2. In the first study, differences of up to $\sim 11\%$ in $|\Gamma_T|$ had been observed, whereas in the second study they are down to $4\% - 9\%$ in the case of antennas 1 and 2 and $\lesssim 3\%$ in the case of antenna 3. This is a significant improvement, considering that normally $|\Gamma| \sim 0.9$.

3. In the first study, no clear agreement in trend is found; on the contrary, in the second study it is clear and evident (see Fig. 8.28).

4. A far wider range of plasma conditions are used as input in the code in the second study, and limits of applicability are explored (e. g. the high density runs at the end of discharges 29822, 29823 and 29833, see Fig. 8.22).

Regarding the experimental investigation of antenna coupling at ASDEX Upgrade, we enumerate the following conclusions:

1. The dramatic increase in antenna loading seen at high δ_o towards the end of discharges 29822, 29823 and 29833 are to be interpreted as *not* a direct effect of the changing separatrix shape in front of the antenna, but rather an indirect effect of global SOL density rise, the cause of which is not clear at the present moment. This is evident from observed relationship between antenna R_L and neutral flux density measured at the same time in the main chamber; in shots 30629 and 30630 no increase in neutral flux density is seen, and no improvement in loading is observed despite high δ_o. Further analysis is required to find the reason for this SOL density increase.

[1] J.-M. Noterdaeme, personal communication.

2. The effect of non-axisymmetric perturbations on antenna coupling, while not as drastic as those obtained in high δ_o shots, has been clearly seen. This amounts to an R_L increase of $30\% - 50\%$ over the baseline value; the effect is not immediate but antenna loading begins to grow after coil switch-on and increases about $\sim 0.5\ \Omega$ in the first 200 ms. This effect was found to have been independent of the perturbation field phasing.

3. Much less clear is the effect of the high δ_o and MPs on the density profile itself. Figs. 7.13 and 7.19, that show R_C computed with FELICE vs. the measured R_L for high δ_o and MPs. Reproduction of the loading trend in these numerical simulations is not very good, and the situation is complicated significantly because in both situations we are clearly dealing with 2D/3D effects, which are neither captured directly by density measurements nor reproducible in the slab plasma model used by the numerical codes. In the triangularity shots, the transition into the type-II ELMy regime at the relevant δ_o additionally complicates the analysis since ELM synchronization is no longer possible. The effects on loading are clear, but the quantitative study of how the density profile is affected by these external parameters must be the subject of subsequent work, outside the limitations of this dissertation.

The remaining important conclusions are related to the modeling of the ITER antenna:

1. The most important observation is that, for the range of the density profiles considered here, the results of the fast code Rsolver have a very good correspondence with the TOPICA results, *where only the total coupled power is concerned.* Even though the R_C calculated by the fast code is not directly related to measurement, a linear relationship exists between it and the 'real life' P_{CPL} from TOPICA (see Figs. 9.11a and 9.11b). This means that P_{CPL} is feasible to compute in parametric or statistical studies where hundreds or thousands of TOPICA runs are impossible. Note that this is valid *only as long as the antenna parameters, such as frequency and phasing, are not changed. For each such set of parameters the linear relationship must be rederived again. Likewise this holds only when a quick estimate of coupled power is required.* This is not a substitute for running TOPICA if more detailed information about the antenna is required, such as the full scattering matrix, RF fields or current distributions. All this is also true for the ASDEX Upgrade antenna.

2. Because of the highly complex nature of the ITER launcher, these results have been derived only for a 50% D - 50% T plasma, at $f = 47.5$ MHz (midband), $(0, \pi, 0, \pi)$ toroidal and $(0, -\pi/2)$ poloidal phasing. The RF

analysis of the transmission lines and service stubs has been greatly simplified by using ideal transmission line models. Non-uniform sections such as vacuum windows have been ignored. Full analysis of the ITER launcher lies outside the scope of this work.

3. Empirical laws, attempting to relate selected plasma parameters to R_C or P_{CPL} directly (without having to go through a numerical simulations) can be obtained and made to predict statistical trends: however, at least in the case of the models presented here, they are of limited applicability due to large scatter (error bars on R_C typically are in the $7\% - 8\%$) range. They are also dependent on assumptions that may or may not be justified in each case; the parameters were selected from a non-rigorous description of the density profile, and only very simple dependencies are analyzed. In the ITER case, we are forced to work with rescaled AUG density profiles, since only two profiles are available for ITER. The impact of these restrictions is not clear. In order to proceed with more caution, presumably one needs to start from the physics of the density profile itself and select parameters and functional dependencies accordingly; unfortunately this lies outside the limits of this work. Limited predictions about ITER antenna behavior can be made (see Fig. 9.17) but it is recommended that an Rsolver (or equivalent fast code) run be used instead for each particular case.

Finally, subsequent work must concentrate on the following lines of inquiry:

1. Find and correct the source of error affecting the operation of the voltage/current probes, with the aim of making them a fully independent diagnostic set as originally intended.

2. Include in the simulations measurements of the density profile directly in front of the ICRF antenna during operation.

3. If empirical formulas for P_{CPL} are still required, start from the relevant density profile physics and modeling codes, in order to derive relevant density parameters (and functional dependencies) on a more rigorous basis.

References

[1] *European Consortium for the Development of Fusion Energy*. https://www.euro-fusion.org/. Accessed 05.25.2015.

[2] S. J. Orfanidis. *Electromagnetic Waves and Antennas*. Rutgers University, New Jersey, 2002.

[3] D. M. Pozar. *Microwave Engineering*. John Wiley & Sons, U. S. A., 1998.

[4] Durodié F. et al. *Design, performance and grounding aspects of the International Thermonuclear Experimental Reactor ion cyclotron range of frequencies antenna*. Phys. Plasmas, 21:061512, 2014.

[5] J. Wesson. *Tokamaks*. Oxford University Press, Oxford, 2011.

[6] Smith C. L. *The need for fusion*. Fusion Eng. Des., 74:3–8, 2005.

[7] *International Energy Agency*. http://www.iea.org/topics/climatechange/. Accessed 05.23.2015.

[8] J. P. Freidberg. *Plasma Physics and Fusion Energy*. Cambridge University Press, Cambridge, 2007.

[9] G. McCracken and P. Stott. *Fusion: the Energy of the Universe*. Academic Press, China, 2013.

[10] *National Ignition Facility and Photon Science*. https://lasers.llnl.gov/science/ignition/ignition-experiments. Accessed 05.23.2015.

[11] W. M. Stacey. *An Introduction to the Physics and Technology of Magnetic Confinement Fusion*. Wiley-VCH, Germany, 2010.

[12] *International Thermonuclear Experimental Reactor*. http://www.iter.org/. Accessed 05.23.2015.

[13] *Wendelstein 7-X*. https://www.ipp.mpg.de/16900/w7x. Accessed 05.23.2015.

[14] M. Kikuchi et al. *Fusion Physics*. International Atomic Energy Agency, 2012.

[15] Koch R. Carolus Magnus Summer School, 2003.

[16] Lamalle P. et al. *Status of the ITER ion cyclotron H and CD system*. Fus. Eng. Des., 88:517–520, 2013.

[17] Mayoral M.-L. et al. *Coupling of the JET ICRF antennas in ELMy H-mode plasmas with ITER-relevant plasma-straps distance*. AIP Conf. Proc., 933:55, 2007.

[18] Lacellotti V., Milanesio D., Maggiora R., Vecchi G., and Kyrytsya V. *TOPICA: an accurate and efficient numerical tool for analysis and design of ICRF antennas*. Nucl. Fusion, 46:S476–S499, 2006.

[19] Milanesio D., Lancelotti V., Colas L., Maggiora R., Kyrytsa V., and Vecchi G. *Analysis of the Tore Supra ICRF antenna with TOPICA*. Plasma Phys. Control. Fusion, 49:405–419, 2007.

[20] Pinsker R. I. et al. *Recent results on coupling fast waves to high performance plasmas on DIII-D*. AIP Conference Proceedings, 1406:313–320, 2011.

[21] Durodié F. et al. *Physics and engineering results obtained with the ion cyclotron range of frequencies ITER-like antenna on JET*. Plasma Phys. Control. Fusion, 54:074012, 2012.

[22] Messiaen A. and Weynants R. *ICRH antenna coupling physics and optimum plasma edge density profile*. Plasma Phys. Control. Fusion, 53:085020, 2011.

[23] Van Wassenhove G. et al. *Impact of gas injection on ICRF antenna loading properties on TEXTOR*. 38th EPS Conf. on Plasma Physics, 35G:P–5.098, 2011.

[24] Stepanov I. et al. *Analysis of ICRH antenna loading data in TEXTOR obtained during gas injection experiments*. AIP Conf. Proc., 1406:85, 2011.

[25] Jaquet P. et al. *Improvement of ICRF antenna loading by local gas injection on ASDEX Upgrade*. Nucl. Fusion, 52:042002, 2012.

[26] Bobkov V. et al. *Influence of gas injection location and magnetic perturbations on ICRF antenna perfomance in ASDEX Upgrade*. AIP Conf. Proc., 1580:271, 2014.

[27] Pinsker R. I. et al. *Experiments on gas puffing to enhance ICRF antenna coupling*. 37th EPS Conf. on Plasma Physics, 34A:O4.124, 2010.

[28] Bilato R. et al. *JET ICRF antennas coupling on extreme plasma shapes*. 31st EPS Conf. on Plasma Physics and Controlled Fusion, 28G:P–5.164, 2004.

[29] Bobkov V. et al. *ICRF antenna coupling dependence on edge plasma conditions in ASDEX Upgrade*. Nucl. Fusion, 46:S469–S475, 2006.

[30] T. H. Stix. *Waves in Plasmas*. American Institute of Physics, New York, 1992.

[31] D. G. Swanson. *Plasma Waves*. Academic Press, Inc., San Diego, 1989.

[32] M. Brambilla. *Kinetic Theory of Plasma Waves: Inhomogeneous Plasmas*. Oxford University Press, Oxford, 1998.

[33] Brambilla M. *The Physics of Ion Cyclotron Heating in Tokamaks*. Technical report, Max-Planck-Institut.

[34] M. Brambilla. *A review of antenna theory for fusion plasmas*. Unpublished.

[35] Porkolab M. *Plasma heating by fast magnetosonic waves in tokamaks*. In AIP Conference Proceedings, pages 99–99, 1994.

[36] E. Philippow. *Grundlagen der Elektrotechnik*. VEB Verlag Technik, Berlin, 1988.

[37] Noterdaeme J. M. et al. *The ASDEX Upgrade ICRH antenna*. Fusion Eng. Des., 24:65–74, 1994.

[38] Swain D. W. et al. APS Division of Plasma Physics Meeting, 2001.

[39] Lombardini P. P. et al. *Criteria for the design of loop-type directional couplers for the L band*. IRE Transactions on Microwave Theory and Techniques, pages 234–239, 1956.

[40] Faugel H. et al. *Measuring impedance and power in ICRF antenna feeding lines with voltage and current probes*. AIP Conf. Proc, 1406:113, 2011.

[41] Parisot A., Wukitch S. J., Bonoli P., Hughes J. W., LaBombard B., Lin Y., Parker R., Porkolab M., and Ram A. K. *ICRF loading studies on Alcator C-mod*. Plasma Phys. Control. Fusion, 46:1781–1792, 2004.

[42] Clairet F. et al. *ICRF coupling and edge density profile on Tore Supra*. Plasma Phys. Control. Fusion, 46:1567–1580, 2004.

[43] Bobkov V. et al. *Influence of ELMs on operation of ICRF antennas in ASDEX Upgrade*. J. Nucl. Mater., 337-339:776–780, 2005.

[44] Nightingale M. P. S. et al. *Overview on experiments on ITER-like antenna on JET and ICRF antenna design for ITER*. AIP Conf. Proc., 1187:213, 2009.

[45] Swain D. W. et al. *Measurements of ICRF loading on DIII-D with and without a Faraday shield*. Nucl. Fusion, 37:211, 1997.

[46] Brambilla M. *Finite Larmor radius wave equations in tokamak plasmas in the ion cyclotron frequency range*. Plasma Phys. Control. Fusion, 31:723–757, 1989.

[47] Brambilla M. *The FELICE code*. Unpublished.

[48] Koch R. *The coupling of electromagnetic power to plasmas*. Fusion Sci. Technol., 53.2T:184–193, 2008.

[49] Maggiora R., Vecchi G., Lancelotti V., and Kyrytsya V. *Efficient 3D/1D self-consistent integral-equation analysis of ICRH antennae*. Nucl. Fusion, 44:846–868, 2004.

[50] Milanesio D. *The TOPICA code*.

[51] Messiaen A., Koch R., Weynants R. R., Dumortier P., Louche F., Maggiora R., and Milanesio D. *Performance of the ITER ICRH system as expected from TOPICA and ANTITER II modelling*. Nucl. Fusion, 50:025026, 2010.

[52] *MATLAB 2013b*.

[53] Myra J. R. *Fast wave evanescence in filamentary boundary plasmas*. Phys. Plasmas, 21:022507, 2014.

[54] Van Eester D., Crombe K., and Kyrytsya V. *Ion cyclotron resonance heating-induced density modification near antennas*. Plasma Phys. Control. Fusion, 55:025002, 2013.

[55] Colas L. et al. *Understanding the spatial structure of RF-induced SOL modifications*. Plasma Phys. Control. Fusion, 49:B35–B45, 2007.

[56] D'Ippolito D. A. et al. *Analysis of RF sheath interactions in TFTR*. Nucl. Fusion, 38:1543, 1998.

[57] Brambilla M. *Numerical simulation of ion cyclotron waves in tokamak plasmas*. Plasma Phys. Control. Fusion, 41:1–34, 1999.

[58] Jaeger E. F. et al. *Global-wave solutions with self-consistent velocity distributions in ion cycloton heated plasmas*. Nucl. Fusion, 46:S397–S408, 2006.

[59] Bilato R., Brambilla M., Hartmann D. A., and Parisot A. *Influence of an evanescence layer in front of the antenna on the coupling efficiency of ion cyclotron waves*. Nucl. Fusion, 45:L5–L7, 2005.

[60] Stober J., Gruber O., Kallenbach A., Mertens V., Ryter F., Staebler A., Suttrop W., Treutterer W., and the ASDEX Upgrade team. *Effects of triangularity on confinement, density limit and profile stiffness of H-modes on ASDEX Upgrade*. Plasma Phys. Control. Fusion, 42:A211–A216, 2000.

[61] Ryter F. et al. *Confinement and transport studies of conventional scenarios in ASDEX Upgrade*. Nucl. Fusion, 41:537, 2001.

[62] Wolfrum E. et al. *Characterization of edge profiles and fluctuations in discharges with type-II and nitrogen-mitigated edge localized modes in ASDEX Upgrade*. Plasma Phys. Control. Fusion, 53:085026, 2011.

[63] Oyama N. et al. *Pedestal conditions for small ELM regimes in tokamaks*. Plasma Phys. Control. Fusion, 48:A171–A181, 2006.

[64] Stober J., Maraschek M., Conway G. D., Gruber O., Herrmann A., Sips A. C. C., Treutterer W., Suttrop W., Zohm H., and the ASDEX Upgrade team. *Type II ELMy H-modes on ASDEX Upgrade with good confinement at high density*. Nucl. Fusion, 41:1123, 2001.

[65] Kallenbach A. et al. *Closed divertor operation in ASDEX Upgdade and JET*. Plasma Phys. Control. Fusion, 41:B177–B189, 1999.

[66] Fischer R., Fuchs J. C., McDermott R., Rathgeber S. K., Suttrop W., Millensdorfer M., and Wolfrum E. the ASDEX Upgrade team. *Spatiotemporal response of plasma edge density and temperature to non-axisymmetric magnetic perturbations in ASDEX Upgrade*. Plasma Phys. Control. Fusion, 54:115008, 2012.

[67] Mueller H. W. et al. *Modification of scrape-off layer transport and turbulence by non-axisymmetric magnetic perturbations in ASDEX Upgrade*. J. Nucl. Mater., 538:S64–S71, 2013.

[68] Krivska A., Ceccuzzi S., Milanesio D., Bobkov V., Braun F., Maggiora R., Noterdaeme J.-M., and Tuccillo A. A. *Density profile sensitivity study of ASDEX Upgrade ICRF antennas with the TOPICA code*. AIP Conference Proceedings, 1406:93–96, 2011.

[69] Ceccuzzi S. et al. *Assessment of ion cyclotron antenna performance in ASDEX Upgrade using TOPICA*. Int. J. Appl. Electrom., 39:59–64, 2012.

[70] Fischer R., Wolfrum E., Schweinzer J., and the ASDEX Upgrade team. *Probabilistic Lithium beam data analysis*. Plasma Phys. Control. Fusion, 50:085009, 2008.

[71] Stepanov I. et al. *Impoved measurements of ICRF antenna input impedance at ASDEX Upgrade during ICRF coupling studies*. AIP Conf. Proc., 1580:275, 2014.

[72] Bobkov V. et al. *Influence of gas injection location and magnetic perturbations on ICRF antenna perfomance in ASDEX Upgrade*. AIP Conf. Proc., 1580:271, 2014.

[73] Goniche M., Brémond S., and Colas L. *Global analysis of ICRF wave coupling on Tore Supra*. Nucl. Fusion, 43:92–106, 2003.

[74] K Rothemund, M Glock, H W annd Borecky, and U Van Rienen. *Eigenmode calculation in long and complex RF structures using the coupled S-parameter calculation technique*. Technical Report DESY-TESLA-2000-33, DESY, Hamburg, Nov 2000.

[75] Verdoolaege G. *Geodesic least squares regression for scaling studies in magnetic confinement fusion*. In AIP Conference Proceedings, pages 564–571, 2014.